Universität Münster

Gauthier Legras

Correlating hard and soft particle production at the LHC via multiplicity-dependent prompt and non-prompt J/ψ measurement

Correlating hard and soft particle production at the LHC via multiplicity-dependent prompt and non-prompt J/ψ measurement

Inaugural-Dissertation
zur Erlangung des Doktorgrades
der Naturwissenschaften im Fachbereich Physik
der Mathematisch-Naturwissenschaftlichen Fakultät
der Universität Münster

vorgelegt von
Gauthier Legras
aus Châtenay-Malabry

– Münster, 2025–

Abstract

The hadronic production of the J/ψ meson, a bound state of a charm and an anticharm quark, is a strong probe of the theory of Quantum Chromodynamics (QCD), which describes the strong interaction between colour charges. Due to their large mass, the heavy quarks are produced in a scattering with a large momentum transfer (hard scattering). In contrast, most charged particles are produced in scatterings with small momentum transfer (soft scatterings). Therefore, measurements of the correlation between J/ψ production and the charged-particle multiplicity in hadronic collisions could provide more information about the interplay and differences between hard and soft particle production.

Previous measurements of the multiplicity dependence of J/ψ production in small hadronic systems have shown a stronger-than-linear increase of the relative yields with the event multiplicity. This trend shows that there seems to exist a fundamental difference between hard and soft particle production. A substantial part of the J/ψ are produced through the decay of beauty hadrons. The analysis of the multiplicity dependence of these non-prompt J/ψ could help to identify the difference in the multiplicity dependence between charm and beauty, and between open heavy-flavor hadrons (i.e. hadrons which have non-zero net heavy-flavor content, e.g. a heavy quark together with a light quark) and quarkonium.

Several models explain the stronger-than-linear trend through either initial-state effects, such as a saturation of the gluon density distribution at small momentum fraction inside the initial proton, or final-state effects, where soft particle production could be saturated within a high-density medium similar to the Quark-Gluon Plasma (QGP) produced in heavy-ion collisions. In addition, studies with the PYTHIA8 generator have demonstrated that the autocorrelations (i.e. particles produced alongside the J/ψ in the same production process) could also influence the trend. These autocorrelation effects could be disentangled by separating the multiplicity in several azimuthal regions with respect to the J/ψ emission direction.

Therefore, this thesis is dedicated to the measurement of the multiplicity dependence of prompt and non-prompt J/ψ production at midrapidity, using data collected by the ALICE experiment at $\sqrt{s} = 13$ TeV during the Run 2 of the LHC. The evolution of the prompt yield is found to be similar to the one of non-prompt yields, with only a slight hint of an increase of the non-prompt fraction with the multiplicity. Thus, the evolution of quarkonia yield with the multiplicity should not present significant differences from the open heavy-flavor ones. This also shows the similarity between charm and beauty evolution with multiplicity.

The J/ψ yields are further measured as a function of the multiplicity in three azimuthal regions. A strong increase as a function of the multiplicity in the toward region is measured, which indicates that the autocorrelations might play a role in the observed multiplicity dependence.

Abstract

In addition, a stronger increase when increasing the p_{T} of the J/ψ is present in the toward region, but not in the transverse region, showing that autocorrelations should be important in explaining the evolution with p_{T}. The increase in the transverse and away region is stronger compared to the expectations of a baseline of soft particle production, demonstrating that the increase of the J/ψ yield is also a global effect of the different scales, and that autocorrelations are probably not the only effects at play.

Zusammenfassung

Die hadronische Produktion des J/ψ-Mesons, einem gebundenen Zustand aus einem Charm- und einem Anticharm-Quark, stellt eine starke Prüfung der Theorie der Quantenchromodynamik (QCD) dar, welche die starke Wechselwirkung zwischen Farbladungen beschreibt. Aufgrund ihrer großen Masse werden die schweren Quarks in Streuprozessen mit großem Impulsübertrag (harte Streuung) erzeugt. Im Gegensatz dazu entstehen die meisten geladenen Teilchen in Streuprozessen mit kleinem Impulsübertrag (weiche Streuung). Daher können Messungen der Korrelation zwischen der J/ψ-Produktion und der Multiplizität geladener Teilchen in hadronischen Kollisionen zusätzliche Informationen über das Zusammenspiel und die Unterschiede zwischen harter und weicher Teilchenproduktion liefern.

Frühere Messungen der Multiplizitätsabhängigkeit der J/ψ-Produktion in kleinen hadronischen Systemen haben einen stärker-als-linearen Anstieg der relativen Produktion mit der Multiplizität gezeigt. Dieser Trend deutet darauf hin, dass ein fundamentaler Unterschied zwischen harter und weicher Teilchenproduktion zu bestehen scheint. Ein wesentlicher Teil der J/ψ-Mesonen stammt außerdem aus dem Zerfall von Beauty-Hadronen. Die Analyse der Multiplizitätsabhängigkeit dieser nicht-prompten J/ψ könnte daher helfen, die Unterschiede in der Multiplizitätsabhängigkeit zwischen Charm und Beauty sowie zwischen offenen Schwerflavour-Hadronen (d. h. Hadronen mit einem Netto-Schwerflavourgehalt, z. B. einem schweren und einem leichten Quark) und Quarkonium zu identifizieren.

Mehrere Modelle erklären den stärker-als-linearen Trend entweder durch Effekte im Anfangszustand, wie die Sättigung der Gluondichteverteilung bei kleinem Impulsanteil im Proton, oder durch Effekte im Endzustand, bei denen die weiche Teilchenproduktion in einem hochdichten Medium – ähnlich dem Quark-Gluon-Plasma (QGP), das in Schwerionenkollisionen entsteht – gesättigt sein könnte. Darüber hinaus haben Studien mit dem Generator PYTHIA8 gezeigt, dass Autokorrelationen (d. h. Teilchen, die zusammen mit dem J/ψ im selben Produktionsprozess erzeugt werden) ebenfalls den beobachteten Trend beeinflussen könnten. Diese Autokorrelationseffekte lassen sich durch die Aufteilung der Multiplizität in verschiedene azimutale Regionen relativ zur Emissionsrichtung des J/ψ voneinander trennen.

Diese Arbeit ist daher der Messung der Multiplizitätsabhängigkeit der prompten und nicht-prompten J/ψ-Erzeugung bei zentraler Rapidität gewidmet, unter Verwendung von Daten, die vom ALICE-Experiment bei einer Schwerpunktsenergie von $\sqrt{s} = 13$ TeV während Run 2 des LHC gesammelt wurden. Die Entwicklung der prompten Erzeugung erweist sich als ähnlich der der nicht-prompten, mit lediglich einem leichten Hinweis auf einen Anstieg des nicht-prompten Anteils mit zunehmender Multiplizität. Somit sollte die Entwicklung des Quarkonium-Erzeugung mit der Multiplizität keine signifikanten Unterschiede zu derjenigen der offenen Schwerflavour-

Hadronen aufweisen. Dies zeigt auch die Ähnlichkeit zwischen der Entwicklung von Charm und Beauty mit der Multiplizität.

Die J/ψ-Erzeugung wird zudem als Funktion der Multiplizität in drei azimutalen Regionen gemessen. Der starke Anstieg als Funktion der Multiplizität in der toward-Region zeigt, dass Autokorrelationen eine Rolle in der beobachteten Multiplizitätsabhängigkeit spielen könnten. Darüber hinaus wird ein stärkerer Anstieg mit zunehmendem p_T des J/ψ in der toward-Region, jedoch nicht in der transverse-Region beobachtet, was darauf hinweist, dass Autokorrelationen eine wichtige Rolle bei der Erklärung der Entwicklung mit p_T spielen. Der stärkere Anstieg in der transverse- und away-Region im Vergleich zu einer Basislinie der weichen Teilchenproduktion zeigt, dass der Anstieg der J/ψ-Erzeugung auch ein globaler Effekt verschiedener Skalen ist und dass Autokorrelationen wahrscheinlich nicht die einzigen wirksamen Effekte darstellen.

Contents

1. Introduction

The theory of Quantum Chromodynamics (QCD) investigate the effect of the strong interaction. In particular, at high enough temperature, such as the ones present in the first microseconds of the universe, a deconfined state know as the Quark-Gluon Plasma (QGP) is present. This state can be recreated in the laboratory by means of collisions of heavy-ions. Recently, it was noticed that some signatures which were normally used to probe the QGP formation could also be present in high-multiplicity proton-proton collisions. This leads to an increased interest for the study of these high-multiplicity pp collisions, and the measurement of the multiplicity dependence of J$/\psi$ production fits within this interest.

This thesis is organized as explained in the following. Chapter 1 is dedicated to an overview of the physical concepts, in particular related to the QGP, necessary to understand the rest of this thesis. Chapter 2 reviews the current experimental and theoretical developments regarding J$/\psi$ production in hadronic collisions, especially with the multiplicity dependence. Chapter 3 presents the ALICE experiment during the Run 2 of the LHC, including the detectors used for the analysis of this thesis, as well as how the reconstruction of events and tracks is performed. The next chapters report the details of the analysis conducted in this thesis. In particular, chapter 4 explains how the multiplicity is computed, while chapter 5 details the measurement of J$/\psi$ yields, and chapter 6 estimates the systematic uncertainties of the measurement. Finally, chapter 7 describes the results obtained within this thesis and gives an interpretation of these results. During the writing of this thesis, AI tools were used for grammar checks only.

1.1. Particles and interactions

1.1.1. The Standard Model

Understanding matter and unraveling its composition to the smallest measurable element has always been a dream of scientists through all ages. The most elementary particles which are currently known are grouped within the Standard Model of particle physics. These particles and their properties (mass, charge, spin) are summarized in Fig. 1.1. They can first be classified between bosons, characterized by an integer spin, and fermions, whose spin is half-integer. Contrary to bosons, fermions obey the Pauli principle, which states that two fermions cannot be found in the same state at the same time.

The Standard Model accounts for the fundamental forces which drive the interactions at the particle level. These fundamental interactions, mediated by gauge bosons, are the electromagnetic interaction, the strong interaction, and the weak interaction. In addition, a fourth known interaction is the gravitation, affecting massive particle. However, no unified theory has been

Standard Model of Elementary Particles

	three generations of matter (fermions)			interactions / force carriers (bosons)	
	I	II	III		
mass charge spin	≈2.16 MeV/c² ⅔ ½ **u** **up**	≈1.273 GeV/c² ⅔ ½ **c** **charm**	≈172.57 GeV/c² ⅔ ½ **t** **top**	0 0 1 **g** **gluon**	≈125.2 GeV/c² 0 0 **H** **higgs**
	≈4.7 MeV/c² −⅓ ½ **d** **down**	≈93.5 MeV/c² −⅓ ½ **s** **strange**	≈4.183 GeV/c² −⅓ ½ **b** **bottom**	0 0 1 **γ** **photon**	
	≈0.511 MeV/c² −1 ½ **e** **electron**	≈105.66 MeV/c² −1 ½ **μ** **muon**	≈1.77693 GeV/c² −1 ½ **τ** **tau**	≈91.188 GeV/c² 0 1 **Z** **Z boson**	
	<0.8 eV/c² 0 ½ **ν$_e$** **electron neutrino**	<0.17 MeV/c² 0 ½ **ν$_μ$** **muon neutrino**	<18.2 MeV/c² 0 ½ **ν$_τ$** **tau neutrino**	≈80.3692 GeV/c² ±1 1 **W** **W boson**	

QUARKS — **LEPTONS** (fermions). **GAUGE BOSONS / VECTOR BOSONS**, **SCALAR BOSONS**.

Figure 1.1.: Particles of the Standard Model of particle physics [1]. Taken from [2].

found to describe gravitation along with particle physics, therefore gravitation is not part of the Standard Model. The electromagnetic interaction, responsible for attraction and repulsion between electrically charged particles, is mediated by the photon. The strong interaction is described via the exchange of gluons. It is able to confine matter into hadrons. The weak interaction, with smaller strength and range than other interactions, is carried by the massive $W^{\pm}$ and Z bosons. Finally, the last boson belonging to the Standard Model, but without mediating an interaction, is the Higgs boson. This boson gives mass to the different particles through the Brout-Englert-Higgs mechanism.

There are two types of elementary fermions: the leptons and the quarks. The leptons, divided into three generation, do not interact strongly. The leptons from different generations exhibit very similar properties except for their mass. The first generation contains the electron (e^-), its antimatter counterpart, the positron (e^+), as well as the electron-neutrino (ν_e) and -antineutrino ($\overline{\nu}_e$). While the electron is charged, the neutrinos are neutral, which means that they can only interact weakly, causing very small cross-sections for interactions between neutrinos and other particles. The second generation consists of the muon (μ^-), the antimuon (μ^+) and the associated neutrinos, while the third generation comprises the tau (τ^-), antitau (τ^+) and neutrinos. The mass of the tau is larger than the one of the muon, which is itself larger than the electron mass. The Standard Model also contains three generations of quarks, ordered by their mass. The first quark generation contains down (d) and up (u) quarks, while the second one includes the strange (s) and charm (c) quarks, and the third one comprises the bottom (b) and top quarks (t). All quarks also have an associated antiquark. The quarks carry a color charge which allows them to interact strongly, and can also interact electromagnetically, through their electric charge of 2/3 for u, c and t and -1/3 for d, s and b. Similarly to the leptons, they can also be affected by the

weak interaction. In particular, quarks and leptons from heavier generations are able to decay to lighter ones via the weak interaction.

Rather than classical particles, a full mathematical description of the Standard Model needs the use of quantum fields. The particles represent the excitations of these fields. Dynamics of these fields and interactions with other fields can be encoded in the Lagrangian of the Standard Model [3], given as:

$$\mathcal{L}_{\mathrm{SM}} = -\frac{1}{4}F_{\mu\nu}F^{\mu\nu} + \sum_j \overline{\psi}_j i\gamma^\mu D_\mu \psi_j + \sum_{i,j} \psi_i y_{ij} \psi_j \phi + \mathrm{h.c.} + \mathcal{L}_{\mathrm{QCD}} - V(\phi) + |D_\mu \phi|^2. \quad (1.1)$$

The first term is the kinetic term for the electroweak field. The kinetics and interactions with gauge bosons for the lepton fields ψ_i are described by the second term, while the following term and its hermitian conjugate account for the Yukawa coupling between the leptons and the Higgs field ϕ. This coupling gives rise to lepton masses. $\mathcal{L}_{\mathrm{QCD}}$ is the Lagrangian of QCD, and will be developed in Sec. 1.1.2. Finally, the last two terms represent the Higgs field potential and its interaction with other electroweak bosons, respectively.

One of the central observables which can be computed from the equations describing the Standard Model and the interactions between the fields are cross-sections, representing interaction probabilities. Although the mathematical calculations of these cross-sections are complex, they can be commonly represented graphically through Feynman diagrams. An example of such diagram is shown in Fig. 1.2. In this case, the diagram represents the annihilation of an electron-positron pair which creates a quark-antiquark pair together with a gluon, $e^+e^- \rightarrow q\bar{q}g$. This interaction is mediated by the electromagnetic interaction through a photon γ. This photon is present neither in the initial nor in the final state, hence it cannot be measured by experiment. Such a particle is called virtual. In the experiments, different cases with the same initial and final particles but with different intermediate virtual particles, e.g. a Z boson, cannot be distinguished one from another. Hence, all possible diagrams, and the interferences between them, must be taken into account. In the diagrams, the different particles are connected through vertices, representing the interactions between the different fields, for example an electromagnetic annihilation of the e^+e^- pair, or the emission of the gluon by a quark through strong force. The Standard Model also characterizes the strength of these interactions through coupling constants. The values of the coupling constants are not predicted theoretically, but have to be measured experimentally. For the electromagnetic force, its value is approximately $\alpha_{em} \approx 1/137$. For the strong interaction, the coupling is stronger and the coupling constant value α_S reaches the order of unity when the momentum transfer is low.

For cross-sections calculations, infinitely many Feynman diagrams would need to be considered. They can be sorted into orders through an expansion on the coupling constant, with the assumption that its value is small. Leading Order (LO) terms usually depend on α_S or α_{em} while Next-to-Leading Order (NLO) and subsequent orders (NNLO,...) depend on powers of α_S or α_{em}. Within the Feynman diagram formalism, loop diagrams containing more vertices represent higher-order terms. Because the number of possible diagrams quickly increases with the number
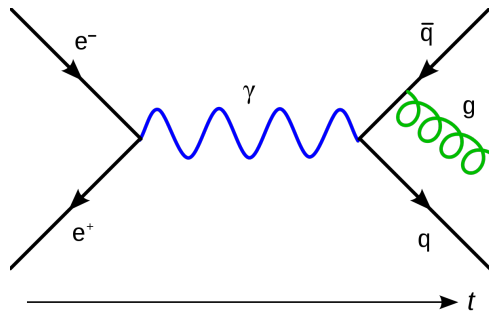
Figure 1.2.: Example of a Feynman diagram, representing the annihilation of an electron and a positron through the electromagnetic interaction, the creation of a quark-antiquark pair from electromagnetic interaction and the emission of a gluon through the strong interaction. Taken from [4].

of vertices, higher-order terms become more and more difficult to calculate. Thanks to the small electromagnetic coupling constant, the higher-order term in the series for electromagnetic interactions become negligible quickly. However, for the strong interaction, the series expansion converges very slowly, leading to large uncertainties in the theoretical calculations.

Nevertheless, the Standard Model is incomplete and cannot explain all phenomena observed in nature. For example, it does not incorporate dark matter, which represent around 25% of the content of the universe. The Standard Model is also not able to explain the asymmetry between matter and antimatter in the universe. In addition, no consistent framework supported by experimental data has been able to account for gravitation within the formalism of the Standard Model of particle physics.

1.1.2. Quantum Chromodynamics (QCD)

QCD is the theory which describes the dynamics of the strong interaction, acting between particles that carry a color charge. The color space is three-dimensional, which means that excitations of the quark fields carry one of the three colors, while gluons, by acting on color charges, carry color and anticolor. Out of the nine possible color-anticolor combinations, one is unphysical, since it cannot modify color states and corresponds to a color singlet. This leaves eight gluon fields, forming a color octet. The Lagrangian of QCD can be written as [5]:

$$\mathcal{L}_{\text{QCD}} = \sum_j \overline{\psi}_j^c i\gamma^\mu D_\mu \psi_j^c + \sum_{i,j} \psi_i^c y_{ij} \psi_j^c \phi + \text{h.c.} - \frac{1}{4} G_{\mu\nu}^a G^{a\mu\nu} \,. \tag{1.2}$$

Here, ψ_j^c represent the quark fields, for the six flavors j and three colors c. The associated terms contain the kinetic component, the interactions with the gauge bosons, and with the Higgs field. $G_{\mu\nu}^a$ represents the gluon field strength tensor, for each one of the eight gluons. It can be written as

$$G_{\mu\nu}^a = \partial_\mu A_\nu^a - \partial_\nu A_\mu^a + g_s f^{abc} A_\mu^b A_\nu^c \,. \tag{1.3}$$

A_ν^a is the gluon field. Because gluons can interact with other gluons, QCD is non-abelian. This fact is represented by the last term.

In ordinary matter, quarks cannot be found isolated, but are observed confined inside hadrons. This property is due to the strong interaction, which cause hadrons to be colorless, i.e. they overall do not carry a color charge. The most simple colorless states can be formed by either three color or anticolor charges or one color with one anticolor charge. The first case corresponds to baryons, whose main constituents are three quarks (or three antiquarks for the antibaryons), while the second case represents mesons, made of a quark and an antiquark. This can also be extended to hadrons containing more quarks, such as tetraquarks, which are formed of two quarks and two antiquarks, or pentaquarks, with four quarks and one antiquark or four antiquarks and one quark.

Particle interactions can be screened when clouds of virtual particles form between the two particles responsible for the original interaction. The strength of this screening vary with the energy scale at play within the interaction. This causes, despite the name coupling constants, the coupling strengths to vary with the energy scale. Nevertheless, this scale cannot affect observable quantities such as cross-sections. When increasing the momentum transfer Q^2, the value of $\alpha_{em}(Q^2)$ slightly increases, while the value of $\alpha_S(Q^2)$ decreases. Such a decrease, towards smaller values at high Q^2, is called asymptotic freedom. The theory of QCD does not predict a value for α_S, but is able to calculate the evolution of its value with the scale, also known as the running of the coupling constant. Taking into account the virtual particle loops in the Feynman diagrams, it can be shown that the coupling constant is written at LO as [6, 7]:

$$\alpha_S(Q^2) \approx \frac{12\pi}{(33 - 2N_f)\ln(Q^2/\Lambda_{QCD}^2)} \,. \tag{1.4}$$

N_f is the number of quark flavors relevant at the given scale (e.g. $N_f = 4$ when $m_c^2 < Q^2 < m_b^2$, where m_c and m_b are the charm and bottom quark mass, respectively). Λ_{QCD} is a parameter which has to be determined by experiment and is found to be around 200 MeV/c.

Fig. 1.3 shows measurements of the strong coupling constant at different values of Q^2. The decrease from low to high momentum transfer is in agreement with theoretical predictions. The strong coupling constant is small at high Q^2, meaning that calculations through expansion in powers of α_S are feasible. The framework for such calculations is called perturbative QCD (pQCD). In contrast, at lower momentum transfer, the value of the coupling constant is too large for such calculations to act as a reasonable approximation.

1.1.3. The Quark-Gluon Plasma (QGP)

It is generally thought that, in the early universe, the energy density in the universe was much higher than what it is nowadays. During its first microseconds, the temperature remained higher than hundreds of MeV/k_B. This was high enough to allow the existence of a state where the quarks were not confined into hadrons: the Quark-Gluon Plasma [8, 9]. Because the universe expanded, it caused a decrease in the energy density and the conditions forced the confinement of the quarks. Understanding the properties of the universe would then necessarily need a better comprehension of this deconfined state of matter and of the transition to hadrons.
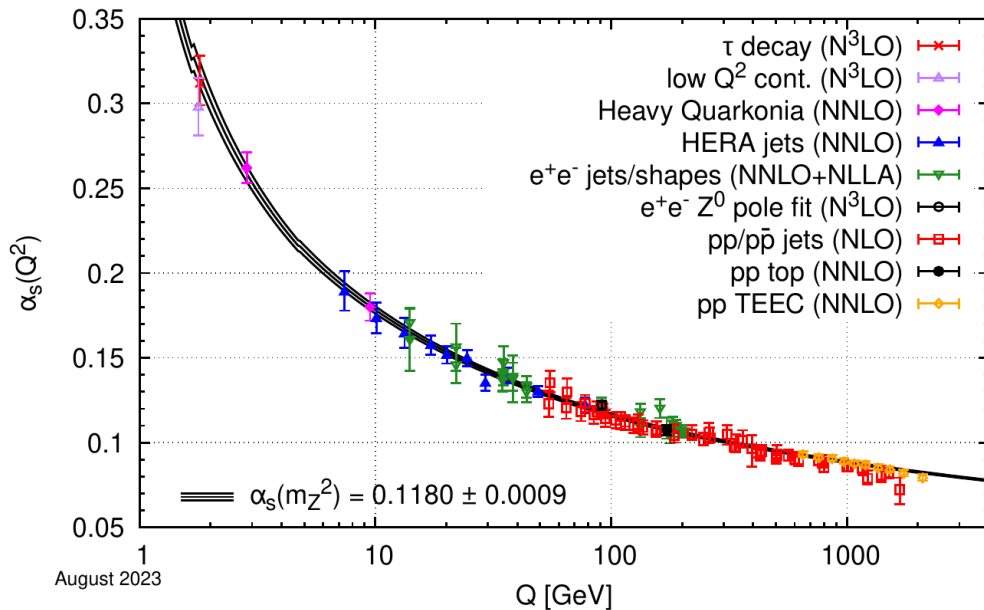
Figure 1.3.: Summary of the measurements of the value of the strong coupling constant at different values of momentum transfer Q^2. Taken from [1].

Deconfinement is qualitatively expected because of the weaker coupling between quarks and gluons at increasing temperature caused by the running of α_s. However, this does not explain quantitatively why quarks and gluons could be observed free, because the deconfinement is observed at temperatures of a few hundreds of MeV/k_B, for which α_S remains large. Properties of the QGP can nevertheless be obtained theoretically through lattice QCD. This theory framework uses a quantized space-time (lattice) in order to compute QCD properties from first principles. Quarks are put on the lattice sites and gluons on the edges. All possible paths are computed from the QCD Lagrangian. Such calculations require very large computational power, which limits the size and spacing of the lattice which can be used. The physical results correspond to the case of an infinitely small spacing and have to be extrapolated from the results with finite spacing.

Because of the degrees of freedom of quarks and gluons within the QGP, while in ordinary matter the degrees of freedom correspond to hadrons, it is expected that the thermodynamic properties are modified when the transition to QGP occurs. At low temperature, these quantities can be determined within the Hadron Resonance Gas (HRG) model [10]. This model considers that the number of hadron resonances becomes exponentially larger at higher masses. Thermodynamical properties can be calculated from a partition function taking into account all these resonances. The hadron mass spectrum provides a value for the so-called "Hagedorn" temperature, $T_H \approx 158$ MeV/k_B. For higher temperatures, the model is not valid anymore, explaining the transition to quarks and gluons degrees of freedom. Fig. 1.4 shows the evolution of energy density, entropy, and pressure as a function of the temperature, calculated through lattice QCD. Such relations between thermodynamical properties are also known as equation of state. These quantities increase with the temperature, and the change in the state of matter causes a departure from the HRG limit. The transition of these thermodynamic properties is continuous. At higher temperature, the values of the pressure, energy density and entropy are larger and close to the

Stefan-Boltzmann limit, obtained in the case of a non-interacting gas consisting of quarks and gluons. Above the transition temperature, but before the non-interacting limit is reached, the interactions between quarks and gluons are still present. The state is therefore often defined as a strongly-interacting QGP.
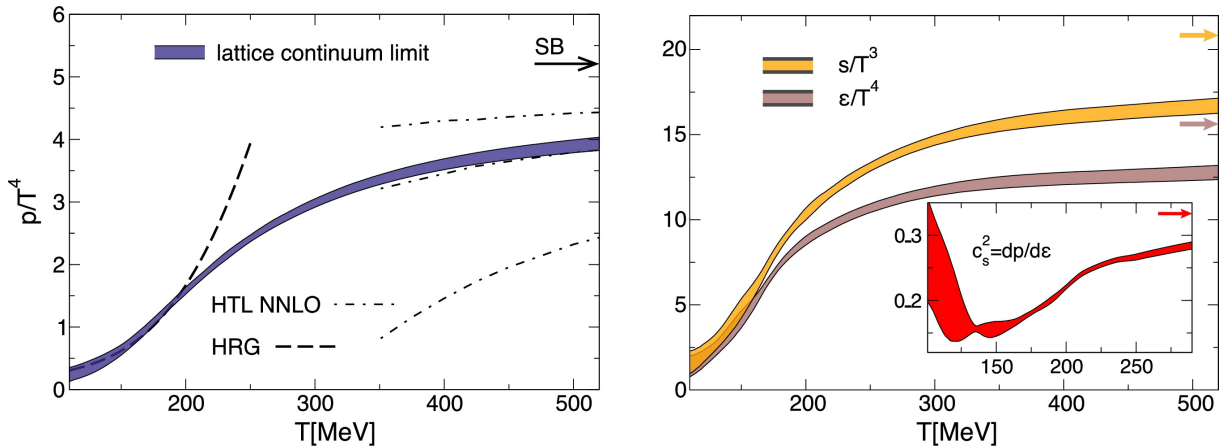
Figure 1.4.: Evolution of the normalized pressure (left) and entropy and energy density (right) as a function of temperature, from lattice QCD calculation. Also shown are the expectation from the HRG and the Stefan-Boltzmann (SB) limit of non-interacting quarks and gluons. Taken from [11].
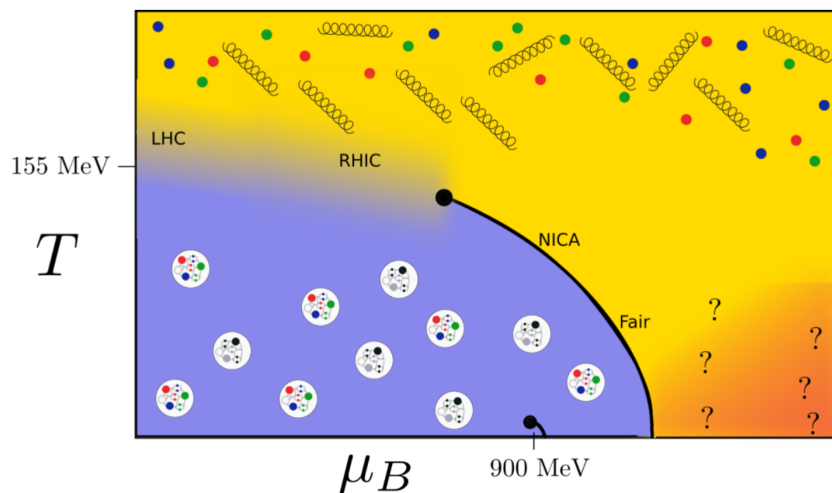
Figure 1.5.: Sketch of the phase diagramm of the different phases of QCD, shown as a function of the temperature and baryonic potential. The hadronic matter is sketched at low temperature and baryonic potential, while, at higher temperature, the quark-gluon plasma is sketched. At high temperature and μ_B, a critical point is depicted, showing the possible transition from continuous to first-order phase transition. Taken from [12].

Such a phase transition can also be seen in the phase diagram of QCD shown in Fig. 1.5. The phase diagram shows the different phases of matter observed in different regions of temperature and baryonic potential μ_B. The baryonic potential is the energy needed to increment the baryonic number by 1, thus characterizing the balance between matter and antimatter. At low baryonic potential, the transition from ordinary matter to QGP is continuous. In contrast, theories predict that a critical point could be reached when increasing μ_B. After this critical point, the transition could be of first order, i.e. the thermodynamical properties would rise infinitely steeply as a function of temperature, rather than increasing continuously as observed at low μ_B. Some lattice

QCD calculations predict a critical transition temperature of $T_c = 156.5 \pm 1.5$ MeV/k_B at low μ_B [13]. This value depends on the exact definition of the critical temperature. However, lattice QCD is not able to explore the phase diagram of QCD at higher values of baryonic potential.

1.2. High-energy hadronic and nuclear collisions

Experiments involving collisions at high energy of protons or heavy ions can recreate the different phases of QCD in the laboratory: the hadrons, the QGP, and the hadronization, i.e. the transition between QGP and hadrons. Such high-energy experiments are conducted in particular at the European Organization for Nuclear Research (CERN), with the Large Hadron Collider (LHC) and previously the Super Proton Synchrotron (SPS), and at the Brookhaven National Laboratory (BNL) with the Relativistic Heavy-Ion Collider (RHIC).

The energy and momentum of the colliding and produced particles can be expressed as 4-vectors $\boldsymbol{p} = (E, p_x, p_y, p_z)$ (note that, here, the notation with $\overline{h} = c = 1$ is chosen). The notation $\vec{p} = (p_x, p_y, p_z)$ will also be used. The norm of the 4-vector $m = \sqrt{E^2 - p_x^2 - p_y^2 - p_z^2}$, corresponding to the particle mass, is independent of the reference frame. The longitudinal direction z is chosen as the direction in which the hadrons with momentum $\boldsymbol{p_1}$ and $\boldsymbol{p_2}$ are moving before the collision. They collide with a center-of-mass energy $\sqrt{s}$, where the Mandelstam variable s is defined as $s = (\boldsymbol{p_1} + \boldsymbol{p_2})^2$. The particles produced in the collision can be characterized by several quantities: their momentum $p = \sqrt{p_x^2 + p_y^2 + p_z^2}$, their transverse momentum $p_T = \sqrt{p_x^2 + p_y^2}$, their azimuthal angle φ (i.e. the angle in the plane perpendicular to the longitudinal direction) or their longitudinal rapidity $y = \frac{1}{2}\ln((E + p_z)/(E - p_z))$. In general, the latter quantity is not accessible directly in the experiments, except if the particle species (hence the mass) is identified. For relativistic particles, the rapidity can be approximated by the pseudorapidity $\eta = -\ln(\tan(\theta/2))$, which only depends on the angle θ between the particle momentum and the longitudinal direction.

1.2.1. Initial state

Nucleons are not point-like particles, and thus, the outcome of the collision depends on the structure of the protons at the collision time. The three main valence quarks, two up quarks and one down quark in the case of protons, interact strongly through the exchange of gluons. The gluons can in turn produce loops of virtual quark-antiquark pairs. Such virtual quarks are known as sea quarks. The content of the protons in terms of valence quarks, sea quarks, and gluons can be parametrized in terms of Parton Distribution Function (PDF). The PDF $f_i(x, Q^2)$ denotes the probability to hit a parton i with a fraction x of the longitudinal momentum of the proton at a momentum scale Q^2 during the collision. The PDFs can be used to connect the cross-sections calculated from pQCD to final observables similar to the ones measured in experimental data. The production cross-sections in proton-proton collisions can be predicted via the collinear factorization formula [14]:

$$\frac{\mathrm{d}\sigma_X}{\mathrm{d}O} = \sum_{i,j} \int_0^1 \int_0^1 f_i(x_1, Q^2) f_j(x_2, Q^2) \frac{\mathrm{d}\sigma_{i,j \to X}(x_1, x_2, Q^2)}{\mathrm{d}O} \mathrm{d}x_1 \mathrm{d}x_2 + \mathcal{O}\left(\frac{\Lambda_{QCD}^2}{Q^2}\right). \tag{1.5}$$

In this case, the cross-section is calculated for particle X as a function of observable O (e.g. the transverse momentum p_{T} or the rapidity y). It can be estimated from the convolution of the PDFs, taken for parton i from the first proton and j from the second proton, with the cross-section for producing X from parton i and j, which can be calculated from pQCD. If X is a hadron, the formula needs to be convoluted in addition with a fragmentation function, which describes phenomenologically the transition from partons to hadrons. Finally, the factorization formula is only valid at leading twist (i.e. at leading order in powers of $1/Q$) and does not incorporate higher twist effects which are suppressed by factors of $1/Q^2$, such as correlation with other partons inside the protons for example.

The PDFs are determined by several collaborations via a parametrization. The set of parameters describing the PDFs are chosen such that they minimize a χ^2 between predictions and experimental data, especially of high-energy proton-proton collisions and Deep Inelastic Scattering of electrons on protons. Some data, especially at low p_{T}, need to be discarded as they are far off the regime of applicability of pQCD calculations. In addition, the PDFs at one value of the scale can be evolved to obtain the PDFs at another value of the scale by means of the DGLAP equations [15]. An example of PDFs, obtained by the NNPDF collaboration [16], is shown in the left panel of Fig. 1.6. First, it can be observed that the PDFs for valence quarks (u_v and d_v) peak at $x \approx 1/3$. This can be understood by the fact that the valence quarks have approximately one third of the momentum of the proton. The PDFs for the sea quarks and the gluons rise with lower x. It can be noticed that the increase is much stronger for gluons than for quarks (the reader should note that, in the figure, the gluon PDF is divided by 10).
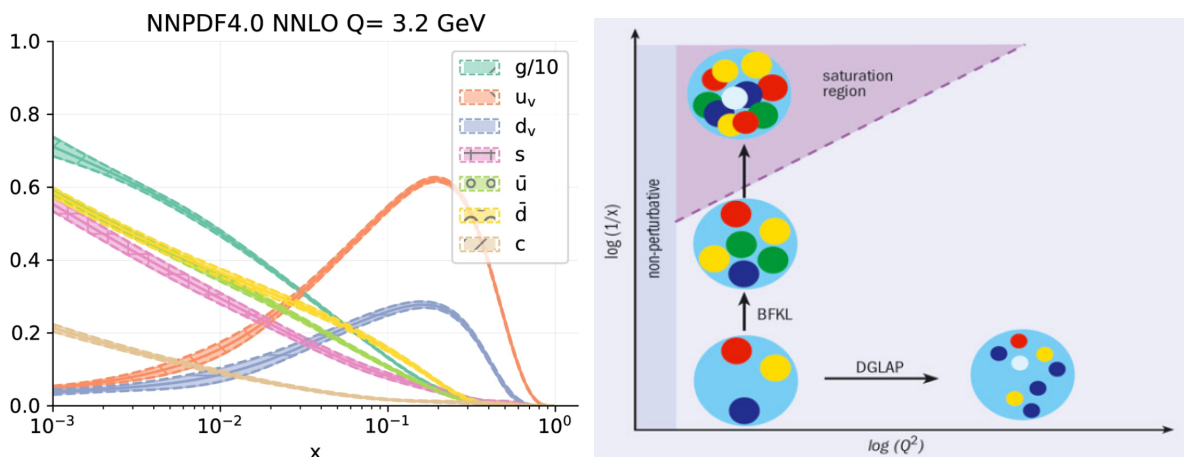
Figure 1.6.: Left: Parton Distribution Functions as a function of the momentum fraction for several partons, determined by the NNPDF collaboration. Taken from [16]. Right: Sketch of the evolution of the proton structure with x and Q^2, towards saturation at low x. Taken from [17].

In addition, when a nucleon is not free, but bound inside a nucleus, its constituents PDFs will be modified. These modified PDF inside a nucleus are known as nuclear Parton Distribution Function (nPDF). The nPDFs can be estimated using, as an example without being restricted

to it, experimental data taken from collisions between a proton and a nucleus. nPDFs represent Cold Nuclear Matter (CNM) effects, which should be distinguished from the hot nuclear matter effects due to the QGP.

While the number of gluons increases strongly when decreasing x, it is generally thought that there exists a value of x for which the increase of their number would saturate. Indeed, when the gluon density is very high, gluons can recombine through processes such as the fusion of two gluons. Contrary to the $g \to gg$ processes, the rate for the $gg \to g$ process depends on the squared gluon density. This implies non-linear effects in the evolution. The non-perturbative evolution of the gluon PDF as a function of x in the linear regime can be described with the BFKL equation [18], as is sketched in the right panel of Fig. 1.6. However, in the non-linear regime, other evolution equations are needed such as JIMWLK or BK equations. When the gluon density becomes high enough such that the $g \to gg$ and $gg \to g$ processes compensate, the number of gluons will stop to increase with decreasing x. The saturation region, visible in the sketch, is then reached. The limit at which saturation effects becomes visible also depends on the momentum scale probed. This can be understood from the fact that the spatial extent of the virtual gluons decreases when the scale at which the system is probed increases. The x-dependent scale at which this saturation occurs is called the saturation scale Q_s^2. The saturation of the gluon density is generally taken into account within the Color Glass Condensate (CGC) framework, where the high-x partons act as color sources, while the dense low-x partons are treated as color fields [19]. When considering a nucleus with atomic mass number A, the Lorentz contraction in the longitudinal direction causes the gluon density to increase by a factor of approximately $A^{1/3}$, causing larger saturation effects. The saturation effects mentioned in this paragraph have not been observed without doubt in experimental data.

1.2.2. Evolution of a heavy-ion collision

The most promising way to recreate conditions of high-energy density close to the ones at the beginning of the universe and necessary for the formation of a QGP is by colliding heavy nuclei accelerated to high energies.

When they are colliding, the large nuclei might not overlap completely. The impact parameter b, i.e. the distance between the centers of the two nuclei, determines the size of the interaction region, as sketched in Fig. 1.7. Depending on the impact parameter, only a fraction of the nucleons participate in the collision, while the other nucleons are known as the spectator nucleons. The number of participating nucleons determines the size of the QGP created in the collision. This can be quantified by the centrality of the collision. The centrality is divided in classes representing percentiles of the impact parameter. For example, the 0–10% class represents the 10% collisions with the smallest impact parameters. The smallest impact parameters form central collisions, while the largest impact parameters inelastic interaction between the nuclei produce peripheral collisions. The impact parameter is not directly measurable experimentally. Therefore, experiments generally use centrality estimators based on the number of particles or the total signal measured in a given detector. A typical model for the nuclei interaction region, the Glauber model, allows to estimate geometrically the number of participating nucleons N_{part},

as well as the number of nucleon-nucleon collision N_{coll}, at a given impact parameter, from the knowledge of the nuclear thickness function and the nucleon-nucleon cross-section [20].
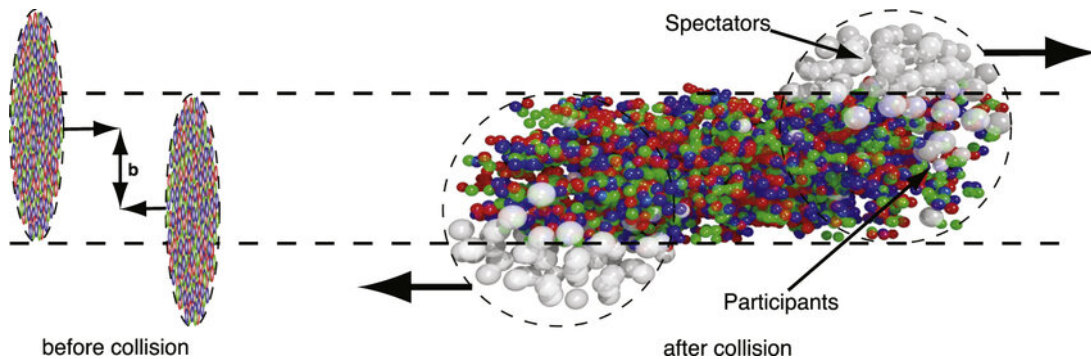

Figure 1.7.: Sketch of the collision between two heavy ions, which are colliding with an impact parameter *b* between their centers. Taken from [21].

The different phases following the collision are sketched in Fig. 1.8. During the collision, many partons can be formed from hard (i.e. coming from high-Q^2 processes) or soft (i.e. coming from low-Q^2 processes, the limit between hard and soft regimes is often considered to be around few GeV) interactions. The number of hard partons created scales approximately with N_{coll}, while the number of soft partons scales with N_{part}. At that point, the energy density is so high (Ref. [22] estimates the energy density after a time of 1 fm/c to be around 12 GeV/fm^3, i.e. roughly 20 times the energy density of a proton) that all these partons start interacting together strongly. Immediately after the collision, the particles are not yet reached thermal equilibrium: this is known as the pre-equilibrium phase. After a time of around 1 fm/c (it might even be shorter), a thermal equilibrium is reached. It had been shown that, at this point, the deconfined quarks and gluons can be described hydrodynamically as a strongly-interacting QGP fluid. This medium expands, and therefore cools down, until around 10 fm/c when the quarks and gluons start to recombine into hadrons. Hadron abundances are fixed when the temperature becomes lower than the chemical freeze-out temperature. Finally, a hadronic rescattering phase, where the hadrons are still able to exchange momentum by elastic interactions, happens until the temperature of the kinetic freeze-out is reached, after which interactions are not possible anymore. Then, several thousands particles per unit of rapidity fly towards the experimental detectors [23].

1.2.3. Experimental signatures of the QGP

The presence of the QGP and its properties can be probed with specific experimental observables. Some of these main signatures are presented thereafter.

A first probe of the QGP comes from the anisotropic flow. In non-central collisions, the geometrical overlap of the two nuclei is not circular, but often almond-shaped. Because partons interact together strongly within the QGP, the pressure gradients in the interaction region are not isotropic, and more particles flow in a direction in which less partons are encountered. The presence of these collective phenomena means that the azimuthal distribution of the produced particles is not flat, as is shown in the measurement of 2-particle correlation visible in the left panel of Fig. 1.9. Such a flow phenomena has been measured and quantified in several heavy-ion experiments [24–26], probing the presence of the QGP. This measurement is particularly

ALI-PUB-583519
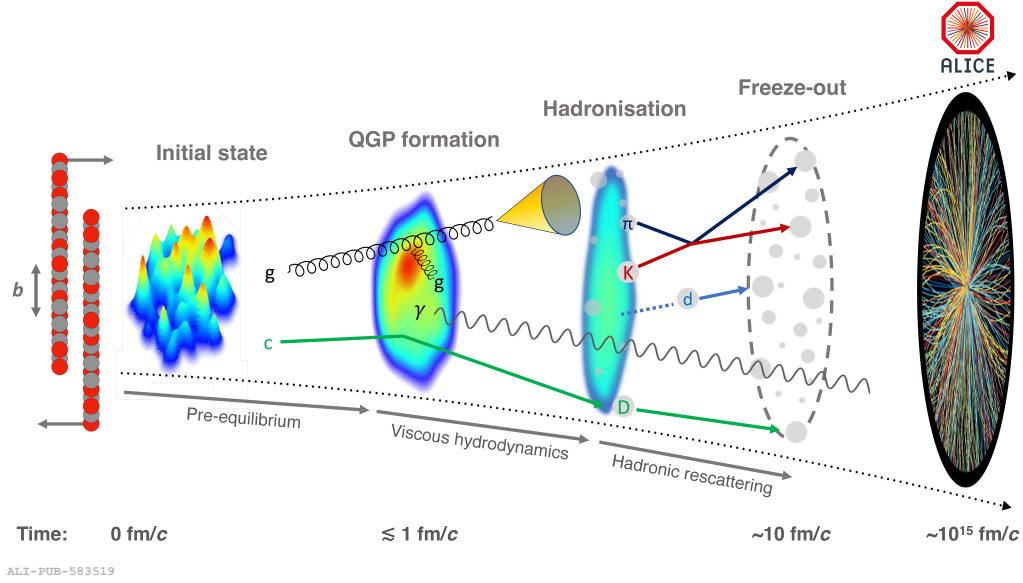
Figure 1.8.: Sketch of the different phases of the evolution of a heavy-ion collision. Taken from [23].

important because the details on how the geometrical anisotropy is converted into momentum anisotropy depend on several properties of the strongly-interacting QGP, such as the ratio between shear viscosity and entropy density η/s. The space-time evolution of the QGP during its expansion can be implemented in hydrodynamic simulations [27, 28] depending on a few parameters. The shear viscosity, as well as other hydrodynamic properties, can be inferred from several experimental measurements, such as flow, particle yields and spectra, using Bayesian analyses [29, 30], which allow to find the values of this hydrodynamical quantities giving the best description of all experimental data. In particular, these studies found η/s to be very small, close to the lower bound theoretically possible of $1/(4\pi)$, which means that the QGP is close to a perfect fluid.

ALI-PUB-583627
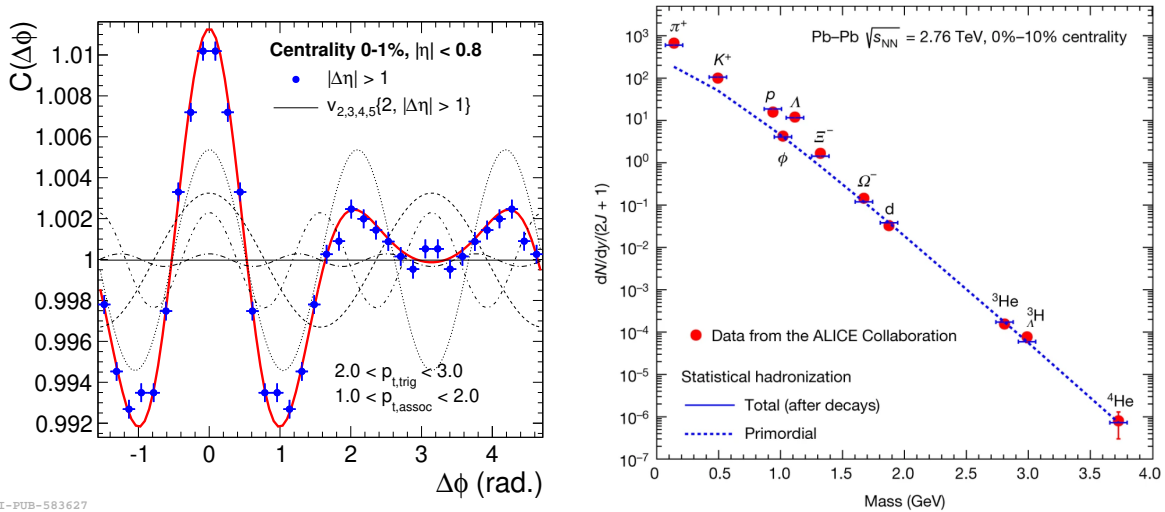
Figure 1.9.: Left: 2-particle correlation in central Pb–Pb collisions measured by ALICE. Taken from [24]. Right: Hadrons yields measured by ALICE in central Pb–Pb collisions compared with the prediction of the SHM, including particles coming from decays of heavier particles. Taken from [31].

Another probe for the QGP properties comes from the measurement of the hadron yields. In presence of a QGP in thermal equilibrium, it could be assumed that the hadronization happens statistically. In this case, the yield for a specific hadron would not depend on the full history of the QGP, but only on few parameters at the moment of the chemical freeze-out, such as the temperature T, the baryonic potential μ_B, or the volume V. This is the hypothesis behind the Statistical Hadronization Model (SHM). The SHM states that, at chemical freeze-out, the yield Y_i for the given hadron i follows the dependence $Y_i \propto m_i^{3/2} \exp(-m_i/T)$, where m_i is the mass of the hadron i [31]. Indeed, heavier hadrons are more difficult to produce thermally than lighter hadrons. In addition, the yields can be modified if it receives feed-down from decays of heavier hadrons. The comparison between the yields measured by ALICE and the predicted yields by the SHM is shown in the right panel of Fig. 1.9. The predicted and measured yield agree for an impressive number of particles, from pions to strange hadrons and even light nuclei. This allows to predict precisely the thermodynamical properties at the chemical freeze-out, making it a powerful experimental probe of the phase diagram of QCD. As an example, for central Pb–Pb collisions at $\sqrt{s_{\mathrm{NN}}} = 2.76$ TeV, the model provides a value of the temperature $T = 156.6 \pm 1.7$ MeV and the baryonic potential $\mu_B = 0.7 \pm 3.8$ MeV, obtained by fitting the hadron yields measured by ALICE. An outstanding result and validation for this model is that the freeze-out temperatures obtained with the SHM for several collision energies are found to coincide to the temperature calculated by lattice QCD at the transition between hadronic matter and QGP.

Because the strange quark mass is lower than the QGP temperature, strange quarks can be created in abundance from partonic interactions and strange hadrons can be produced thermally. Therefore, the yields per event of strange hadrons increase in Pb–Pb collisions with respect to pions, a phenomenon known as strangeness enhancement. Such effect has been measured for example in Ref. [32]. The effect is even stronger for hadrons containing more than one strange quark. Alternatively, the measurements can also be interpreted as a canonical strangeness suppression in pp collisions, which comes from the need of exact conservation of the strangeness number within a small volume. Indeed, in this case the volume is small compared to the large volumes reached in Pb–Pb collisions which allow grand-canonical thermal production.

Additionally, the QGP has been also probed experimentally by measurement of jet quenching. The high-momentum partons can interact with the QGP fluid when passing through the medium. Such interactions can happen via collisions with the medium particles or radiative gluon emissions, and are expected to happen more often when the path length of the particle inside the medium is higher. The additional energy loss compared to vacuum can be observed from the suppression of high momentum jets in Pb–Pb collisions compared to pp collisions, as was done for example by ATLAS in Ref. [33], which showed that dijets are less balanced in energy in Pb–Pb collisions compared to pp collisions.

The deconfinement of the quarks inside the QGP can finally be probed by the measurement of quarkonium yields. The corresponding phenomena will be described in detail in Sec. 2.1.3.

Taking into account these several probes, which can be completed by other QGP signatures mentioned for example in Ref. [34], show with very strong evidence that a QGP medium is created in high-energy heavy-ion collisions.

1.2.4. Signs of collectivity in small systems

Although originally a QGP medium was thought to be present only in heavy-ion collision, recently, several signs of collectivity have been found also in smaller systems such as pp or p–Pb collisions, which were traditionally thought as a reference for studying QCD effects without the presence of a medium (see Ref. [35] for a review on the subject). Signs of collectivity have been even searched in smaller systems like e^+e^- or ep collisions, with no strong conclusion yet on whether collective effects can explain the observations. Such collectivity could indicate that the formation of a QGP happens as soon as the particle density is large enough, independently on the collision system.

The signs of collectivity which were measured include in particular azimuthal correlations. Collectivity could be seen when the 2-particle correlation depends on the azimuthal difference. Indeed, in this case there could be an increase of the yield when the azimuthal difference between the two particles is small, corresponding to the near-side region, or close to π, corresponding to the away-side region. Non-flow effects, due to correlated contributions such as jets or resonance decays, can be subtracted in the near-side region by requiring a gap in pseudo-rapidity. The yield in this region, where uncorrelated contributions have been removed by subtracting the minimum yield in the azimuthal distribution [36], is shown as a function of the multiplicity in pp collisions in the left panel of Fig. 1.10. It is also compared with the same measurements in e^+e^- collisions. This near-side ridge yield increases with the multiplicity, and, even at low multiplicity, it is significantly non-zero. Since the yield is not reproduced in event simulations which do not include collective effects, this shows that collectivity can be observed to a surprisingly large extent in all colliding systems.
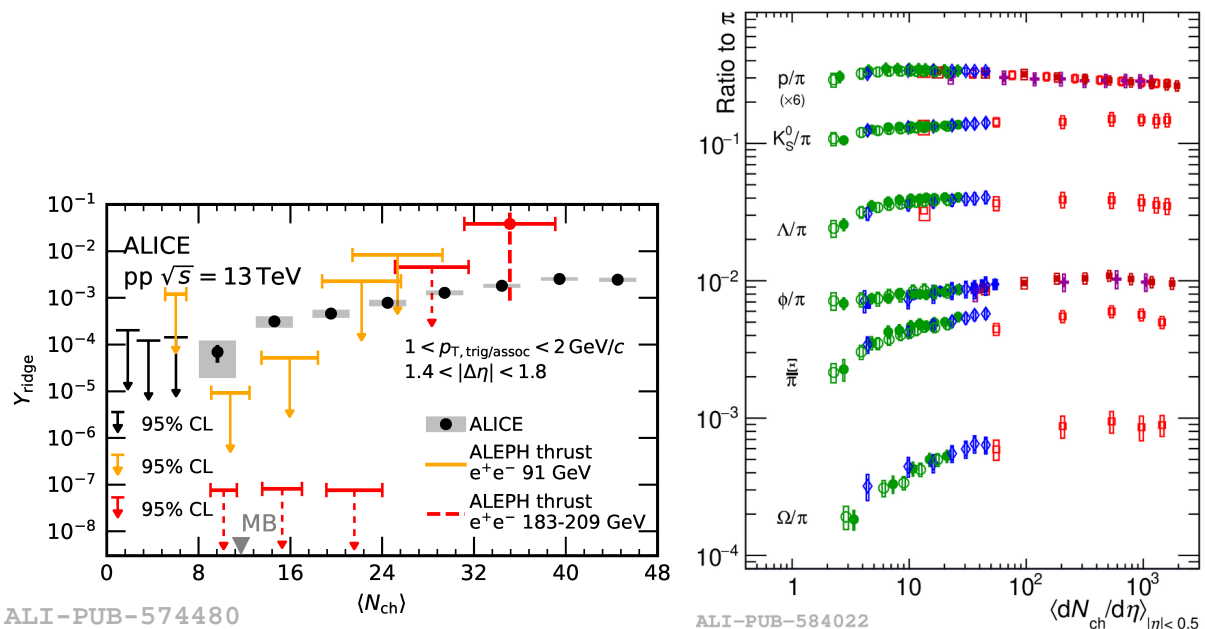
Figure 1.10.: Left: Near-side ridge yield as a function of multiplicity in pp collisions, measured by ALICE. Taken from [36]. Right: Yields of strange particles, normalized by pion yields, as a function of charged-particle multiplicity in several colliding systems, measured by ALICE. Taken from [23].

The measurement of strange particles as a function of charged-particle multiplicity [23, 37] also present strong indication for thermal effects in small systems. Indeed, as can be seen in the right

panel of Fig. 1.10, the yields of strange baryons, normalized to the pion yields, continuously increase as a function of charged-particle multiplicity in all the colliding systems. This is a sign for the presence of strangeness enhancement, even in pp or p–Pb collisions. At the same value of multiplicity, the yield ratios are very similar between the different colliding systems, indicating that the strangeness enhancement could be only driven by the multiplicity density and not by the colliding system.

However, there exists possible explanations for collective effects other than final-state effects through particle interactions inside the QGP. Indeed, also initial-state correlations inside the colliding protons could result in collectivity. For example, it is possible that, in the CGC framework, fluctuations of color fields inside the proton create a correlation between the different partonic interactions, and favor particles to be emitted either in the same direction or back-to-back [38].

The presence in small systems of highly-dense matter such as a QGP, although pointed at by several measurements, is then not yet completely confirmed. Therefore, additional measurements are needed in order to characterize more precisely high-multiplicity pp and p–Pb collisions and to distinguish the relative impact of initial-state and final-state effects on the observables.

1.2.5. Simulation of a collision

In order to get a better understanding of the complex processes happening in a collision, and to make predictions which can be compared to the experimental results, several frameworks intend to precisely simulate the collisions. Due to the random nature of the processes involved, these simulation frameworks are called Monte-Carlo (MC) generators. Perturbative effects, such as the initial partonic interaction in a collision, can be estimated from calculations, while non-perturbative effects, such as QGP hydrodynamics or hadronization, need precise modeling, which often varies from one generator to the other. Comparison to experimental data can be used to rule out one implementation or the other of a particular phenomenon, or for the tuning of the model parameters used in the simulations. In the following, two of the main MC generators which intend to describe proton-proton or nuclei collisions are presented, namely EPOS and PYTHIA. They both implement different assumptions on the sequence of events happening during a collision. For example, EPOS assumes the formation of a QGP independently from the colliding system and implement hydrodynamic simulations, while in PYTHIA the processes are supposed to happen in vacuum.

PYTHIA:

An overview of the latest version of the PYTHIA multi-purpose event generator, PYTHIA 8.3, can be found in Ref. [39]. This framework contains many settings which can be chosen by the user. PYTHIA also provides tunes, which are a set of predefined values for the many parameters which need to be defined in PYTHIA. These parameters have been chosen in a so-called tuning procedure by comparing the results of the simulations with different values of these parameters to experimental data. One of the most widely used tune is the Monash tune [40]. In addition,

the Angantyr framework [41] allows to simulate heavy-ion collisions without the assumption of a QGP formation.

PYTHIA simulates collisions through Multiple Partonic Interactions (MPI). The simulation of the collision starts by the choice of the hardest interaction in the event, often a $2 \to 2$ or $2 \to 3$ process. It depends on PDFs and on the calculations of the cross-sections for different processes. It is also possible for the user to select a specific process. In parallel, the value of the impact parameter between the two colliding protons is determined, and other Partonic Interaction (PI) are added. These PI are ordered, starting from the hardest one, and going softer. The probability for selecting a subsequent PI is higher when the impact parameter is smaller, meaning that n_{MPI} is increased with smaller the impact parameters [42].

For each of the partonic interactions, a parton shower can be initiated. This parton shower contains initial-state (coming from the incoming partons) and final-state (coming from the outgoing partons) radiations. A shower is a recursive emission of partons through individual splittings such as $g \to gg$, $g \to q\bar{q}$ or $q \to qg$. Splitting kernels give the probability for such splitting to happen with a given sharing of the energy between either of the daughters. The partons are emitted iteratively one by one, ordered by a scale from the hardest emission to softer ones until a hadronization scale is reached.

Once the partons are formed, the hadronization occurs according to the Lund string model [43]. A color and an anticolor charge (e.g. within a quark and an antiquark) can be connected by a string. This string represents a flux tube between them, carrying a potential energy which depends linearly on the distance between the color charges. This picture is motivated by lattice QCD results. The string can also contain gluons in between the two main color charges, these gluons acting as kinks on the string. As the quarks fly apart one from each other, the potential energy between them increases. When this potential energy becomes large enough, the string can break into two pieces, and at the break point a new quark-antiquark pair created. The string pieces evolve in turn through the string breaking mechanism. The probability to create a quark and antiquark is suppressed by a factor $\propto \exp(-\pi m^2/\kappa)$, where m is the quark mass and κ is a parameter giving the string tension. This means that strangeness is suppressed by a factor ≈ 0.2, while heavier quarks cannot be produced in the string breaking mechanism. An illustration of this mechanism is shown in the left panel of Fig. 1.11. After all string breaking have happened, the remaining string pieces fragment to hadrons, depending on their masses. It is also possible to create baryons by considering diquarks in the string breaking mechanism.

In a collision with several PI, due to the finite number of colors $N_c = 3$, it is possible that a quark from one PI would interact with a quark from another PI. This is modeled by implementing Color Reconnection (CR) mechanism. This mechanism allows to merge several consecutive (considering the ordering by hardness) PI together, and creates new string connections which would minimize the total string length. The length of a string piece can be in general defined as $\lambda \approx \ln(1+m/m_0)$, where m is the mass of a string piece, and m_0 a parameter. The total length of the string is obtained by summing the individual lengths of all string pieces. Quarks and gluons from one PI can be inserted into a string from another PI, if the configuration would provide a smaller total string length, as illustrated in the right panel of Fig. 1.11. The CR mechanism could in particular
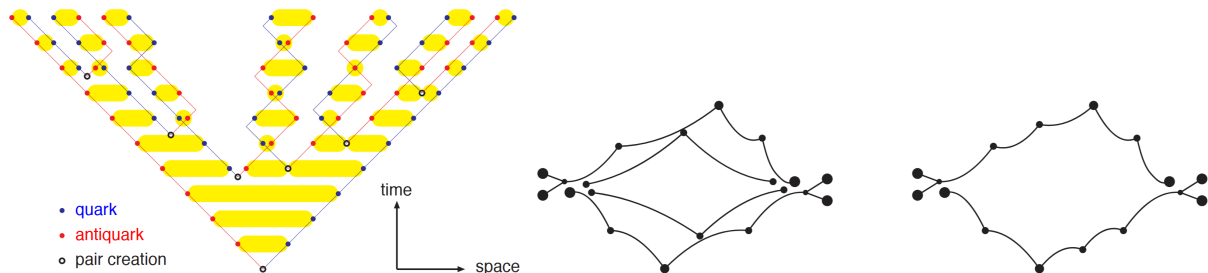
Figure 1.11.: Left: Illustration of the Lund string model. The potential energy stored between the quarks and the antiquarks is represented as a string. When the quark and the antiquark fly apart, strings can break into several pieces, at the end of which a new quark-antiquark pair is formed. Taken from [44]. Right: Illustration of the color reconnection mechanism, where quarks and gluons coming from another partonic interaction can be included inside a string, in order to minimize the total string length. Taken from [45].

explain the increase of the $\langle p_{\mathrm{T}} \rangle$ with the multiplicity, since the string reorganization when there are many PI would reduce the number of hadrons produced per partonic interaction, while conserving energy and momentum. Several advanced CR mechanisms exist, such as the QCD-based Color Reconnection Beyond Leading Color (CR-BLC) [46]. In this case, the quarks and gluons are given specific color and anticolor indices. These indices are used to create strings and junctions (a piece connecting three partons together) which can reconnect different quarks and gluons together independently from their original PI. In particular, it gives a better treatment of the color algebra rules, where two partons chosen randomly can be correlated in several multiplet states. For example, with CR-BLC, an uncorrelated quark-antiquark pair can be either in an octet state or a singlet state, while in the basic CR it can only be in an octet state. The chosen configuration is the one minimizing the total string length. An improvement of the CR-BLC model is that the addition of junctions allows an increase of the baryon yields, which was found to better reproduce experimental data. Several modes for the CR-BLC model exist (mode 0, 1, 2 and 3), depending on additional space-time constraints on the partons authorized to form a connection.

Additional interactions between the strings are available through rope hadronization [47], and string shoving [48]. In the rope hadronization mechanism, several strings which are overlapping are allowed to merge together into a rope, which would then obtain a higher effective string tension. A larger string tension results in particular in the increase of the probability to create strange quarks during string breaking. This mechanism can in particular cause strangeness enhancement at high multiplicity when the string density is higher [49]. String shoving mechanism allows to induce an additional repulsive transverse kick between several strings if they are close one from another, modeling collective effects when the string density is high.

EPOS:

EPOS stands for Energy conserving quantum mechanical approach, based on Partons, parton ladders, strings, Off-shell remnants, and Saturation of parton ladders. In EPOS4, the latest available version of EPOS, the collision happens through parallel scatterings between the projectile and target nucleons [50]. High-multiplicity events occur when there is a large number of

such scatterings. One particularity of EPOS is that, once the number of scatterings is determined, no ordering is chosen between these scatterings. This means that the fraction of the energy x_i taken by each one of these scatterings are chosen all at the same time, only requiring energy and momentum conservation. Afterward, each of these scatterings, represented by pomerons (i.e. parton ladders), is evolved through perturbative calculations of partonic interactions with the DGLAP equations [51]. These pomerons from multiple parallel scatterings are sketched in the left panel of Fig. 1.12. In order to model the non-linear saturation effects at high-gluon density, a saturation scale is introduced for the evolution of the pomeron, modifying the low-x processes. Due to strict energy-momentum conservation, when there are more scatterings for a particular nucleon, pomerons with lower momentum fractions are favored. This would increase the soft particle yields and decrease the hard ones compared to the one-pomeron case. Therefore, the choice of the saturation scale is made, depending on the number of scatterings (hence depending on the multiplicity of produced particles) and their momentum, in order to cancel exactly this increase of the low-momentum probability. This choice of saturation scale allows in addition to recover factorization for minimum-bias cross-sections, stating that the minimum-bias cross-sections are equivalent to the ones obtained in the one-pomeron case [52].
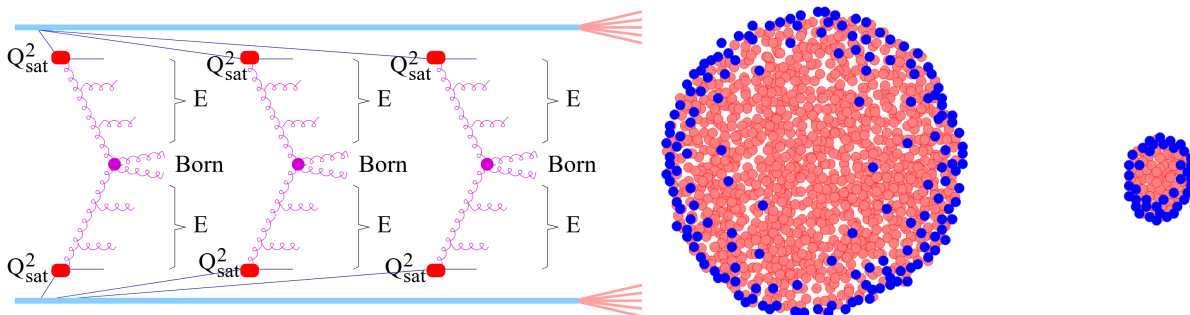
Figure 1.12.: Left: Sketch of multiple parallel scatterings between two protons. For each of such scattering, a pomeron is represented, with resulting partons. In addition, the red dot represent the saturation scale, which mimic non-linear saturation effects. Taken from [52]. Right: Sketch of the core (red dots) and corona (blue dots) prehadrons, for a big and a small system. Taken from [53].

Strings are formed between the partons produced in the evolution of one parton ladder. Breakpoints within the strings are created, and the string fragments between two breakpoints decay to pre-hadrons, which are chosen depending on string flavor and mass [54]. Afterward, the event is separated into two parts: a high-density core, which behaves hydrodynamically as a QGP fluid, and a low-density corona, which is not further evolved. The decision on whether a pre-hadron belongs to the core depends on the parametrized energy loss when passing through the rest of the system. If it could escape the system after considering this energy loss, then it belongs to the core, and fuses to become part of the fluid. Otherwise, it becomes part of the corona and only suffers from energy loss. In general, only the pre-hadrons initially close to the surface or with a large momentum constitute the corona, as can be seen in the right panel of Fig. 1.12. Even small systems such as proton-proton collisions possess a significant core part, which is nevertheless in a smaller proportion compared to the case of large heavy-ion collisions. The fluid expansion is simulated through viscous hydrodynamic calculations. The hypersurfaces falling below a given freeze-out energy density decay to hadrons micro-canonically, following a thermal distribution and respecting the conservation of the quantum numbers (baryon number,

electric charge, strangeness) [53]. After hadronization, the rescattering of the hadrons is handled with the UrQMD transport model [55, 56]. Finally, the unstable particles are decayed successively until only stable particles are present.

Due to their large mass, the heavy quarks (charm and bottom) will not fuse in the medium, and require a special treatment, handled in EPOS4HQ [57, 58]. In the standard EPOS4, or when they are part of the corona, the heavy quarks directly fragment after being created in the parton ladder evolution, without interacting with the medium, into heavy-flavored hadrons. However, EPOS4HQ simulations implement collisional (elastic scattering with partons inside the medium) and radiative (inelastic scattering with gluon emission) energy loss for the heavy quark inside the QGP, calculated using pQCD cross-sections. When the heavy quark inside the QGP pass through a hypersurface whose energy density reaches the freeze-out value, it can hadronize through coalescence with thermalized light quarks from the medium. The coalescence probability depends on the Wigner density, which is maximal when the relative difference in heavy and light quarks momentum is zero. Coalescence happens mainly at low momentum. If the heavy quarks do not hadronize via coalescence, they hadronize via fragmentation.

1.2.6. Particle production

Analyzing the complex phenomena of how particle are produced in the collision would allow to gain understanding into both the perturbative (production of hard probes such as jets) and non-perturbative (soft particle production which represent most of the charged particles) processes. This can be probed by basic measurements such as the number of charged particles produced in such a collision, also known as charged-particle multiplicity. This allows a comparison to models, in particular MC generators, as described in the previous section, for which similar quantities are easily accessible. The measurements can also be used for the tuning of the generators. In heavy-ion collision, the multiplicity distribution also becomes interesting through the direct relations between the number of produced charged particles and thermodynamical properties such as the entropy.

Such a measurement is shown in the left panel of Fig. 1.13. In this case, the average charged-particle multiplicity has been determined in several colliding systems as a function of the center-of-mass energy, and normalized by the number of participants. It is interesting to see that the results for inelastic pp and Non-Single Diffractive (NSD) pA collisions (i.e. either both the proton and the nuclei diffract, meaning that they exchange a color singlet and produce particles exclusively at forward rapidity in their traveling direction, or neither of them do) follow the same power-law trend, the average multiplicity increasing with the energy, while in AA collisions, there is also a power-law trend, but it is much stronger. That could indicate a difference in the particle production between collision systems, being more efficient in heavy-ion collisions compared to minimum-bias pp and pA collisions. The full probability distribution of the number of charged particles produced in a proton-proton collision, measured at midrapidity by ALICE [60], is shown in the right panel of Fig. 1.13, for several center-of-mass energies. It is often considered that the self-normalized multiplicity distributions, i.e. the distributions of $P(N_{ch})/\langle N_{ch} \rangle$, are independent of the energy, a phenomenon which is known as KNO scaling. The shape of such a
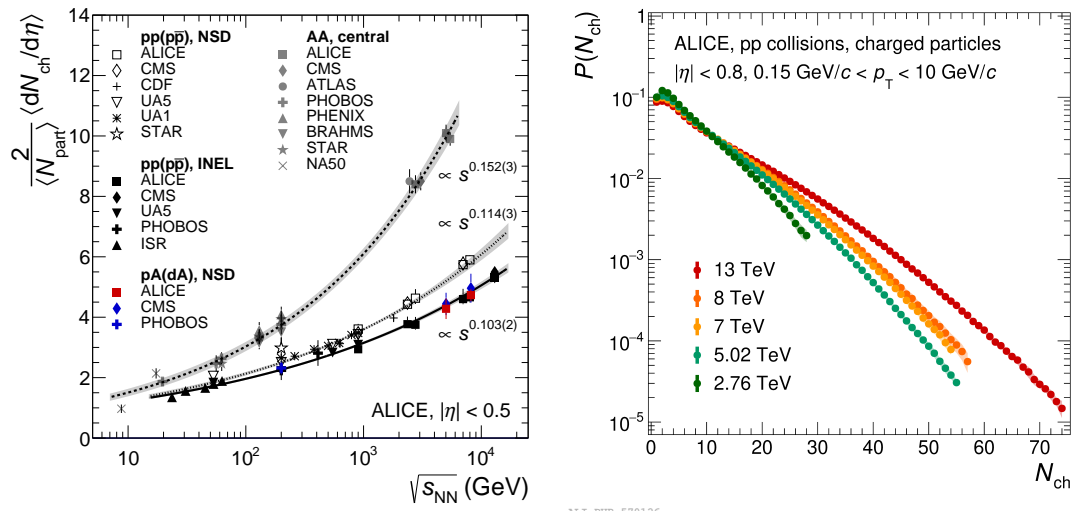
Figure 1.13.: Left: Average charged-particle multiplicity for several collision systems, normalized by the number of participating nucleons, measured as a function of center-of-mass energy. Taken from [59]. Right: Charged-particle multiplicity probability distribution in pp collisions at midrapidity, measured at several center-of-mass energy by ALICE. Taken from [60].

steeply-falling distribution can be approximately reproduced by a negative binomial distribution (NBD). Sometimes, the convolution of several NBD is necessary. An example comes from several CGC computations of this distribution, where fluctuations of several quantities are considered, such as the impact parameter between the two protons, the density of color charges, or the saturation scale [61].

2. Quarkonium production and dependence on multiplicity

While the previous chapter introduced the basic theoretical concepts necessary to understand the measurement and challenges of high-density QCD, this chapter has a more specific focus. It is dedicated to the state of the art of the measurements and modeling relevant for the analysis presented in this thesis. This includes a description of the current understanding of the quarkonium and its production mechanisms, as well as the recent measurements and modeling of the multiplicity dependence of quarkonium production.

2.1. The J/ψ meson and its production mechanisms

2.1.1. J/ψ properties

A quarkonium is a bound state of a heavy quark (charm or bottom) with the corresponding heavy antiquark ($c\bar{c}$ for charmonium and $b\bar{b}$ for bottomonium). The first discovery of a quarkonium happened unexpectedly in November 1974 both at BNL and SLAC laboratories at the same time. It was observed as a peak in the dilepton invariant mass spectrum around the mass of the J/ψ meson [62, 63], whose measured value is currently 3096.900 ± 0.006 MeV/c^2 [1]. This was the first discovery of a fourth quark flavor.

A summary of all the charmonium states measured since then, with their quantum numbers and masses, can be found in Fig. 2.1. In analogy to the hydrogen atom or to the positronium, quarkonium states can be represented by their total spin S, their orbital angular momentum L and their total angular momentum J. Because of its constituent quarks spins, S can be either 0 or 1, while J can be thought of as the vector sum of L and S. The charmonium quantum numbers are usually written as J^{PC}, where P is the parity number $P = (-1)^{L+1}$ and C is the charge conjugation number $C = (-1)^{L+S}$. For example, J/ψ has $J^{PC} = 1^{--}$, which means $L = 0$, $S = 1$ and $J = 1$. In particular, these are the same quantum numbers as for a photon, which is why J/ψ can decay to dileptons via a virtual photon. States with $L = S = 0$ are generally noted as η_c, while states with $L = 0$, $S = 1$ are noted with ψ, and states with $L = S = 1$ are noted with χ_c. An additional quantum number n represents the radial excitation. For example, the $\psi(2S)$, with $n = 2$, is the radial excitation of the J/ψ, which has $n = 1$. It is also possible, in analogy to the electronic layers in atomic physics, to use the $S, P, D, ...$ notations for $L = 0, 1, 2, ...$ (note that the S notation representing $L = 0$, e.g. in $\psi(2S)$, should not be confused with the S representing the spin). As an example, the quarkonia χ_{cJ}, with $L = 1$, $S = 1$ and $J = 0, 1, 2$

constitute *P*-wave states. The quantum numbers of the quarkonia can be noted as $n^{(2S+1)}L_J$. For example, the quantum numbers of the $\psi(2S)$ could be noted as 2^3S_1.
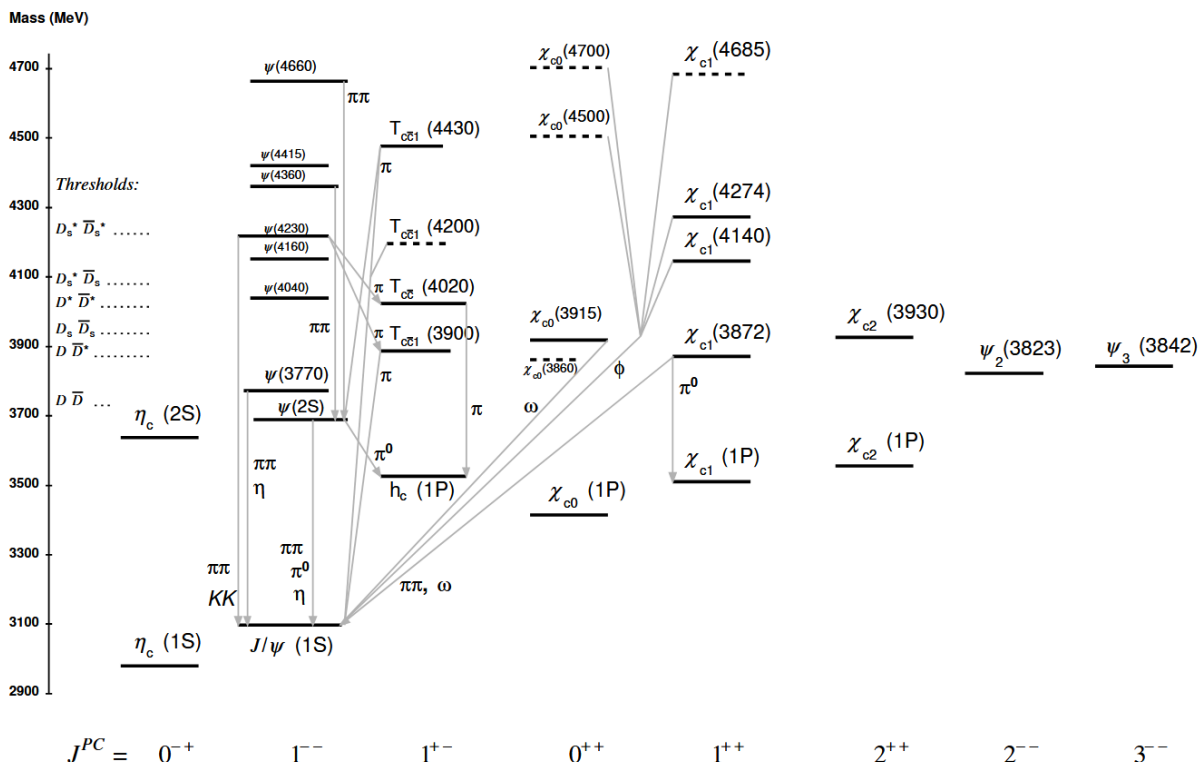
Figure 2.1.: Different measured states of charmonium, separated by their masses and quantum numbers. Also tetraquark states are shown. The arrows represent the strong decays from one charmonium state to another, while radiative decays are not shown. Taken from [1].

The non-relativistic potential between a heavy quark and the corresponding heavy antiquark within a quarkonium can in general be described by the Cornell potential [64]. This potential, whose choice has been confirmed by lattice QCD, depends on the distance r between the quark and the antiquark:

$$V(r) = -\frac{4}{3}\frac{\alpha_S}{r} + \sigma r\,. \tag{2.1}$$

The first term represents a short-distance strong Coulomb-like potential, while the second term represents a long-distance string-like confining potential, with a parameter σ. The Cornell potential is able to explain the different masses of the quarkonium states. In particular, the excited states differ from the ground state by having lower binding energies and larger radii.

Additionally to the state itself, its production channel can be specified. When considering all J/ψ regardless of their source, one speaks of inclusive J/ψ. Nevertheless, not every J/ψ is produced directly in the collision. A part of the J/ψ comes from the decay of beauty hadrons, while another part comes from the decay of higher-mass charmonia, such as $\psi(2S)$ and χ_c. The former are called non-prompt J/ψ (in comparison to prompt J/ψ), while the latter are called non-direct J/ψ (in comparison to direct J/ψ). These additional production mechanisms are referred to as feed-down effects. A careful estimation of their contributions is necessary to disentangle the different

hadronization processes. More details on non-prompt J/ψ production mechanisms are given in Sec. 2.1.4. While non-prompt J/ψ can be distinguished from prompt J/ψ experimentally, see Sec. 5.3, this is not feasible for indirect J/ψ. It is thus necessary to rely on the measurements of higher-mass charmonia in order to understand their contributions to prompt J/ψ.

2.1.2. Quarkonium production models

The production of quarkonia in colliders involves processes acting on different scales which thus require specific theoretical treatments. On the one hand, the characteristic scale for the production of the heavy quark-antiquark pair $Q\overline{Q}$ is the mass of the heavy quark m_Q. The relatively large value of m_Q allows the production of the heavy quarks to be described via pQCD calculations. On the other hand, the typical scale for the hadronization of the quarkonium is usually the quark momentum in the quarkonia rest frame $m_Q v$, or its binding energy $m_Q v^2$, where v is the relative velocity of a heavy quark in the quarkonium rest frame. Typical values of v amount to $v^2 \sim 0.3$ for charmonium and $v^2 \sim 0.1$ for bottomonium. At these scales in the soft processes pQCD calculations are not applicable. The hadronization must then be described by non-perturbative models. These models especially differ on their treatment of the transition from a $Q\overline{Q}$, which can be in any state of color, to a quarkonium, which must be a color singlet. A review of several of these models can be found for example in Refs. [65, 66]. Precise modeling and measurements of quarkonium production in pp collisions can improve the understanding of hadronization processes and test the accurateness of pQCD calculations. In addition, these measurements provide a reference for the production of J/ψ mesons in heavy-ion collisions, which will be described in Sec. 2.1.3. The main models are presented in the following.

Color Evaporation Model (CEM):

In the CEM model [67], the transition from the $Q\overline{Q}$ to the quarkonium $\mathcal{Q}$ occurs when the mass of the $Q\overline{Q}$ system $m_{Q\overline{Q}}$ is larger than the quarkonium mass, but smaller than twice the D meson (B meson respectively) mass for charmonium (bottomonium respectively). Indeed, within this mass range, the heavy quark and antiquark cannot hadronize separately due to an overall energy which is insufficient to create two heavy-flavor hadrons. Instead, the transition to a color singlet happens randomly, characterized by a probability factor $F_\mathcal{Q}$. The transition occurs via the emission of an arbitrary number of soft non-perturbative gluons, which causes a decorrelation between the $Q\overline{Q}$ and quarkonium color state i.e. the color "evaporates". The charmonium production cross-section can then be written as (m_D should be replaced by m_B for bottomonium cross-section):

$$\sigma_\mathcal{Q} = F_\mathcal{Q} \int_{2m_Q}^{2m_D} \frac{d\sigma_{Q\overline{Q}}}{dm_{Q\overline{Q}}} dm_{Q\overline{Q}}. \tag{2.2}$$

$F_\mathcal{Q}$ can be obtained from fits to data. In addition, a reasonable assumption is that the random emission of gluons would give a color singlet in approximately one ninth of the cases. That would lead to $F_\mathcal{Q} \approx 1/9 \times (2J_\mathcal{Q} + 1)/\sum_i (2J_i + 1)$, where the sum runs over the orbital momentum of all quarkonium states.

The Improved Color Evaporation Model (ICEM) [68] refines this picture by taking into account the fact that the mass difference between the $Q\overline{Q}$ and the quarkonium would also modify the kinematics after gluon emissions. The momentum of the quarkonium is thus lowered by a factor $m_{\mathcal{Q}}/m_{Q\overline{Q}}$ compared to the momentum of the $Q\overline{Q}$ in the calculation.

Color Singlet Model (CSM):

In contrast to the CEM case, where the $Q\overline{Q}$ could be in every color state, in the CSM case [69], it is assumed that the $Q\overline{Q}$ must exactly be in a color singlet state with the correct spin to be able to hadronize to the relevant quarkonium. This is due to the fact that the emission of additional gluons is suppressed by powers of $\alpha_S(m_Q)$. The cross-section for quarkonium production can directly be deduced from several independent elements. These elements include the PDFs, the production cross-section for an heavy-quark pair in a singlet state $(Q\overline{Q})^{[1]}$, as well as the square of the Schrödinger wave function at the origin in the position space $|R(0)|^2$, which can be determined from the quarkonium decay width. The production cross-section is thus expressed as:

$$\sigma_{\mathcal{Q}} = \sum_{i,j} \int_0^1 \int_0^1 \mathrm{d}x_1 \mathrm{d}x_2 f_i(x_1) f_j(x_2) \sigma_{i+j\to(Q\overline{Q})^{[1]}} |R(0)|^2 \,. \tag{2.3}$$

Quantum numbers, such as the spin state, impose constraints on the possible partonic interactions leading to a quarkonium at LO. For example, for J/ψ production in hadronic collisions from gluon-gluon fusion, an additional gluon must be considered: the LO process is therefore $gg \to$ J/ψg. In contrast, $gg \to \eta_c$ is allowed because of the spin $S = 0$ of the η_c.

Non-Relativistic Quantum Chromodynamics (NRQCD):

The CSM is known to underestimate the cross-sections for J/ψ production. It can be naturally enhanced by also considering the cases when the $Q\overline{Q}$ is produced as a color-octet, as implemented in the NRQCD framework [70]. The $Q\overline{Q}$ could also have different spin and angular momentum quantum numbers than the quarkonium. The transition to a color-singlet state would then happen by the emission of a few soft gluons. Contrary to the CEM model, these gluons would not completely decorrelate the color state of the quarkonium from the one of the $Q\overline{Q}$.

For cross-section calculations, the NRQCD framework utilizes an expansion not only in α_S, but also in v, the relative velocity of the quarks in the quarkonium rest frame. The CSM gives the leading-order term in this expansion. The production cross-section can be written as:

$$\sigma_{\mathcal{Q}} = \sum_{i,j,n} \int_0^1 \int_0^1 \mathrm{d}x_1 \mathrm{d}x_2 f_i(x_1) f_j(x_2) \sigma_{i+j\to(Q\overline{Q})_n} \langle \mathcal{O}_{\mathcal{Q}}^n \rangle \,. \tag{2.4}$$

Here, $(Q\overline{Q})_n$ represents a heavy quark-antiquark pair in a given state of color, spin and angular momentum. $\langle \mathcal{O}_{\mathcal{Q}}^n \rangle$ are the Long-Distance Matrix Elements (LDME). They represent

the transition between such a $(Q\overline{Q})_n$ and a quarkonium. The LDME cannot be inferred from theory and needs to be extracted from fits to data [71].

Coalescence:

The coalescence model relies on the possibility for two heavy quarks to recombine into a quarkonium if they are close in space and momentum. The probability to produce a quarkonium state $\mathcal{Q}$ via coalescence, $P_{\mathcal{Q}}(\vec{R}, \vec{P})$, where $\vec{R}$ and $\vec{P}$ are the position and momentum of the quarkonium, can be calculated in the Wigner density formalism. The expression relies on the projection of the density matrix of the quantum system formed by the N heavy quark and antiquarks on the density matrix of the quarkonium [72]:

$$\frac{dP_{\mathcal{Q}}}{d^3\vec{R}d^3\vec{P}} = \sum \int \frac{d^3r d^3p}{(2\pi)^6} W_{\mathcal{Q}}(\vec{r}, \vec{p}) \prod_{j>2} \int \frac{d^3r_j d^3p_j}{(2\pi)^{3(N-2)}} W^{(N)}(\vec{r_1}, \vec{p_1}, ..., \vec{r_N}, \vec{p_N}) . \tag{2.5}$$

$W_{\mathcal{Q}}(\vec{r}, \vec{p})$ is the Wigner density of the quarkonium, representing the phase-space distribution of the quarkonium. $\vec{r}$ and $\vec{p}$ are the relative coordinates and momenta between the heavy quark and antiquark. $W^{(N)}(\vec{r_1}, \vec{p_1}, ..., \vec{r_N}, \vec{p_N})$ is the Wigner density of the system formed by the N heavy quarks and antiquarks. For simplicity, it can be replaced by the average of the classical phase-space distribution. The sum in the right hand side of the equation is performed over all the possible heavy quark-heavy antiquark pairs in the system, while the product sum involves all the remaining heavy quarks and antiquarks, in order to retain only one pair at a time [72].

A Gaussian distribution can be assumed for the relative distance $\vec{r}$ between the heavy quarks in the $Q\overline{Q}$ pair, while the distribution of the relative momentum $f(\vec{p})$ can be calculated via pQCD. With these assumptions, the Wigner density for a heavy quark and antiquark can be expressed as:

$$W^{(2)}(\vec{r}, \vec{p}) \sim r^2 \exp(-\frac{r^2}{\sigma_{Q\overline{Q}}^2}) f(\vec{p}) . \tag{2.6}$$

$\sigma_{Q\overline{Q}}$ is a free effective parameter representing the standard distance between a quark and an antiquark at their production vertex. $\sigma_{Q\overline{Q}}$ differs depending on whether the two corresponding quarks originate from a common vertex or not.

The Wigner density can be written as a function of the relative momentum and coordinate between the heavy quarks. For a $1S$ state such as the J/ψ, it can be expressed as [73]:

$$W_{1S}(\vec{r}, \vec{p}) = 8 \cdot \exp(-\frac{r^2}{\sigma^2} + \sigma^2 p^2) . \tag{2.7}$$

Here, σ, different from $\sigma_{Q\overline{Q}}$, is a parameter representing the width of the specific quarkonium, and is chosen so that the wave function allows to reproduce the quarkonium mass. Expressions for the Wigner density of other quarkonia states can be found in Ref. [73]. The Wigner density formalism

is not restricted to quarkonium formation, and can also explain, for example, coalescence between a heavy quark and other light quarks which would form an open-charm hadron.

Additional remarks to the models:

The models presented before (CEM, CSM, NRQCD, coalescence) all differ in the hadronization mechanisms. In addition, the calculation of the production cross-section of the heavy quarks, which mainly come from gg processes, may differ from model to model. For example, k_T-factorization [74, 75] also takes into account the transverse momentum of the gluons inside the colliding protons, which is neglected in the usual PDFs. This generalization of the PDFs is known as Transverse-Momentum Dependent (TMD) distributions (or unintegrated PDFs). Similar to the PDFs, they are extracted from fits to experimental data [76], and a factorization formula allows to compute cross-sections. At low J/ψ transverse momentum, the momentum distributions for soft gluons can also be extracted within the CGC framework. This allows to reduce the momentum threshold for calculations of quarkonium production. The results in this case were found compatible to the ones at higher p_T without the use of the CGC framework [77]. Due to the large gluon densities at low momentum fraction inside the proton, higher-twist effects could play a role. Such effects come for example from the three-gluon contribution $ggg \to J/\psi$ to the cross-section (compared to e.g. $gg \to gJ/\psi$ in the leading-twist color singlet case), when two gluons would come from one proton and one gluon from the other one. This would introduce a modified dependence of J/ψ production on the gluon density inside the proton [78, 79]. Such effects could also be relevant for the multiplicity dependence, as will be seen in Sec. 2.2.1.

Comparison to experimental results:

In order to validate the models for J/ψ production, it is necessary to compare them to measured experimental data. In the left panel of Fig. 2.2, the J/ψ production cross-section measured by ALICE as a function of transverse momentum [80] is compared with several models [71, 74, 75, 77, 81]. Due to the large model uncertainties, all the models are compatible with measured data. Thus, the measurement of more discriminatory observables is needed.

One of such observable could be the quarkonium polarization. The polarization represents how much a certain angular momentum eigenstate J_z, defined with respect to a given axis, would be preferred [83]. It can be measured experimentally via the angular distribution of dilepton decays in a given reference frame. In the ICEM, due to the decorrelation between the $Q\overline{Q}$ and the quarkonium via soft gluon emissions, the quarkonium is expected to be unpolarized. However, for CSM and NRQCD, the polarization would depend on the relative abundances of the different $(Q\overline{Q})_n$ states, and also on the quarkonium momentum. Experimental data tend to support little to no polarization for the J/ψ [84, 85]. This was at first not expected for NRQCD (it was known as the polarization puzzle) [86] in which case the transversely-polarized $^3S_1^{[8]}$ state was expected to dominate (the spin states notation have been defined in Sec. 2.1.1, while the [8] superscript mean that this is an octet state. Similarly, a singlet state is noted as [1]). However, subsequent model calculations have improved the level of agreement with the measurement [87].
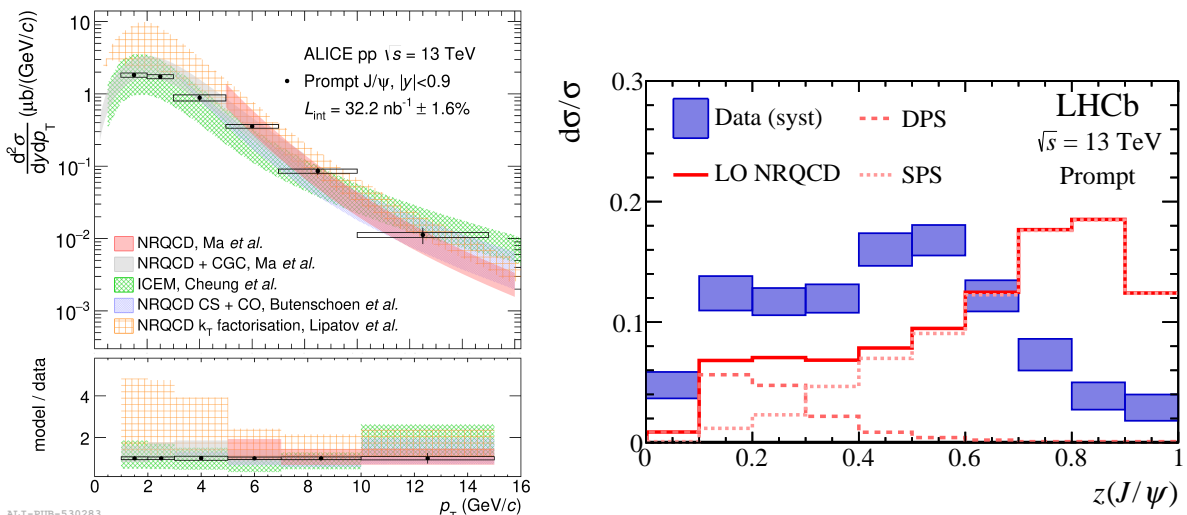
Figure 2.2.: Left: Prompt J/ψ production cross-section at midrapidity as a function of transverse momentum at $\sqrt{s} = 13$ TeV, measured by ALICE, and compared with several models [71, 74, 75, 77, 81]. Taken from [80]. Right: Distribution of the fraction of the transverse momentum carried by a prompt J/ψ meson within a jet, measured by LHCb. Taken from [82].

The J/ψ production mechanisms can also be tested by identifying the emitted energy in a similar direction as the J/ψ, since this energy could be related to the J/ψ hadronization process. The emitted energy could be affected both by the hard perturbative gluons emitted during production of the $Q\overline{Q}$, and by the soft non-perturbative gluons emitted during hadronization, which would differ between ICEM, CSM and NRQCD. For example, when the $Q\overline{Q}$ is in a color-singlet state, since it carries no color charge, it cannot exchange gluons. Thus, there is less energy emitted in its direction compared to the case of a color-octet state. However, the additional hard gluon emission in the LO process compared to a LO color octet might be found azimuthally backward compared to the J/ψ.

The distribution of the emitted energy in the J/ψ direction can be measured through the correlation between J/ψ and other charged particles [88], or through the measurement of the fraction of the momentum carried by the J/ψ within a jet [82, 89]. The latter has been in particular measured by LHCb, as is shown in the right panel of Fig. 2.2. The result is compared to an estimation from PYTHIA, which uses NRQCD. PYTHIA seems to overestimate the fraction of the momentum carried by the J/ψ, i.e. it predicts the J/ψ to be more isolated than what the experiment shows. However, the mismatch between PYTHIA and data was explained by a missing treatment of higher-order terms for the J/ψ production, and actually several sets of LDME could reproduce the experimental data [90]. Such a measurement is also very dependent on the kinematics probed for the J/ψ and the jet. This has been shown for example with ψ(2S) [91], measured for several jet momenta. While at low jet p_{T}, the ψ(2S) takes a large fraction of the jet momentum, at higher jet p_{T}, a two-peak structure appears. This two-peak structure, which does not have yet a theoretical explanation, contains one peak at lower momentum fraction, in addition to another peak appearing when the ψ(2S) is completely isolated and carries the full jet momentum.

Finally, the quarkonium-energy correlator, representing the correlation between J/ψ and hadrons weighted by the energy of the hadrons, has recently been proposed as an observable to investigate the quarkonium production processes [92]. This correlator presents the advantage that it is independent of the exact definition of a jet, and only weakly dependent on the hadronization for the other hadrons.

2.1.3. Quarkonium production in heavy-ion collisions

Besides its relevance for pQCD calculations and hadronization modeling, quarkonia has also an important role in the study of the QGP properties. The first concept for using J/ψ to probe the QGP was mentioned in Ref. [93]. It was proposed that, if a deconfined QGP state was formed, the color charges for the charm and anticharm quarks would be Debye-screened by the medium. The screening radius, i.e. the maximal distance between the heavy quarks at which the interaction between their color charges remain sufficient to keep them confined, is expected to decrease with the temperature. When the temperature is such that the screening radius becomes smaller than the J/ψ radius, the production of the J/ψ is largely suppressed. This leads to a suppression of the yields obtained in heavy-ion collisions compared to the ones in pp collisions where supposedly no QGP is formed. In addition, excited states such as the $\psi(2S)$ have a larger radius, and hence could suffer larger suppression compared to the ground states.

The potential which describes the quarkonium has been found to depend on the Debye mass, m_D, and the temperature T. A possible formulation of this potential is [94]:

$$V(r,T) = -\frac{g^2 C_F}{4\pi}\left(m_D + \frac{\exp(-m_D r)}{r}\right) - i\frac{g^2 T C_F}{4\pi}\phi(m_D r)\,. \tag{2.8}$$

m_D itself increases with the temperature. The real part of the equation represents the attractive potential between the heavy quark and antiquark, while the imaginary part represents dissipative effects through interaction with color charges from the medium which can dissociate the quarkonium state. In the limit of zero temperature, this potential is equivalent to the Cornell potential. When the temperature increases, the real part of the potential could be modified, as can also be seen from lattice QCD calculations [95] in the left panel of Fig. 2.3. Due to the color screening effect, the potential at large distance between the heavy quarks becomes flatter with increasing temperature. The rising confining potential, which is strong within the vacuum, is largely reduced, and the probability for the quarkonium to "melt" inside the medium increases. The excited states have lower binding energy and therefore start to melt at lower temperature than the ground states. The higher the degree of excitation, the stronger the melting. This hierarchy between different quarkonia states is called sequential suppression. Due to sequential suppression, the measurement of the yields of several quarkonia states could even contribute to the determination of the temperature of the medium. Nevertheless, recently, some lattice QCD calculations have predicted that the real part of the quarkonium potential is not modified, contrary to the imaginary part [96]. This would suggest that the suppression of quarkonia yields can be predominantly attributed to dissociation of the quarkonium caused by gluons from the medium, rather than screening between the color charges of the heavy quark and antiquark.
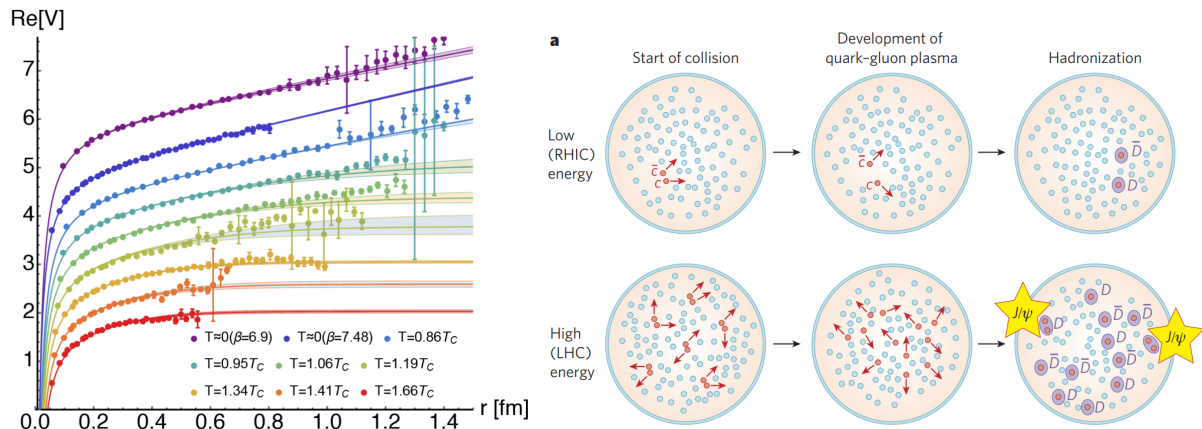
Figure 2.3.: Left: Evolution with the temperature of the real part of the in-medium quarkonium potential in thermal equilibrium, calculated with lattice QCD. The y values are shifted arbitrarily for visibility. Taken from [95]. Right: Sketch of the evolution of the charm quarks within a QGP. At low energy, the number of produced $c\bar{c}$ is low and they fly apart and hadronize to D^0. At higher energy, the number of produced $c\bar{c}$ is much higher, and some charm quarks originating from different initial $c\bar{c}$ pairs can recombine together, increasing the J/ψ yield. Taken from [97].

Quarkonium regeneration is another effect which can happen within the QGP medium. Such an effect is illustrated in the right panel of Fig. 2.3. When there are many heavy quark pairs produced in the medium, it is possible that two quarks which were at first uncorrelated would recombine together to hadronize into a quarkonium. The probability for this to happen depends approximately quadratically on the number of heavy quarks. Thus, this phenomenon is relevant only when the number of heavy quark pairs is large enough, hence only for charm quarks at LHC energies. This effect is observed mainly at low p_{T}, for which the charm quark density is larger than for high p_{T}.

Such suppression and regeneration effects can usually be analyzed through the nuclear modification factor R_{AA}:

$$R_{AA}(p_{\mathrm{T}}) = \frac{dN_{AA}/dp_{\mathrm{T}}}{\langle T_{AA} \rangle d\sigma_{pp}/dp_{\mathrm{T}}} \ . \tag{2.9}$$

N_{AA} is the production yield per event, while σ_{pp} is the production cross-section in pp collisions. $\langle T_{AA} \rangle$ is the nuclear overlap function, estimated through the Glauber model, and proportional to the average number of binary nucleon-nucleon collisions in the considered centrality interval. If there were no QGP effects, the yield in Pb–Pb collisions could be obtained from the yield in pp collisions, simply by scaling it with the number of binary collisions. In this case, $R_{AA} \approx 1$, although there could also be CNM effects. A departure from unity would then be a direct probe for these effects.

Several heavy-ion experiments have probed the presence of these medium effects through measurement of the quarkonium nuclear modification factor. In the left panel of Fig. 2.4, R_{AA} is shown as a function of the number of participating nucleons, as measured by CMS [98] for the bottomonium states $\Upsilon(1S)$, $\Upsilon(2S)$ and $\Upsilon(3S)$. The average number of participants increases when considering more and more central collisions. It is also correlated with an increase of the

energy density within the medium. The observed decrease with N_{part} of R_{AA} for Υ yields could come from a progressive melting of the quarkonium states within the medium with increasing temperature. The sequential suppression can also be inferred from the reduction of R_{AA} for excited states compared to the ground state. In the right panel of Fig. 2.4, R_{AA} is shown for J/ψ as a function of the charged-particle multiplicity of the collision, which also increases for more central and higher energy density collisions. The measurement is done for several nucleon-nucleon center-of-mass energies. This includes NA50 measurements [99] at $\sqrt{s_{NN}} = 17$ GeV, STAR measurements [100] at $\sqrt{s_{NN}} = 200$ GeV and ALICE measurements [101] at $\sqrt{s_{\text{NN}}} = 5.02$ TeV. STAR and NA50 results show a decrease of the R_{AA} with the multiplicity similar to the bottomonium case. However, for ALICE, after a small decrease for peripheral collisions, the R_{AA} starts increasing when the collisions become more and more central. This is a strong sign that the recombination from uncorrelated charm quarks increases the J/ψ yields at LHC energies, while at lower energies this effect is not present. Another frequently studied observable is the elliptic flow of the quarkonium. This observable depends on the degree of thermalization: if their heavy quark constituents are thermalized within the medium, heavy-flavored hadrons would have a larger flow, similar to the one for light flavor hadrons, than if the heavy quarks are not thermalized. Therefore, elliptic flow provides an additional discrimination power between the different models describing J/ψ production in heavy-ion collisions. This observable will not be extended here.
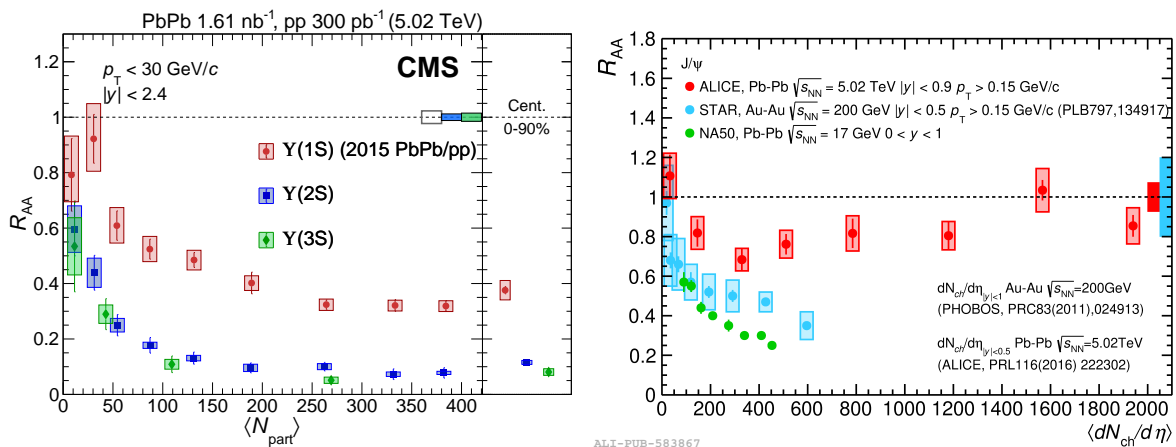
Figure 2.4.: Left: Nuclear modification factor of $\Upsilon(1S)$, $\Upsilon(2S)$ and $\Upsilon(3S)$ as a function of the number of participating nucleons, measured by CMS. Taken from [98]. Right: Nuclear modification factor of J/ψ as a function of the charged-particle multiplicity. Comparison between measurement by NA50 [99], STAR [100], and ALICE [101] experiments, operating at different center-of-mass energies. Taken from [23].

The models intending to describe the quarkonium nuclear modification factor can be grouped into three categories.

First, the Statistical Hadronization Model for charm (SHMc) assumes that the charm quarks are not confined within the QGP but fully thermalized [102, 103]. In this case, similar to for the light hadrons, the yields of open-charm hadrons and quarkonia can be estimated directly from the characteristics of the medium at the exact time of the chemical freeze-out. Because the mass of the charm quark is large compared to the temperature of the QGP, thermal production of charm is expected to be small. However, the initial heavy quarks would survive in the plasma. The

primordial charm is taken into account via a fugacity factor g_c. The yields of open-charm hadrons containing one charm quark would thus be multiplied by g_c compared to thermal production yields, while the yields of charmonium or open-charm hadrons containing two charm quarks would be multiplied by a factor g_c^2. g_c is itself estimated through cross-sections of open-charm production in pp collisions, corrected by the nuclear thickness function and for CNM effects. The SHMc approach for calculating the yields could in particular be validated by the J/ψ-to-D^0 ratio. Indeed, this ratio, measured to be higher in central than semi-central Pb–Pb collisions, is well reproduced by the SHMc within uncertainties [101]. However, the statistical model is not able to reproduce the p_T dependence of the charmonium production cross-section [104]. This could indicate that a part of the charm quarks is not fully thermalized, or at least not during the full evolution of the medium, or that the charm quarks have different spatial distributions compared to light quarks.

The second kind of approach for a description of the J/ψ yield in heavy-ion collisions is based on transport models. Transport models do not assume that an equilibrium is reached, but calculate the full evolution with time of the quarkonium yield within a medium. This evolution can be calculated via a Boltzmann-type equation. This equation assumes that the change in quarkonium yield in a small time period can be estimated through a dissociation term, which is proportional to the yield itself via a temperature-dependent dissociation probability, and through a regeneration component, which depends on the heavy-quark density inside the medium [105, 106]. The evolution can also be modeled via a kinetic-rate equation. With this equation, the change of the yield through dissociation is assumed to be proportional to the difference between the current yield and the yield in the thermal equilibrium case [107]. The transport model approach also requires knowledge of the initial charm density, as well as characteristics of the medium, such as the evolution of the temperature, often determined through a lattice QCD equation of state.

The last type of models relies on the quantum mechanical evolution of heavy quark pairs inside the medium through open quantum systems [108–110]. The quarkonium states are described through their density matrix, whose evolution with time is described by quantum master equations such as the Lindblad equation. The first term in a Lindblad equation describes the evolution of the $Q\overline{Q}$ systems by themselves. It uses the Hamiltonian of the quarkonium, which depends on the kinetics and real potential of the quarkonium. Other terms in the Lindblad equation describe the interaction with the external environment. Using the density matrix, the full evolution with time of the probabilities for the different color and spin states of the heavy quark pairs can be determined. The advantage of this type of models is that they rely only on first principles. However, their applicability depends on several assumptions, especially on the different time scales at play. These include for example the relaxation time of the $Q\overline{Q}$ systems after perturbation from the medium, or their intrisic time, related to the temperature above which the different quarkonium states are no longer well defined. An important time scale is also the autocorrelation time of the environment, which is often assumed small compared to the relaxation time of the $Q\overline{Q}$ systems, so that the evolution of the environment after the interaction with the $Q\overline{Q}$ can be neglected. In addition, the parallel evolution of many pairs, which would

be needed to account for the regeneration from uncorrelated pairs in the charmonium case, is difficult to model.

In addition, the production of charmonia can be analyzed in proton-nucleus collisions in order to determine the impact of the CNM effects. Such effects include for example the modification of the PDFs of the nucleon inside a nuclei compared to a free nucleon, additional saturation within the CGC framework or energy loss and nuclear absorption while the $Q\overline{Q}$ pass through the nucleus.

2.1.4. Non-prompt J/ψ

A substantial fraction of the J/ψ mesons come from the weak decay of beauty hadrons. In pp collisions, this fraction has been measured to be around 10 to 15% at low p_{T}, and increases with the J/ψ transverse momentum, as can be seen in the left panel of Fig. 2.5 [80]. Analyzing non-prompt J/ψ probes hadronization or medium effects of a heavy quark within an open heavy-flavor hadron, rather than effects on the quarkonium. In addition, the decay process might modify the p_{T} spectra of the non-prompt J/ψ compared to the one of the beauty hadrons. However, this effect could be unfolded using the knowledge of the decay kinematics [111].
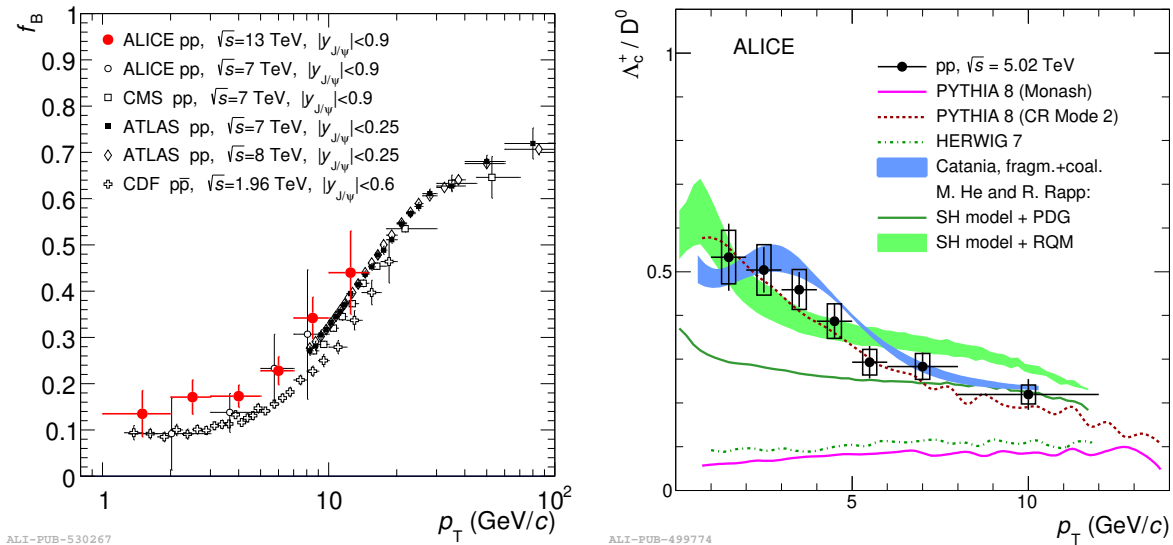
Figure 2.5.: Left: Fraction of non-prompt J/ψ as a function of p_{T}, measured by several experiments. Taken from [80]. Right: Ratio between Λ_c^+ and D^0 production cross-section as a function of p_{T}, measured by ALICE. The measurement is compared to several models. Taken from [112].

Open heavy-flavor production and hadronization:

The production of open heavy-flavor hadrons in pp and p–Pb collisions can generally be described by the factorization formula (see Eq. 1.5). In the case of heavy-flavor hadrons, this formula uses in particular the cross-section for the production of a heavy-quark pair. Several frameworks are able to calculate this cross-section. Among them are for example the Fixed Order plus Next-to-Leading Logarithm (FONLL) [113] or the General-Mass Variable-Flavor-Number Scheme (GM-VFNS) [114]. These two frameworks have the advantage that they are working well both at

low and high p_{T}. The main differences between the calculations within these frameworks, which are often expanded at NLO in powers of α_S, are either the treatment of the heavy-quark mass, the possible inclusion of logarithm terms depending on powers of $\alpha_S \ln(p_{\mathrm{T}}^2/m_Q^2)$, the number of quark flavors inside the proton contributing to the cross-section, or the subtraction of potentially-double-counted terms to avoid divergence at low p_{T}. The uncertainty on the cross-sections can be evaluated via the uncertainty on the PDFs, via the variation of the renormalization scale μ_R and of the factorization scale μ_F used in the calculation, as well as via the variation of the value of the heavy quark mass, which is not precisely known. The larger mass of the b quark compared to the c quark cause the uncertainties to be smaller for the $b\bar{b}$ cross-sections than for the $c\bar{c}$ cross-sections. However, the uncertainties still remain large, especially at low p_{T} (e.g. for FONLL at heavy quark $p_{\mathrm{T}} = 2$ GeV/c and LHC energies, the uncertainty is $\approx 50\%$ for the $b\bar{b}$ cross-section, and $\approx 140\%$ for the $c\bar{c}$ cross-section).

In addition, in order to calculate the production cross-section of heavy flavor hadrons, it is necessary to convolute the cross-section for heavy quark production with fragmentation functions $D_Q^H(z)$. The fragmentation functions describe the probability for a heavy quark Q to fragment into a hadron H carrying a fraction z of the heavy quark momentum. It is usually assumed that the fragmentation process is universal, which means that the fragmentation is independent of the collision system. Therefore, fragmentation functions have been extracted from the results of e^+e^- and ep collisions [115].

However, several LHC measurements [112, 116, 117] have shown a possible breaking of the assumption of universal hadronization. One of such measurements is shown in the right panel of Fig. 2.5. There, the ratio between Λ_c^+ baryons (*udc* quarks) and D^0 mesons (*cd* quarks) cross-sections, measured by ALICE in pp collisions, is shown as a function of p_{T}. The ratio is found to decrease with p_{T}, from ~ 0.5 at $p_{\mathrm{T}} \sim 1$ GeV/c, to 0.2 at $p_{\mathrm{T}} \sim 10$ GeV/c. This is compared to several models. First, PYTHIA with Monash tune predicts an almost flat ratio of ~ 0.1. This is due to the assumption of universality of the hadronization. The large discrepancy with experimental results shows the limits of this hypothesis. However, when adding effects from CR-BLC mode 2 [46], PYTHIA reproduces the data. This could show that other production mechanisms than fragmentation are at play in baryon formation. While fragmentation might be the dominant process at high p_{T}, higher-twist effects, such as color correlation between the MPI, play a role at low p_{T}, where the parton density is larger. The larger baryon-to-meson ratio at lower p_{T} can also be explained via the addition of a coalescence mechanism to the fragmentation process. Coalescence is applied through the Wigner formalism by the Catania model [118]. In this case, the presence of a deconfined medium, where u, d, s quarks and gluons are thermalized, is assumed. Due to the small QGP lifetime in pp collisions, it is not assumed that the charm quarks thermalized. On the contrary, they are expected to follow a momentum distribution calculated from pQCD. The baryon-to-meson ratio can also be explained by the Statistical Hadronization Model, when the feed-down from the charm hadrons which have been predicted by the Relativistic Quark Model (RQM) but not measured experimentally is also taken into account [119].

Propagation of heavy quarks in the QGP:

In contrast to light quarks, heavy quarks are produced only at the beginning of a heavy-ion collision (during the first fm/c), and are neither annihilated nor produced thermally within the QGP. This means that they experience the full lifetime of the QGP. Therefore, properties of the medium could be extracted by analyzing how the heavy quarks interact with the QGP and propagate within it. In particular, during their propagation, heavy quarks could experience collisional and radiative energy loss.

Collisional energy loss comes from elastic collisions with the QGP particles, from processes such as $gQ \rightarrow gQ$ or $qQ \rightarrow qQ$. Such energy loss happens especially at relatively low momentum. In general, the total energy loss depends linearly on the length traversed by the particle in the medium. Therefore, this path length dependence also causes a dependence of the energy loss on the geometry of the collision.

Radiative energy loss comes from inelastic collisions with the QGP, when a gluon is radiated afterwards, from processes such as $gQ \rightarrow ggQ$ or $qQ \rightarrow gqQ$. This type of energy loss happens generally at higher momentum compared to collisional energy loss. The energy loss through gluon emission by high-energy particles is higher for gluons than for quarks, due to the Casimir color factors, $C_A = 3$ for gluons and $C_F = 4/3$ for quarks, which enter in the cross-section calculations. In addition, the energy loss is larger for lighter particles. This is in particular due to the dead-cone effect, which states that the radiation of a massive quark is suppressed within an angle $\theta = M/E$ relative to the quark momentum direction, where M is its mass and E its energy. Energy loss via radiation depends in general on the square of the medium length traversed.

The propagation of the heavy quarks can also be described as a Brownian motion. Hence, transport equations can be used [120], such as the Boltzmann or Fokker-Planck equations. They can be approximated by a Langevin equation, describing the change in momentum by a friction force and a stochastic noise. The equations often introduce a spatial diffusion coefficient D_s, representing the average squared displacement per unit of time, which is smaller in strongly-coupled environment. This coefficient can be calculated with pQCD or determined from lattice QCD. However, the value of D_s can vary up to one order of magnitude between the different models. D_s is also proportional to the thermalization time, and it has been proposed that $2\pi T D_s \propto 4\pi\eta/s$ [121].

Measurement of the p_T dependence of the nuclear modification factor could help to discriminate the models. An example of such measurement for D mesons in central collisions by ALICE is shown in the left panel of Fig. 2.6. When taking into account energy loss, the expectation for the p_T dependence of R_{AA} is of the form $\propto \sigma(p_T + \Delta p_T)/\sigma(p_T)$, where Δp_T is the amount of energy loss and $\sigma(p_T)$ represents the cross-section in pp collisions. In this case, the increasing or decreasing trend of R_{AA} is highly dependent on the shape of $\sigma(p_T)$, explaining the non-monotony of the R_{AA}. The trend is reproduced by all models. The curves also show a maximum of R_{AA} around $p_T = 2$ GeV/c. This maximum is due to contributions from charm quarks which have higher initial momentum and suffer energy loss, but also from charm quarks with lower initial momentum which are pushed by flow. However, the measurement does not have yet the
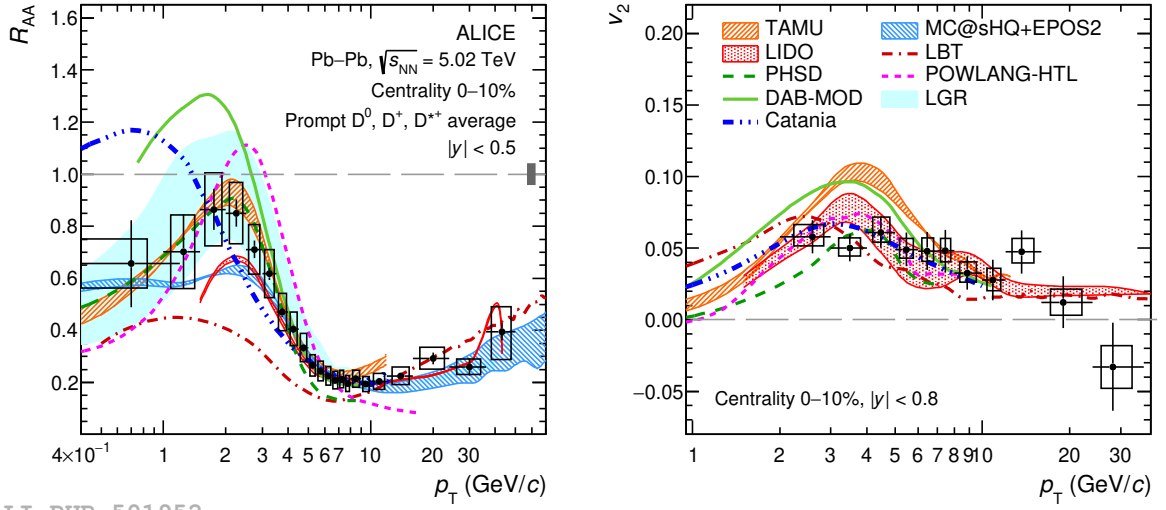
Figure 2.6.: Nuclear modification factor R_{AA} (left) and elliptic flow v_2 (right) for D mesons, measured by ALICE, and compared to several models for heavy quark transport. Taken from [122].

required precision for discriminating between the models. In addition, also the measurement of the D meson elliptic flow v_2 in central collisions is shown in the right panel of Fig. 2.6. Its value is finite and positive with a maximum around 0.05. This shows that the charm quarks also have been thermalized, at least partially, through the interactions with the medium. Most models can reproduce this value, meaning that more precision is also needed there.

This section has shown how the production and evolution of open heavy-flavor hadrons and quarkonia can be described, both in vacuum and inside a strongly-interacting QGP medium. These production mechanisms also depend on the initial state of the collisions. However, the presence of collectivity in high-multiplicity proton-proton collisions indicates that the transition regime between vacuum and QGP is not yet clearly understood. Such transition could be analyzed through the multiplicity dependence of the production of heavy-flavor hadrons, as will be seen in the following section.

2.2. Multiplicity-dependent quarkonium production

As explained in the previous section, heavy quarks are created in hard scatterings, with high momentum transfer. In contrast, most charged particles come from soft scatterings, with low momentum transfer. Thus, a question could be raised on whether hard and soft particle production are similar, or whether they present some fundamental differences. It could also be asked how these different modes of particle production are connected. An example of a possible interplay between hard and soft particle production would be when a hard scattering emits soft particles in addition, or if the environment created by soft scatterings would affect the hard particle produced directly (such as medium effects) or indirectly (for example as a selection effect, where selecting a specific configuration on the environment would bias the production of the hard particle). Therefore, as was proposed in Ref. [123], correlating the production

of quarkonia with the multiplicity could improve the understanding of the interplay and the differences between hard and soft particle production. This correlation can be analyzed via the per-event-yield of quarkonia determined as a function of multiplicity. In addition, both quantities can be self-normalized, i.e. divided by their average values in minimum-bias events. The advantage of the self-normalization lies in uncertainty cancellations, both for experimental measurement and theoretical calculations.

The expectations for the results of such a measurement could be diverse. The first possible expectation is that the production of J/ψ could be independent of the multiplicity, giving a flat correlation. This is unlikely because the presence of MPI is in general assumed, although terminology is inconsistent throughout in the models (number of parallel scatterings, number of pomerons, number of gluon-gluon fusion processes, ...). With this assumption, high-multiplicity events would occur when the total number of MPI is high. The total number of particles produced would be approximately proportional to the total number of MPI, while the number of hard particles produced would be approximately proportional to the number of hard MPI. The number of hard MPI is itself proportional to the total number of MPI, hence a proportionality between quarkonium yield and multiplicity could be assumed. In case of proportionality, it is expected that the J/ψ behaves similarly as any charged particle. This case will be referred to as the baseline in the following. Due to the self-normalization, the increase of J/ψ yield with multiplicity would be linear with slope unity.

However, it should be noted that this picture, where no difference in hard and soft particle production corresponds to a linear baseline, applies only when the quarkonium and the multiplicity are measured in the same region of the momentum space. Indeed, when they are measured in different regions, a decorrelation effect would appear, i.e. it is expected that the correlation becomes weaker. This is due to the correlation between the number of MPI (or, without losing any generality, the multiplicity) in these different momentum space regions. Indeed, even if the multiplicity is high in one region, it does not necessarily mean that, within the same event, the multiplicity is high in other regions of the phase-space where the quarkonium might be measured. This effect is particularly enhanced by the fact that the multiplicity distributions are decreasing steeply in pp collisions. Therefore, having a high multiplicity in one region happens so rarely that it becomes unlikely to obtain two regions with high multiplicity at the same time. Hence, even if the number of the quarkonium produced would increase linearly with the total number of particles produced in the same region, the quarkonium yield would appear relatively lower if it is measured in a region separated in rapidity compared to the region where the multiplicity is measured.

Besides, in the case where production of hard particles and soft particles would act differently, a departure from linearity would be observed. This departure from linearity could occur for example when more soft particles are emitted alongside the quarkonium in the same production process (these will be called autocorrelations in the following), resulting in a stronger-than-linear increase. A departure from linearity could also be observed if the production of soft or hard particles would be saturated. For example, saturation of soft particles would happen if the number of soft particles produced per MPI, or the number of soft MPI, would be reduced in a high-density environment compared to a low-density one. If the hard particles get saturated, the

increase of the quarkonium yield with multiplicity would be weaker compared to the baseline. In contrast, if the soft particles undergo saturation, the increase of the quarkonium yield with multiplicity would be stronger than the baseline. The understanding of such effects needs theoretical modeling, which will be presented in the next section.

In addition, because of the self-normalization, a larger self-normalized yield at high multiplicity comes with a lower yield at low multiplicity. When comparing two theoretical or experimental curves, the multiplicity value for which the first curve is lower than the second at lower multiplicity than this value and the other way around at higher multiplicity is often found to be around 1–2 times the average multiplicity. This is also the case when making comparison to the reference curve $y = x$. Therefore, for the rest of this thesis, when comparing two results, it is the comparison in the high-multiplicity region which will be implied, as high-multiplicity events are the main focus of this thesis.

2.2.1. Theoretical modeling

As will be seen in Sec. 2.2.2, the increase of the quarkonium yields with multiplicity has been found stronger-than-linear in experimental data when the quarkonium and the multiplicity are measured in the same rapidity region. Several models intend to describe this trend, implementing different effects which are explained in the following.

PYTHIA:

The evolution of the quarkonium yields with multiplicity can be simulated with the PYTHIA generator [39], which have already been described in Sec. 1.2.5. In PYTHIA, prompt quarkonia can be produced by different mechanisms. First, within the NRQCD mechanism, $Q\overline{Q}$ pairs are created in the initial partonic scattering, in any of the color and spin states. Then, the color octet spin states decay to a physical quarkonium state via emission of one gluon. In addition, quarkonia can be created through the cluster collapse mechanism [124]. Within this mechanism, two quarks with a very similar momentum direction and an invariant mass too small to induce the string breaking mechanism would form a cluster. The cluster can directly collapse to a hadron with a similar mass, via the exchange of gluons with the environment. In this case, the Q and $\overline{Q}$ do not necessarily come from the same PI. Therefore, such effect, although it represents only a small fraction of the J/ψ production, happens more frequently when the number of PI is high. The yield of J/ψ produced with the cluster collapse mechanism increases approximately quadratically with the multiplicity.

A process giving the possibility to produce quarkonia through NRQCD within the parton shower was recently added to PYTHIA [125]. This process replaces the quarkonium production via NRQCD in the initial process. The inclusion of such process was motivated by the poor description by PYTHIA of the J/ψ jet fragmentation measurements (see the discussion in Sec. 2.1.2). As long as the scale of the evolution within the parton shower is large enough, splittings producing quarkonia can happen anywhere within the parton shower, via e.g. $g \rightarrow g(Q\overline{Q})_n$ or $Q \rightarrow Q(Q\overline{Q})_n$ where n is the color and spin state of the $Q\overline{Q}$. In addition, if it is in a color-octet state, the $Q\overline{Q}$ can emit gluons, through $g \rightarrow gg$ splitting kernels. The quarkonium

is, in this case, seen as a massive gluon rather than as the superposition of its two constituent quarks. If the quarkonium is produced within the parton shower, it is likely that more particles are emitted in the same PI as the quarkonium.

EPOS:

In order to produce prompt quarkonia, EPOS4HQ uses the coalescence model from Wigner projection. The basics of the EPOS model has been already described in Sec. 1.2.5. Heavy quarks and antiquarks, potentially coming from different $Q\overline{Q}$ pairs, can recombine together when they have similar momentum and are produced close to each other spatially. The distribution of the distance between both quarks before they hadronize is assumed Gaussian, with different widths depending on whether they come from the same or a different $Q\overline{Q}$. These widths are not directly available theoretically and must be tuned from data. The yields of quarkonia from uncorrelated pairs increase faster with multiplicity than the ones of quarkonia from correlated pairs.

In addition, when measuring heavy-flavor production as a function of multiplicity, a stronger-than-linear increase is observed without activating the hydrodynamic evolution. With the hydrodynamic evolution, this increase is even stronger [52]. This could be due to a saturation of the soft particles, which compresses the multiplicity axis: in a saturated environment, the number of soft particles produced per pomeron (i.e. per gluon ladder) becomes lower than in a non-saturated low-multiplicity environment. In contrast, heavy quarks are expected to be less subject to the saturation effects, resulting in the stronger-than-linear increase. When there is no hydrodynamic evolution, the saturation of soft particles in this model is caused by the introduction, in order to mimic non-linear effects, of the saturation scale in the initial state. When hydrodynamic evolution is activated, additional saturation appears because a part of the energy normally available for particle production is converted into flow.

CGC-based calculations:

Several calculations based on the CGC framework make predictions on the multiplicity dependence of quarkonia or open heavy-flavor hadrons. In this framework, the gluon density can be calculated using evolution equations and starting from given initial conditions at the saturation scale. In general, it is assumed that high-multiplicity events are obtained as rare configurations with a higher number of partons probed inside the initial proton. Therefore, at high multiplicity, the high parton density makes saturation effects more likely to happen, corresponding to higher values of the saturation scale in high-multiplicity events compared to the one in minimum-bias events. When the saturation scale increases, there is a larger number of soft partons, main contributors to the multiplicity, which are within the saturation regime. In contrast, the harder partons responsible for charm production suffer less than the soft partons from saturation effects. Therefore, the initial-state saturation could be responsible for the stronger-than-linear increase because its effect is larger for soft particles compared to J/ψ. In addition, within the NRQCD framework, different color and spin states of the $Q\overline{Q}$ have different dependence on the gluon distributions, thus causing different dependence of J/ψ production on the multiplicity [126].

This increase can similarly be calculated for D^0 mesons. It becomes weaker when the rapidity increases and the multiplicity remains measured in the same rapidity region as the D^0 [127]. At very forward rapidity, the increase with multiplicity is expected to be linear. This is due to the increase of the saturation scale with the rapidity of the particle, or equivalently to the lower x values probed within the proton at higher values of rapidity, which cause the hard partons to also suffer from saturation effects.

The CGC framework can also be applied to p–Pb collisions [128]. In this case, saturation effects are enhanced in the Pb nucleus due to the increase of the gluon density by a factor depending on the longitudinal size of the nucleus. This calculation also introduces additional event-by-event fluctuations of the saturation scale and of the size of the hot spots around the quarks. It is found that these additional fluctuations can influence the correlations between J/ψ production and multiplicity. At forward rapidity, the p-going and the Pb-going case can be distinguished. In the p-going case, by probing smaller values of the momentum fraction inside the Pb nucleus, the J/ψ yield could suffer additional saturation effects, and thus would show a weaker increase compared to the Pb-going case.

The three-pomeron CGC model [129, 130] also uses the CGC framework, but proposes a different approach to explain the stronger-than-linear increase of the J/ψ yields with multiplicity. In this case, rather than being created by gluon-gluon fusion with emission of soft gluons during hadronization, J/ψ can be produced by the three-pomeron mechanism. The J/ψ is thus connected by two pomerons to one of the protons, and by one pomeron to the other one. These three pomerons would then cause a different dependence on the gluon distributions inside the proton compared to gluon-gluon fusion. Such mechanism would be largely enhanced at high multiplicity. Indeed, high-multiplicity configurations are usually obtained with large fluctuations on the number of hadrons produced from either one of the pomerons. The presence of the three pomerons is thus responsible for an increase of the number of configurations producing a given number of hadrons, particularly for high event multiplicity. The increase of the J/ψ yield then becomes stronger-than-linear when the J/ψ and the multiplicity are measured in the same rapidity region. When the multiplicity is measured in a different rapidity region than the J/ψ, only the contributions from one or two pomerons connected to one of the protons can enter in the multiplicity, leading to a reduced phase-space of configurations. The increase is thus weaker compared to the case where all three pomerons contribute to the multiplicity at the same time.

Geometric model:

The stronger-than-linear increase of the J/ψ yields with multiplicity can also be explained by a specific geometrical structure of the colliding protons [131]. Indeed, in this model, it is assumed that the parton density follows a Y shape when probed at a large enough Q^2 allowing the quarks and gluons to be resolved. The gluons would be located at the center of the proton, while the valence quarks would be found at the extremities of the Y shape. The pp collision can be analyzed geometrically using the Glauber model, in which the traditional nucleon degrees of freedom in heavy-ion collisions have been replaced by partonic degrees of freedom. Because of the different spatial configurations of the quarks and the gluons, the gluon thickness function is more peaked

at smaller impact parameter than the quark thickness function. In this geometric picture, the high-multiplicity configurations correspond to collisions with small impact parameter. Therefore, at high multiplicity, gluon-gluon collisions are favored. Because the cross-section for $gg \to c\bar{c}$ is higher than the cross-section for $q\bar{q} \to c\bar{c}$ at high center-of-mass energy, quarkonium production is strongly enhanced for ultra-central (i.e. high-multiplicity) collisions.

Coherent Particle Production:

The Coherent Particle Production (CPP) model [132, 133] draws a parallel between pA collisions and high-multiplicity pp collisions. This parallel is motivated by the fact that, at the high energies reached at the LHC, the nucleus is Lorentz-contracted in the longitudinal direction and the gluons from different nucleons overlap. This overlap occurs similarly as in the case when the gluons come from a single nucleon with high gluon density, and the scatterings of pomerons from the same or from different nucleons could be identical. Due to this similarity, phenomenological parametrizations typically used for pA collisions can be applied to high-multiplicity pp collisions. In particular, in nucleus collisions, the number of hard scatterings scales with N_{coll}, and consequently the J/ψ production shows the same scaling behavior. Corrections for nuclear shadowing have to be applied, but are relatively small. In contrast, for inclusive charged hadrons, the scaling with N_{coll} is not realized. The hadron multiplicity increases as $N_{\mathrm{ch}} \propto 1 - \beta + \beta N_{coll}$, with $\beta \sim 0.5 - 0.65$ extracted from data. The fact that β is smaller than unity can be related to saturation effects, explaining the stronger increase of the J/ψ production compared to charged hadrons.

Moreover, during the multiple scatterings within the nucleon, the gluons obtain a kick in their momentum, broadening their momentum distribution by a term Δp_{T}^2. These kicks increase the typical scale of the process Q^2. Gluons at lower scale become less common, which is equivalent to introducing a saturation scale $Q_s^2 = \Delta p_{\mathrm{T}}^2$. At high multiplicity, when the number of scatterings is larger, the scale Q^2 of the processes increases. Due to the DGLAP evolution, the gluon density is increased, thus causing also an increase of the J/ψ yield. However, for low-p_{T} hadron production, the distribution of soft gluons is constrained by saturation effects and cannot increase further. This means that, contrary to the J/ψ yields, the multiplicity is not affected by this additional initial-state effect, hence the stronger-than-linear increase. This model also predicts a stronger increase of the J/ψ yields at high p_{T}.

Percolation:

The percolation model [134] implements final-state effects via the presence of strings responsible for particle production. It is assumed that the number of J/ψ produced in the collisions is proportional to the number of strings produced N_s. The number of charged particles also depends on the total number of strings, but the dependence follows $N_{\mathrm{ch}} \propto F(\rho)N_s$. Here, $F(\rho)$ decreases when the string density $\rho = N_s \sigma_0 / \sigma$ increases, where σ_0 is the transverse area of a string and σ is the transverse area of the collision. Therefore, at high multiplicity, for which the string density is much higher, these strings start to overlap. Each string produces less charged particles compared to an average string at low multiplicity. The dependence of the midrapidity quarkonium yields on

charged-particle multiplicity is then approximately linear at low multiplicity, and quadratic at high multiplicity. The stronger-than-linear increase of the J/ψ yields therefore happens because of the saturation of the number of the soft strings. At forward rapidity, since the average number of strings is smaller, the increase is supposed to be weaker compared to midrapidity.

Comover interactions:

The comover interaction model [135, 136] assumes that the quarkonium can be dissociated by particles moving in the same direction as the quarkonium. The probability for the quarkonium to be dissociated depends on the density of these comovers and on a dissociation cross-section. Therefore, this probability increases with the multiplicity of the collision. The model is in particular able to compute nuclear modification factors in heavy-ion collisions. Furthermore, excited quarkonium states have lower binding energies than ground states, and thus a larger dissociation cross-section. The ratio between the production cross-section for excited and ground quarkonium states is then expected to decrease with the multiplicity of the collision, also in pp collisions.

Presence of a QGP medium:

Due to the signs of collectivity observed in high-multiplicity pp collisions, several models have made the assumption that a small QGP droplet is created [137, 138]. The pp collisions can be evolved from their initial temperature and energy density profile up to the freeze-out time using hydrodynamical simulations. In Ref. [137], the quarkonia can be evolved inside this medium using a temperature-dependent potential, allowing to estimate the amount of their suppression after the evolution within the QGP. This model can in particular estimate the multiplicity dependence of the ratio between $\psi(2S)$ and J/ψ. Because of the lower binding energy and higher suppression for $\psi(2S)$, this ratio decreases with the event multiplicity. When increasing the value of the initial temperature, the decrease is stronger, making it possible to estimate the temperature of the medium by comparing to experimental data. In the Unified Model of Quarkonia Suppression [138], the quarkonia yields are evolved in the small medium through equations taking into account gluon dissociation, color screening, and regeneration from correlated pairs. The hydrodynamic evolution results in a stronger-than-linear increase for J/ψ as a function of the multiplicity. The model also predicts a stronger suppression for $\psi(2S)$ than for J/ψ for all multiplicities, although the difference between the suppression for both states is smaller at high multiplicity.

2.2.2. Published experimental results

Several high-energy experiments at LHC and RHIC have measured the multiplicity dependence of open heavy-flavor hadrons, prompt and non-prompt quarkonia and ratios between excited and ground quarkonia states, in pp and p–Pb collisions. This substantial amount of measurements can be used for comparison to theoretical models.

**Multiplicity-dependent open charm and beauty production:**

One of the first measurements of open heavy-flavor production as a function of multiplicity in pp collisions at the LHC was conducted by ALICE [139]. The yields of both D mesons and non-prompt J/ψ were measured, the latter accounting for open beauty hadrons. As can be seen in the left panel of Fig. 2.7, the increase for the D mesons is clearly stronger than linear. Due to the large number of models able to explain such an increase, no firm conclusion can be reached on the effects at play using this measurement alone. For non-prompt J/ψ, the experimental uncertainties do not allow a firm conclusion on whether the increase is also stronger than linear, and whether there is a difference between charm and beauty production. This clearly appeals for a more precise measurement of the multiplicity dependence of open-beauty, especially through non-prompt J/ψ, in order to understand if the heavy-quark mass has an influence on the multiplicity dependence.
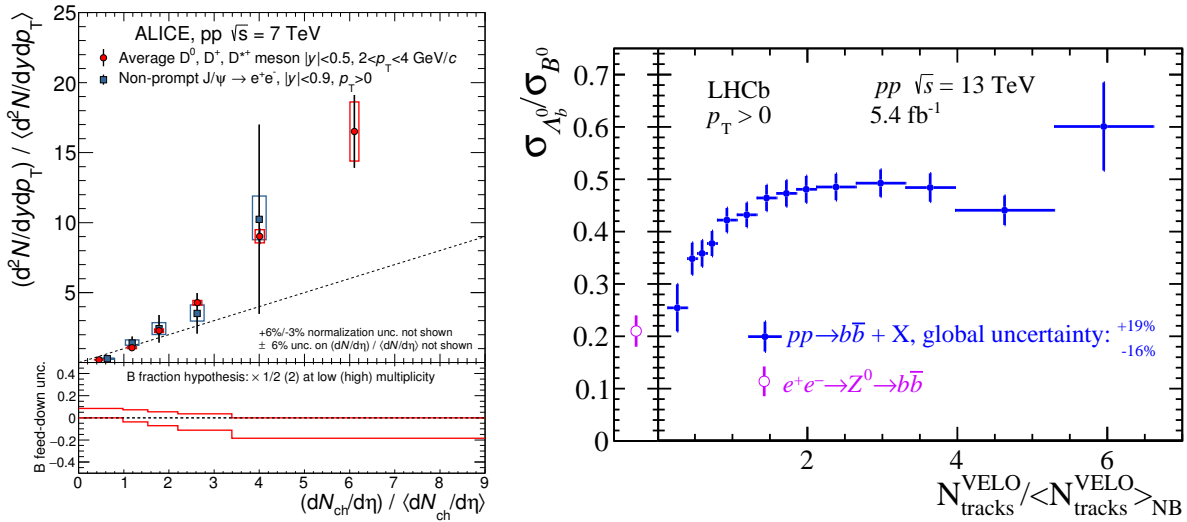
Figure 2.7.: Left: Multiplicity dependence of D mesons and non-prompt J/ψ, measured by ALICE in pp collisions. The heavy-flavor hadrons and the multiplicity are measured at midrapidity. Taken from [139]. Right: Multiplicity dependence of the ratio between Λ_b and B^0, measured by LHCb at forward rapidity. Taken from [117].

In addition to D mesons, also the dependence of the baryon-to-meson ratio on multiplicity has been measured. This can probe whether the hadronization of heavy quarks depends on the density of the environment. The hadronization could be affected by color reconnections, coalescence, or thermal production of the different hadrons, allowing to check the importance of the final-state effects. In the right panel of Fig. 2.7, the multiplicity dependence of the ratio between Λ_b and B^0, measured by LHCb at forward rapidity [117], is shown. This value increases with multiplicity, until a plateau is reached when the multiplicity estimator reaches twice the average number of tracks in the LHCb innermost detector. At low multiplicity, the ratio is compatible with the one obtained in e^+e^- collisions. This ratio has also been measured at midrapidity by ALICE in the charm sector [140]. Although a clear modification of the p_T distribution of the ratio is observed, the uncertainties do not allow to determine whether the ratio between p_T-integrated yields of charm hadrons at midrapidity presents a multiplicity dependence or not.

The multiplicity dependence has also been measured by ALICE for electrons coming from the semi-leptonic decays of heavy-flavor hadrons in pp and p–Pb collisions [141]. The yields in pp collisions are shown in the left panel of Fig. 2.8. Both the electrons and the multiplicity are measured at midrapidity. The electrons are separated intp several momentum intervals, and, in all these intervals, the increase of the self-normalized yields with self-normalized multiplicity is stronger than linear. In addition, it can be noticed that the higher the p_{T}, the stronger the increase. However, this increase with p_{T} is not observed specifically for hadrons containing charm or beauty quarks. Indeed, ALICE has also measured the multiplicity dependence of high-p_{T} charged particles in pp collisions [142], as shown in the right panel of Fig. 2.8. Likewise, a stronger-than-linear increase which varies with p_{T} has been measured. The trend is well reproduced by MC generators, especially by EPOS LHC. That is a clear indication that the dependence on multiplicity of the yields of a given probe is probably dominated by the hardness of the selected probe.


ALI-PUB-559750
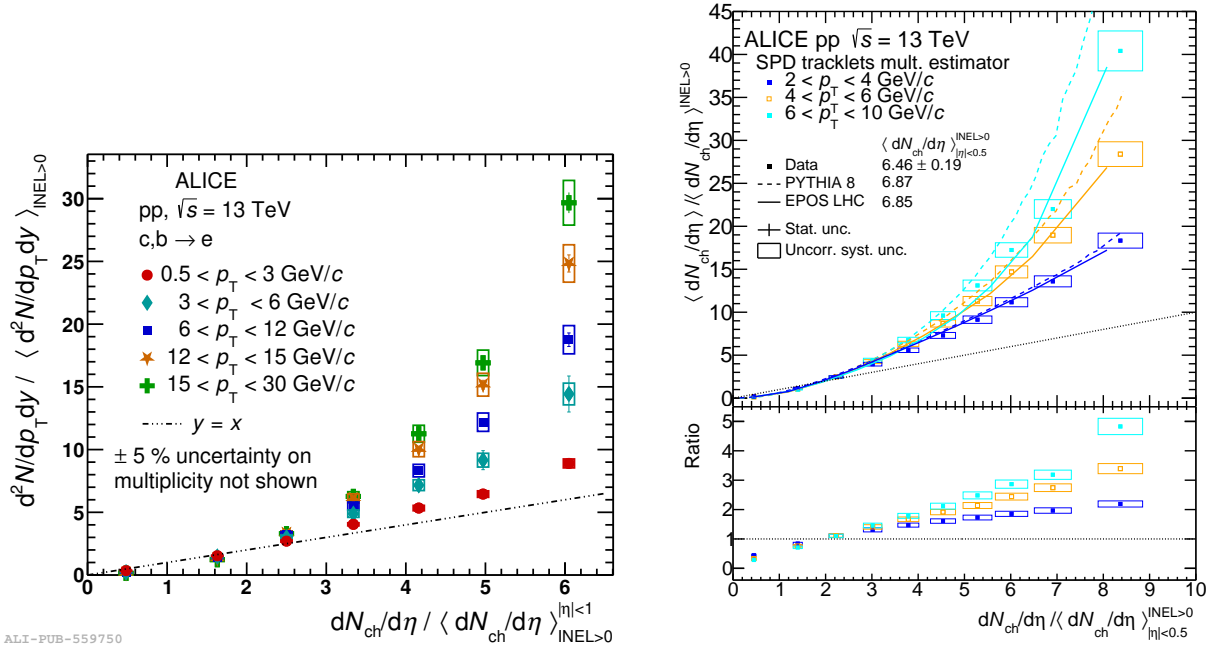
Figure 2.8.: Left: Multiplicity dependence of electrons from heavy flavor decays, measured by ALICE in pp collisions. Both the electrons and the multiplicity are measured at midrapidity. Taken from [141]. Right: Multiplicity dependence of charged particles, measured by ALICE in pp collisions. Taken from [142].

For p–Pb collisions, both initial-state effects, due to the scaling of the CGC saturation effects with $\mathrm{A}^{1/3}$, and final-state effects, because of the larger density of produced particles, could be enhanced. Surprisingly, although also in this case a stronger-than-linear increase is observed, the difference in the trend with the p_{T} of the probe for heavy-flavor electrons is not as significant in p–Pb collisions as in pp collisions [141]. A weak dependence on the momentum was also observed in p–Pb collisions for D mesons [143], although with lower statistical significance. This could indicate different mechanisms responsible for this increase depending on the colliding system. For example, if there was a strong influence of the autocorrelations on the momentum dependence, their impact would be considerably reduced by the larger average particle multiplicity and the less steep decrease of the multiplicity distribution in p–Pb collisions compared to pp collisions.

Autocorrelation effects are likely stronger at higher p_T, when the J/ψ might be produced within a jet where a large number of associated particles is emitted. Thus, a varying influence of the autocorrelation effects could explain the difference between pp and p–Pb collisions. However, in order to distinguish between the various possible effects, more measurements in proton-nucleus collisions would be needed.
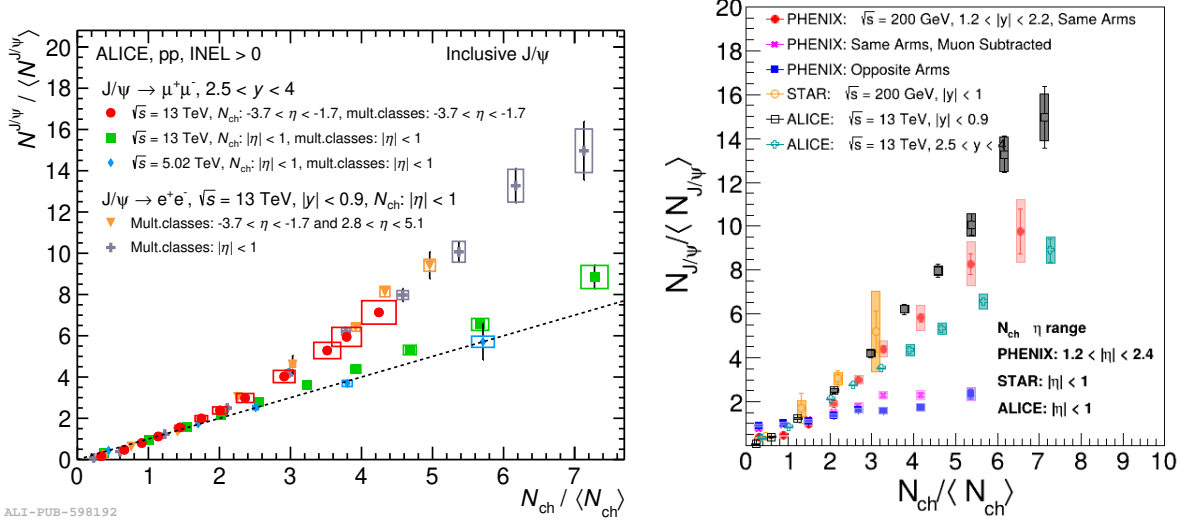
Multiplicity-dependent quarkonium production:

A variety of measurements of the multiplicity dependence of several different quarkonia have also been conducted. First, the multiplicity dependence of inclusive J/ψ production has been measured by ALICE at midrapidity ($|y| < 0.9$) as a function of midrapidity multiplicity ($|\eta| < 1$) [144]. The J/ψ yields have also been measured at forward rapidity ($2.5 < y < 4$), both as a function of midrapidity multiplicity ($|\eta| < 1$)[145] and forward multiplicity [146] ($-3.7 < \eta < -1.7$, note that, in this case, the sign of the pseudorapidity for the multiplicity selection is defined oppositely compared to the sign of the J/ψ rapidity; they actually correspond to the same rapidity region).
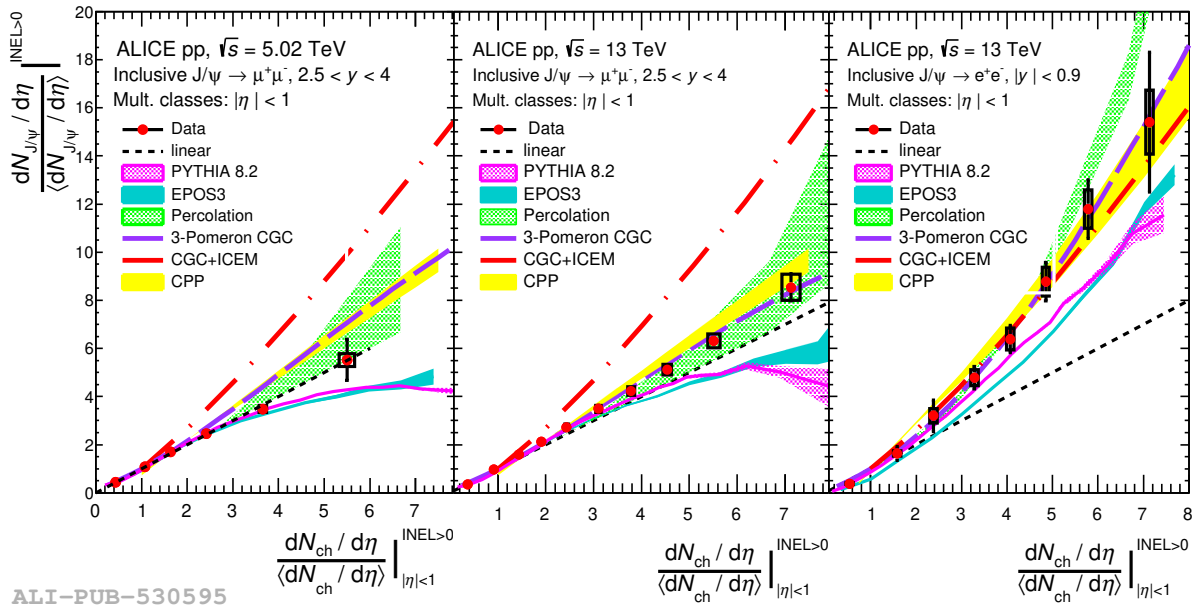
Figure 2.9.: J/ψ production as a function of the multiplicity within $|\eta| < 1$ in pp collisions, measured by ALICE, and compared with available theoretical models. J/ψ is either measured at forward rapidity at $\sqrt{s} = 5$ TeV (left) or $\sqrt{s} = 13$ TeV (middle), or at midrapidity at $\sqrt{s} = 13$ TeV (right). Taken from [145].

As seen in Fig. 2.9, when both the J/ψ production and the multiplicity are measured at midrapidity, the increase is stronger than linear. However, when there is a rapidity difference between the hard and the soft probe, the increase is close to linear. As explained earlier in this section, a weaker increase in the latter case is, at least partially, a correlation effect between different rapidity regions. Therefore, the linearity does not mean that hard particle production is similar to soft particle production in this case. However, this explanation remains qualitative and there could be additional effects influencing the different trends. For example, autocorrelation effects may appear when J/ψ and multiplicity are measured in the same region, although the

Figure 2.10.: Left: Multiplicity dependence of forward J/ψ production as a function of forward multiplicity, measured by ALICE, and compared with previous multiplicity-dependent J/ψ measurements. Taken from [146]. Right: Multiplicity dependence of J/ψ production in several pseudorapidity regions, measured at LHC and RHIC. Taken from [147]

forward rapidity region might also contain autocorrelations from the recoil present in the same partonic interaction as the one producing the J/ψ. There could also be an effect due to the specific rapidity region analyzed. Forward rapidity regions probe partons with lower values of x inside the initial proton, and hence are more subject to initial-state saturation effects. In addition, the charged-particle pseudorapidity density is lower at forward rapidity, modifying the impact of possible effects due to high charged-particle density. In addition, in the case of midrapidity J/ψ, the multiplicity dependence of J/ψ was measured in several p_T intervals. Similarly as for heavy-flavor electrons, the increase of the yields with multiplicity is stronger at higher p_T.

This comparison between different rapidity regions has also been studied via the measurement of forward J/ψ as a function of forward multiplicity, shown in the left panel of Fig. 2.10. In this case, the increase is stronger-than-linear, and close to the one observed when J/ψ and multiplicity are measured in the same midrapidity region. This likely indicates that the strong increase is indeed correlated with the fact that the hard and soft probes are measured in the same rapidity region, independently of the specific definition of this rapidity region. However, it should still be noted that the latter study has larger systematic uncertainties, and that, in contrast to the midrapidity case, the J/ψ daughters are removed from the multiplicity estimator.

The experimental measurements are also compared in Fig. 2.9 with predictions from theoretical calculations. In most of the cases, the predictions reproduce the stronger-than-linear trend when the J/ψ is measured at midrapidity, as well as the dependence on the rapidity region. However, PYTHIA and EPOS consistently underestimate the trend at high-multiplicity. The fact that J/ψ are produced more isolated in PYTHIA than found in experiments could explain, due to an underestimation of the autocorrelations, the weaker increase compared to data. In addition, the CGC+ICEM model [126] does not predict any reduction of the high-multiplicity yields when a rapidity difference is introduced. Because all the models implement different effects, no strong conclusion can be taken regarding the specific effect, or combination of effects, causing the

45

different trends. This means that additional measurements of other discriminating quantities are needed in order to complement the knowledge on the correlations between hard and soft particle production.

The multiplicity dependence of J/ψ production has also been analyzed by STAR [148] and PHENIX [147] experiments at RHIC. The measurements can be seen in the right panel in Fig. 2.10. As was observed for ALICE, both STAR and PHENIX indicate a stronger-than-linear increase when J/ψ and multiplicity are measured in the same rapidity region. Although the midrapidity results by STAR are limited by uncertainties, the yields measured by PHENIX at forward rapidity show slightly lower increase than ALICE. The main difference with respect to the LHC results is due to the center-of-mass energy of $\sqrt{s} = 200$ GeV. This has several consequences. First, it is not possible to reach values of x inside the proton as low as the ones reached at the LHC, which means that initial-state saturation effects are expected to be smaller. At this energy, the average multiplicities are much lower and the multiplicity distribution is falling much steeper compared to what is observed at the LHC. Due to the lower charged-particle density, final-state effects could be smaller. The combination of both effects could thus explain the lower increase for PHENIX. However, at RHIC energies, effects due to autocorrelations could be much stronger. Indeed, the additional particles produced alongside with the J/ψ have a much stronger impact on the multiplicity when the multiplicity distribution falls steeply. This effect can also be observed when the J/ψ daughters are removed from the estimation of the multiplicity. It was observed by PHENIX that the increase is much smaller than when these particles are not subtracted. Finally, because of the steeply decreasing distributions, the correlation between the multiplicity densities in different regions is even weaker. Therefore, the possibility of obtaining a large multiplicity both at forward rapidity and at backward multiplicity is even more suppressed compared to LHC energies. This leads to a weaker-than-linear increase when there is a large pseudorapidity difference between the J/ψ and the multiplicity measurement.

In order to understand if there is an influence due to the mass of the heavy quark, several experiments (CMS [149], ALICE [150], STAR [151]) have also measured the multiplicity dependence of the bottomonium Υ mesons. Qualitatively, similar trends as for the J/ψ measurement have been found, the increase being either stronger-than-linear or close-to-linear depending on the rapidity region and on the presence of a rapidity difference between the quarkonium and the multiplicity. In particular, the measurement by CMS is shown in the left panel of Fig. 2.11. The increase seems stronger than for J/ψ measured at midrapidity by ALICE. However, the pseudorapidity selection for the charged particles differs, CMS selecting larger regions than ALICE, and the center-of-mass energy is also different ($\sqrt{s} = 2.76$ TeV for CMS compared to $\sqrt{s} = 13$ TeV for ALICE). ALICE itself did not observe a significant difference between J/ψ and $\Upsilon(1S)$ production.

Furthermore, J/ψ and Υ have also been measured as a function of multiplicity in pA collisions. When multiplicity and quarkonia are both measured at midrapidity [149, 153, 154], the increase of yields is stronger than linear. The increase seems nevertheless slightly lower than in pp collisions. This could for example be due to a smaller impact of autocorrelations. The quarkonium could also itself enter a saturation regime in high-multiplicity p–Pb collisions, due to either initial-state or final-state effects. In the right panel of Fig. 2.11, the J/ψ production at forward
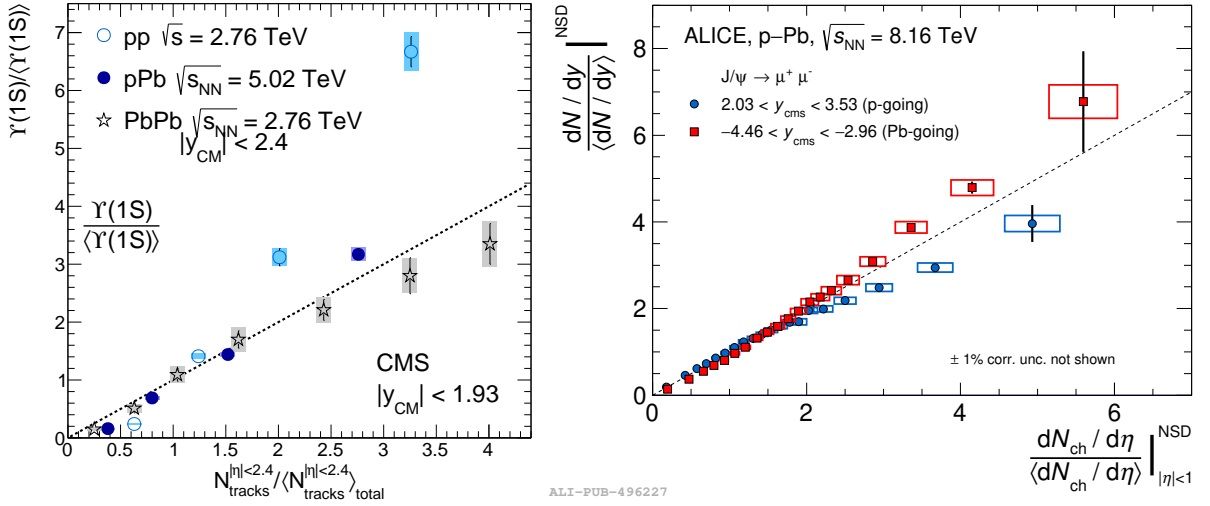
Figure 2.11.: Left: Multiplicity dependence of $\Upsilon(1S)$ production measured by CMS in pp, p–Pb and Pb–Pb collisions. The quarkonium and the multiplicity are both measured at midrapidity. Taken from [149]. Right: Multiplicity dependence of J/ψ production in p–Pb collisions, measured by ALICE. J/ψ is measured either at forward or backward rapidity, while multiplicity is measured at midrapidity. Taken from [152]

and backward rapidity is shown as a function of midrapidity multiplicity [152]. Forward rapidity corresponds to the p-going direction, where the yields increase slightly weaker than linearly, while backward rapidity corresponds to the Pb-going direction, where the yields show a slightly stronger-than-linear increase. While the closeness to a linear increase is expected from the rapidity difference, the rapidity selection does not explain at first order the difference between both results, since in both cases the rapidity difference is similar.

The difference between forward and backward rapidity could be due to initial-state effects. This is due to the fact that, for a J/ψ at $p_{\mathrm{T}} = 0$ GeV/c, the p-going region probes very low values of momentum fraction inside the Pb ($x_{Pb} \sim 10^{-5}$), while the Pb-going region probes higher values $x_{Pb} \sim 10^{-2}$. Because saturation effects are enhanced at low x_{Pb}, a larger saturation is expected for the J/ψ at forward rapidity compared to backward rapidity, an effect which is likely stronger at high multiplicity. However, the multiplicity density is also higher in the Pb-going direction than in the p-going direction [155], possibly causing additional final-state saturation effects for the soft particles. The difference in multiplicity also possibly affects the rapidity correlations between different regions. Indeed, when selecting events at a given midrapidity multiplicity, the average value of the self-normalized multiplicity at forward rapidity could be smaller than the one for backward rapidity. This would be due to the steeper decrease in the multiplicity distribution in the p-going direction compared to Pb-going direction, affecting the correlation with midrapidity multiplicity. The difference of the average midrapidity multiplicity values probed in the forward and in the backward rapidity case could then cause a reduced multiplicity dependence when the J/ψ is measured at forward rapidity and the multiplicity at midrapidity compared to the case when the J/ψ is measured at backward rapidity. Therefore, also in p–Pb, initial-state and final-state effects, as well as autocorrelations and rapidity correlations effects, remain possible causes for the observed trends.

Excited-to-ground states quarkonium production ratio:

Finally, several experiments have also measured the multiplicity dependence of the ratio between excited and ground states. This ratio is particularly interesting because, while ground states and excited states are likely affected by the same initial-state effects, the final-state effects could be different. Indeed, the lower binding energy of the excited states could reduce their yield at high-multiplicity in high-density environment compared to the J/ψ or $\Upsilon(1S)$ ground states.

The inclusive $\psi(2S)$-to-J/ψ ratio has been measured as a function of multiplicity by ALICE [156] and PHENIX [147]. No significant modification was observed within the large uncertainties. LHCb has also conducted the measurement of this ratio for prompt and non-prompt quarkonium [157]. This measurement is shown in the left panel of Fig. 2.12. In this measurement, which has smaller uncertainties than in the previous ALICE and PHENIX results, a decrease of the prompt ratio was observed, while the non-prompt ratio was found to be flat with multiplicity. This confirms the impact of final-state effects on the suppression of excited quarkonia states in high-multiplicity pp collisions. The breaking by comovers or the color deconfinement in a high-temperature medium could both explain this suppression.
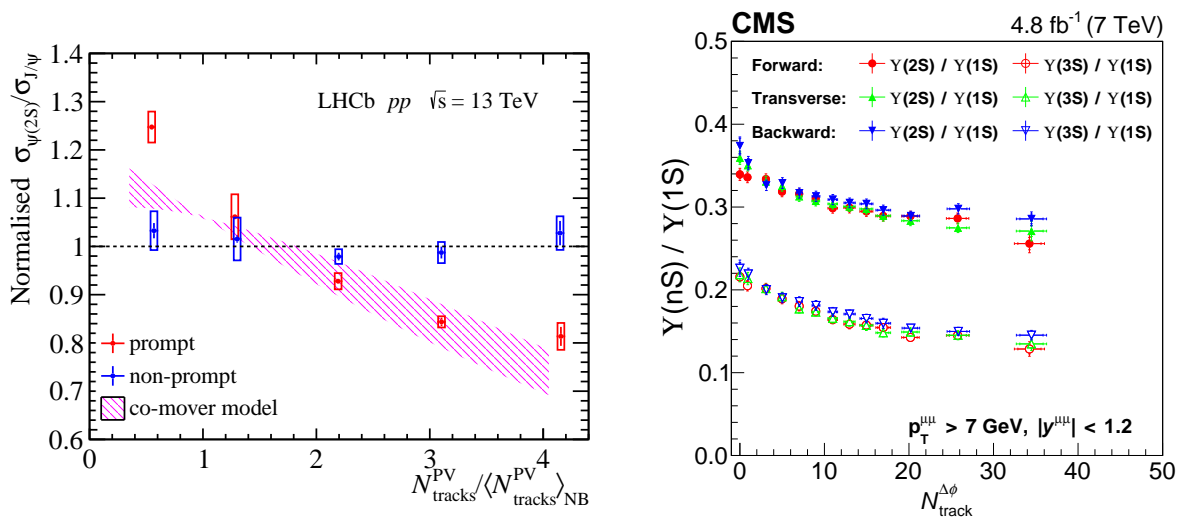
Figure 2.12.: Left: Multiplicity dependence of the ratio between $\psi(2S)$ and J/ψ, measured by LHCb. Taken from [157]. Right: $\Upsilon(2S)$-to-$\Upsilon(1S)$ and $\Upsilon(3S)$-to-$\Upsilon(1S)$ ratios as a function of multiplicity measured in azimuthal angle regions with respect to the bottomonium emission direction, measured by CMS. Taken from [158].

The measurement of excited-to-ground state ratios was also conducted for $\Upsilon(nS)$ by ALICE [150], STAR [151], LHCb [159] and CMS [158]. Similar to charmonium, when the precision was sufficient, a decrease of the bottomonium ratios was observed as a function of multiplicity. In addition, in the CMS analysis, the multiplicity was estimated in different azimuthal regions with respect to the J/ψ emission direction. The same measurement of the ratios was carried out as a function of the multiplicity in the regions. This allows to understand if the suppression is mainly a global effect depending on global event properties, or a local effect arising from autocorrelations or from the local density of particles emitted in the same direction. This measurement is shown in the right panel of Fig. 2.12. The ratios show similar trends for the three regions. This could underline that the suppression of the excited states relative to the ground state depends on the

underlying event property. However, it should still be noted that the multiplicity values in the different regions are correlated. For example, when the multiplicity transverse to the quarkonium is increased, also the selection on the toward multiplicity changes. A remnant of a local effect might then still appear in other regions. Besides that, CMS also measured the dependence of this ratio on the spherocity variable. This quantity measures whether the particle emission in an event is isotropic, or whether the particles are found only in specific directions (i.e. a jet-like event). The analysis showed that the decrease of the ratio occurs mainly for isotropic events and not when the quarkonium is localized inside a jet. This is another indicator that the decrease of the ratio might come from global event properties, such as the ones of a high-density and high-temperature QGP medium.

Conclusions on the multiplicity-dependent experimental results:

LHC and RHIC experiments have measured in small systems the dependence of the yields of several open heavy-flavor and quarkonia on multiplicity, leading to several conclusions.

First, for both open heavy-flavor and quarkonia, a stronger-than-linear increase of the yields with multiplicity has been observed when both the yields and the multiplicity are measured in the same region. The increase is also stronger at high p_{T} than at low p_{T}. This increase could be explained by initial-state and final-state effects, but also by autocorrelations from particles produced in the same production process. In addition, the uncertainties on the measurement for the case of the beauty hadrons are currently quite large. A precise measurement of the evolution with multiplicity of the prompt and non-prompt J/ψ yields could then help to disentangle the different impact of charm and beauty quarks on the correlation, as well as to shed light on possible differences between open heavy-flavor and quarkonia.

In addition, ratios between excited and ground state quarkonia show a slight decrease as a function of multiplicity. This demonstrates that final-state effects can impact excited quarkonia yields in high-multiplicity pp collisions.

Finally, the quarkonium yields have also been measured as a function of the multiplicity separated in rapidity compared to the J/ψ measurement region. In this case, the increase with multiplicity is found close to linear. However, part of the difference with respect to the case when the quarkonium and multiplicity are measured in the same rapidity region comes from the correlations between multiplicities in different rapidity regions. This effect could be addressed in future measurements by measuring the ratio to charged hadrons, which are also affected by these rapidity correlations. By construction, the increase of the charged hadron yields with multiplicity is linear when the multiplicity is measured in the same region and p_{T} interval. However, it is expected to be weaker than linear when the multiplicity is measured in a different rapidity region. Besides, due to the rapidity difference between the J/ψ and multiplicity measurement regions, the impact of autocorrelations is expected to be smaller. However, there could also be an influence due to the specific rapidity region measured. Therefore, as was done by CMS in order to understand the local or global nature of the decreases of $\Upsilon(nS)$ ratios [158], the measurement could be conducted by separating the J/ψ and multiplicity measurement in azimuthal angle rather than separating them in rapidity.

2.2.3. Event activity in azimuthal regions

A pp collision is often constituted of several partonic interactions. A small portion of these PI results in a large momentum transfer (hard scattering), while most of the PI amount to a small momentum transfer (soft scattering). When there is a hard scattering in a collision, a large amount of particles is often emitted in a specific direction. In contrast, each soft scattering usually results in the emission of a small number of particles, and these scatterings are often assumed to be relatively uncorrelated in azimuthal angle in pp collisions. These soft scatterings represent the underlying event, and a hard interaction may lie on top of it. The distinction between hard and soft events is in particular necessary because a high multiplicity can be obtained when a hard jet is present, but also when there are many soft PI. Both cases are not comparable, and the latter one is probably more prone to contain a high-density medium environment. In order to separate the different classes of events, the collisions can be separated for example based on the event activity in the region azimuthally transverse to the leading jet. This underlying event activity can be related to the number of MPI and the impact parameter of the collision with less biases from the hard jet than the azimuthally-integrated multiplicity, helping to disentangle the different hadronization mechanisms [160].
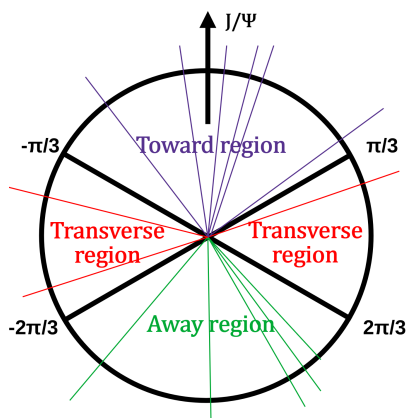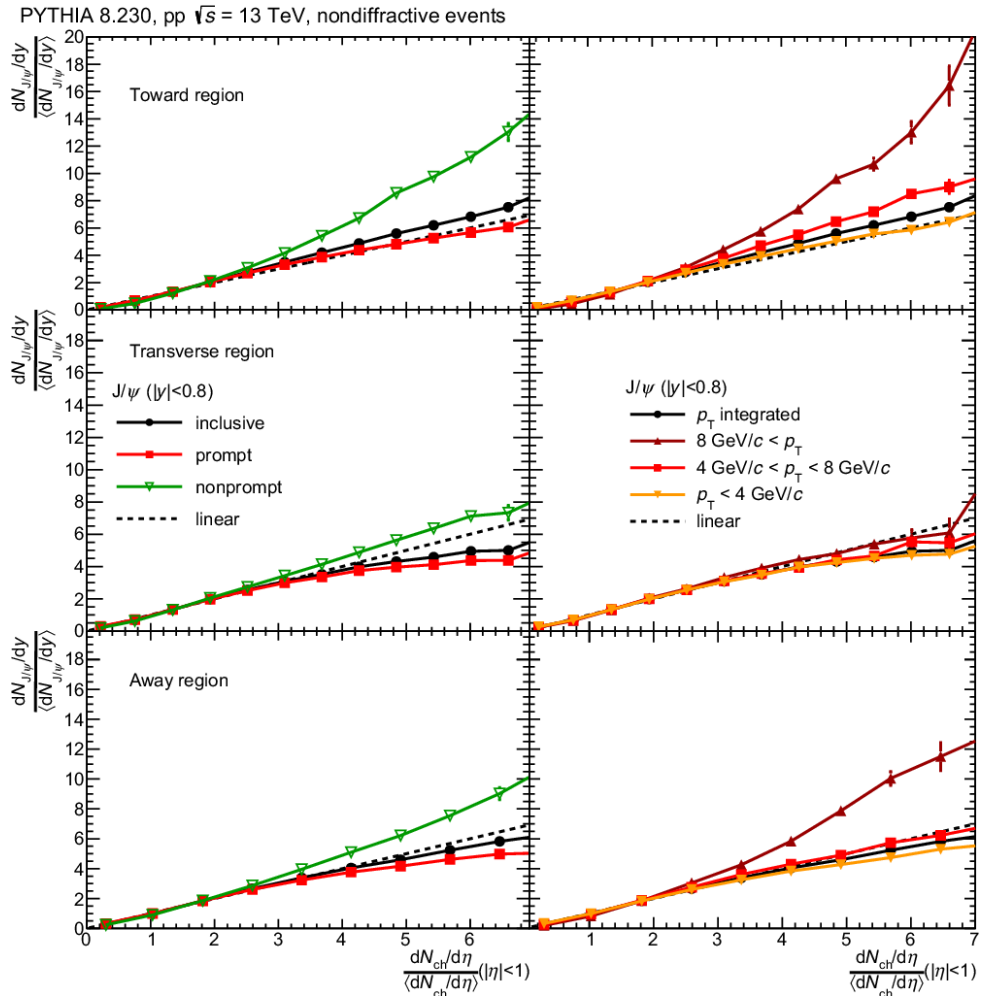

Figure 2.13.: Definition of the azimuthal regions with respect to the J/ψ emission direction.

This separation between the particles possibly produced in the hard scattering from the underlying event can also be done when a J/ψ is present. In this case, azimuthal regions can be defined with respect to the J/ψ emission direction. This definition is illustrated in Fig. 2.13. The toward region contains all particles which satisfy $|\varphi_{\text{particle}} - \varphi_{\text{J}/\psi}| < \pi/3$. When this quantity is between $\pi/3$ and $2\pi/3$, the particles are in the transverse region. Finally, for an azimuthal difference larger than $2\pi/3$, the particle belongs to the away region. Then, the dependence of the J/ψ yield can be analyzed as a function of the multiplicity in either of these regions. The toward region probably contains most of the autocorrelations from particles produced in the same production process as the J/ψ. This can include, for example, additional gluons emitted during hadronization of the J/ψ, other jet constituents if the J/ψ is produced within a jet, or the other decay products of the beauty hadron when the J/ψ is non-prompt. In contrast, the transverse region represents a less biased estimate of the underlying event activity. Finally, the away region could contain a recoil jet, provided this recoil falls into the acceptance considered.

It could either come from the other b quark in the $b\bar{b}$ pair for the case of non-prompt J/ψ, or from a potential recoil gluon balancing the momentum of the J/ψ for the prompt J/ψ case.

A measurement of the evolution of the yields with the multiplicity separated in regions would allow a better understanding of the impact of the autocorrelations on the stronger-than-linear increase observed for multiplicity-dependent J/ψ. If a stronger increase of hard particle production compared to soft particle production could only be observed when considering the multiplicity in the toward region, this increase would probably be due to autocorrelations. In contrast, if the stronger increase for hard particles could be observed as a function of the multiplicity in all three regions, the trend would likely be due to global effects influencing the full event, such as initial CGC saturation or high-density medium effects. In addition, effects happening early within the collision could have a larger influence than later effects for correlations of particles with large angle difference. Although final-state effects in a small system are potentially more local than initial-state effects, it is unlikely that such a difference on the azimuthal correlations between initial and final state would be visible in such a measurement.

Figure 2.14.: Prediction by the PYTHIA MC generator using the Monash tune of the self-normalized yield of J/ψ as a function of self-normalized multiplicity in the toward (top panels), transverse (middle) and away (bottom) azimuthal regions. Inclusive, prompt and non-prompt J/ψ yields are shown separately in the left panels, while inclusive J/ψ yield is separated in several p_T intervals in the right panels. Taken from [161].

A study of J/ψ production as a function of the multiplicity separated by regions has been conducted with PYTHIA using the Monash tune in Ref. [161]. Fig. 2.14 presents the PYTHIA predictions for the evolution of J/ψ yields with the multiplicity in regions. The J/ψ are separated between prompt and non-prompt in the left panels, and between several p_{T} intervals in the right panels. PYTHIA predicts a stronger increase for non-prompt J/ψ compared to prompt J/ψ. This difference between prompt and non-prompt J/ψ is particularly visible in the toward and away region, where autocorrelation effects are stronger. In contrast, the increase of the prompt J/ψ yield is linear for the toward region, and slightly weaker than linear for the other regions. While the trend is independent of the J/ψ p_{T} for the transverse region, the increase becomes much stronger at high p_{T} for the toward and away regions. These studies show that the impact of the autocorrelations could be relevant to explain the stronger-than-linear trend measured by the experiments. In addition, because PYTHIA with the Monash tune underestimates the high-multiplicity J/ψ yield, the effects from autocorrelations could be larger in data.

Therefore, the measurement in pp collisions of J/ψ as a function of the multiplicity in regions of azimuthal angle could help disentangling the effect of autocorrelations from the global effects at play in the stronger-than-linear increase of the yields with multiplicity. The autocorrelation effects could in addition be different for prompt and non-prompt J/ψ. Thus, all subsequent chapters are dedicated to the measurement of the dependence of the prompt and non-prompt J/ψ yields with the multiplicity in azimuthal angle regions using data from the ALICE experiment.

3. ALICE experiment

This chapter describes A Large Ion Collider Experiment (ALICE), the experiment whose data have been used to obtain the results presented in this thesis. First, the Large Hadron Collider (LHC), at which ALICE is located, is described. Then, the detectors constituting ALICE are presented, along with a description on how they are used to reconstruct collisions and tracks, as well as to identify to which species the measured particles belong. Finally, the upgrades of the experiment made for the Run 3 of the LHC are presented, along with a work on the gain calibration of ALICE Transition Radiation Detector for Run 3 for which the author of this thesis contributed.

3.1. The LHC

The LHC is a 27-kilometer-circumference collider located in a tunnel deep underground within the European Organization for Nuclear Research (CERN), at the French-Swiss border. It can in particular collide protons together (pp collisions) at a center-of-mass energy ranging from $\sqrt{s} = 0.9$ TeV up to $\sqrt{s} = 13.6$ TeV, as well as lead ions (Pb–Pb) at a nucleon-nucleon center-of-mass energy from $\sqrt{s_{NN}} = 2.76$ TeV to $\sqrt{s_{NN}} = 5.36$ TeV and protons with lead ions (p–Pb) from $\sqrt{s_{NN}} = 5.02$ TeV to $\sqrt{s_{NN}} = 8.16$ TeV. Other collisions which took place at the LHC include Xe–Xe, pO, OO and Ne–Ne. Such high energies are reached with the help of a complex system of injectors, shown in Fig. 3.1. These include among others the Proton Synchrotron (PS) and the Super Proton Synchrotron (SPS), where each accelerator successively increase the energy up for the next requirement.

The schedule of the LHC include several years of running, separated by periods of Long Shutdowns (LS), where upgrades and repairs can be done in the experiments and the accelerator. The typical energies increase for each of these running periods. For example, during Run 1, the typical energies for pp collisions were $\sqrt{s} = 7$ TeV or $\sqrt{s} = 8$ TeV, while it was $\sqrt{s} = 13$ TeV during Run 2 and $\sqrt{s} = 13.6$ TeV during Run 3. In addition, there are also short periods of running were the center-of-mass energy for pp collisions is lower, equal to the value reached for the nucleon-nucleon center-of-mass energy in nuclei collisions. This is done in order to provide a reference for Pb–Pb collisions which occur only at these lower energy. Each year is typically further divided between 7 months for pp collisions, 1 month for ion collisions, and the rest for technical stop and commissioning. The data used for this thesis was collected at a center-of-mass energy of $\sqrt{s} = 13$ TeV during Run 2 of the LHC, which lasted from 2015 to 2018.

The protons or ions are grouped in the LHC into several bunches which circulate in the LHC either clockwise or anticlockwise. The number of bunches and protons per bunch depend on the
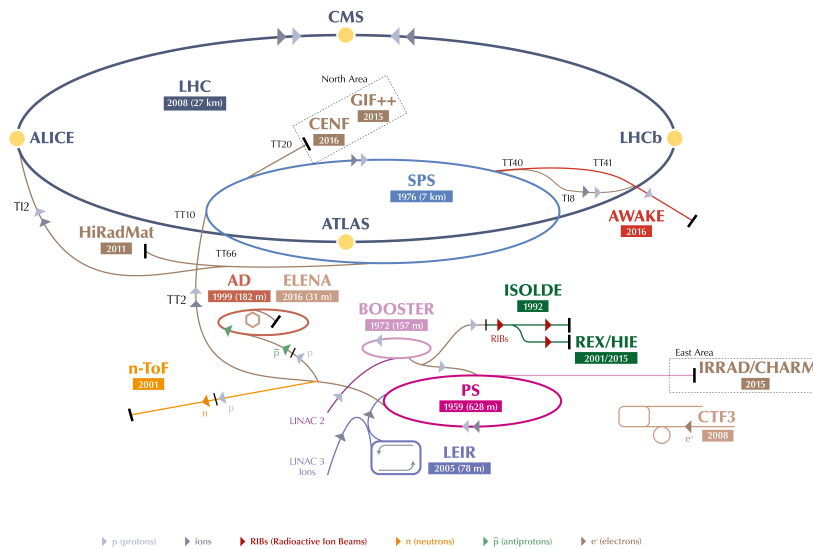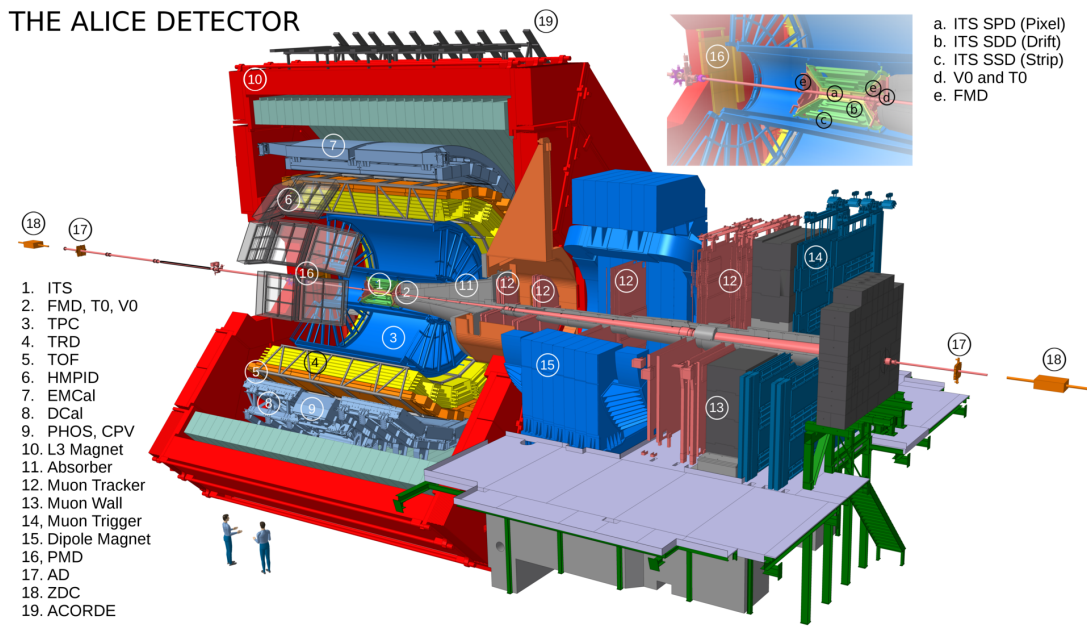
Figure 3.1.: Sketch of the accelerator complex at CERN. Taken from [162]

colliding system. For proton collisions, more than 2400 bunches circulate in the LHC, and each bunch is constituted of around 10^{11} protons. The bunches circulating clockwise and anticlockwise are allowed to cross in several collision points, and the intervals between one crossing of two bunches and the next one is a multiple of 25 ns. This interval of time is defined as one Bunch Crossing (BC). By modifying the separation between the two beams while they cross, it is possible to increase or decrease the average number of collisions happening at the collision point per BC, also called interaction rate. If several collisions happen in the same BC, one speaks of pile-up. By increasing the interaction rate, an experiment will collect more data, however the quality of this data might be worsened if the pile-up is too high. The computing power of the experiment also set a limit to the data flow an experiment is able to handle. Therefore, each experiment must find an optimal point of operation which provides a compromise between data quantity and quality.

Several experiments are hosted within the collider. The four main experiments are A Toroidal LHC ApparatuS (ATLAS) [163], Compact Muon Solenoid (CMS) [164], Large Hadron Collider beauty (LHCb) [165], and ALICE [166]. ATLAS and CMS are general-purpose experiment dedicated to the understanding of the properties of the Standard Model, in particular through the discovery of the Higgs boson [167, 168], and search of physics beyond the Standard Model. They operate at a very high interaction rate and pile-up level, ATLAS collecting an integrated luminosity of 140 fb^{-1} in pp collisions during Run 2 for example, with similar values for CMS. They mostly trigger on high-momentum rare signals, which allows them to decrease by a large factor the quantity of data recorded. LHCb is a forward rapidity experiment which, thanks to a good vertexing resolution allowing to detect and trigger on displaced vertices, can study the physics of beauty hadrons, in particular by searching for CP-violation in beauty hadron decays. ALICE is dedicated to the study of QCD and hadronization, with a strong focus on heavy-ion collisions, and will be described in detail in the following paragraphs.

3.2. ALICE detectors

THE ALICE DETECTOR

a. ITS SPD (Pixel)
b. ITS SDD (Drift)
c. ITS SSD (Strip)
d. V0 and T0
e. FMD

1. ITS
2. FMD, T0, V0
3. TPC
4. TRD
5. TOF
6. HMPID
7. EMCal
8. DCal
9. PHOS, CPV
10. L3 Magnet
11. Absorber
12. Muon Tracker
13. Muon Wall
14, Muon Trigger
15. Dipole Magnet
16, PMD
17. AD
18. ZDC
19. ACORDE

Figure 3.2.: Sketch of the ALICE Experiment during Run 2. See text for details on the different detectors.

ALICE is located in the cavern at point 2 of the LHC. A sketch of ALICE experiment during Run 2 operations, with all its detectors, is shown in Fig. 3.2. Charged particles can be tracked in the central barrel at midrapidity ($-0.9 < \eta < 0.9$), while muons can be detected in the muon spectrometer at forward rapidity ($2.5 < \eta < 4$). Multiplicity can also be measured with forward detectors in a large pseudo-rapidity range. Each detector has one or several special goals, ranging from triggering to tracking or Particle IDentification (PID), and their combined operation is necessary for the large range of physics results obtained by ALICE. ALICE operates at low pile-up levels, with an average number of collisions per BC in pp collisions never exceeding 0.06, and in most cases between 0.01 and 0.02. The requirement of the detectors have been chosen in order to allow good tracking and PID capabilities, especially in the very high density environment of Pb–Pb collisions where many particles are produced simultaneously.

A detailed description of all the detectors can be found in Ref. [166]. The most important properties of the detectors used for the analysis presented in this thesis are summarized in the following.

The V0 detector [169]: The V0 system is composed of two parts: the V0A and the V0C detectors. The V0A is located in the A side of ALICE (for particles going in the anticlockwise direction of the LHC, towards ATLAS), at 340 cm from the interaction region, and covers $2.8 < \eta < 5.1$. The V0C is located in the C side of ALICE (for particles going in the clockwise direction of the LHC, towards CMS), at 90 cm from the interaction region, and covers $-3.7 < \eta < -1.7$. Both detectors are separated in four rings covering different pseudorapidity regions, and each of these rings is divided in 8 channels covering 45° each. The channels measure the signal from incoming particles via scintillators connected to photomultiplier tubes.

The main advantage of the V0 is its quick response, delivering fast minimum-bias or multiplicity trigger, which allows to send a signal to the other detectors so that they start the readout of the event. It gives also a precise time resolution for the collision, around 1 ns per individual channel. When all channels are considered, the resolution even reaches 450 ps for the V0A and 350 ps for the V0C. The V0 is also able to reject the background interactions, for example between one of the beams and some background gas inside the beam pipe, distinguishable from beam-beam interaction by the discrepancy between the arrival time of the signal in either the V0A or V0C and the time expected from the bunch crossing time and propagation time from the interaction point (11 ns for V0A, 3 ns for V0C). The V0 detector additionally provides measurement of the luminosity, which is directly connected to the interaction rate and the inelastic cross-section for the considered collision system. Finally, the V0 can give information on the total amplitude of its measured signal, correlated with the energy deposited by all the charged particles reaching the detector. The signal in each channel is tuned so that a minimum ionizing particle gives an amplitude of 1. However, the measured signal can vary with the aging of the detector. The total amplitude can be used for triggering or for determination of the multiplicity or centrality of the event.

The Inner Tracking System (ITS): The ITS is the innermost detector of ALICE. It participates in tracking and in the precise reconstruction of the point where the collision happened (the collision vertex) and of the impact parameter of the tracks (i.e. the smallest distance between the prolongation of the track and the collision point). The ITS tracks particles with $p_\mathrm{T} > 0.1$ GeV/c, and $|\eta| < 0.9$. It is composed of six cylindrical layers of silicon detectors, sketched in Fig 3.3:

- 2 layers of Silicon Pixel Detectors (SPD, located at 3.9 and 7.6 cm from the interaction vertex). Being very close to the interaction point, they encounter very high charged-particle density, and thus need high granularity to diminish the radiation load on single pixels. The high granularity also enables a good impact parameter resolution requirement in the transverse plane. Both layers are constituted of a 2-dimensional matrix of binary-readout pixels, measuring each 50 μm (in the plane transverse to the beam direction) $\times$ 425 μm (in the longitudinal direction z). The pixels are also able to transmit a fast signal to the trigger system, with a frequency of 10 MHz. The first and second layers cover the pseudorapidity range of $|\eta| < 2$ and $|\eta| < 1.4$, respectively.

- 2 layers of Silicon Drift Detectors (SDD, located 15 and 23.9 cm away from the interaction vertex). Each detection element has a sensitive area of $\sim 70 \times 75$ mm^2, where the charges created by particle energy deposition in the detector drift in the tranverse direction, towards the collection anodes. Due to the sampling frequency of ~ 40 MHz, the position resolution in the detector can reach 35 μm in the transverse direction and 25 μm in the z direction.

- 2 layers of Silicon Strip Detectors (SSD, located 38 and 43 cm away from the interaction vertex). It needs a good two-dimensional spatial resolution in order to allow the matching

with the Time Projection Chamber. A distance from strip to strip (pitch) of 95 μm allows to obtain a spatial resolution of 20 μm in the transverse direction.

In order to reduce multiple scattering, which could alter the impact parameter resolution, all layers have been built with low material budget ($\sim$1.1% of radiation length X_0 per layer). In addition, due to their analogue readout, the SDD and SSD provide particle identification via energy loss at low momentum.
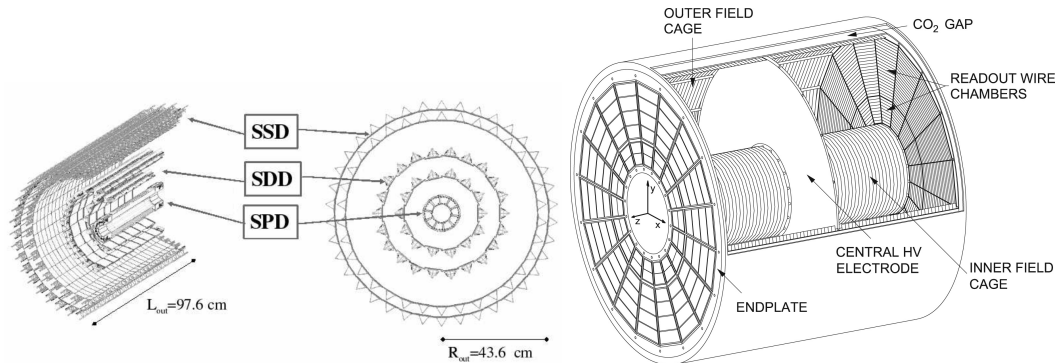
Figure 3.3.: Left: Sketch of the ALICE ITS. Taken from [166]. Right: Sketch of the ALICE TPC. Taken from [170].

The Time Projection Chamber (TPC): The TPC is the main tracking device of ALICE. It is a cylindrical volume of gas (a mixture of Ar–CO_2 or Ne–CO_2–N_2, depending of the data taking periods), covering a radial range between 0.85 and 2.5 m around the ITS detector, with a length in the beam direction of 5 m. It is separated in two drift regions by a central electrode at $z = 0$, where ionization happens when charged particles pass through the gas volume. The electrons then drift along the longitudinal direction towards the end-caps on both sides of the TPC, while the ions drift in the other direction. Multi-Wire Proportional Chambers (MWPC) collect the charges deposited by the particles in 159 possible clusters with increasing radius. The information on the position of these clusters allows to reconstruct the track position in the transverse plane, while the arrival time of the charges in the readout chambers can be used to reconstruct the z position. A magnetic field of 0.5 T (0.2 T in few data taking periods) along the longitudinal direction bends the tracks in azimuthal angle, allowing computation of their momentum. Particles can be tracked until $p_{\mathrm{T}} > 0.1$ GeV/c and $|\eta| < 0.9$. A sketch of the TPC is shown in Fig. 3.3.

The TPC is particularly efficient for tracking when confronted with the high density of particles present in Pb–Pb collisions, and the number and size of the readout chambers were chosen in order to allow a maximum occupancy of 40% per readout chamber and per collision in the most central Pb–Pb collisions. The drift velocity for electrons of $\sim$ 2.7 cm/μs causes the drift time to reach up to $\sim$ 90 μs, with a time resolution for the tracks which is on the order of few μs. Because the interaction rate could reach up to 250 kHz in pp collisions during Run 2, several collisions can accumulate in the volume during one drift length. In this case, the matching to ITS tracks allows to reject tracks from pile-up events. In addition, due to the much slower drift of ions created in the ionization, and to the backflow of ions inside the gas volume when the electrons enter the MWPC, all the charges present inside the gas volume create a huge electromagnetic

field, which can deviate the trajectory of the drifting electrons. This effect is called space-charge distortion, and it should be avoided at maximum in order to keep the good tracking resolution. In order to reduce the ion backflow, gating grids between the readout chambers and the gas volume are closed after one full drift time following the collision, for up to ~ 180 μs [171]. During this time, it is not possible to record other events, constraining the recording rate of minimum-bias collisions. After mitigation, the remaining distortions, on the order of few mm, are calibrated and corrected during tracking.

The TPC also allows to identify particles by using their mean energy loss per unit length $\langle \mathrm{d}E/\mathrm{d}x \rangle$. The particle identification will be described in detail in Sec. 3.4.

The Transition Radiation Detector (TRD): The principle of the TRD relies upon the transition radiation emitted by ultra-relativistic particles when they cross the boundary between materials with different dielectric constants. The radiation is emitted by particles with $\gamma \geq 1000$, which means that, in the momentum range covered by ALICE, only electrons are able to emit this radiation. The TRD contains 522 chambers, which are distributed in 18 supermodules covering the full azimuthal angle. Each supermodule is further divided into 5 stacks in the longitudinal direction (some stacks are not installed in order to reduce the material budget in front of the PHOS detector), with a pseudorapidity coverage of $|\eta| < 0.84$. Each stack contains six chambers in the radial direction.
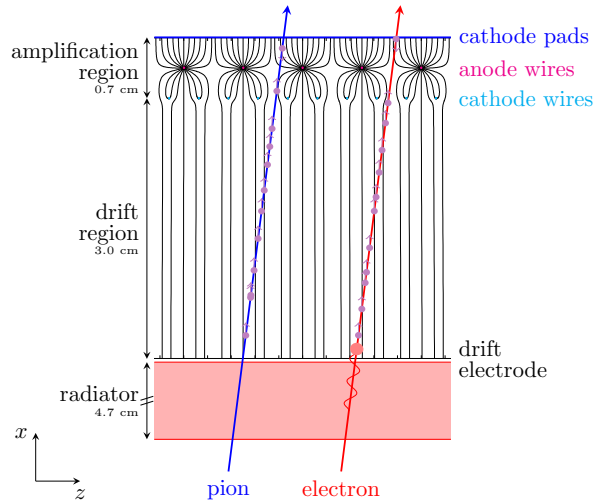
Figure 3.4.: Sketch of a particle crossing one chamber of the TRD. Taken from [172].

An example TRD chamber is sketched in Fig. 3.4. When a particle cross a TRD chamber, it first encounters a 4.8-cm-long radiator, which induces the transition radiation, before traversing a 3-cm-long drift region composed of a Xe–CO$_2$ mixture, where the particle passing through will ionize the gas, creating electron-ion pairs. The created electrons drift towards the MWPC from this chamber, allowing to reconstruct a tracklet. The tracklets from different layers can be combined together and matched to TPC tracks, improving the momentum resolution at high p_{T} by giving additional lever arm to the tracking. In addition, the TRD also provide triggers for electrons, nuclei and jets.

Other detectors present during Run 1 and 2 [173]:

- The **Time-Of-Flight detector (TOF)**: It provides particle identification in the central barrel at intermediate momentum. This is done via measurement of particles time-of-flight with very high precision (~ 80 ps) inside Multigap Resistive Plate Chambers.

- The **ElectroMagnetic CALorimeter (EMCAL)**: It allows to measured jets as well as high-momentum electrons and photons in the central barrel with limited azimuthal acceptance (distributed between EMCAL with 127° coverage and DCAL with 67° coverage in the opposite side). It is composed of 12 288 towers of alternating layers of lead and scintillators, with the ability to provide triggers for high-energy deposition from jets, photons or electrons inside the towers [174].

- The **Photon Spectrometer (PHOS)**: It is an electromagnetic calorimeter, specifically dedicated to photons and neutral meson measurements. Composed of lead-tungstate scintillator, it has higher granularity than the EMCAL, but covers a more limited acceptance ($|\eta| < 0.125$ and 70° in azimuth). It is preceded by a gas detector with MWPC for charged-particle veto [175].

- The **High-Momentum Particle IDentification detector (HMPID)**: It identifies high-momentum hadrons by means of a ring-imaging Cherenkov detector, providing π/K separation up to 3 GeV/c, and K/p separation up to 5 GeV/c. It has acceptance of $|\eta| < 0.6$ and $\Delta\varphi = 57.6°$.

- The **ALICE COsmic Ray DEtector (ACORDE)**: It is a scintillator-based detector whose goal is to provide a fast trigger for the detection of muons from cosmic-rays, when no beam are colliding in ALICE. These events, beyond their own physics interest, are especially important for the calibrations and alignment of all detectors.

- The **Muon spectrometer**: Its goal is to detect muons at forward rapidity ($-4 < \eta < -2.5$). First, an absorber of 10 interaction lengths reduces the contamination from hadrons. Then, the muons pass through five tracking stations, while a dipole magnet of 3 Tm allows for measurement of the muon momenta. Each tracking station is composed of two chamber planes of MWPC, providing a position resolution of $\sim 70\ \mu$m. Finally, a trigger system, composed by 4 planes of Resistive Plate Chambers, and protected by another front absorber of 7.2 interaction lengths in order to reduce the low-momentum flux, selects events with at least one or two muons passing a given p_{T} threshold requirement.

- The **T0 detector**: It is a Cherenkov detector divided into T0A ($4.61 < \eta < 4.92$) and T0C ($-3.28 < \eta < -2.97$). It provides a precise measurement of event time, which is used by the TOF detector to calculate PID from particle time-of-flight. This resolution depends on the event multiplicity and ranges from 50 ps in low-multiplicity pp collisions to 25 ps in Pb–Pb collisions [176].

- The **Forward Multiplicity Detector (FMD)**: It is composed of 5 rings (3 in the A side, 2 in the C side) of silicon strip detectors, which provide a measurement of charged-particle multiplicity with a large pseudorapidity coverage ($-3.4 < \eta < -1.7$ and $1.7 < \eta < 5$).

- The **Photon Multiplicity Detector (PMD)**: It is able to determine the multiplicity and spatial distribution of photons at forward rapidity ($2.3 < \eta < 3.7$). Each detection module is composed, following a gas detector used for charged-particle veto, of an absorber of 3 radiation lengths which generates a particle shower, before another gas detector measures this shower.

- The **Zero-Degree Calorimeter (ZDC)**: It is a set of several calorimeters located at 116 m from the interaction points on both sides, with the goal of measuring the number of spectator nucleons during Pb–Pb collisions. The ZN and ZP detectors measure respectively spectator neutrons and protons, which take a different path due to their different charge. The measurement is made by means of the generation in an absorber of a particle shower which is measured by Cherenkov radiations inside quartz fibres. In addition, also electromagnetic calorimeters (ZEM) are located at 7 m from the interaction point.

The combined use of the information from all these detectors allow an excellent tracking, especially at low momentum, as well as good particle identification. It can also operate in high charged-particle densities such as the ones present in heavy-ion collisions. This makes it an excellent detector for studying the QGP produced in heavy-ion collisions.

3.3. Event and track reconstruction

3.3.1. Data acquisition and triggers

In Run 1 and 2, ALICE could not record all the collisions, mostly due to the large busy time of the TPC when the gating grids are closed. Thus, it had to rely on triggers to select some events with interesting but rare properties. These triggers could be based on specifically chosen signals, such as the triggers on high-energy deposition on the calorimeters, or on some event topologies, such as a high track density in a detector. The fastest detectors are able to make a quick decision, and directly send this decision to the Central Trigger Processor (CTP). There are three different trigger levels, depending on how fast after the collision they are transmitted: Level 0 (L0) after 1.2 μs (sent by the very fast detectors, such as V0 or SPD), L1 after 6.5 μs (sent by slower detectors, such as TRD or EMCAL), and L2 after 100 μs (the drift time of the TPC, might be used to reject some events, for example with pile-up). After a L0 trigger, the CTP sends a first information to the readout of the detectors in order to start recording the event. After L1, a new decision is issued and sent to all detectors. When the detector readout is finished, the detector data are sent to the data acquisition system, where a high-level trigger will start the reconstruction and compress the data in order to keep up with the data rate requirement.

The triggers used in this analysis are the following:

- **Minimum-Bias trigger**: The Minimum-Bias (MB) trigger requires the coincidence of a signal in the V0A and V0C detectors, compatible with the crossing of two proton bunches in the interaction region. The goal is to provide a fast trigger at L0 as close as possible to an average inelastic collision, which should still be able to remove background interactions.

- **High-Multiplicity trigger**: The High-Multiplicity (HM) V0 trigger requires the V0M signal (i.e. the sum of the V0A and V0C signal in all channels) to be higher than a threshold value. This threshold value depends on the detector conditions and corresponds approximately to the 0.1% events with the highest V0M signals.

- **TRD electron trigger**: The TRD, even though being a slow detector due to the few μs drift time inside the gas chamber, is able to provide a L1 trigger for high-momentum electrons. Tracklets matched together in at least five layers (out of six possible) are combined to give an online fast estimation of the track p_T. For each chamber, the values of the charge deposited by the particle in several time windows is converted, using a look-up table, to an electron likelihood. The electron likelihood of the track is further combined in all chambers, to obtain a PID value. The event is triggered if the online p_T is higher than 2 GeV/c, and the PID value is higher than a given threshold.

3.3.2. Vertex reconstruction

The reconstruction of the primary collision vertex is essential for assigning tracks to events. Indeed, once the vertex is reconstructed, particles pointing far from the vertex can be rejected, as the probability is high that they come from another collision. In addition, if the spatial resolution of the vertex is good, secondary vertices, located at the decay point of open charm and beauty hadrons which can be displaced of several hundreds of μm from the primary vertex, can be reconstructed.

The reconstruction of the vertex happens in two steps. The first one uses only information from the SPD. Due to the parameters of the crossing point of the two beams, which are transversely collimated in an area of around hundred μm in x and y coordinate (the diamond), while having a higher longitudinal extension in z coordinate of $\sim$ 5 cm, the vertex position in the xy plane can already be well constrained. Pairs of hit points in the two SPD layers with similar azimuthal angle (the curvature of the tracks is neglected in the vertexing) are combined to form tracklets. The three-dimensional position of the vertex is obtained by finding the point which minimizes the quadratic sum on all the tracklets of the minimal distance between this point and the tracklet, weighted by the inverse of the uncertainty. This vertexing algorithm is applied twice, and between each step, tracklets pointing too far from the previously obtained vertex are rejected, with selections becoming progressively tighter [177].

The procedure for the final vertexing algorithm is done on a very similar way, but using all reconstructed tracks (the description of the tracking algorithm is given in Sec. 3.3.3) rather than SPD tracklets. Also in this case, the final vertex minimizes the distance to all tracks, with several reconstruction steps implemented where tighter and tighter selections on the tracks are applied. Studies [177] show that the reconstruction efficiency, as well as the position resolution of the vertex, is highly dependent in the number of tracks contributing to the vertex computation.

3.3.3. Track reconstruction

A good tracking performance is necessary to reconstruct all the charged particles and their momenta with great precision. ALICE tracking detectors provide a good tracking resolution for charged particles with $p_T > 0.15$ GeV/c, even in the very challenging environment of Pb–Pb collisions with high charged-particle density.

A charged particle in a constant magnetic field (in the ALICE case, this magnetic field is directed towards the longitudinal direction z) follows an helix trajectory. Indeed, in a transverse plane, the track rotates in a circle around the magnetic field, with a radius which is proportional to the momentum in the direction transverse to the magnetic field. In ALICE, the tracks are parametrized with five helix parameters: $(y, z, \sin\varphi, \tan\lambda, q/p_T)$. φ is the azimuthal angle, λ is the angle between the track momentum and the transverse plane, q is the charge, and y and z are two spatial coordinates. In this case, this parametrization is valid for a detection plane x. The parametrization can be extracted at any other point of the helix, by updating the values of y, z, and φ. The propagation from one point to another also needs to take into account the energy loss by the particle when interacting with the detectors, which modifies the trajectory and depends on the mass and momentum of the particle. The propagation also accounts for multiple scattering, which randomly modifies the direction of the momentum of the particle when interacting with matter.

The subsequent tracking makes use of the Kalman filter algorithm. The goal of this method is to estimate, from several measurement point, the optimal parameters which are the most likely to represent these measurement points, given the uncertainties. It works in an iterative way, by adding the measurement points one by one, and provides each time a measurement point is added a more refined estimation of the track parameters. In addition, also the uncertainties of these parameters, as well as the correlations between these uncertainties, are provided as a covariance matrix. At each step, starting from the current estimation of the track parameters, it is possible to estimate what should be the track parameters when propagating to the next measurement point. However, some random noise (e.g. due to the position resolution of the detectors, or to multiple scattering) can affect any measurement, which means that the expected parameters and the measured ones would differ. Then, the difference between the expected parameters and the measurement, multiplied by a Kalman gain matrix, is used to correct the track parameters. This Kalman gain comprise information about the track covariance matrix and the random noise, and is the optimal way of updating the track parameters, provided that the uncertainties are well estimated [178, 179].

The tracking starts at the outer edge of the TPC. TPC clusters are propagated from their measurement point in the readout chambers to the position where the ionization happened. Distortion maps correct this position when space-charge effects influence significantly the drift of the electrons. For each cluster at large radius, a search window is created at a lower pad row for which the curvature should be compatible with a primary track given a certain momentum threshold. The large radius cluster is paired with all the compatible clusters in the search window, and the combination of each one of these pairs with the preliminary determined primary vertex
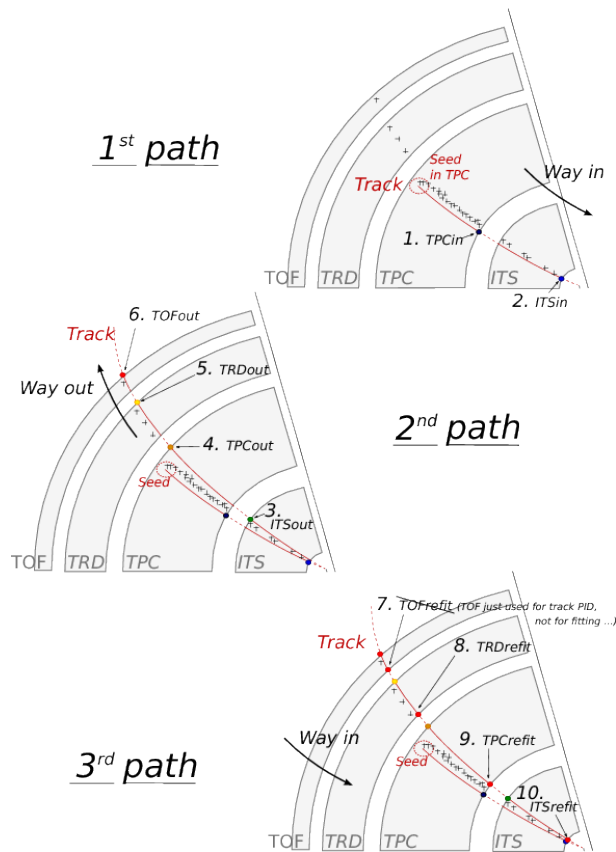
Figure 3.5.: Illustration of the tracking in ALICE. Taken from [180]

is called a seed. Each seed, from which preliminary track parameters can be extracted, is the starting point for one track hypothesis [173, 181].
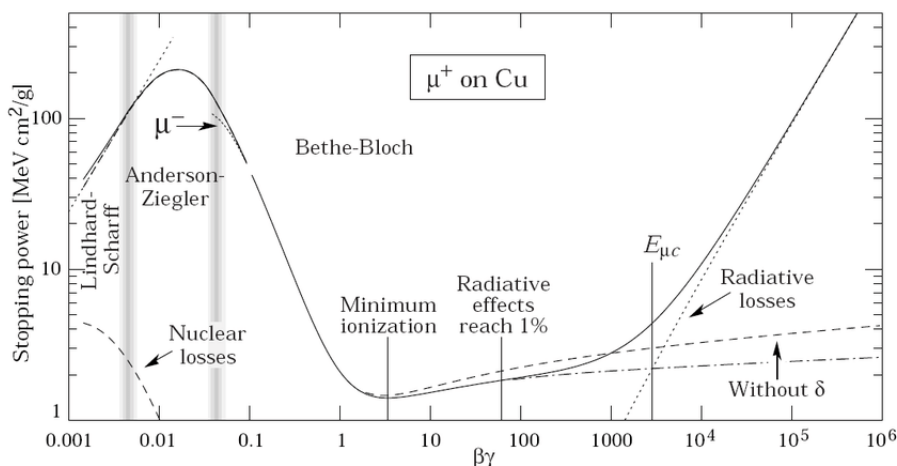
For each seed, the tracking starts in the outward part of the TPC, and goes inward. For each pad row, the nearest cluster to the current track is added to the Kalman filter algorithm for update of the track parameters. Clusters can be used by several seeds, thus duplicated tracks using a large fraction of common clusters are removed. The TPC track then serves as a seed for the matching to ITS. Each one of these seeds is propagated to the six ITS layers, adding clusters one by one for the Kalman filter. The main difference with the TPC tracking is that, rather than selecting only the nearest cluster, all clusters in a given search window are selected. Then, each seed is associated to several track hypothesis, and, once the inner ITS layer is reached, only the best track is selected. After this first step, a new fit of the track is done, starting from the inner layer of the ITS towards the outer layer of the TPC. If possible, the track is also matched to tracklets in the TRD. The matching to the TRD allows a stronger lever arm which improves the momentum resolution especially at high p_{T}. The track is also matched to clusters in the TOF and in the calorimeters, which will be used for identification of the particle species. Finally, a last inward refit of the track is done, in order to refine again the estimation of the track parameters. The tracking procedure is illustrated in Fig. 3.5.

3.4. Particle IDentification

The achievement of the physics goals of ALICE necessitates the identification of a large range of particles, from electrons or muons to protons, kaons, pions, and even light nuclei, in a large momentum range. The identification usually relies on different properties of the particle, often dependent on its velocity which can be directly related to its mass at a given momentum, or even dependent on its charge in the case of light nuclei. Several detectors operating with diverse technologies provide different separation capabilities between particle species in various momentum ranges.

One typical example of particle identification method relies on the measurement of the energy loss per unit of length of a high-energy particle in a material. This energy loss typically happens through multiple collisions with the electrons bounds in the atoms. It can typically be expressed with the Bethe-Bloch formula [1]:

$$\left\langle -\frac{\mathrm{d}E}{\mathrm{d}x} \right\rangle = K z^2 \frac{Z}{A} \frac{1}{\beta^2} \left[\frac{1}{2} \ln \left(\frac{2 m_e c^2 \beta^2 \gamma^2 W_{max}}{I^2} \right) - \beta^2 - \frac{\delta(\beta\gamma)}{2} \right]. \tag{3.1}$$

Figure 3.6.: Energy loss per unit of length for a muon in Cu, as a function of $\beta\gamma$. Taken from [1].

This formula depends on properties of the material (I, Z/A), on the charge z of the particle, and on its velocity $\beta = v/c$ (with $\gamma = 1/\sqrt{1 - \beta^2}$. An example of the values of $\langle \mathrm{d}E/\mathrm{d}x \rangle$ as a function of $\beta\gamma$ for muons in Cu is shown in Fig. 3.6. The curve shows a minimum, around $\beta\gamma \approx 3$ in this case, which corresponds to a Minimum Ionizing Particle (MIP).

The Bethe-Bloch formula provides the value of the mean energy loss. However, this energy loss can fluctuate and a particle can deposit more or less charge in the detector than the average. At a given velocity, the distribution of energy loss values typically follows a Landau distribution. This distribution first rises quickly towards its most probable value, then decreases, with a large tail which represents few events with very large energy loss. In addition, the errors on the measurement of the deposited charge, typically Gaussian, should also be taken into account.

In the ALICE TPC, the material that the particles traverse is the gas volume. Since the energy deposited by the particle when passing through the material can be measured, its velocity can be retrieved from the Bethe-Bloch formula. The total energy loss of the particle in the

TPC is directly proportional to the charge measured in the clusters assigned to the track. However, only a part of the clusters are used for the calculation of dE/dx. Indeed, the ones with higher energy loss, corresponding to the tail of the Landau distribution, are rejected. Afterwards, the distribution of specific energy loss for a given particle at given momentum becomes approximately Gaussian.
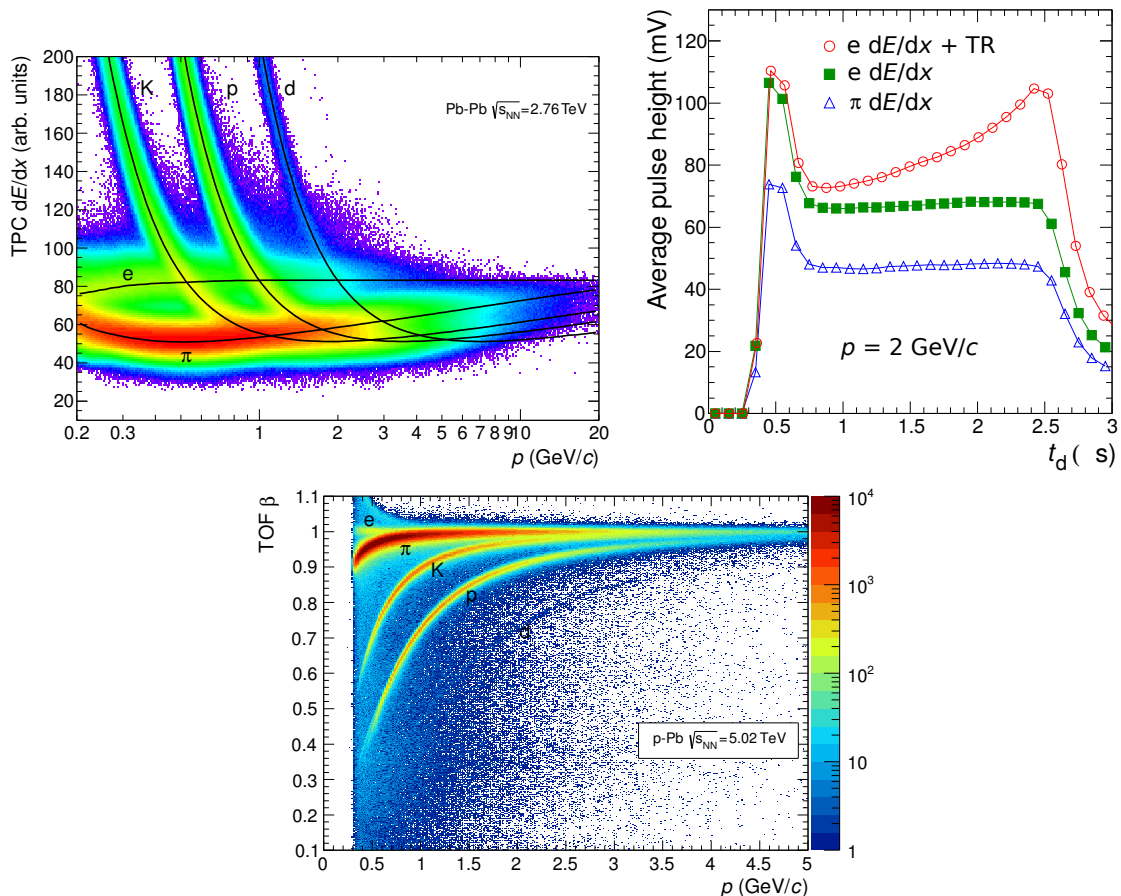
Figure 3.7.: Top left: particle identification via dE/dx in the TPC. Figure taken from [173]. Top right: Illustration of the principle for identification of electrons in the TRD. Figure taken from [172]. Bottom: particle identification from TOF β. Figure taken from [173].

The distribution of energy loss in the TPC for all the measured tracks as a function of momentum is shown in Fig. 3.7. The curves corresponding to the mean expected energy loss for different particle species are also shown. The distributions of energy loss corresponding to these different species can be distinguished, except in few regions where the curves of average expected energy loss for different species cross. These mean energy loss curves for several species are calibrated with a Gaussian fit to the distribution of energy loss in many momentum intervals. In order to do the Gaussian fit, a clean sample of the considered particle species is needed. The clean samples are constituted of the daughters of particles with some specific V0 decay topologies. These decay topologies are recognizable from their decay vertex few centimeters from the primary vertex ($\Lambda \to p\pi^-$, $K_S^0 \to \pi^+\pi^-$, conversions in the material $\gamma \to e^+e^-$). Additional selections are made with the TOF detector. The Gaussian fit also provides the standard deviation of the energy loss. The mean energy loss is then fitted as a function of momentum, using the so-called ALEPH parametrization [182]:

$$\frac{a_1}{\beta^{a_4}} \left[a_2 - \ln\left(a_3 + \frac{1}{(\beta\gamma)^{a_5}} \right) - \beta^{a_4} \right] . \tag{3.2}$$

The dependence on other parameters, such as η and number of clusters of the tracks in TPC, is also taken into account. The calibration allows to extract, for every track, the number of standard deviations of $\mathrm{d}E/\mathrm{d}x$ with respect to the expected mean of each particle i (where i can stand for electrons, pions, protons...):

$$n\sigma_i = \frac{\mathrm{d}E/\mathrm{d}x_{meas} - \langle \mathrm{d}E/\mathrm{d}x \rangle_{exp,i}}{\sigma_i} . \tag{3.3}$$

A similar method is used for identification in the ITS SDD and SSD, while, in this case, the particle species can only be separated at lower momentum ($p < 1 \ \mathrm{GeV}/c$).

The TRD is able to measure the time dependence of the energy loss of the particle in each chamber. Similarly to what happens in the TPC, the amplitude of the energy loss in the drift chamber can be used for particle identification. In addition, electrons with $\gamma \geq 1000$ in the radiator emit a transition radiation, made of low-energy photons. These photons travel until reaching the inner edge of the drift region. There, they provoke ionization of the gas atoms, and the ionization electrons drift towards the MWPC. The long travel time from the inner part of the chamber to the MWPC makes the transition radiation appearing as a late peak, located at the end of the time distribution of the charge collection. The peak can then be used to identify electrons, by estimation of an electron likelihood for the tracklet. This information can be combined between the several tracklets belonging to the same track for each of the six layers of the TRD. The principle of the TRD is illustrated in the right panel of Fig. 3.7.

Particle identification in the TOF is done through estimation of the arrival time of the particle in the TOF. The velocity β of the particle can then be obtained, if the arrival time is compared to the collision time, generally measured by the T0 detector. Adding information on the momentum allows identification of the particle species. The bottom panel of Fig. 3.7 shows the TOF measured β, for many particles at several momentum values, along with the mean expected curves for different species. It provides good separation between pions and electrons at low momentum values, as well as separation to protons and kaons for intermediate momenta.

Other detectors are able to provide separation power between hadrons, electrons or photons in different momentum ranges. This is for example the case for the HMPID, which uses a ring imaging Cherenkov detector for identification of high-momentum hadrons. Calorimeters, such as the EMCAL are also able to identify high-momentum electrons, which becomes particularly useful in the region where the electron identification in the TPC becomes harder due to the crossing with the Bethe-Bloch curve for pions. For particle identification, the EMCAL uses the ratio between the total deposited energy and the track momentum. This quantity is close to 1 for electrons, but is lower for hadrons, since hadrons do not deposit all of their energy in the calorimeter.

3.5. ALICE in Run 3

3.5.1. ALICE upgrades during LS2

In Run 2, ALICE could only record minimum-bias collisions at a low interaction rate (3.5 kHz maximum in pp collisions, and only up to 500 Hz in Pb–Pb collisions [183]). The collected data sample in pp collisions corresponds to only ~ 30 nb^{-1} of minimum-bias events and several pb^{-1} for central barrel rare triggers, while, in minimum-bias Pb–Pb collisions, it corresponds to only ~ 40 μb^{-1}. This amount was mainly limited by the TPC, for which the gating grids must remain closed between two events in order to limit the space-charge distortions, as well as due to limitations in the readout electronics in Pb–Pb collisions.

In order to collect a larger statistical sample and sustain higher interaction rates in Run 3 (500 kHz for pp collisions, 50 kHz for Pb–Pb collisions), a full upgrade of the main ALICE detectors was necessary. This upgrade enables the possibility of a continuous readout. This means that ALICE collects, and sends for data reconstruction, all information and signals, recorded without any interruption or dead time. For the TPC, the higher interaction rate, and the impossibility to close the gating grid in order to suppress the ion backflow, means that the space-charge distortion would increase significantly. This problem is mitigated with, on the one hand, an upgrade in the readout from MWPC to Gas Electron Multipliers (GEM) [184], which are able to reduce the ion backflow to a maximum of 2%, and, on the other hand, with a better calibration of these space-charge distortions.

The second main upgrade is the one for the ITS. The 6 layers of SPD, SDD and SSD, were replaced by 7 layers of Monolithic Active Pixel Sensors. The first three layers constitute the new inner barrel. The smaller pixel size, the position of the first layer of the new inner barrel which was brought closer to the interaction point (22.4 mm in Run 3 compared to 39 mm in Run 2), as well as a reduced material budget in the inner barrel, improve the impact parameter resolution by a factor 2 in the transverse direction and 5 in the longitudinal direction.

A new system for triggering was installed in order to replace the T0 and V0 detectors: the Fast Interaction Trigger (FIT), composed of FT0, FV0 and FDD subdetectors, which cover various pseudorapidity regions at forward rapidity. The FIT can participate in the estimation of multiplicity and centrality, and provides triggers for the detectors which did not benefit from an upgraded readout, or that are not able to sustain the higher interaction rate in Run 3 (TRD, EMCAL, PHOS, HMPID).

In addition, a Muon Forward Tracker (MFT), employing the same technologies as the new ITS, was installed at forward rapidity before the absorber. Its goal is to track the muons detected in the muon spectrometer closer to the interaction vertex, and reconstruct the secondary vertices at forward rapidity.

With the continuous readout, because the data rate has increased, reconstruction and data storage also needed an upgrade. All detector signals are transmitted, at fixed time intervals which depend on the detectors, to First Level Processors (FLP). A specific FLP combine all the data collected by a specific detector during a Time Frame (TF) which lasts around several ms. Then, the data are sent to the Event Processing Nodes (EPN) which combine the data sent by

the FLP from all the detectors for one TF, reconstruct all the events which occurred during this TF, and save a compressed version of the data. Due to the large size of the data collected in pp collisions, a software-based trigger, applied after a few weeks of reconstruction and calibrations, allows to keep only interesting events while deleting the rest of the pp data.

3.5.2. Calibration of the gain of the TRD

This section presents the work on the calibration of the gain of the TRD which was conducted by the author of this thesis. The TRD was first presented in Sec. 3.2, while the method for particle identification was described in Sec. 3.4. Because the TRD is a gaseous detector, the response of the system to the passage of a particle depends on the gas properties. Depending on the TRD chamber or on the moment at which the data taking happens, an identical particle can produce a higher or a lower charge deposition in the detector. A calibration becomes necessary when identifying the particle through energy loss in order to correct for this effect.

The gain in gas detectors is usually defined as the ratio between the charge measured in the MWPC and the one deposited by the particle. It depends on the full history of the electron drift. The electrons from primary ionization, created by the passage of the high-energy charged particle, follow a direction which has a given angle with respect to the electric field lines, due to the deflection by the 0.5 T magnetic field. These electrons induce secondary ionizations inside the gas, quickly producing an avalanche of electrons. The drift velocity depends on the electric field inside the TRD chamber (with values typically around 700 V/cm). A stronger electric field would increase the velocity of these electrons, inducing a larger collected signal [172].

During the drift, the electrons lose energy by collision with the gas atoms. It means that a higher gas pressure would reduce the size of the avalanche created, inducing a lower charge deposition, thus a lower gain would be measured. The gain could also be affected by the gas composition, of around 85% of Xenon and 15% of CO_2, but which can vary with time, for example due to contamination by N_2. The choice of the Xenon was made due to its good properties for absorption of the low-energy X-rays photons produced as transition radiation. The CO_2 acts as a quencher gas which reduces the probability of secondary avalanches, keeping the avalanche localized. The pressure inside the chambers is always a fraction of a millibar higher than the atmospheric pressure [172].

During data taking, for each tracklet, the information on the deposited charge by the particle is collected in three time windows, which can also be noticed in Fig. 3.7: a strong increase when the particle is traversing the amplification region, a plateau corresponding to the electrons coming from ionization when the particle pass through the drift region, and the transition radiation region, which produces another increase in the charge deposition only if the particle is an electron. Due to constraints in the size of the transmitted data, the number of bits available to encode the information on the charge for each time window is limited. 7 bits of information are used for encoding the charge in the amplification and in the transition radiation region (leading to an integer value between 0 and 127 in both cases) while 6 bits of information are used for the drift region (leading to an integer value between 0 and 63).

When calibrating the gain, only the time-dependent relative variation in each TRD chamber, and not the absolute gain values, will be analyzed. The calibration is done in a data-driven way. When a track is matched between the TPC and at least five TRD tracklets, the dE/dx values for all these TRD tracklets are collected. The matching to TPC ensures a good tracklet quality. A selection on the momentum ($0.5 < p < 1$ GeV/c) and dE/dx in the TPC is also done in order to mainly select MIP pions. The value of dE/dx in the TRD is estimated by summing the charge values in the three time windows, divided by the length traversed in the TRD chamber, which is estimated from track azimuthal and polar angle. In addition, all the charge values are corrected for the spatial dependence on the gain inside the chamber. The spatial dependence was estimated in a specific calibration run without collisions, by using a Krypton source to produce radiations, and measuring them in every detector pad, which provides a much finer granularity than just the chamber. The calibration is done every 15 min, using all dE/dx values collected during this period. If the collected statistics are not enough, this period of time can be extended.

The distribution of the measured dE/dx values, for one TRD chamber and during one run of Pb–Pb collisions, is shown in Fig. 3.8. The data is fitted with a function which is the convolution of, on the one hand, a Landau distribution multiplied by an exponential function, and, on the other hand, a Gaussian function. This convolution reproduces better the distribution than a simple Landau distribution, which is also shown on the same figure. The choice of this fitting function is motivated by the fact that the Landau distribution could represent the energy deposition by the charged particle, while the exponential function would account for the signal loss happening between the point where the particle deposited its energy and the measurement point. Indeed, if every drift electron has a fixed survival probability, a larger absolute loss would happen when the charges or the avalanche are larger. The convolution with the Gaussian would be necessary to take into account the uncertainty in the measurement [185].
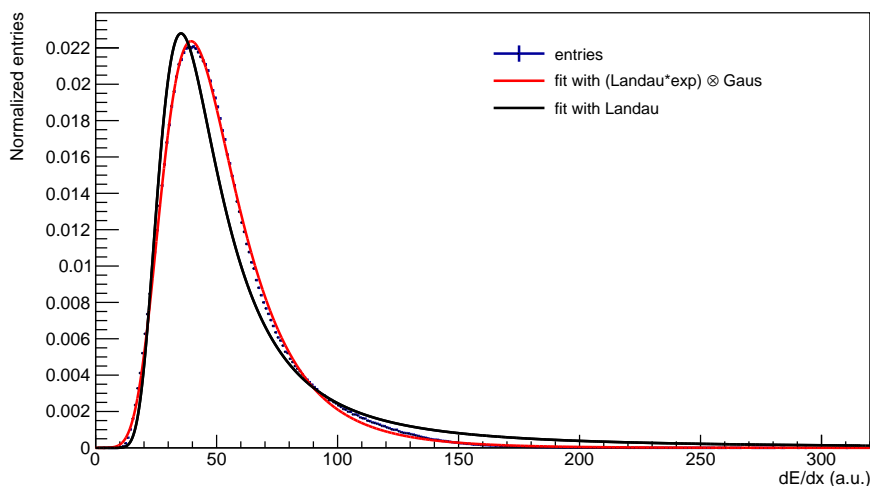
Figure 3.8.: Distribution of energy loss per unit length, in one TRD chamber and during one run, for selected tracklets. The data is fitted with a Landau function (in black), as well as the convolution between a Gaussian function and the product of a Landau and an exponential (in red).

The fit allows to extract the Maximal Probable Value (MPV) of the distribution with better precision. Although the fit is not perfect, especially in the elbow region around 110, the position

of the MPV seems well reproduced with the fit, and the relative variations of the MPV are less affected by the fit quality than absolute values. It is assumed that the MPV of the distribution, which is the monitored quantity during data taking and which will be corrected for during PID calibration, is proportional to the gain.
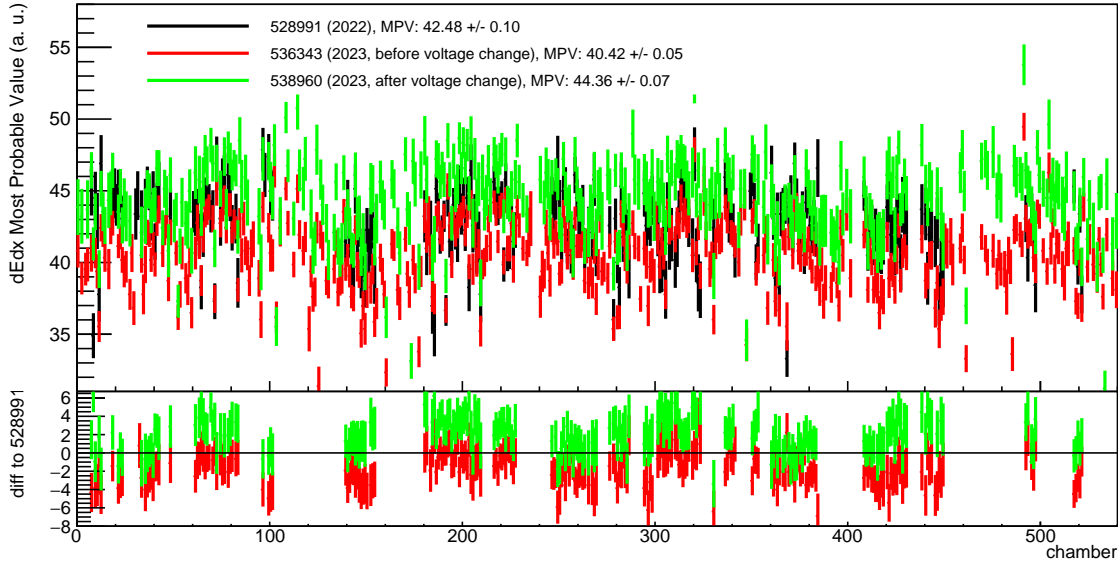

Figure 3.9.: Most probable value of energy loss per unit length extracted from the fit as a function of chamber number. The results are compared between three runs: 528991 (pp data taken in 2022, in black), 536343 (pp data taken in 2023, in red), and 538980 (pp data taken in 2023, in green). Lower panel shows the difference to the first run.

The MPV extracted from the fits is shown for all the TRD chambers, numbered from 0 to 539, and compared between three runs of pp collision data, in Fig. 3.9. For the cases when the chamber was deactivated, the statistics were too low (only a small fraction of data from the run was used), or the fit failed, no value is shown. The difference of the gain between chambers is quite small, while the difference is higher when comparing several runs. The gain value averaged on all chambers is 42.48 ± 0.10 for the first run, 40.42 ± 0.05 for the second one, and 44.36 ± 0.07 for the third one (the uncertainty here is statistical). The reason for the difference between the first run, taken in 2022, and the second one, taken in 2023, is likely due to the change in gas composition, with the contamination from N_2 slowly increasing with time. Even though the different pressure values also could have an impact, in this case the pressure was lower for the second run, which means that, from the pressure only, a higher gain would be expected for the second run. In order to compensate for the lower gain, the voltage in the amplification region was increased by 20V. The third run was taken after this voltage change, which caused the gain to increase again.

The average gain values for the different runs of Pb–Pb collisions, for which data was collected in October 2023, are shown in the left panel of Fig. 3.10. Because only three weeks happened between the first and last run shown in the figure, the variations in the contamination from N_2 are not expected to play a major role in the differences observed, contrary to the variations in atmospheric pressure. Indeed, the evolution of the pressure, shown in the same figure, follows exactly the same variations but in an opposite way: when the pressure increases, the gain
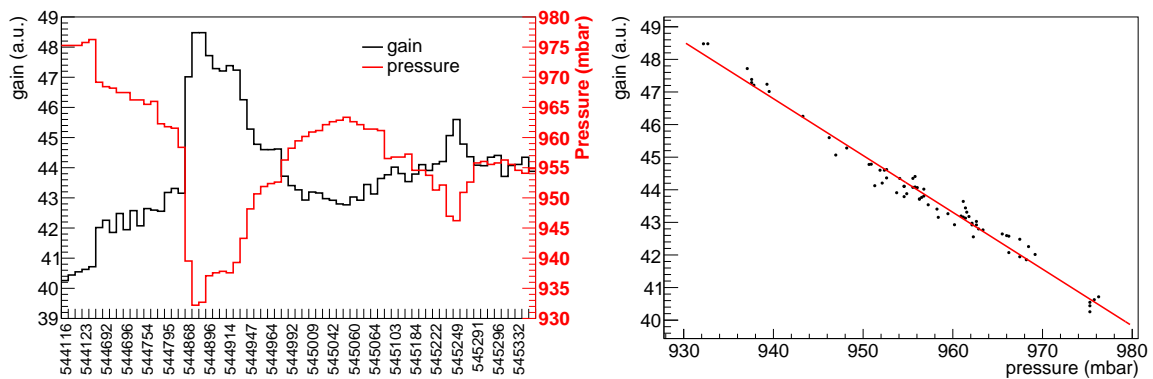
Figure 3.10.: Left: Evolution with the run number of the gain, averaged over all chambers (in black). This is compared with the evolution of the pressure (in red). Right: Correlation between the average of the gain and the pressure. This is fitted with a linear function.
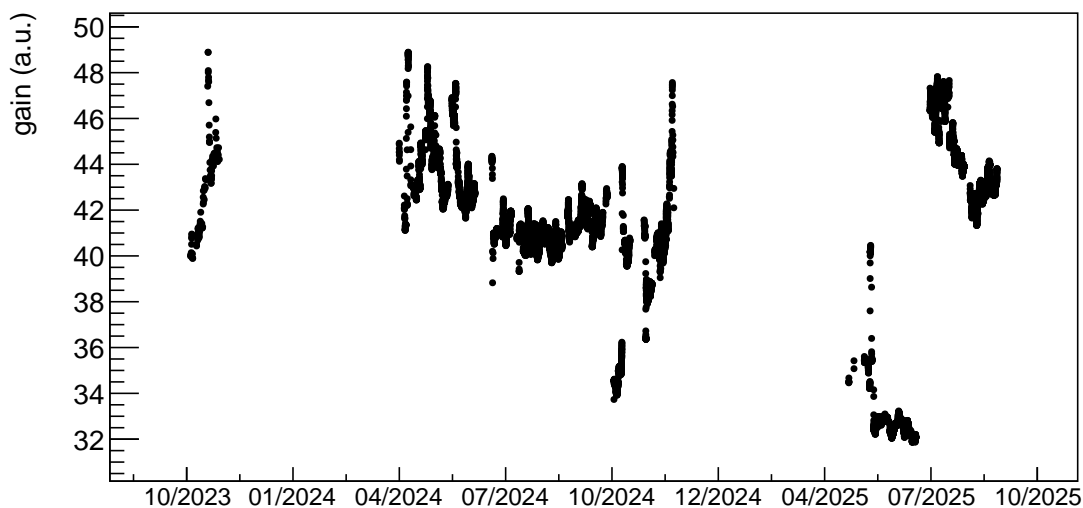
Figure 3.11.: Long-term evolution of the gain of the TRD, averaged on all chambers.

decreases, and the other way around. The correlation between both quantities is shown in the right panel of Fig. 3.10. A fit of the average correlation with a linear function shows that the gain decrease by 4% when the pressure increases by 10 mbar. Fig. 3.11 shows the evolution of the TRD gain value through several years of data taking. Several peaks are present, happening for small period of times. They probably correspond to large variations of the atmospheric pressure during short periods of time. In addition, there is a slowly decreasing trend, which is probably correlated with the slow variation of the gas composition in the TRD. The decrease is even stronger between the end of 2024 and the beginning of 2025, a period in which a higher xenon leak rate was found. Finally, in July 2025, some xenon was reinjected, causing the gain to rise again. This shows that the evolution of the gain of the TRD chambers can be explained by variations of pressure and gas composition.

4. Charged-particle multiplicity measurement

In the following chapters, the details of the main work realized during this thesis are presented. It consists of the analysis of data of proton-proton collisions collected by ALICE. The main goal is to obtain results on the correlation between prompt or non-prompt J/ψ at midrapidity and the charged-particle multiplicity N_{ch} produced in the event at midrapidity, either in the full azimuth or in azimuthal regions. This is done by extracting the number of prompt and non-prompt J/ψ, decaying to an electron and a positron, in several intervals defined by the number of tracks measured in the detector N_{tracks}, with several corrections needed. The yields of J/ψ as well as the multiplicity are further normalized by their average values in inelastic events with at least one charged-particle at midrapidity in $|\eta| < 1$ (INEL>0). The analysis is conducted using the ROOT framework [186], as well as the ALICE framework for analysis which contains AliRoot and AliPhysics repositories.

The work presented in this thesis mostly consists in looking at the J/ψ self-normalized yields, defined as:

$$(N_{\mathrm{J}/\psi}/\langle N_{\mathrm{J}/\psi}\rangle_{\mathrm{INEL>0}})_i = \frac{N^i_{\mathrm{J}/\psi,\,\mathrm{raw}}/(A^i \times \varepsilon^i)}{N^i_{\mathrm{evt,\,corr}}} \frac{N^{\mathrm{INEL>0}}_{\mathrm{evt,\,corr}}}{N^{\mathrm{INEL>0}}_{\mathrm{J}/\psi,\,\mathrm{raw}}/(A^{\mathrm{INEL>0}} \times \varepsilon^{\mathrm{INEL>0}})}\,. \qquad (4.1)$$

The raw numbers of J/ψ in the N_{tracks} interval and in INEL>0 events are corrected for acceptance and reconstruction efficiency, while the number of events are corrected for vertex reconstruction and trigger efficiency when applicable. The yields are correlated with the self-normalized multiplicity, defined as the average charged-particle multiplicity in the N_{tracks} interval for unbiased events (in this case, unbiased by whether a J/ψ is present or not in the event), divided by the average charged-particle multiplicity in inelastic events.

This chapter presents the selection and measurement of the charged-particle multiplicity, to which the measurement of J/ψ will be correlated. First, the selection of events and tracks used for the multiplicity estimator will be presented. Then, the different corrections necessary to obtain the final charged-particle multiplicity will be described. The analysis is also done with the multiplicity separated in azimuthal angle regions, as shown in the final part of this chapter.

4.1. Data selection

4.1.1. Event selection and triggers

The first necessary step is to select which events will be used in the analysis. Not all data is good for physics analysis. Events with a vertex too far from the center of the interaction region do not benefit from the full acceptance of the detectors. Therefore, a selection is then applied to keep only vertices with coordinate in the longitudinal direction $|\text{vtx}_z| < 10$ cm. Collisions with pile-up, when several collisions happen at the same time, either in the same bunch-crossing (in-bunch pile-up), or in different ones but still in the same readout window of the main detectors (out-of-bunch pile-up), should be rejected. This is done both by rejecting events when several vertices can be reconstructed, and when correlations between multiplicity estimators with different readout windows (V0 multiplicity, number of tracklets in the SPD, number of contributors to the primary vertex...) show values out of the main correlation lines. Indeed, when there is no pile-up, all these estimators are approximately proportional.

As described in Sec. 3.3.1, the data collected with three triggers are selected: the Minimum-Bias trigger (the sample of events collected with this trigger is denoted MB sample in the following), the High-Multiplicity trigger (HM sample), and the TRD electron trigger (TRD sample). The total number of selected events amounts to 1.7 billion, 880 million and 159 million, for the MB, HM, and TRD triggers respectively.

The data from these three triggers should in theory be combined to obtain a final result independent of the selected trigger. The typical normalization is done to the INEL> 0 event class, which considers all inelastic events with at least one charged particle within $|\eta| < 1$. The goal of the MB trigger is to introduce as little bias as possible, the correction will then be small. The fact that the TRD triggers on the specific physics signal of interest (the electron from J/ψ decay) means that it is also possible to correct for the trigger efficiency without bringing any bias. The corrected results obtained with both these trigger could therefore be merged, the final self-normalized yield being the weighted mean of self-normalized yield. The weight is proportional to the inverse quadratic sum of the statistical uncertainties and uncorrelated systematic uncertainties (discussed in Sec. 6). In order to cancel some systematic uncertainties, in the MB case, the INEL>0-integrated yield is estimated from the MB sample, while in the TRD case, the INEL>0-integrated yield is estimated from the TRD sample, with a correction for the TRD trigger efficiency. In both cases, the multiplicity distributions are estimated from the MB sample, which is the less biased distribution, which does not suffer from statistical uncertainties compared to the J/ψ yield for which the TRD trigger increases significantly the number of raw counts.

However, for the HM trigger, the trigger being on high-multiplicity at forward rapidity, it selects an other class of physics events (the events with a high-multiplicity at forward rapidity are not necessarily the ones with a high-multiplicity at midrapidity), with possibly different properties and multiplicity dependencies. A dedicated study on this bias using the PYTHIA 8 generator will be shown in Sec. 5.8. It cannot be combined within the INEL>0 class and is analyzed independently into a specific event class: V0M 0-0.1%, representing the 0.1% events with the highest signal in the V0M detector. For the self-normalization by the yields in INEL>0 events,

both the J/ψ yield and multiplicity corrections are extracted from MB sample, corrected for MB trigger efficiency.
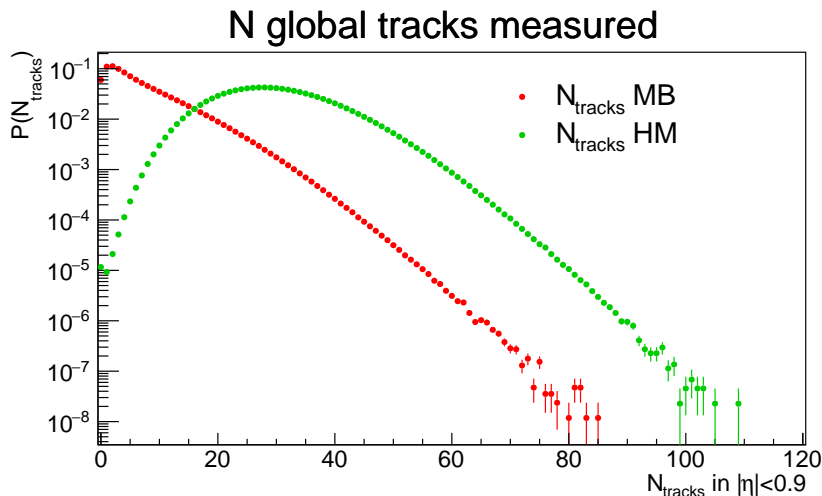
4.1.2. Track selection

The next step is to define, for every event, an estimator for the primary charged-particle multiplicity in $|\eta| < 0.9$. The primaries represent all particles produced in the collision whose mean lifetime is larger than 1 cm/c, excluding the daughters of such particles (a list of the primary particles can thus be found in [187]). This means in particular that particles coming from the weak decay of strange hadrons are not considered primaries, but secondaries. The number of charged primaries is estimated through the number of global tracks N_{tracks} matched in the ITS and TPC. These requirements are shown in Table 4.1 and are similar to the ones in [188], where more details on the selections can be found.

Selection	Value
pseudorapidity $|\eta|$	< 0.9
transverse momentum p_{T}	> 0.15 GeV/c
geometric length L	$> 130 - 1 \cdot p_{\text{T}}^{-1.5}$ cm
excluded area for geom. length	3 cm close to sector boundaries
number of crossed rows	$> 0.85 \cdot L$
number of TPC clusters	$> 0.7 \cdot L$
crossed rows/findable clusters	> 0.8
fraction of shared TPC clusters	> 0.4
χ^2_{TPC}/N_{cls}	< 2.5
χ^2_{ITS}/N_{hits}	< 36
$\chi^2_{TPC-ITS}$	< 36
DCA$_z$	< 2 cm
DCA$_{xy}$	$< 0.0182 + 0.035/p_{\text{T}}^{1.01}$ cm (7σ)
Hit in SPD	at least in one layer
kink topologies	daughters rejected

Table 4.1.: Track selection criteria for the global tracks used in the estimation of the charged-particle multiplicity

Several quality requirements are requested, in order to ensure good tracking of the charged particles (e.g. minimum p_{T} of 0.15 GeV/c, χ^2 of the track fit, or number of crossed rows, which corresponds to several clusters found consecutively), as well as correct reproduction by the Monte-Carlo. The quality requirements in several detectors make tracking more robust and less sensitive to the data taking condition and accurate simulation in a single detector. In addition, the requirements on Distance of Closest Approach (DCA) allow to reduce the contamination from secondary particles originating from the largely-displaced decays of primary particles or from conversion of photons to e^+e^- in the detector material. They also allow reduction of the pile-up tracks coming from other events.

Each event having been assigned a value of N_{tracks}, the distribution on all events of the number of global tracks for Minimum-Bias and High-Multiplicity triggered events is shown in Fig. 4.1.

Figure 4.1.: Probability distribution of measuring N_{tracks} (MB and HM triggers)

Now that events are selected, and the estimator for the multiplicity is defined, several corrections are needed to obtain the full distribution in INEL>0 events. Monte-Carlo simulations are needed to perform most of these corrections.

4.2. Minimum-bias Monte-Carlo simulations

The multiplicity estimator described in previous section is only an estimator in the sense of it not being the true charged-particle multiplicity because not all particles are detected. Corrections are necessary to take into account this difference. An important ingredient for the corrections are MC simulations of the events.

MC simulations are composed of two steps. First, an event generator, typically PYTHIA 8, is used to generate a collision event. All the information on the produced particles are kept, with their 4-momentum and position at production. The second part consists in simulating the interaction of the final particles with the detectors, in order to keep track of all the signals left by the particles when they traversed the different detectors. This is typically done using GEANT3 [189]. It is also possible to simulate different detector conditions (for example one part of the detector not functioning) which can depend on the data taking period. Once the responses of the detectors are simulated, the reconstruction can be done the same way as in real data. The comparison between the reconstructed tracks and the particles before interaction with the detectors allow in general to correct the effects due to ALICE detectors, such as the efficiency for particle detections, or the difference between measured and true quantities such as the transverse momentum.

4.3. Event efficiency correction

A necessary correction comes from the event selection. Indeed, it is possible that, when applying selections to the analyzed events, the multiplicity distributions become biased, for example if mainly low-multiplicity events are removed. It is then necessary to correct for it, in order to obtain a correct estimation of average multiplicity in INEL>0 events and in the intervals where the efficiency loss appear. The correction also affects the total number of events, which will be necessary later when calculating J/ψ yield per event.

The event selection which could introduce a bias are the selection done by the Minimum-Bias trigger, as well as the effect of requiring to have a vertex reconstructed in the event. The properties of the event being independent of the position of the vertex, the z_{vtx} selection does not need a correction. The bias in the multiplicity distribution when introducing pile-up rejection was found negligible.

The efficiency of finding a vertex depends directly on the number of measured tracks. The efficiency at N_{tracks} is then computed from data by dividing the number of events with a vertex reconstructed (independently of z_{vtx}) and N_{tracks}, by the number of MB triggers with N_{tracks}, with or without a vertex reconstructed. Because the selection for global tracks are tighter than the ones used for reconstructing the vertex, it is possible to have a vertex even with $N_{\text{tracks}} = 0$ if the tracklets are not matched to TPC tracks. Therefore, the efficiency is not zero at $N_{\text{tracks}} = 0$. When an event does not have a vertex, it is not possible to define a DCA. Therefore, the requirement on the track cuts linked to the vertex (DCA$_{xy}$, DCA$_z$, $\chi^2_{ITS-TPC}$ which is the χ^2 between the tracks parameters using ITS and TPC tracks and the one using the TPC track and the position of the vertex) are not used to calculate the efficiency. In order to obtain the efficiency as a function of N_{tracks} with standard cuts, the correlation between N_{tracks} without cuts linked to the vertex, and N_{tracks} with standard cuts is used:

$$\varepsilon_{vtx}(N_{\text{tracks}}) = \frac{N_{\text{rec. vtx}}(N_{\text{tracks}})}{\sum_N N_{\text{evt}}(N) \times N_{\text{rec. vtx}}(N,\ N_{\text{tracks}})/\ N_{\text{rec. vtx}}(N)} \,. \tag{4.2}$$

Here, N represents the number of tracks without requirements linked to the vertex. The correlation matrix $N_{\text{rec. vtx}}(N,\ N_{\text{tracks}})$ is taken from data using all events which have a vertex. The efficiency is shown in Fig. 4.2. Most events without vertex have $N_{\text{tracks}} = 0$.

For the MB-trigger efficiency, it depends directly on energy deposit on the V0A and V0C. It is extracted from MC as a function of the minimum of V0A and V0C multiplicity, as the ratio between events with INEL>0 and MB trigger to the ones with INEL>0. The choice of min(V0A,V0C) is done because it reproduces better the V0AND condition: if either V0A or V0C is too small, the event will not be triggered by V0AND and min(V0A,V0C) would be small, but if both are high enough, the trigger will be fired and min(V0A,V0C) will be higher. This efficiency is shown in the right panel of Fig. 4.2. It is converted to a trigger efficiency as a function of midrapidity multiplicity using the correlation between min(V0A,V0C) and N_{tracks} from data, with the formula:
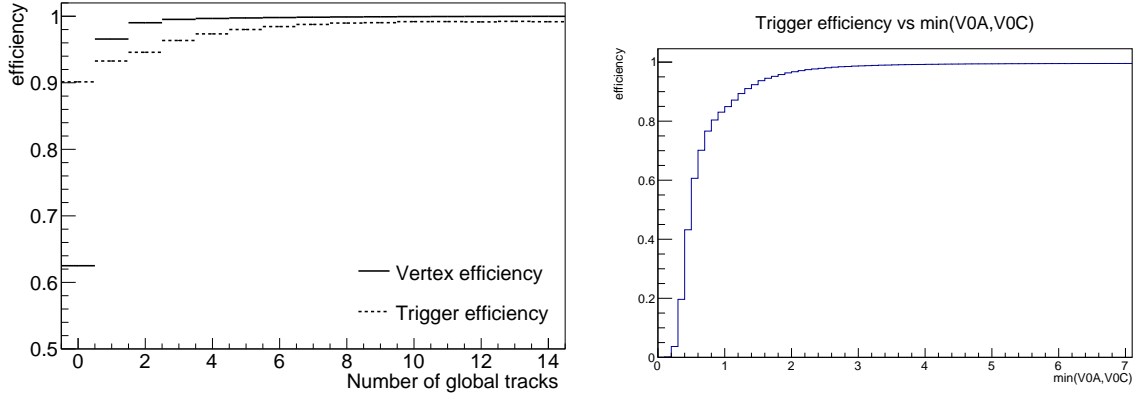
Figure 4.2.: Left: Vertex reconstruction and trigger efficiency as a function of N_{tracks}. Right: Trigger efficiency as a function of min(V0A,V0C).

$$\varepsilon_{trigger}(N_{\text{tracks}}) = \frac{\sum_m N_{\text{MB\&INEL}>0,\ \text{MC}}(m) \times N_{\text{MB, data}}(m,\ N_{\text{tracks}})/\ N_{\text{MB, data}}(m)}{\sum_m N_{\text{INEL}>0,\ \text{MC}}(m) \times N_{\text{MB, data}}(m,\ N_{\text{tracks}})/\ N_{\text{MB, data}}(m)} . \qquad (4.3)$$

Here, m represents the min(V0A,V0C) amplitude. In theory, it could have been possible to extract directly the trigger efficiency as a function of N_{tracks} in the MC. However, the chosen method allows to use the correlation between mid- and forward-rapidity multiplicity from data, while this correlation might not be completely reproduced in MC. The trigger efficiency obtained as a function of N_{tracks} is shown in the left panel of Fig. 4.2. The number of events which escape triggering is not negligible, even at values such as $N_{\text{tracks}} = 10$. This is due to the fact that a very low V0 multiplicity is not always correlated with a very low midrapidity multiplicity.

Both trigger and vertex corrections are applied to the N_{tracks} distribution in the data and in the MC (in both cases, the efficiency is still calculated from the data), by dividing the number of events for each N_{tracks} by the vertex and the trigger efficiency at this value of N_{tracks}.

After applying the trigger correction, the N_{tracks} distribution in the INEL>0 event class is obtained. But, in data, there could also be a contamination from triggered events which have no charged particles at midrapidity (and then are technically not INEL>0). It should also be paid attention to the $|\eta| < 1.0$ limit used in the definition of the contamination compared to the 0.9 limit for the global tracks. This contamination is determined from the MC and the probability to have a contaminating event is computed as a function of N_{tracks}. This is done by dividing the number of events with N_{tracks} which do not belong to the INEL>0 class by the total number of events with N_{tracks}. The contamination probability is around 5% at $N_{\text{tracks}} = 0$ (i.e. in the MC, only 5% of events triggered by MB and with no global tracks measured within $|\eta| < 0.9$ belong to the INEL = 0 event class), and is negligible afterwards.

4.4. Charged-particle multiplicity unfolding

4.4.1. Correlation between N_{ch} and N_{tracks}

The difference between the number of global tracks obtained previously and the true charged-particle multiplicity is due to several effects, such as detector inefficiencies, particles outside of the detector acceptance or the presence of secondaries from photon conversions or V^0 decays. This folding of the multiplicity by the detectors differs on an event-by-event basis, preventing a linear correlation between N_{ch} and N_{tracks}. Events with a given N_{ch} value do not all have the same N_{tracks} value, and two events with the same N_{tracks} value could have a different N_{ch} value. Therefore, it is necessary to deal with probability distributions rather than determining the true multiplicity for each event. Unfolding the multiplicity means that these detector effects need to be deconvoluted in order to obtain the primary charged-particle multiplicity distribution.

The correction uses the MC sample which was described previously in this chapter. From this sample, it is possible to extract from each event the true number of primary charged particle in $|\eta| < 0.9$ N_{ch} (without selection on p_T), and the number of global tracks N_{tracks}. A 2D detector response matrix can be constructed, as shown in Fig. 4.3, with N_{tracks} on the x axis, and N_{ch} on the y axis.
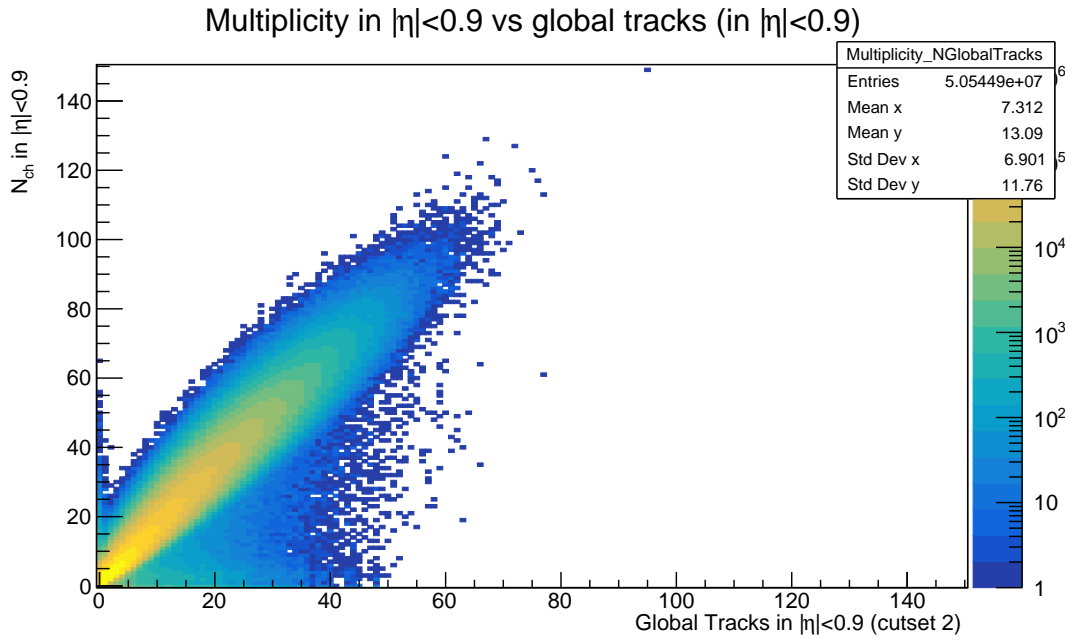
Figure 4.3.: Correlation between the primary charged-particle multiplicity and the number of global tracks in the MC events generated with PYTHIA 8 and propagated to the detectors using GEANT

At a constant N_{ch}, and after row-wise normalization, this matrix can provide the probability distribution on all events of measuring N_{tracks}, $P(N_{tracks}|N_{ch})$. This correlation characterizes the efficiency of particle detection and reconstruction in an event-by-event way. If the matrix is normalized column-wise, it provides the probability distribution of measuring N_{ch}, $P(N_{ch}|N_{tracks})$.

Since the simulation of the detector effects starts from particles (hence N_{ch}) and provides tracks (hence N_{tracks}), the row-wise normalization is the most natural way to look at this detector response. The correlation after such normalization does not suffer from any bias except for

imperfect simulation of the effects of the detectors and of the reconstruction. In particular, at a fixed N_{ch} value, the N_{tracks} distribution approximately follows a Poisson distribution with a mean value of εN_{ch} where ε is the average charged-particle detection efficiency. Differences to the Poisson distribution can appear for example due to the presence of secondaries and pile-up tracks. The latter are especially visible in the detector response matrix within the events which are far from the main correlation line, with high N_{tracks} (which can include tracks from pile-up events) compared to N_{ch} (which excludes pile-up events).

However, if the response matrix was normalized column-wise (thus using directly the $P(N_{ch}|N_{tracks})$ values), it would have introduced a dependence on the charged-particle multiplicity distribution at the generator level. For example, if the generated probability for a given N_{ch} value is artificially increased, more events are found in this specific row in the detector response matrix. In this case, the probability of having N_{ch} particles for a given N_{tracks} is overestimated. This is especially relevant when analyzing the HM-triggered distribution, for which the N_{ch} distribution is quite different from the generated MC distribution, which only represents MB events.

Contrary to the approximate linearity observed in the value of $\langle N_{tracks} \rangle$ as a function of N_{ch}, which depends only on track-level efficiency, a non-linearity in $\langle N_{ch} \rangle$ as a function of N_{tracks} appears. This is due to the fact that higher multiplicity events are less probable, because the multiplicity distributions decrease very steeply. Events with lower N_{ch} are then favored because they are produced more often by the event generator. In this case, the response is not Poissonian anymore, but results from the convolution between the Poissonian detector response matrix and the steeply decreasing multiplicity distribution.

4.4.2. Particle composition in the Monte-Carlo

The detector response matrix between true and measured multiplicity depends on the detection efficiencies of all the particles. However, the efficiency is highly dependent on the particle species and transverse momentum. Therefore, the response matrix, even if it mostly account for the propagation to the detectors from GEANT and the reconstruction of the event, cannot be completely independent from the initial MC generator. The response matrix could therefore be affected by the fact that particle yields and kinematics might not be well reproduced in the MC. This is for example the case for the distribution of hadron with strange quarks in PYTHIA.

As an illustration of this problem, comparison is done between the detector response from PYTHIA and the one from EPOS LHC. In particular, the profile of $\langle N_{tracks} \rangle$ as a function of N_{ch} from the response matrices (i.e. the global efficiency) is compared in the left panel of Fig. 4.4 between PYTHIA (in red) and EPOS (in black). A fit with linear function gives a slope of 0.58 and 0.56 respectively. This difference in the response matrix could cause a similar difference in the results unfolded using different generators.

In order to remove the dependence of the detector response on the event generator, a method for reweighting the particle composition in the MC had already been developed and used [60]. In this Particle Composition Correction (PCC) method, a weight is applied to each MC particle and track. This weight depends on the generator used, and on the p_T, particle species, and multiplicity class (defined from the V0 detector) of the considered particle. The weight is equal
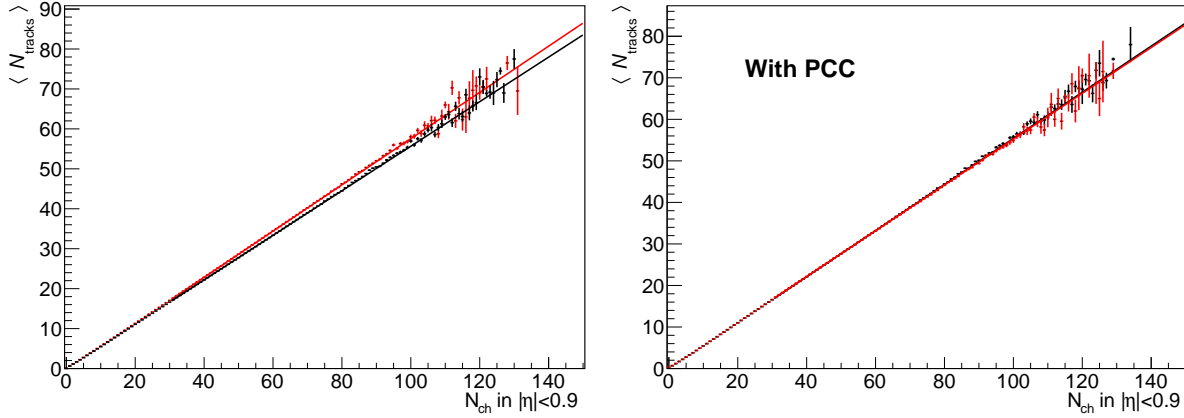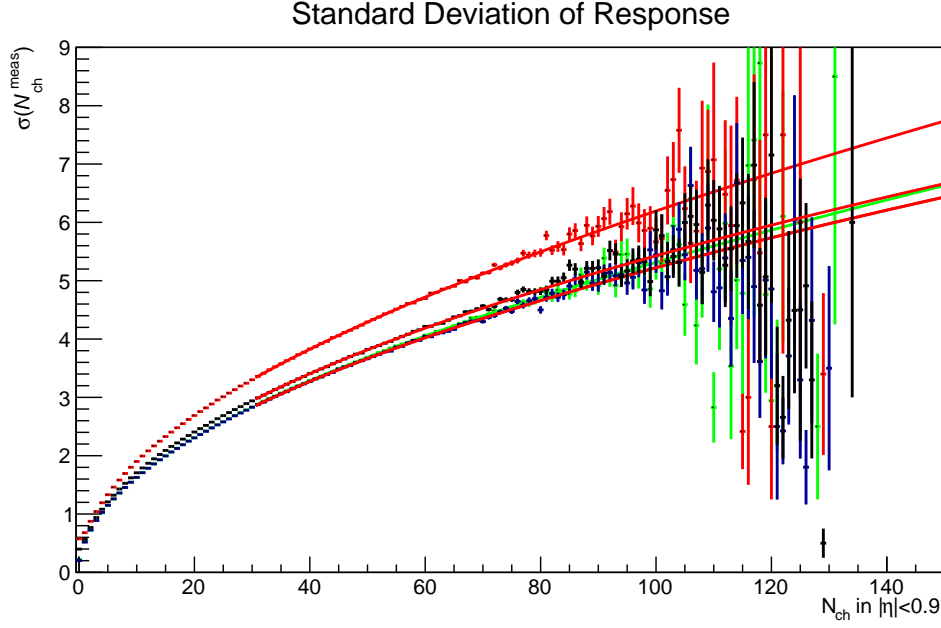
Figure 4.4.: Mean N_{tracks} as a function of N_{ch} from the MC response matrix, and linear fitting, for PYTHIA (in red) and EPOS (in black). Left: Without PCC. Right: With PCC.

to f_{data}/f_{MC}, where f are the relative fraction of the considered species in data (calculated from previously published results) and in MC.

When calculating N_{tracks} and N_{ch}, each particle is counted with the weight factor. In order to keep integer multiplicity values, this weight is rounded to either the integer immediately before or the one immediately after (the choice is done randomly). After applying this weight, the relative fractions in MC become the same as the one in data, and the global efficiency becomes more reliable. A special treatment is also applied to secondaries from weak decays, whose weights are obtained from the species and p_{T} of the mother. Since EPOS reproduces quite well the abundances, the N_{ch} distribution is not changed significantly while reweighting EPOS. The impact of the modification of particle compositions is much higher for PYTHIA.

After applying this reweighting, the slope in the profile of mean N_{tracks} vs N_{ch} becomes similar between PYTHIA and EPOS, as can be seen in the right panel of Fig. 4.4. However, this method is not perfect. One problem appears when looking at the standard deviation $\sigma(N_{\text{tracks}})$ as a function of N_{ch}: it is larger when applying the weights for particle composition correction, as seen in Fig. 4.5. This is due to the fact that few events contain a particle with a large weight, and one particle with a large weight does not have the same statistical power as many particles with a weight of one. Therefore, if the particle is counted in N_{ch} but not in N_{tracks}, the efficiency will be artificially largely reduced in these few events. The Poisson fluctuations are amplified, and they could have a large influence when doing unfolding, especially at high multiplicity. Larger fluctuations would mean that an event with a given N_{tracks} would be more likely to come from a lower N_{ch} with upper fluctuations on the efficiency. The PCC might bring their estimation to an unrealistic level. The PCC is nevertheless applied in the following, because of the better estimation of average track reconstruction efficiency which likely provides a better estimate of $\langle N_{\text{ch}} \rangle$.

Figure 4.5.: Comparison of standard deviation of N_{tracks} as a function of N_{ch} from the MC response matrix for PYTHIA without PCC (green), PYTHIA with PCC (red), EPOS without PCC (blue), EPOS with PCC (black).

4.4.3. Iterative Bayesian unfolding

In order to obtain an accurate N_{ch} distribution, the measured distribution needs to be unfolded. A common algorithm is the iterative Bayesian unfolding [190], available through the RooUnfold package [191].

The algorithm uses an iterative procedure. Its basic feature is that, at each step, the estimation of the N_{ch} distribution and of the unfolding matrix (which is defined as the matrix containing the probabilities $P(N_{\text{tracks}}|N_{\text{ch}})$) is improved by reinjecting information from the measured N_{tracks} distribution. In the ideal case, the N_{ch} distribution will converge to the correct one. This can be checked by smearing the N_{ch} distribution using the detector response matrix and checking if the N_{tracks} distribution can be obtained. The algorithm for Bayesian unfolding is described in the following.

The algorithm starts with a prior $P(N_{\text{ch}})$ distribution. Usually, this distribution is extracted from MC. Then, the Bayes theorem is used in order to estimate $P(N_{\text{ch}}|N_{\text{tracks}})$:

$$P(N_{\text{ch}}|N_{\text{tracks}}) = \frac{P(N_{\text{tracks}}|N_{\text{ch}}) \times P(N_{\text{ch}})}{P(N_{\text{tracks}})} = \frac{P(N_{\text{tracks}}|N_{\text{ch}}) \times P(N_{\text{ch}})}{\sum_{N'} P(N_{\text{tracks}}|N'_{ch}) \times P(N'_{ch})} \,. \tag{4.4}$$

$P(N_{\text{tracks}}|N_{\text{ch}})$ is taken from the detector response matrix, while $P(N_{\text{ch}}|N_{\text{tracks}})$ gives the unfolding matrix. Afterward, the unfolding matrix is used in order to obtain a new estimate of $P(N_{\text{ch}})$:

$$P(N_{\text{ch}}) = \sum_{N'} P(N_{\text{ch}}|N'_{\text{tracks}}) \times P(N'_{\text{tracks}}) \,. \tag{4.5}$$

$P(N'_{\text{tracks}})$ is taken from the measured data distribution, and is already corrected for vertex and trigger efficiency. The contamination from INEL $= 0$ events is handled in the algorithm by adding a point in the N_{ch} distribution representing these contaminating events. Then, in the detector response matrix, a full row is added, with the number of contaminating events for each N_{tracks}.

At this step, information from the measured distribution has been used in order to gain information on the true distribution. However, the unfolding matrix itself depends on the prior N_{ch} distribution, and hence is not accurately described. It becomes then necessary to inject the newly obtained N_{ch} distribution as a prior in 4.4, giving a better description of $P(N_{\text{ch}}|N_{\text{tracks}})$. This procedure is iterated several times. After each iteration, the distribution becomes closer to the correct one. The whole unfolding procedure is sketched in Fig. 4.6.
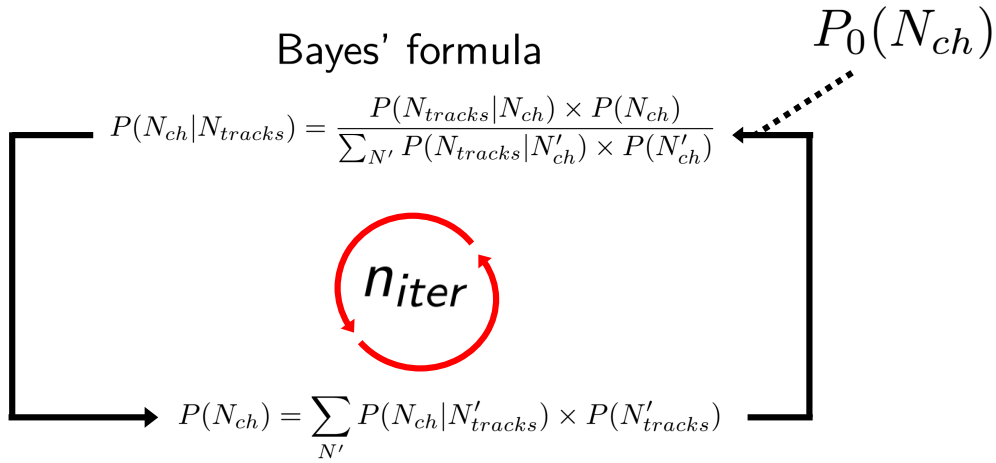
Figure 4.6.: Sketch of the unfolding steps during Bayesian iterative unfolding, which estimates N_{ch} using information from N_{tracks}.

Typically, it takes a few iterations, at maximum a dozen, to obtain a convergence. The algorithm is stopped when the unfolding does not modify $P(N_{\text{ch}})$ between two consecutive iterations significantly anymore (χ^2 of change < 1). This allows to keep an optimal number of iterations without deteriorating the quality of the unfolding. Indeed, since at each iteration the measured distribution is injected in the calculations, statistical errors increase with the number of steps, because the measured distribution brings at each step its own statistical fluctuations in addition to the ones from the previous iteration. Hence, statistical fluctuations could be amplified with many iteration. The error propagation is described in [192]. The statistical uncertainties take into account these statistical fluctuations and increase at each iteration.

The unfolded distribution in INEL>0 events is presented in the right panel of Fig. 4.7. It differs from the generated distribution in the MC, and also with the one obtained when using $P(N_{\text{ch}}|N_{\text{tracks}})$ directly from the response matrix with column-wise normalization. The latter case is equivalent to Bayesian unfolding with only one iteration and is called in the following reweighting. This shows the importance of iterative Bayesian unfolding in order to obtain the

correct N_{ch} distribution. The same distributions are shown for the HM-triggered sample in Fig. 4.8.
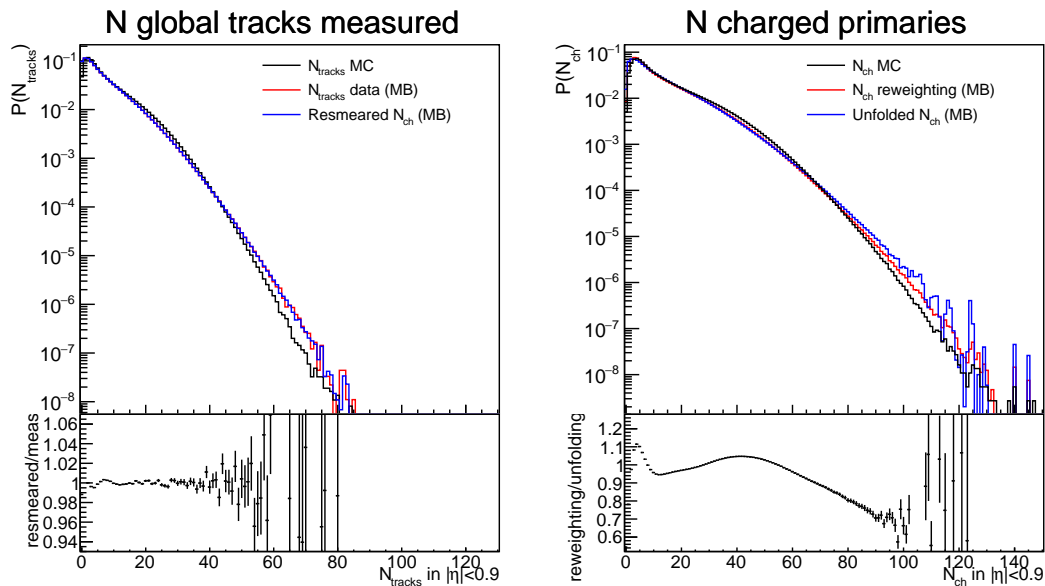
Figure 4.7.: Left: Comparison of N_{tracks} distribution measured in data (MB trigger) with the MC and the same distribution which was unfolded and then resmeared (in blue). The bottom plot shows the resmeared/measured ratio. Right: Unfolded N_{ch} distribution from Data, compared with N_{ch} from reweighting, and generated MC distribution (PYTHIA 8). The Minimum Bias trigger only is used. The bottom plot shows the reweighted/unfolded ratio

A check is done by smearing again the unfolded distribution with the detector response matrix (called resmeared in the following), and comparing to the distribution of N_{tracks} measured in data. Ideally, both distribution should be the same, showing that the unfolded distribution is consistent with the measurement. As shown in Fig. 4.7, both distributions are consistent, demonstrating that a good estimation is achieved.

4.4.4. Extrapolation at high multiplicity

At high multiplicity in the MB and HM sample, the statistical fluctuations become large, for data but also for MC (which especially lacks a correct high-multiplicity trigger). In order to deal with this problem, a possibility could be to extrapolate the detector response matrix by assuming a linear response for the average representing a constant track detection efficiency. In this case, for each N_{ch}, it is assumed that $P(N_{\text{tracks}}|N_{\text{ch}})$ follows a Gaussian distribution, with mean value (Fig. 4.9, linear fit) and standard deviation (Fig. 4.9, fit with a function $f(x) = ax + b\sqrt{x} + c$) extrapolated from lower multiplicity.

The results, after Bayesian unfolding with the extrapolated detector response matrix, on the multiplicity distribution for HM trigger (which is more affected by the lack of MC statistics) are shown in Fig. 4.10.

For the unfolded distribution, an unphysical bump structure appears, which may be due to some uncontrolled propagation of the statistical fluctuations. Indeed, it is possible that there is a small fluctuation in the measured distribution which will lead to a small bump after the
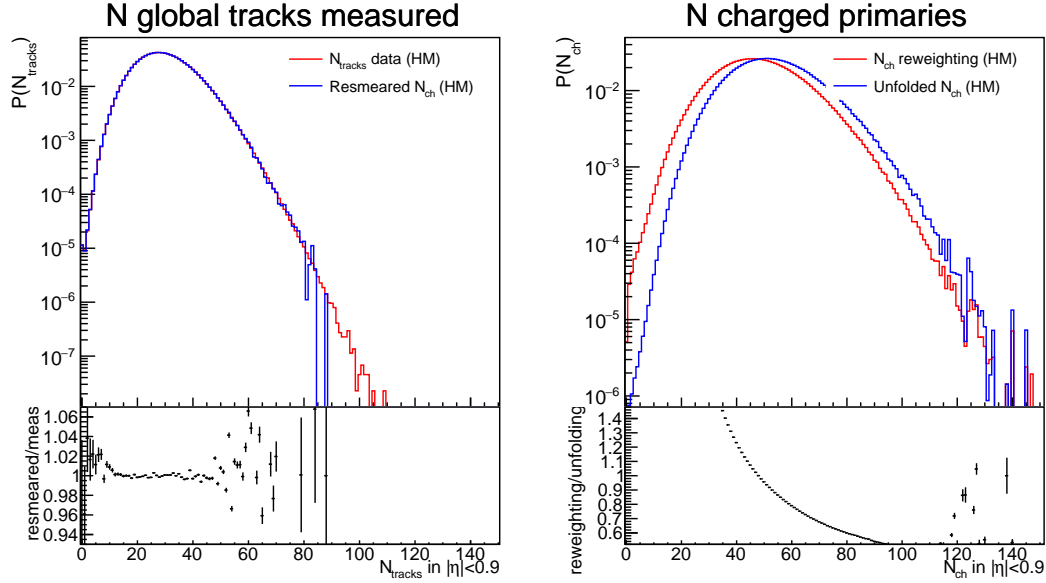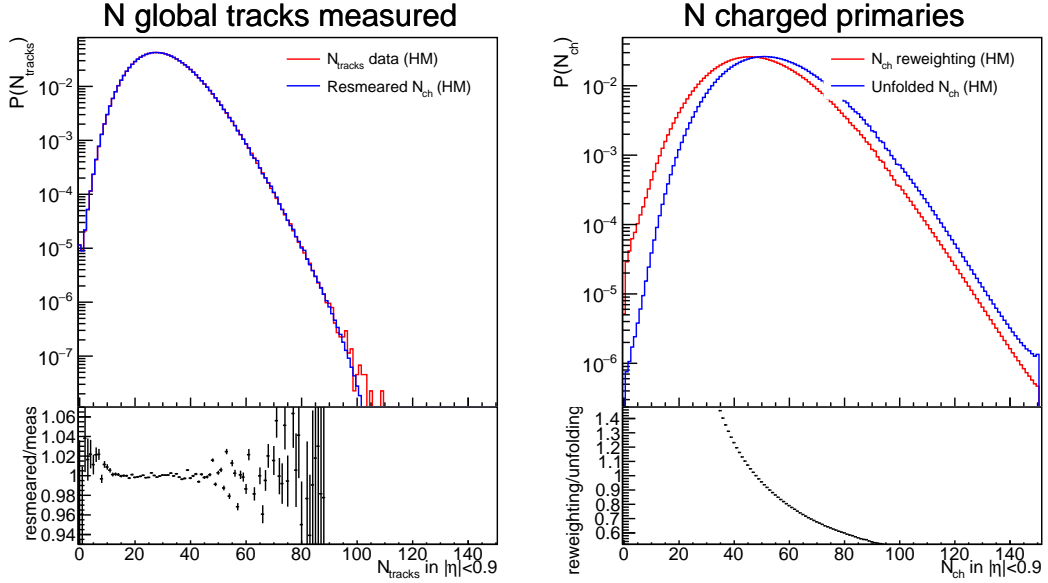
Figure 4.8.: Left: Measured and resmeared multiplicity distribution, using HM trigger. The ratio resmeared/measured is plotted below. Right: Unfolded multiplicity distribution, compared with reweighting, using HM trigger. The ratio reweighted/unfolded is plotted in the bottom panel
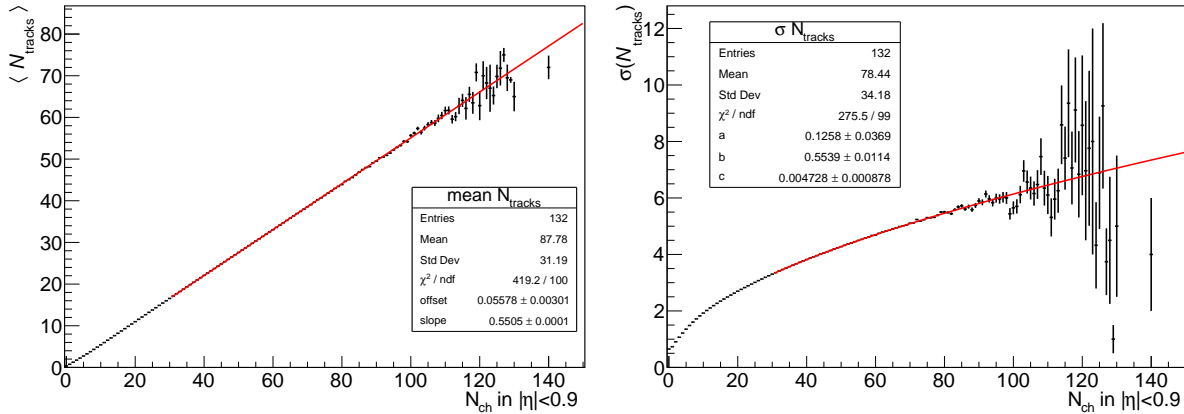
Figure 4.9.: Extrapolation of the mean (left) and standard deviation (right) of the N_{tracks} distribution at a constant N_{ch}, as a function of N_{ch}, from the detector response matrix.

first iteration. Then, at the next iteration, the same statistical fluctuation will contribute to this bump, amplifying it again, and so on for each of the following iterations. In fact, even without extrapolation, the same problem could occur. The fluctuations would be of the same order of magnitude in both cases, but they would be hidden by the statistical uncertainties when there is no extrapolation. The only difference is that, without extrapolation, there would also be fluctuations on the MC prior and on the MC detector response matrix, and the fluctuations would not appear continuous.

The evolution of the unfolded distribution in the bump region as a function of number of iteration is shown in the right panel of Fig. 4.11. It can be noticed that, at every iteration, the bump is higher. The resmeared distribution is shown in the left panel, and there also a slight bump appears at multiplicity values about 100-105. This peak coincides with an upward statistical fluctuation in the measured distribution, likely responsible for the peak in the unfolded

Figure 4.10.: Left: Measured and resmeared multiplicity distribution, using HM trigger and extrapolation at high multiplicity. The ratio resmeared/measured is plotted below. Right: Unfolded multiplicity distribution, compared with reweighting, using HM trigger and extrapolation at high multiplicity. The ratio reweighted/unfolded is plotted in the bottom panel

distribution. The presence of the bump in the resmeared distribution mimics the effect of that count, because the bump allows to minimize the error between the measured distribution and the resmeared distribution. The algorithm applies a fine-tuning in order to reproduce the statistical fluctuations, but this fine-tuning is too strong.

This shows the cause for the statistical fluctuations, which can be reduced with an extrapolation. However, the impact of this high-multiplicity extrapolation is found negligible for the final results, as the analysis of systematic uncertainties will show in chapter 6. For this reason, it is chosen not to apply extrapolation of the MC detector response matrix at high multiplicity.

4.4.5. Unfolding in different N_{tracks} intervals

The full charged-particle multiplicity distribution is obtained now. However, when it will be correlated to the J/ψ production, measured in different N_{tracks} intervals, it would become necessary to unfold the multiplicity in each of these intervals. Hence, it is decided to use the full information from the unfolding matrix, and for each bin of measured multiplicity, determine the full unfolded N_{ch} distribution. For every interval I with N_{tracks} in $[i_0, i_1]$, this is determined with:

$$P_I(N_{\text{ch}}) = \sum_{N'=i_0}^{i_1} P(N_{\text{ch}}|N'_{\text{tracks}}) \times P(N'_{\text{tracks}}). \tag{4.6}$$

where the unfolding matrix is the one obtained after iterations of the Bayesian unfolding.

The full N_{ch} distribution, superimposed with the multiplicity distribution corresponding to each one of the chosen N_{tracks} intervals, is shown in Fig. 4.12, in the left panel for the Minimum-Bias
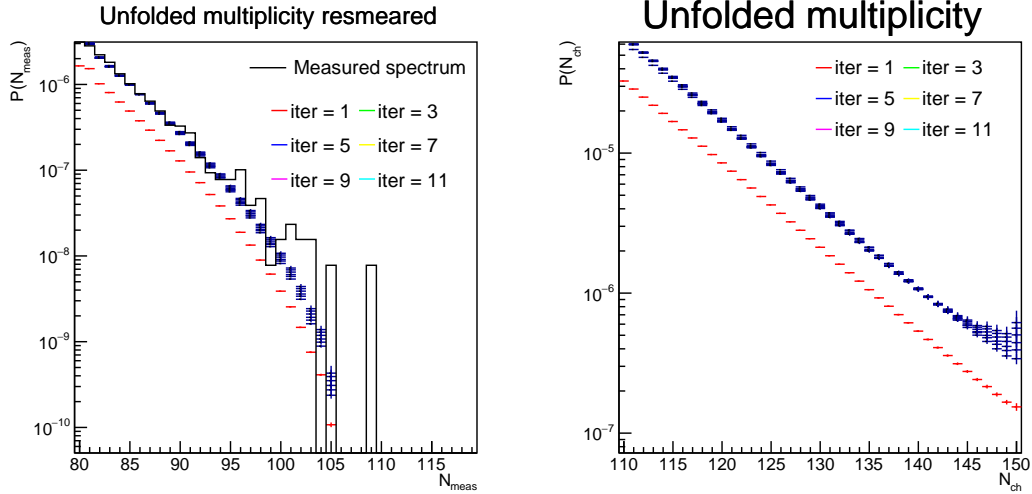
Figure 4.11.: Left: Measured and resmeared multiplicity distribution, using HM trigger and extrapolation at high multiplicity, in the high-multiplicity zone. For resmeared distribution, the number of iterations is varied. Right: Unfolded multiplicity distribution, using HM trigger and extrapolation at high multiplicity, in the high-multiplicity zone. The number of iterations is varied.

trigger, and in the right panel for the High-Multiplicity trigger. Then, from the full distribution in the interval, it is possible to extract its average value in this interval, and divide by the mean value in MB. The mean value in the interval for HM events might be slightly different from the one for MB events.
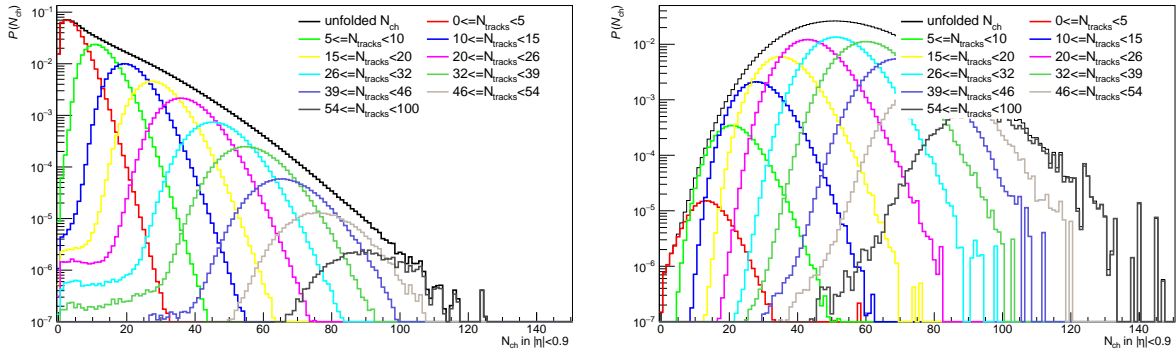
Figure 4.12.: Unfolded N_{ch} distribution, shown integrated in multiplicity and for every N_{tracks} interval. Left: MB trigger. Right: HM trigger.

4.5. Multiplicity in azimuthal angle regions

As explained in Sec. 2.2.3, it was decided to separate the multiplicity in three regions based on the azimuthal angle. When there is a J/ψ candidate, the regions are well-defined with respect to its emission direction, as will be explained in the next chapter. However, when analyzing the distribution for events unbiased by the presence of a J/ψ, it is not possible to define such a reference angle based on a defined probe. Hence, regions are defined relative to a random reference angle. That also means that the multiplicity distribution is very similar for all three

regions, with a mean value equal to one third of the mean value in the full azimuth. The $N_{\text{tracks,region}}$ distribution is shown in the left panel of Fig. 4.13.

The same unfolding procedure is done for the regions as for inclusive azimuth multiplicity: the unfolded N_{ch} distribution for every N_{tracks} bin is shown in the right panel of Fig. 4.13. For the trigger and vertex efficiency as a function of $N_{\text{tracks,region}}$, they are extracted using the efficiency as a function of N_{tracks} and the correlation between N_{tracks} and $N_{\text{tracks,region}}$.
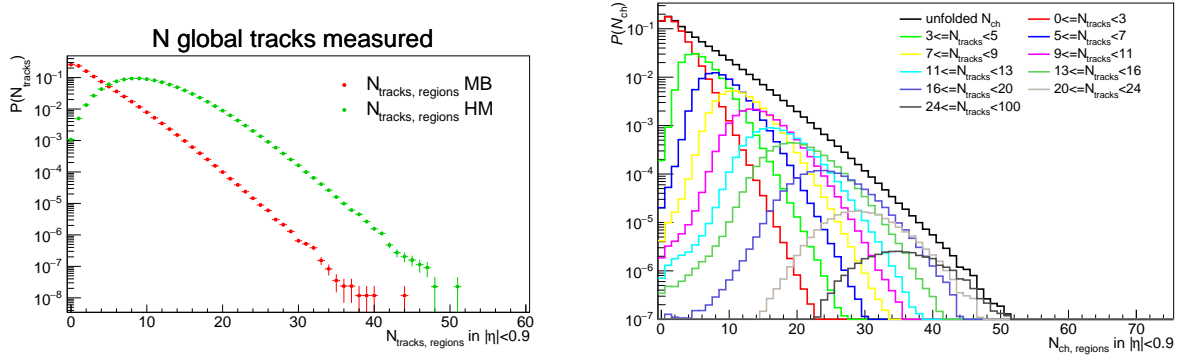
Figure 4.13.: Left: $N_{\text{tracks,region}}$ distribution. Right: $N_{\text{ch,region}}$ distribution, in every $N_{\text{tracks,region}}$ interval.

From the unfolding multiplicity distribution in MB events, it can be noticed that, even if $\langle N_{\text{ch,region}} \rangle$ is one third of $\langle N_{\text{ch}} \rangle$, the unfolded $N_{\text{ch,region}}$ distribution gets to a probability of 10^{-7} at $N_{\text{ch,region}} = 50$, while the same probability is reached at around $N_{\text{ch}} = 120$ for inclusive multiplicity, meaning that the factor here is less than three. This could be explained by larger Poisson fluctuations in the number of charged particles when considering a smaller region with only one third of the total acceptance. A multiplicity in a region which is high relative to its mean value can be reached from a high multiplicity in the full acceptance. However, it can also be reached from a lower multiplicity in the full acceptance, but with more particles in a specific direction. An example could be because of a hard jet, or, when considering a MPI-based picture, if more partonic interactions are happening with azimuthal angles close to each other. In this case, the considered region will have higher-than-average multiplicity, while the other regions will have lower-than-average multiplicity. Due to the rapid decrease of the multiplicity distribution, the effect due to many particles in a specific direction becomes non negligible.

This can be seen in Fig. 4.14. In the left panel, the $N_{\text{tracks,region}}$ distribution is shown at fixed N_{tracks}, for few values of N_{tracks}. It can be seen for example that, at $N_{\text{tracks,region}} = 20$, it is most probable to have $N_{\text{tracks}} = 28$ or $N_{\text{tracks}} = 40$ than to have $N_{\text{tracks}} = 55$, even if $N_{\text{tracks,region}} = 20$ is the most probable value when having $N_{\text{tracks}} = 55$. In the right panel, is reported the average value of self-normalized multiplicity in the full azimuthal angle, as a function of the value of self-normalized multiplicity in one region. The dashed line shows a case of linear increase with slope 1. The increase which is weaker-than-linear shows again that the self-normalized values which can be reached are higher in azimuthal regions, and a given self-normalized multiplicity value in azimuthal region corresponds in average to a lower value of self-normalized azimuth-inclusive multiplicity in the same event.

Then, a high multiplicity in a region occurs more frequently. However, in this case, it does not necessarily means that there is a high multiplicity in the full azimuth, therefore it does not
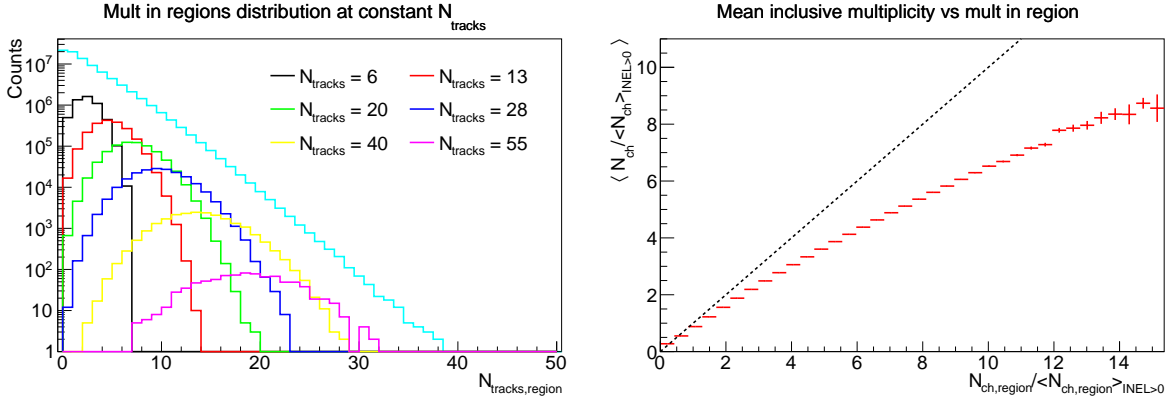
Figure 4.14.: Left: $N_{\text{tracks,region}}$ distribution for different values of N_{tracks}. Average value of self-normalized multiplicity in the full azimuthal angle, as a function of the self-normalized multiplicity value in one region.

necessarily mean that the total number of J/ψ is enhanced. It could then be expected that the number of J/ψ per event would appear on average smaller compared to the case when the multiplicity is calculated in the full azimuth. If the correlation in the right panel of Fig. 4.14 was used in order to convert between multiplicity in region and multiplicity in the full azimuthal angle, the increase of the J/ψ yields as a function of multiplicity estimated in regions might be closer to the one as a function of the multiplicity in full acceptance.

5. J/ψ measurement and correlation with the multiplicity

The second part of the analysis consists in establishing the correlation between the production of J/ψ mesons and the multiplicity estimated in the previous chapter, by counting the number of J/ψ in the different intervals defined by the number of global tracks. First, the selection and identification of the decay daughters of the J/ψ is explained. Then, the extraction of the number of inclusive, prompt and non-prompt J/ψ counts is described. Further corrections for the acceptance and efficiency of J/ψ detection are presented. Finally, several possible bias are analyzed. These biases include, for example, the bias on the multiplicity unfolding correction when it is correlated to the J/ψ production, or the autocorrelation bias due to the presence of the decay daughters in the multiplicity.

5.1. Selection of the daughters

Since the J/ψ decays before reaching the detectors, it cannot be observed directly, but its decay products can. Out of the several decay channels which could be analyzed, the decay to lepton pairs is the most promising. This is due to the fact that leptons are produced less often in the collisions than hadrons, reducing the background coming from other processes compared to hadronic J/ψ decay. In addition, the identification of muons in ALICE central barrel is challenging due to their mass which is close to the pion mass, making the distinction between muons and pions challenging. Hence, the J/ψ is identified through its decay to an electron and a positron (dielectron decay) at midrapidity ($|\eta| < 0.9$), which has a branching ratio of $5.971 \pm 0.032\%$ [1]. The electron and the positron (in the following, the term electron can be used to also imply positron) are identified as global tracks in the ITS and the TPC. The track requirements are shown in Table 5.1.

The selections should allow to keep as much signal as possible, while removing as much background as possible, the background coming either from pions or protons which were incorrectly identified as electrons or from electrons which do not come from the decay of a J/ψ meson. Several selection criteria (TPC χ^2 or $N_{clusters}$) are required to ensure good quality of the tracking. Selections on DCA can remove pile-up or secondary electrons. However, these selections cannot be too tight, otherwise they could remove a part of the electrons from non-prompt J/ψ, which are displaced from the primary vertex due to the large lifetime of the B hadrons ($c\tau \sim 500~\mu$m). The requirement of at least one hit in the SPD allows better DCA resolution, and participates to the rejection of secondary electrons from photon conversions. Due to the large kinematical phase-space brought by the large difference in mass between the

Selection	Value
pseudorapidity $|\eta|$	< 0.9
transverse momentum p_T	> 1.0 GeV/c
DCA$_z$	< 3.0 cm
DCA$_{xy}$	< 1.0 cm
χ^2_{TPC}/N_{cls}	< 4
TPC N_{cls}	> 70
Hit in SPD	at least in one layer
kink topologies	daughters rejected
TPC $|n\sigma_{el}|$	< 3
TPC $n\sigma_\pi$	> 3
TPC $n\sigma_p$	> 3
prefilter selection	dielectron with $m_{ee} < 50$ MeV/c^2 rejected

Table 5.1.: Track selections for the J/ψ daughter candidates.

J/ψ and its decay products, electrons from J/ψ decay typically have large p_T, which explains the requirement in transverse momentum. In contrast, the background electrons from other sources than J/ψ mesons have in general lower p_T values.
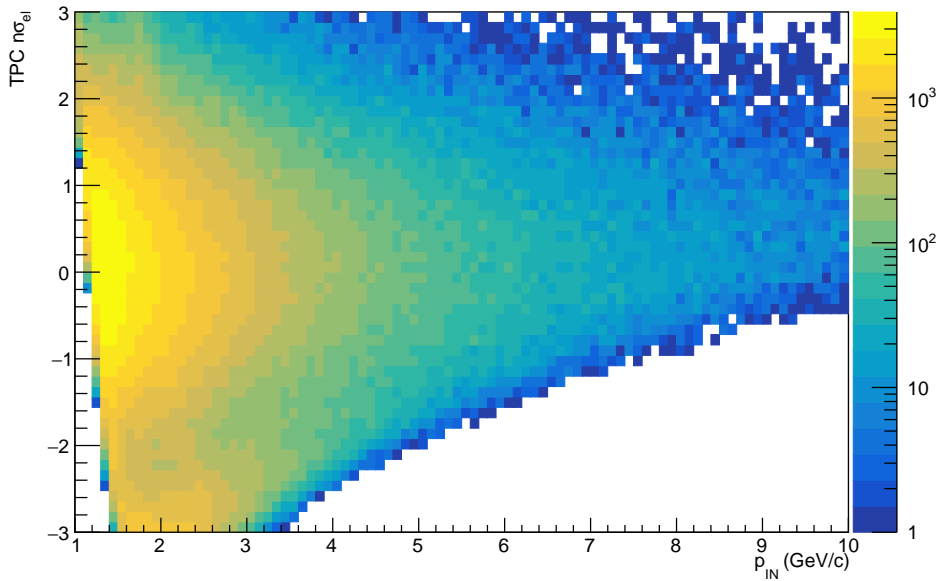
Figure 5.1.: Number of electron candidates as a function of TPC $n\sigma_{el}$ and momentum at the inner point of the TPC p_IN. Only shown are electrons which are part of an electron-positron pair. MB, HM and TRD triggers are combined.

In addition, the particle identification through specific energy loss in the TPC is used to select electrons and reject hadrons. From the approximate Gaussian distribution of the dE/dx values, a selection with 3 σ inclusion on $n\sigma_{el}$ would keep more than 99% of the electron yield. However, due to their higher production yields compared to the electron ones, the protons, pions and kaons must be rejected through tight selections (the kaons having lower dE/dx values in this momentum range, a selection on TPC $n\sigma_{Kaon}$ is not necessary). This selection is illustrated in

Fig. 5.1 where the TPC nσ_{el} is shown as a function of the momentum in the TPC for all selected tracks. It shows that the hadron rejection removes electrons especially at high momentum, where the pion expected energy loss curve increases to come closer to the one of the electron (cf. Fig. 3.7). There is also a visible rejection at momentum close to 1 GeV/c due to the proton rejection constraint.

Finally, a large part of the background electrons are produced by the conversion of photons to dielectrons in the detector material, as well as by the decays $\pi_0, \eta \to \gamma e^+ e^-$ (Dalitz decays). In this case, the electron is always produced with a partner, and the invariant mass of the dielectron is low. To use this property, it is tried to pair each electron (or positron respectively) candidate with positrons (electrons respectively) from the same event selected with looser criteria (looser quality selections, $p_T > 0.2$ GeV/c, no TPC nσ pion and proton rejection). If the invariant mass of the pair is lower than 50 MeV/c^2, it is likely that they come from a photon conversion or Dalitz decay, hence both tracks are rejected.

5.2. Extraction of the J/ψ signal

Once the J/ψ daughter candidates have been selected, the reconstruction of the J/ψ is done by combining pairs of tracks selected from the same event. The pairs are required to have $|y| < 0.9$ (so that the electrons are in the central barrel acceptance) and $p_T > 1$ GeV/c (to be able to separate prompt and non-prompt J/ψ, as will be explained in Sec. 5.3). The distribution of the invariant mass m_{ee} is shown for the selected dielectrons with $p_T > 1$ GeV/c in the MB sample in the top left panel of Fig. 5.2, in the HM sample in the top right panel, and in the TRD sample in the bottom panel.

A peak for the J/ψ candidates is seen around the J/ψ mass at $m_{J/\psi} = 3.097$ GeV/c^2. Two factors explain the width of this peak. First, the momentum resolution is not perfect, and the momentum of the daughters tracks being overestimated or underestimated can lead to higher or lower measured invariant mass, which would give a Gaussian shape. Second, the electrons lose energy via Bremsstrahlung radiation when interacting with the material of the detectors, leading to a lower measured invariant mass, which gives a power-law tail for lower invariant mass than the peak.

The combination of these two effects can be described by a Crystal Ball function. However, for this analysis, the shape is estimated from Monte-Carlo simulations. Because of the low J/ψ production cross section, the number of J/ψ in the minimum-bias simulation, which is described in Sec. 4.2, is not enough for the analysis of the J/ψ expected signal shape. For this reason, another MC simulation is created, where J/ψ signals are injected on top of the PYTHIA event simulation. Prompt J/ψ are added directly, while, for non-prompt J/ψ, $b\bar{b}$ pairs are created, hadronized, and the beauty hadrons are forced to decay in a decay channel containing a J/ψ. J/ψ mesons are then forced to decay to a dielectron, using the EvtGen package [193]. In addition, the decay J/$\psi \to e^+ e^- \gamma$, which has an effect similar to the Bremsstrahlung, with branching ratio of $0.88 \pm 0.14\%$ [1], is also taken into account with the PHOTOS package [194]. Reconstruction
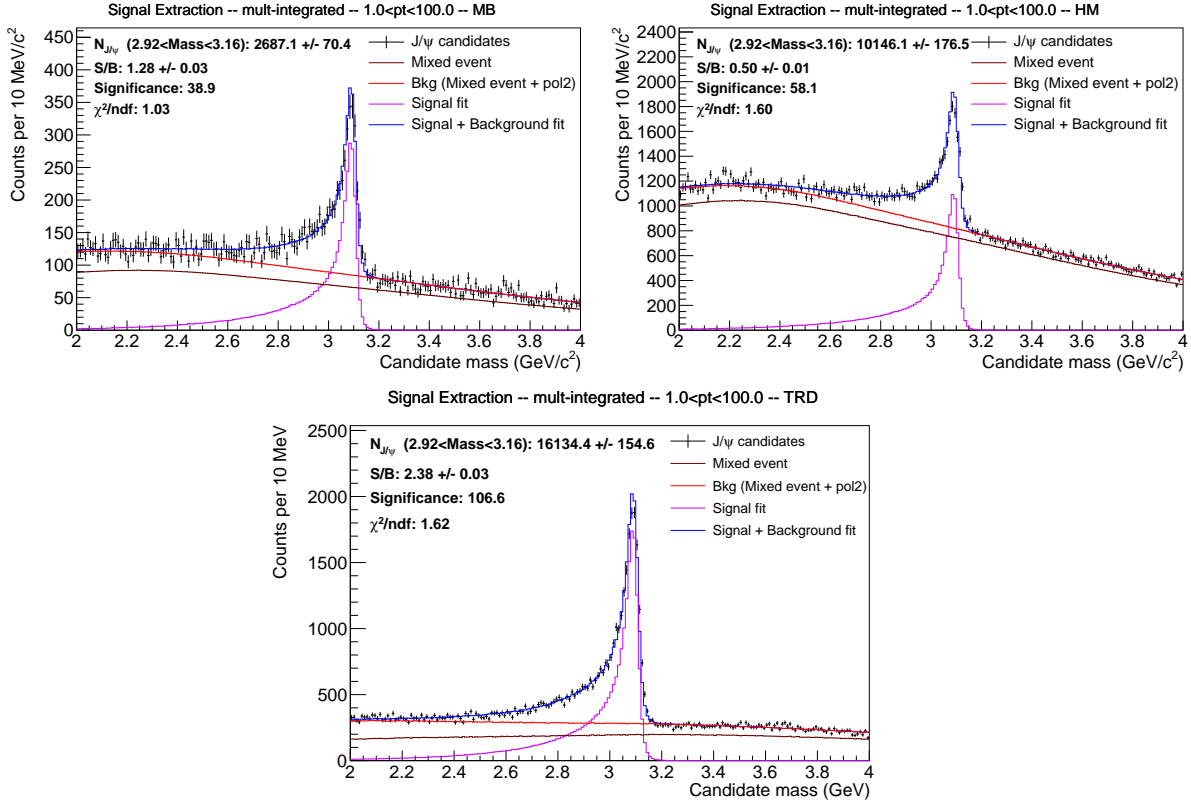
Figure 5.2.: Invariant mass distribution of electron candidate pairs with $p_{T, ee} > 1$ GeV/c, in the MB (top left), HM (top right), and TRD (bottom) samples. The fitted signal and backgrounds components are also shown.

of the event is done similarly as in data, and the distribution of reconstructed invariant mass for the true J/ψ signals can be extracted, after applying the same selections as in data.

Some background can be found in addition to the J/ψ peak. Two different backgrounds are identified: uncorrelated background, when the electron and the positron candidate come from two different processes, and correlated background when they come from the same process. An example for correlated background is when a heavy quark pair is created, both heavy quarks hadronize separately and decay semi-leptonically (e.g. $D^0 \to K^- e^+ \nu_e$ and $\overline{D^0} \to K^+ e^- \overline{\nu_e}$).

The MC is not able to reproduce correctly the shape of the background, possibly due to different proportions of different uncorrelated processes in the MC compared to data. It is then necessary to model the background shape using a data-driven way. The contribution from uncorrelated pairs can be modeled in two ways: either by pairing together tracks with the same sign (e^+e^+ or e^-e^-), which is called like-sign background, or by pairing an electron from one event with a positron from another event, which is called event-mixing background. Due to possibly different event properties, only events with similar vtx$_z$ (hence similar detector acceptance) and similar multiplicity are mixed together. Because of the symmetry between electrons and positrons, the number of like-sign pairs is expected to be the same as the number of uncorrelated opposite-sign pairs, while the number of pairs from event-mixing can be much higher. The shape of the uncorrelated background is then modeled with event-mixing, which has negligible statistical uncertainties compared to pairs from the same event, while the absolute normalization of the

uncorrelated background is fixed to reproduce the number of like-sign pairs. While the event-mixing shapes in the MB and HM sample are similar, the one from the TRD sample is biased by the transverse momentum cut used in the trigger. Consequently, the same event-mixing shape is used in all multiplicity intervals for the MB and HM samples, and an independent one is used for the TRD sample.

The correlated background is modeled by a second-order polynomial. Its parameters are not fixed, but extracted from a binned likelihood fit to the invariant mass distribution, where the only other free parameter is the absolute normalization for the J/ψ signal. Fig. 5.2 shows the signal and background components after the fit. The number of uncorrelated pairs increase approximately quadratically with the total number of tracks. This is responsible for the lower signal-to-background ratio in the HM sample compared to the MB sample. This ratio is much higher in the TRD sample, which is due, not only to a higher purity of electrons selected by the triggers, but also to the fact that most electrons and J/ψ candidates are selected at higher transverse momentum, where the background is smaller.

The number of J/ψ signals inside the considered sample is extracted as the total number of candidates minus the estimated number of background counts in the signal region, which is defined by $2.92 < m_{ee} < 3.16$ GeV/c^2. This is repeated for every triggered sample, in several intervals of N_{tracks}. The extraction of the number of counts is also done within azimuthal angle regions. For each candidate, the number of tracks can be extracted in each one of the three regions in the same event, where the region for each track is defined by the azimuthal angle of the track relative to the emission direction of the J/ψ candidate. The number of raw J/ψ counts can thus be extracted in every interval of $N_{\text{tracks, toward}}$. This is done by considering the invariant mass of all the candidates which have a number of tracks in the toward region within this interval. The background is estimated as a sum of the mixed-event distribution and a second-order polynomial and subtracted from all the candidates, allowing to obtain the raw yield of J/ψ within this interval of $N_{\text{tracks, toward}}$. The same procedure can also be repeated for intervals of $N_{\text{tracks, transverse}}$ and $N_{\text{tracks, away}}$.

5.3. Separation between prompt and non-prompt J/ψ

From the fit of the invariant mass distribution, the number of inclusive J/ψ counts can be obtained for all the multiplicity intervals. The next step in the analysis consists in obtaining the number of raw counts for both prompt and non-prompt J/ψ for all these intervals.

5.3.1. Displaced vertex

Experimentally, non-prompt J/ψ can be distinguished thanks to the large lifetime of the beauty hadron decaying weakly to J/ψ, compared to the much faster strong or electromagnetic decay of a quarkonium. The ITS requirement is to provide a good resolution of the impact parameter, ranging from a few dozens μm at high momentum to hundreds of μm at low p_{T}. Experimentally, it is then possible to reconstruct the decay vertex of the beauty hadron (also called secondary vertex), since this vertex is displaced from the primary vertex by a mean decay length of e.g.

$c\tau = 455 \pm 1$ μm for B^0, or $c\tau = 441 \pm 3$ μm for Λ_b [1]. A sketch of the decay $B^+ \rightarrow K^+\mathrm{J}/\psi(\rightarrow e^+e^-)$, where the Kaon is not reconstructed is shown in Fig 5.3 as an example.
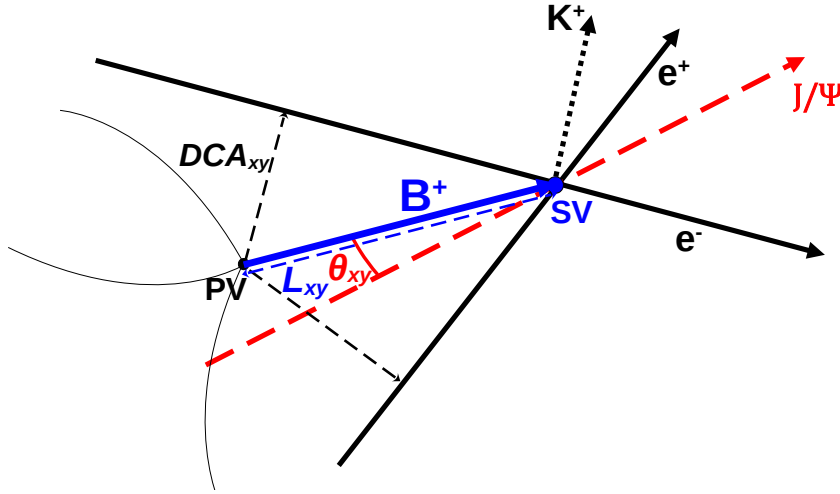
Figure 5.3.: Sketch of the decay $B^+ \rightarrow K^+\mathrm{J}/\psi(\rightarrow e^+e^-)$. Only the two electron tracks are reconstructed. Shown on the sketch are: the signed DCA in xy plane (DCA$_{xy}$) for electrons, the Primary Vertex (PV), the Secondary Vertex (SV), the distance between both vertices (L_{xy}), and the pointing angle between the flight vector of the B hadron and the momentum of the J/ψ (θ_{xy}).

The Distance of Closest Approach (DCA) of a track is the minimal distance between any point of the helix trajectory and the primary vertex. Its sign depends on whether the vector between the point of closest approach and primary vertex has an angle of $+90°$ or $-90°$ with the momentum vector (for example, in Fig. 5.3, the two electrons would get a different sign on their DCA value). For prompt J/ψ, the DCA of its daughter electrons only depends on the resolution of the detector while non-prompt J/ψ have usually higher DCA. It is also important that this resolution is well reproduced in the MC simulation. However, studies have shown that there is a discrepancy in the resolution of DCA in transverse plane between MC and data which can reach 15% [195]. In order to mitigate this discrepancy, the tracks parameters in the MC are smeared with [196]:

$$y_{new} = y_{MC} + (y_{old} - y_{MC}) \times \frac{\sigma_{data}}{\sigma_{MC}} + \mu_{data} - \mu_{MC}. \tag{5.1}$$

y_{new}, y_{old} and y_{MC} are the modified, old and MC true y parameter of the helix respectively, σ_{data} and σ_{MC} are the resolutions in data and MC respectively, and μ_{data} and μ_{MC} are the average DCA, in general small compared to the resolution, in data and MC respectively. The track parameters in the calculation also need to be estimated at the point of closest approach to the true MC origin of the track (either the primary or the secondary vertex).

The DCA$_{xy}$ resolution in the corrected MC is extracted from a fit of the DCA distribution of electrons coming from prompt J/ψ, and shown in the right panel of Fig. 5.4. The fit uses the sum of two functions. The first one is a Gaussian function, whose σ parameter is taken as the resolution. The second one is an exponential function of $|\mathrm{DCA}_{xy}|$, convoluted with the Gaussian resolution function. Fit examples at low and high p_T are shown in the left panel of Fig. 5.4.

The resolution is worse at low momentum, where the effect of multiple scattering is strong, and amounts to $\sim 70~\mu$m at $p_T = 1$ GeV/c, a value still allowing to distinguish the displaced electron tracks. At higher momentum, the multiple scattering effect is much weaker, amounting to ~ 25 μm at $p_T = 7$ GeV/c, and the resolution is mainly determined by the size of the silicon pixels of the SPD. At low p_T, the worse DCA resolution, and the shorter distance flown on average by the beauty hadron before decaying, lead to necessity of a requirement $p_T > 1$ GeV/c for the J/ψ candidate in order to separate prompt and non-prompt J/ψ.
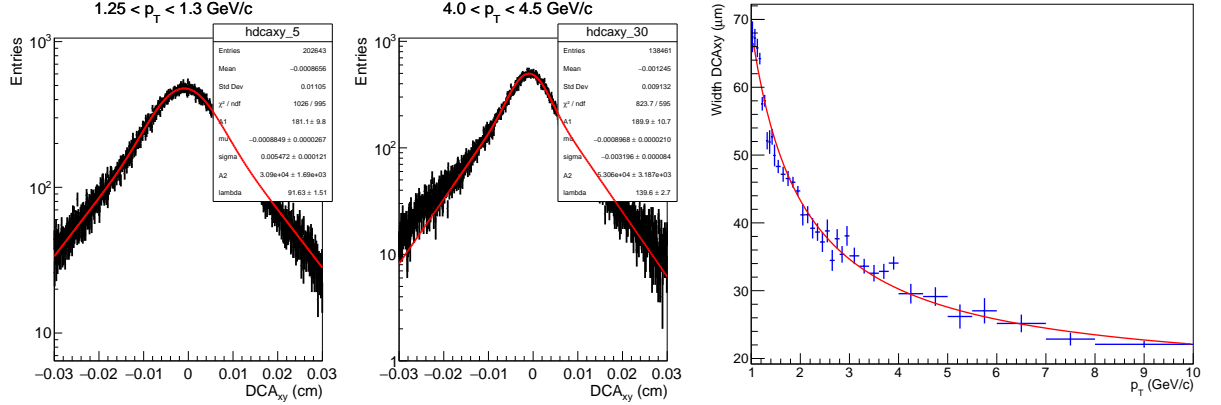
Figure 5.4.: Left and middle: fit of the DCA distribution of electrons from prompt J/ψ in the MC, for $1.25 < p_T < 1.3$ GeV/c, and $4 < p_T < 4.5$ GeV/c. Right: DCA resolution extracted from the fit as a function of p_T. A fit function $A + B \times p_T^C$ is superimposed.

From two tracks, it is also possible to reconstruct the position of a secondary vertex using their track parameters. This can be done using a Kalman filter algorithm [197]. The tracks are parametrized with a vector $r = (x, y, z, p_x, p_y, p_z, E, s)$, where $s = l/p$ with l the mother particle path length between production point and decay point and p its momentum. The reconstruction of the mother particle is done by adding one by one the parameters of the daughter tracks (they correspond to the measurement points), a procedure which is repeated several times in order to refine the estimation of the mother track parameters.

When a secondary vertex is reconstructed, it is possible to define the pseudo-proper decay length as:

$$x = \overrightarrow{L_{xy}} \cdot \frac{\overrightarrow{p_{Tee}}}{p_{Tee}} \frac{m_{J/\psi}}{p_{Tee}} = L_{xy} \cos(\theta_{xy}) \frac{m_{J/\psi}}{p_{Tee}} . \qquad (5.2)$$

Here, $\overrightarrow{L_{xy}}$ represents the vector between the primary and secondary vertex, projected in the xy plane, while L_{xy} is the norm of this vector, i.e. the distance between both vertices, and θ_{xy} is the angle between the transverse momentum direction of the J/ψ and $\overrightarrow{L_{xy}}$. These quantities are also shown in Fig. 5.3.

If the J/ψ is prompt and thus originated from the primary vertex, L_{xy} is driven only by the resolution of the primary and secondary vertex, and its angle with respect to $\overrightarrow{p_{Tee}}$ can take arbitrary values. If the J/ψ is non-prompt, then the distance between both vertices is higher and corresponds to the flight length of the beauty hadron, convoluted with the resolution. If the decay of the beauty hadron was exclusive, the direction of the momentum of the beauty hadron

would be the same as the direction between primary and secondary vertex, except for detector resolution. In the case of an inclusive decay, the rather small angle between the J/ψ and the beauty hadron (driven by the mass difference between both hadrons and the boost of the beauty hadron) would give a relatively small value of θ_{xy}. The background can contain correlated and uncorrelated sources, and both the electron and positron candidates can either come from the primary vertex or be displaced from this vertex, e.g. when it comes from the semi-leptonic decay of a open charm or beauty hadron. If the electron or the positron is displaced from the vertex, the pseudo-proper decay length x is higher, but the electron and the positron do not come from the same mother particle decay, meaning that there is no strong constraint on the sign of x.

The pseudo-proper decay length distributions are thus quite different for different sources. This is shown in Fig. 5.5, where the prompt and non-prompt J/ψ samples are extracted from MC simulations with injected J/ψ, while the background sample is taken from data as all dielectrons candidates within the invariant mass side bands $2 < m_{ee} < 2.6$ GeV/c^2 and $3.2 < m_{ee} < 4$ GeV/c^2.
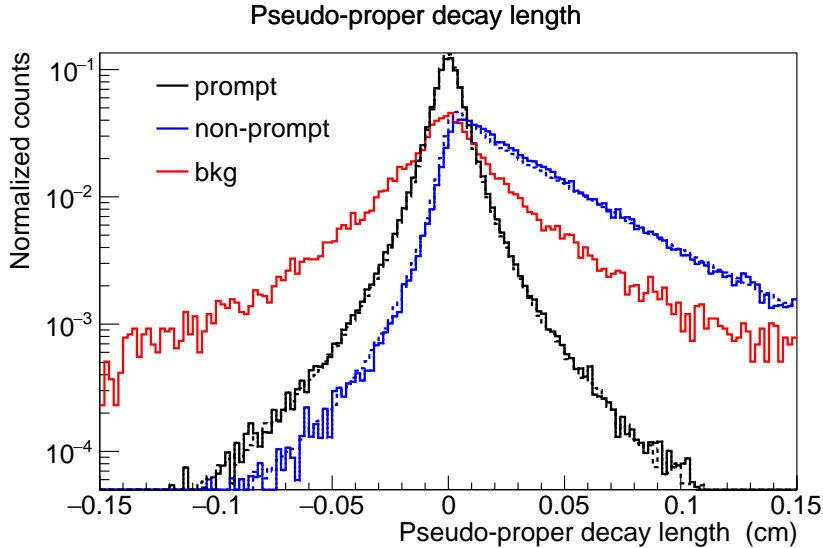
Figure 5.5.: Pseudo-proper decay length distribution for J/ψ candidates for prompt J/ψ, non-prompt J/ψ, and background. All dielectrons have $p_{\mathrm{T}} > 1$ GeV/c.

The pseudo-proper decay length could be used directly in combination with the mass in a two-dimensional likelihood fit to determine the fraction of non-prompt J/ψ, as was done in [80] for example. However, other variables can be used to distinguish between prompt and non-prompt J/ψ, for example the DCA$_{xy}$ of the daughters. Additionally, at high multiplicity, the measurement becomes dominated by combinatorial background. The measurement using a two-dimensional likelihood fit thus becomes very sensitive to the accurate modeling of the pseudo-proper decay time distribution of the background, which needs to be extracted from data because the MC cannot describe the background distributions properly. Hence, a rejection of a larger part of the background could significantly improve the precision of the results.

Therefore, a multivariate analysis, taking into account many variables as well as all their correlations, could improve both the separation between prompt and non-prompt J/ψ and

the background rejection. Machine learning techniques, such as Boosted Decision Trees (BDT) algorithm, could then be a perfect tool for this kind of analysis.

5.3.2. General principle of the Boosted Decision Trees

One of the simplest and most often use of machine learning in high-energy physics is classification with decision trees. When there are two classes to be distinguished (e.g. signal and background), every candidate is assigned a score, which gives the probability for this candidate to be a signal, depending exclusively on the values of few variables for the candidate (e.g. its pseudo-proper decay length).

A decision tree is a set of branches, where each branch represents a condition applied on one of these variables, splitting in two the initial sample. If the condition is realized (e.g. the pseudo-proper decay length is larger than a given value), the candidate follows the first branching towards the next node, otherwise it follows the other branching. Several successive branchings are applied, further splitting the sample. After these successive branchings, a leaf is reached, to which a score is assigned. In the simplest case, the score assigned would be 1 if the leaf corresponds mainly to signal and -1 for mainly background. More complex scores can be chosen, such as the leaf purity ($p = S/(S + B)$). A sketch of a decision tree is shown in Fig. 5.6. Rather than using only a single tree, which is just a succession of few selections on few variables, a forest composed of many different trees gives the possibility to learn more complex correlation patterns between the different variables. The scores of each individual tree are summed, in order to obtain a final score with better classification power than a single tree. It is also possible to give a different weight to each tree. If the classification is done with more than two classes, every class can be assigned its own forest of decision trees, where it is considered signal and all other classes are considered background. For each candidate and for each class, a score is assigned using the forest corresponding to that class, giving the probability for the candidate to correspond to this specific class. The score for the different classes can be rescaled so that their sum is equal to 1.

What makes Boosted Decision Trees relevant as a machine learning algorithm is the ability to determine which variable should make the selection for each branching, at which value of the variable should the samples be split, and what should be the weights and output scores for each tree and leaf. Different algorithms for training exist, with small differences, such as XGBoost [198], or the algorithm implemented in the TMVA package of ROOT [199]. A short description is given for the latter, since it is the training algorithm used for the results presented in this thesis.

The algorithm builds the trees successively. When building a tree, for each splitting, the algorithm must choose which variable and which selection value should be applied. In the ideal case, all signals would follow one branching and all backgrounds would follow the other one, giving a purity $p = 1$ in the signal branch, and $p = 0$ in the other one. In practice, this is not the case. Therefore, a selection criteria needs to be chosen. The value of this criteria would be optimal when the splitting provides a perfect separation between signal and background. In contrast, the least favored case occurs when the signal purity is $p = 0.5$ in either branch and should be
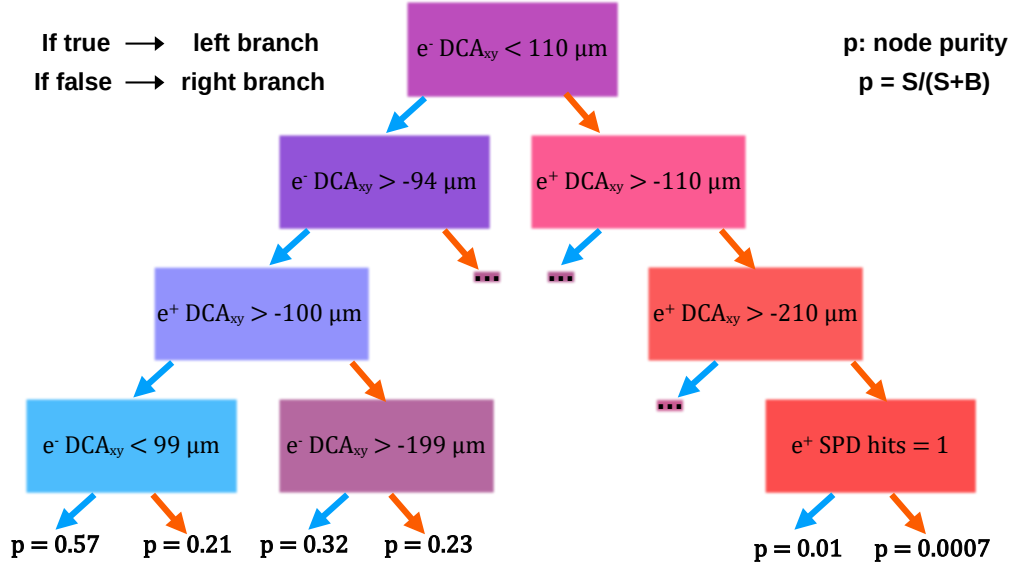
Figure 5.6.: Example of a decision tree of classification between signal (prompt J/ψ) and background (a sample with equal proportion of non-prompt J/ψ and background). For each node and each candidate, if the condition is true, left branching is taken, otherwise right branching is taken. At the end of each branching, the purity of the leaf is given. Nodes with blue shade represent higher signal purity, nodes with red shade represent lower signal purity. Some branchings are not represented to improve visibility.

avoided. An example of separation criteria is the Gini index, $p \cdot (1-p)$, maximal for $p = 0.5$ and minimal for $p = 0$ or $p = 1$, but other functions are possible. Each splitting should improve the current separation index of the whole tree. Therefore, the variable and selection value chosen by the algorithm for a specific splitting optimize the difference between the separation index of the node before splitting and the sum of separation indices for the two nodes after splitting. The splitting algorithm is then iterated until an ending condition is reached. Possible ending conditions are that the node contains either only signal or only background, that the sample size in this node is lower than a defined fraction of the original sample, or that the number of successive splittings reaches a defined number.

If all trees were built with the same initial sample, the optimal choice for the splittings would always be the same, and the separation would not be improved when increasing the number of trees. An improvement of the training can be achieved by boosting. Boosting the trees means that, when building a tree, a common weight is given to the elements which were misclassified in the previous tree, and this weight is higher than the one for correctly classified elements. This weight for misclassified elements, as well as the common weight given to all output scores of this tree, are chosen such that a loss function can be minimized. Different choices of the loss function are possible, with the requirement that this loss function is optimal when, for each training element, the score obtained with the weighted sum of the outputs from all previously built trees reflects the true class to which this element belongs. The minimization is done by choosing both weights in the direction of the steepest-gradient of the loss function.

A problem which can occur when training a machine learning algorithm is overtraining. This occurs when the model learned features which are too specific to the dataset used for the training

and lost generality and prediction power for other independent datasets. This can happen for example when the training sample is too small or when too many trees are built. The problem with overtraining is that the model can become unstable with respect to small discrepancies between the training sample, usually taken from MC simulations, and the sample on which the model is applied, usually real data. In order to avoid overtraining, it is possible to split the initial sample into two independent samples: a training sample, as well as a testing sample. The model can be validated by checking whether its response is different for the two samples. A typical check comes from the Receiver Operating Characteristic (ROC) curve, which shows the background rejection as a function of signal efficiency, when the selection on BDT score is varied. For a specific signal efficiency, a better model would reject more background. Thus, it becomes natural to judge a model overall from the area under its ROC curve (ROC AUC). If the performance of the model is much better for the training sample than for the testing sample, there is likely overtraining. If the performances are similar, the model is probably robust against change of dataset.

The training of the BDT model depends on some general parameters chosen by the user, called hyperparameters. Examples of these hyperparameters in the TMVA framework are:

- NTrees: the total number of trees built. A higher number causes a longer training, hence a potentially lower error in the loss function, but also a higher probability of overtraining.

- GradBaggingFraction: in order to limit overtraining, only a fraction of the training sample, determined via this parameter, is used when building each decision tree.

- Shrinkage: the learning rate of the algorithm, related to the weight given to the trees when optimizing the loss function through gradient descent. Smaller values result in a slower training, which should be compensated with a higher number of trees. Smaller values also cause less sensitivity to overtraining.

- MaxDepth: the highest number of consecutive node splittings allowed. A value which is too high (a limit could be around 4 according to Ref. [199]) will increase the probability that there is overtraining.

- nCuts: this parameter determines how many selection values are tested for the splitting of a node, when the splitting variable and selection value is chosen.

These hyperparameters must be chosen carefully in order to optimize the performance of the model. The simplest way to choose them is by performing a grid search on all parameters, and taking the combination which returns the highest ROC AUC. However, this technique might be computing-intensive when there are many hyperparameters to optimize. Therefore, advanced methods for hyperparameter optimization are required, an example being bayesian optimization [200]. A bayesian optimization algorithm finds the point (in this case, the set of hyperparameters) which maximizes the response of a complex function (in this case, the response of the function is the ROC AUC after training of the model) in an iterative way. At each iteration, using information on the values of the function for all previous iterations, the algorithm determines at which point the function would need to be evaluated next. This choice is made in order to maximize the gain of information on the location of the point with maximal performance. This

can be done, for example, by testing a region where no previous point was tested, or making more tests in a region where the performance is already high.

5.3.3. BDT training samples and variables

The BDT are used to classify the J/ψ candidates between three classes: prompt J/ψ, non-prompt J/ψ and background. The training samples for prompt and non-prompt J/ψ are taken from MC simulations, with J/ψ signals injected on top of minimum-bias events. The training sample for the background uses J/ψ candidates in the data sample, but outside from the mass peak region ($2 < m_{ee} < 2.6$ GeV/c^2 and $3.2 < m_{ee} < 4$ GeV/c^2). Due to a biased p_{T} distribution caused by the trigger threshold, an independent BDT is trained for the TRD triggered sample, while the same BDT model is applied to MB- and HM-triggered samples. In the following, unless stated otherwise, the different figures shown use this latter model. In order to have similar classification performance for all three classes, all three training samples have similar size. An exception is done when the analysis is repeated at high p_{T} (J/ψ $p_{\mathrm{T}} > 4$ GeV/c or higher) or with the TRD trigger. In these specific cases, the combinatorial background during signal extraction is low, which means that improving background rejection is not necessary. Therefore, a larger sample size is used for prompt and non-prompt J/ψ than for background, to improve specific separation power between prompt and non-prompt J/ψ. In all cases, the part of the sample which is not used in the training is assigned as testing sample.

The choice of the training variables is important. Only variables which are different enough in the three samples and allow a better discrimination power, either directly or through the correlations with other variables, should be selected. Additionally, one should make sure that the variables used are well reproduced in the MC sample, otherwise the distribution of the output scores of the BDT for the signals might differ in the MC compared to reality. If the variables are not correctly described in the training samples, the BDT model might learn and use discrepancies between MC and data for classification, rather than true differences between a prompt J/ψ, a non-prompt J/ψ or a background in real data. Quantities highly correlated with mass should also be avoided since they could bias the mass templates necessary for extracting the signal.

The training variables used in this analysis are

- the pair pseudo-proper decay length (defined in Eq. 5.2)

- DCA$_{xy}$ for electron and positron

- TPC $n\sigma_{el}$ for electron and positron

- SPD hits for electron positron (this variable is set to 3 when there are hits on both SPD layers, 2 when there is only a hit in the first layer of the SPD, and 1 when only in the second SPD layer)

These variables combine the displacement from the primary vertex for single tracks (DCA$_{xy}$) and for the reconstructed secondary vertex (pseudo-proper decay length) with TPC $n\sigma$ in order to reduce the amount of misidentified particles in the background. SPD hits information is useful because the DCA resolution (and then secondary vertexing) is better when tracks have a hit in

the first SPD layer, compared to the case the first hit is in the second SPD layer. It can also help rejecting electrons from photon conversions, for which the first detector hit might occur later, depending on the conversion point.

The distribution of these variables for the 3 classes and in data (for both $2 < m_{ee} < 4$ GeV/c^2, and $2.92 < m_{ee} < 3.16$ GeV/c^2, the latter having a higher signal fraction) are shown in Fig. 5.7. For most of the variables, their distribution in data is close to a weighted average of the distribution in the three classes, with a higher signal fraction for $2.92 < m_{ee} < 3.16$ GeV/c^2. This indicates a good reproduction in data of the chosen variables, although small discrepancies might still be present.
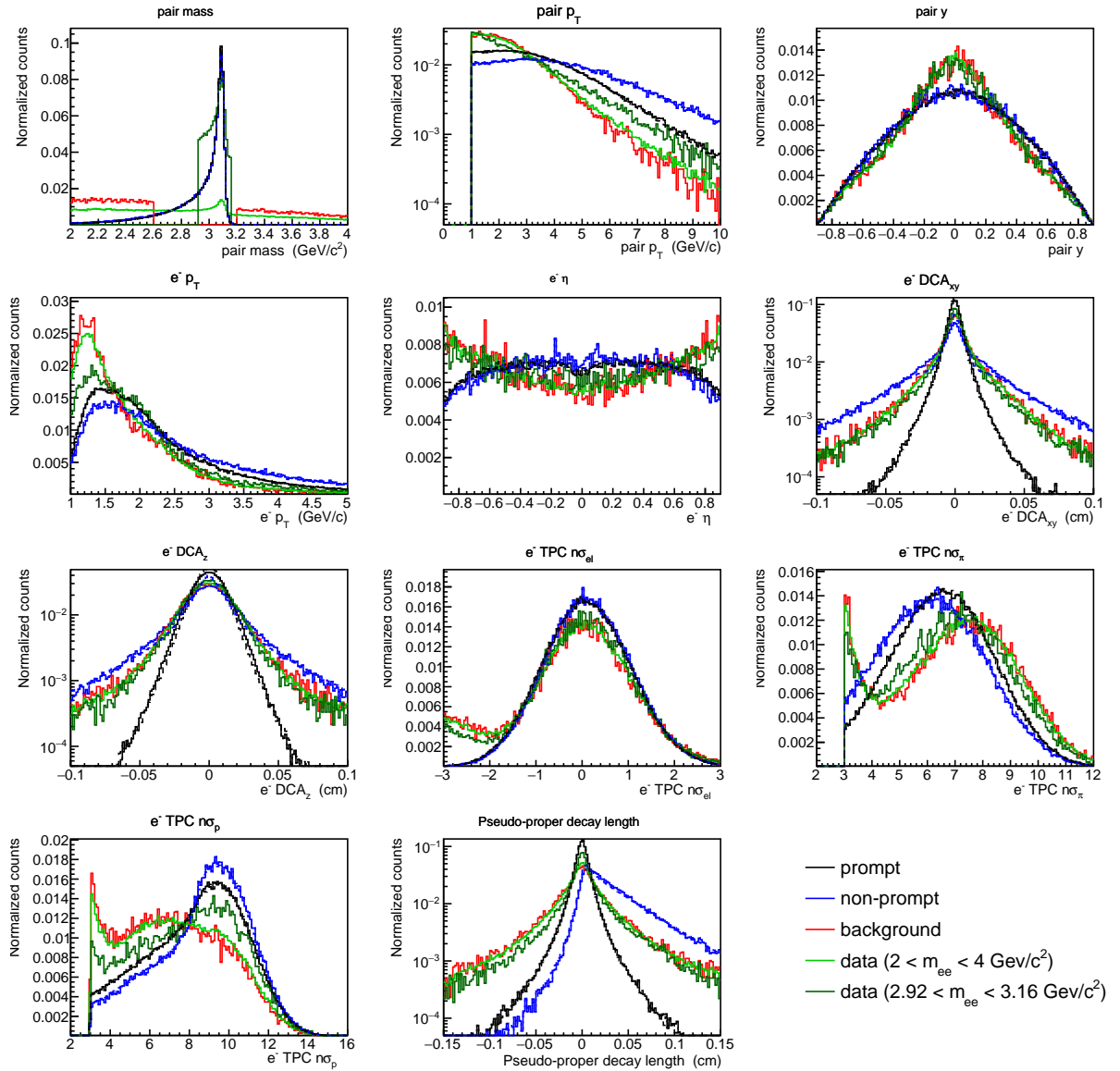
Figure 5.7.: Distribution of several variables in prompt, non-prompt and background sample and for data candidates within $2 < m_{ee} < 4$ GeV/c^2 and $2.92 < m_{ee} < 3.16$ GeV/c^2. From top left to bottom right: pair invariant mass, pair p_T, pair rapidity, electron p_T, electron η, electron DCA$_{xy}$, electron DCA$_z$, electron TPC nσ_{el}, electron TPC nσ_π, electron TPC nσ_p, electron SPD hits.

In addition, the correlations between the variables used for training are shown for the three classes in Fig. 5.8. They also look different for the three classes, increasing the separation power between classes. An example is the correlation between DCA_{xy} for the electron and the positron are which are anticorrelated only for the non-prompt sample: when one has a positive DCA, the other one often has a negative DCA, as has been shown in Fig. 5.3, while for prompt J/ψ only the resolution matters which acts on the sign of the DCA randomly. In contrast, the correlation coefficient between pseudo-proper decay length and DCA_{xy} is almost zero in the non-prompt class. It could be explained by the fact that, even if its absolute value is high in both cases, the DCA is either positive or negative, while the pseudo-proper decay length is almost always positive.
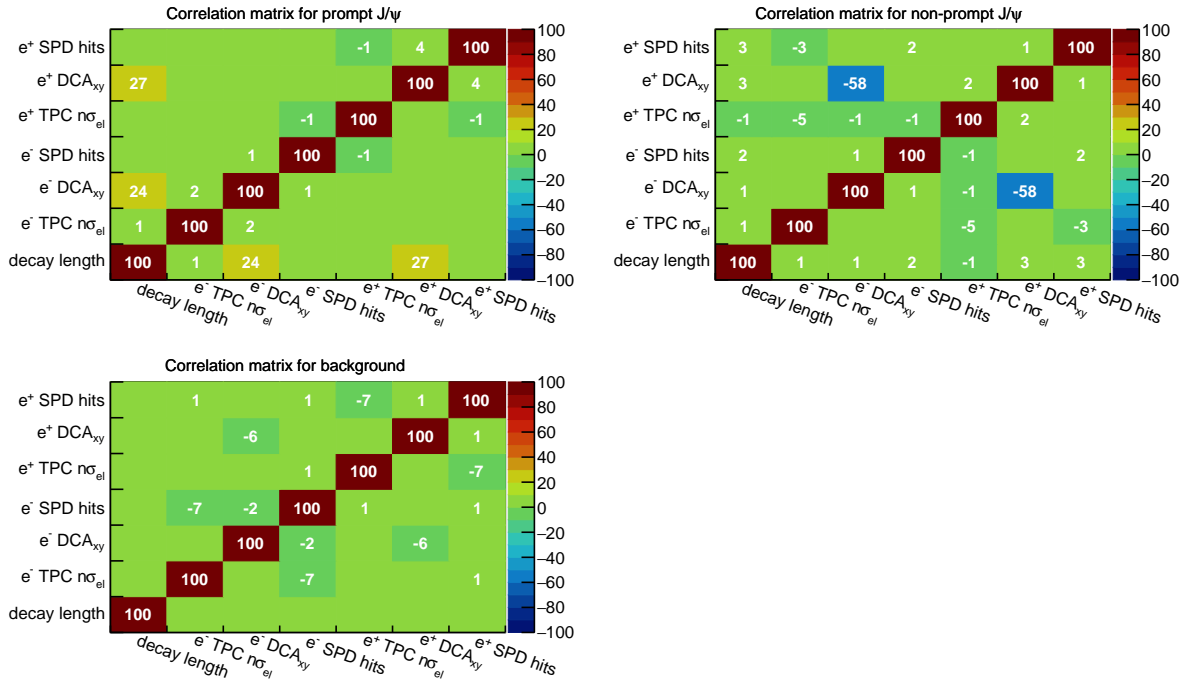
Figure 5.8.: Correlation coefficient (in %) between training variables for prompt J/ψ (top left), non-prompt J/ψ (top right) and background (bottom) classes.

The hyperparameters were chosen using the bayesian optimization framework described in [200], optimizing the average of the six possible ROC AUC. Indeed, in the testing sample, the ROC curve can be built by taking any class as signal and any of the two other classes as background. The number of steps in the optimization is kept low, because few iterations already give good performance. It is also possible that further optimization would only improve the performance on this specific MC sample, without improving the performance when applied to a different sample. The model would therefore be overoptimized, with increased instability with respect to the sample on which it is applied. This results in values of nTrees = 1430, shrinkage = 0.18, GradBaggingFraction = 0.5, maxDepth = 4, nCuts = 100. After optimization, the obtained ROC AUC for the testing sample is 0.8258, while for the training sample (a higher value represent a higher probability of overtraining) it is 0.8724.

The variables can be ranked according to how important they are for separation between classes. This is done through an importance score counting how much each variable is used in the decision

trees, weighted by the gain in separation between different classes they bring. The sum of all scores is scaled to 1. The most important variable is TPC $n\sigma_{el}$ (importance score is 0.241 and 0.240 for the two daughters, the difference between the two could be due to a statistical uncertainty), followed by DCA (importance score is 0.134 and 0.128 for the two daughters), pseudo-proper decay length (0.098) and SPD hits (0.082 and 0.077).

For each pair candidate, the BDT outputs one value per class, representing the probability for the candidate to belong to this class. The distribution of these three BDT scores for the test sample of each of the three classes and for data is presented in Fig. 5.9. The algorithm performs well: in the test samples, the BDT output score for the class to which the candidate belongs is rather high, whereas the BDT output score for the other classes is rather low.
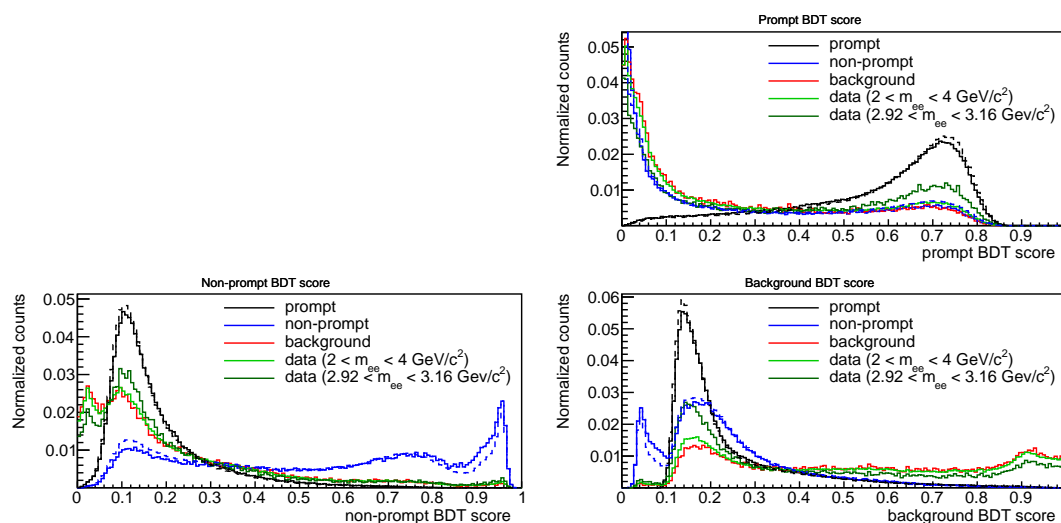
Figure 5.9.: BDT output score for data and three classes prompt J/ψ, non-prompt J/ψ and background, evaluated on the testing sample. Top right: prompt J/ψ score. Bottom left: non-prompt J/ψ score. Bottom right: background score. Dashed lines represents the same distribution for low multiplicity only ($N_{\text{tracks}} < 4$).

However, the distributions do not peak at 0 and 1: it is unlikely that the category is known for certain, because a part of the candidates from different classes might be similar. For example, the background from prompt electrons or the non-prompt J/ψ decaying very fast are difficult to distinguish from prompt J/ψ. Hence, a signal with high prompt probability is not with 100% confidence a prompt J/ψ, explaining the peak at 0.7 only in the prompt BDT score. This can also be observed, to a certain extent, in the sketch in Fig. 5.6, where the purity for prompt J/ψ is only 0.57 at maximum. In contrast, vertices with a large displacement with respect to the primary vertex give a high confidence that the J/ψ is non-prompt, explaining the peak at 0.95 in non-prompt BDT score for non-prompt signals. For non-prompt BDT score, the background peaks at 0, possibly due to high confidence that there is a misidentified pion and proton. Another peak around 0.1 possibly contains well-identified prompt electrons.

From the distribution of BDT scores, it is possible to determine the efficiency of a BDT selection. In the following, this efficiency is defined as the fraction of signals remaining when selecting only candidates with, respectively, a prompt BDT score smaller than a given value, a non-prompt BDT score higher than a given value, or a background BDT score smaller than a given value.

5.3.4. Background rejection

After each candidate in the data sample has been assigned a score for each of the three classes, and before separating the prompt from the non-prompt J/ψ, the scores can be used in order to reject more background. The background rejection is done via a selection on the background BDT score, rejecting all candidates with a background score higher than a certain value. This selection allows to improve both signal over background ratio and significance.
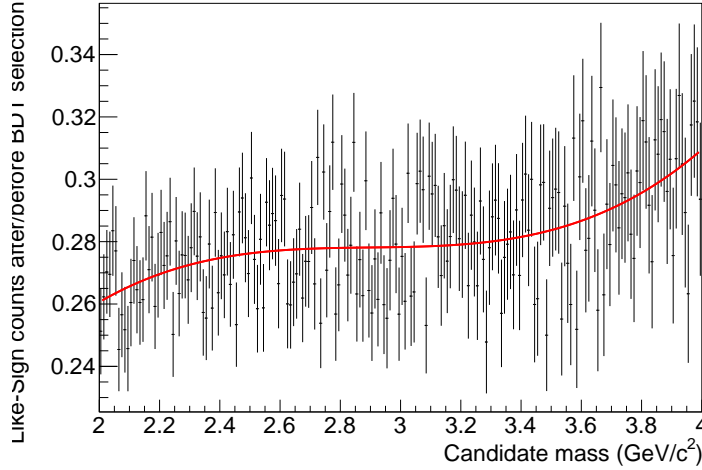

Figure 5.10.: Ratio between the number of like-sign pairs with $p_\mathrm{T} > 1$ GeV/c in the HM sample after a BDT selection at 0.4 in background score and the number before this selection, fitted with a third-order polynomial.

An important check to do when training a BDT is to check that the BDT scores are not correlated with the pair invariant mass. Indeed, if such correlation was present, the mass templates for signal and background would be modified. It would be possible that the background creates an artificial peak when a selection on the BDT score is applied. Such correlation with the mass can for example happen through correlations with the kinematic variables such as the transverse momentum. The signal template should be reproduced in the MC when using the same selection. For the correlated background, it can still be modeled by the second-order polynomial fit function with free parameters. Regarding the combinatorial background, it is not possible to assign a score for each candidate in mixed events. Therefore, the modification in mass templates is checked with like-sign pairs. The ratio between the number of like-sign pairs before and after a selection in the background score at 0.4, in the HM sample, is shown in Fig. 5.10. The modification in the mass template is small, showing that there is only little correlation with the mass. It is fitted with a third-order polynomial, and this correction is applied to the event-mixing shape when doing selection on BDT score.

The selection on background BDT score is varied in every multiplicity interval, in order to obtain a better significance. Few examples for several multiplicity bins ($10 \leq N_\mathrm{tracks} < 15$, $26 \leq N_\mathrm{tracks} < 32$ and $N_\mathrm{tracks} \geq 54$) of the signal extraction with different selections on the background score (no selection, or selection at 0.4) are shown in Fig. 5.11. It can be observed that the impact of the BDT on the signal significance through background rejection is larger at higher multiplicity, as is expected due to the larger combinatorial background. More examples of
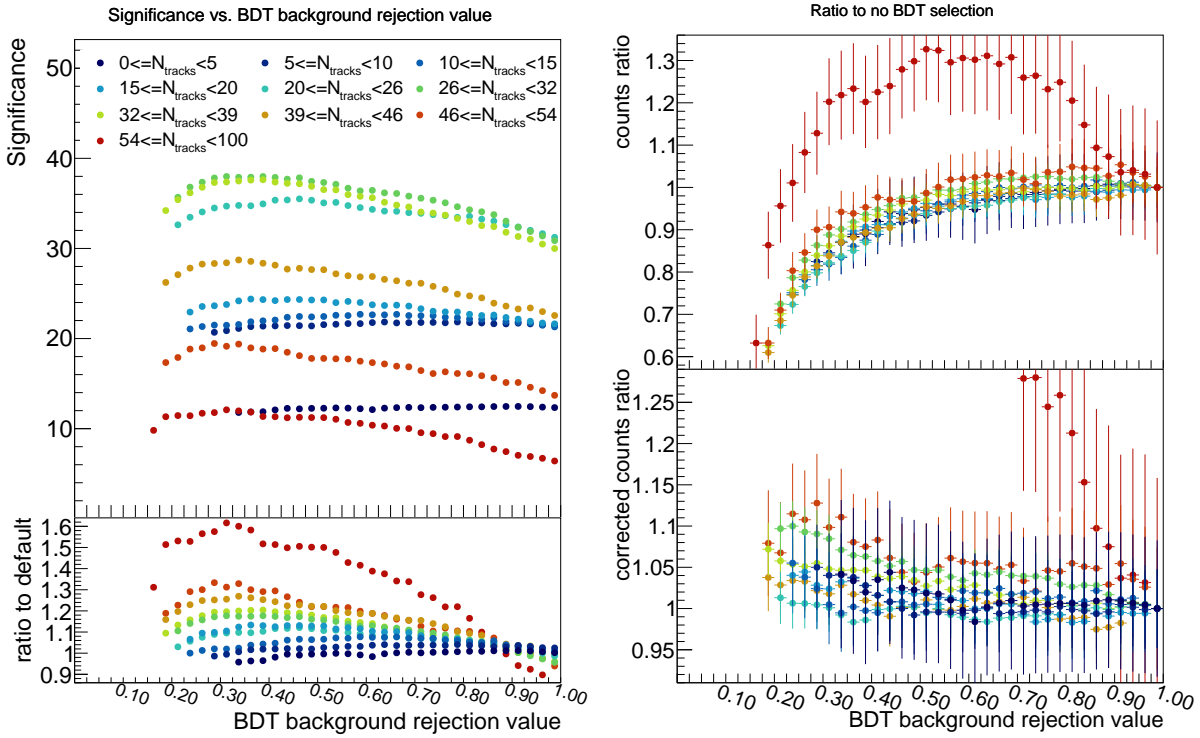
the signal extraction in several multiplicity intervals, including when the multiplicity is calculated in regions of the azimuthal angle, and for the three triggered samples are shown in Appendix A.
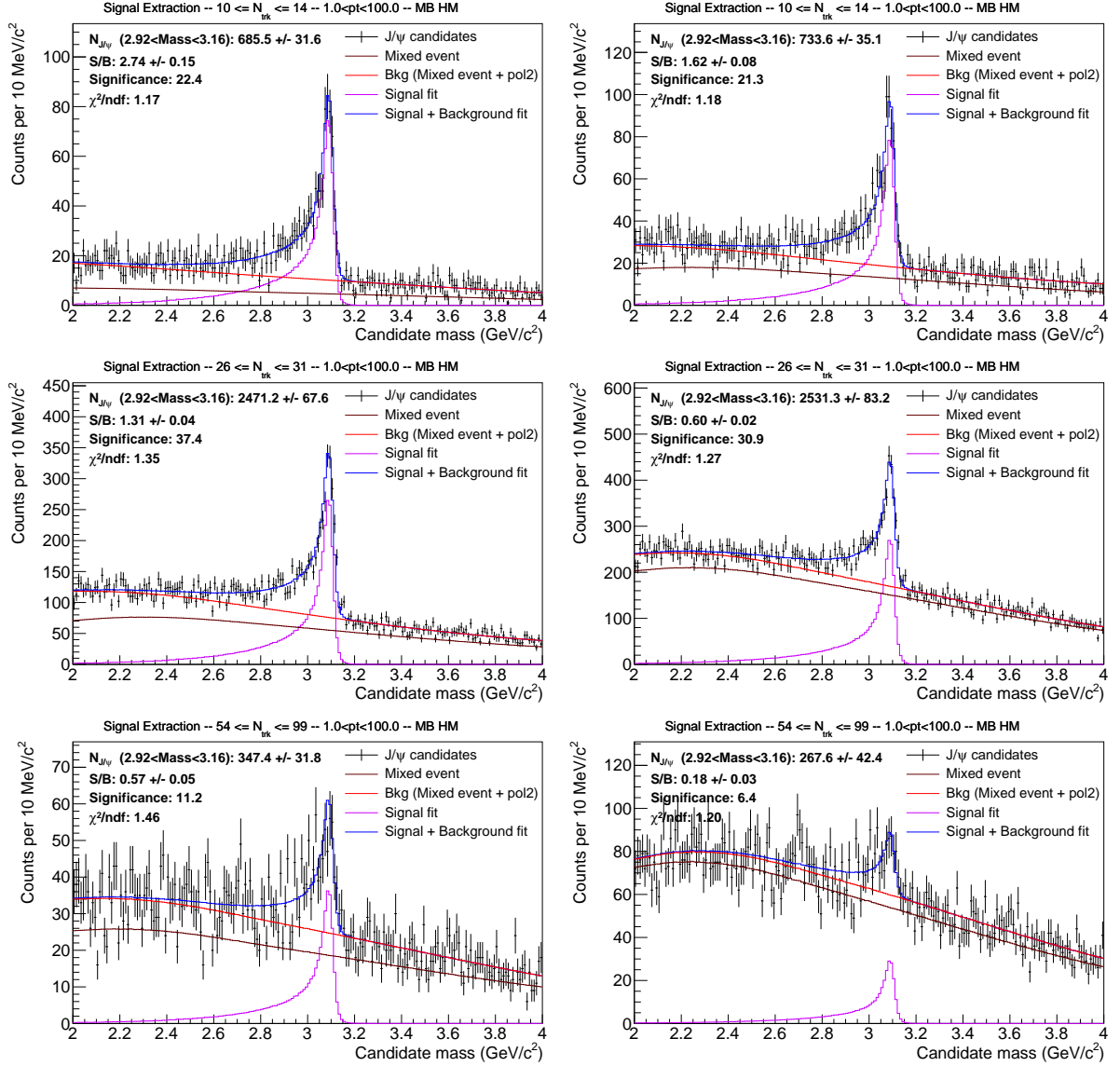
Figure 5.11.: Signal extraction for $p_T > 1$ GeV/c with a BDT selection on the background score at 0.5 (left) and no BDT selection (right), for $10 \leq N_{\text{tracks}} < 15$ (top row), $26 \leq N_{\text{tracks}} < 32$ (middle row) and $N_{\text{tracks}} \geq 54$ (third row), using MB and HM triggers together.

In the left panel of Fig. 5.12, the significance is shown as a function of the BDT selection for several multiplicity intervals. In this figure, MB and HM triggers are merged together. The significance increases with a tighter BDT selection. This increase gets stronger with a higher multiplicity, which is expected because of the larger background which can be rejected. For the lowest multiplicities, where the background is low, a rejection of the background is not really necessary, and the BDT does not significantly improve the significance. In contrast, at the highest multiplicities, the improvement in the significance caused by the background rejection is much better. The bottom left panel shows the ratio between the significance obtained after applying background rejection with the BDT and the significance with a default selection which does not use the BDT. For the default selection, the PID hadron rejection is done with tighter selection

of TPC $n\sigma_\pi > 3.5$ and TPC $n\sigma_p > 3.5$. At the highest multiplicity, the significance with a BDT selection reaches up to 1.6 times the default significance.

Figure 5.12.: Top left: J/ψ signal significance in several multiplicity intervals when the BDT background rejection value is varied. The J/ψ candidates have $p_T > 1$ GeV/c and are selected with MB and HM triggers. Bottom left: ratio between significance with BDT selection and default significance which does not use BDT selection. Top right: ratio between number of signal counts after BDT selection to before BDT selection. Bottom right: ratio between number of signal counts after BDT selection, corrected from the efficiency of the BDT selection, to the number of counts before BDT selection.

The results with the number of signal counts obtained as a function of rejection value, normalized to the number of counts without any BDT selection is shown in the top right panel of Fig. 5.12. As expected, the number of counts always decreases with a tighter cut. The only exception is the highest multiplicity interval where a selection at 0.9 gives more counts than no BDT selection. This is assumed to be due to a better signal extraction when more background is rejected. The estimation of the J/ψ counts is probably more accurate with this selection, if the signal is underestimated when a large background is present.

Applying a BDT selection still removes a fraction of the signal, so a correction for the efficiency of the BDT selection is needed. The efficiency of this selection is extracted in the testing sample of the prompt and non-prompt J/ψ BDT classes. Since the efficiencies as a function of background selection are slightly different for prompt and non-prompt J/ψ, the fraction of non-prompt J/ψ in the sample, f_B, is needed for this step. The next section explains how to extract f_B. The bottom right panel of Fig. 5.12 shows the ratio between the number of counts with BDT selection, corrected by the efficiency of the BDT, and the number of counts without BDT selection. When the efficiency of the BDT is corrected, the results should not, within uncertainties, depend anymore on the selection value. If a significant dependence on the selection value was observed, it would mean that the efficiency extracted from the MC sample does not really reproduce the

one in data. But the constant value within uncertainties as a function of the BDT selection indicate a good description of the BDT efficiency, at least for selection values higher than ≈ 0.3. The BDT selection value would in any case not be smaller than 0.3, because of the large efficiency and significance loss beyond this value. The only exception to a constant value of J/ψ counts after efficiency correction occurs in the highest multiplicity interval. However, it is assumed that the discrepancy for this interval is due to a better signal extraction, rather than a wrong description of the BDT score distribution. Indeed, a wrong description would also be observed in the other multiplicity intervals, which is not the case there.

The background BDT rejection value which is chosen for the following results is the one giving the maximum expected significance. The expected significance is not exactly the same as the signal significance during signal extraction, which is likely to be affected by upward or downward fluctuations on the number of counts. A choice using the maximal significance could just select this upward fluctuation. In contrast, the expected significance for a given selection on the BDT background score is not affected by statistical fluctuations, and is defined as:

$$\varepsilon_{BDT} \times S_{\text{noSel}}/\sqrt{S+B}\,. \tag{5.3}$$

$S+B$ is the number of pair candidates in the signal rejection with the chosen BDT selection, ε_{BDT} is the efficiency of the BDT selection and S_{noSel} is the number of signal counts without BDT selection. It is also required that the BDT efficiency with this BDT selection should not be smaller than 85%. Indeed, a too strong selection would lead to too few signal counts, while the separation between prompt and non-prompt J/ψ, explained in next section, still needs enough signals for a correct extraction of non-prompt signals. The chosen BDT rejection value fulfills this requirement, while keeping the best expected significance.

5.3.5. Prompt vs non-prompt separation

Although it is not possible to determine directly for each candidate whether it is prompt or not, the number of prompt and non-prompt J/ψ in the different samples can be extracted on a statistical basis. The idea for the separation between prompt and non-prompt signals also relies on doing several selections on the BDT score. In this case, candidates with a low non-prompt score are rejected. Tighter selections allow to progressively increase the purity of non-prompt J/ψ. For each selection value, the number of inclusive J/ψ counts is extracted from a fit on the invariant mass. This cut variation method has been used in Ref. [201], for example. The efficiency of each one of these selection for prompt and non-prompt J/ψ is known from the BDT testing sample. Thus, the extraction procedure will consist in finding the total number of prompt and non-prompt counts in the original sample which gives the best agreement between the expected and the measured number of J/ψ, for all the different selections. It is also important to take into account the fact that the number of J/ψ counts with different selection values are correlated.

Finding the best fit is equivalent to find N_p and N_{np} which minimize the χ^2 in the matrix equation:

$$\chi^2 = \delta^{\mathbf{T}} \mathbf{C}^{-1} \delta \,. \tag{5.4}$$

Here, δ represents the vector of the residuals, i.e., for the i-th selection on non-prompt score:

$$\delta_i = \varepsilon_i^p N_p + \varepsilon_i^{np} N_{np} - Y_i \,. \tag{5.5}$$

N_p and N_{np} are respectively the number of prompt and non-prompt J/ψ in the original sample without any BDT selections, ε_i^p and ε_i^{np} are the efficiencies of the BDT selection for prompt and non-prompt J/ψ respectively, considering both the background rejection and the i-th selection on non-prompt score. Y_i is the raw number of signal counts, extracted from an invariant mass fit applying these BDT selections. N_p and N_{np} are the unknown values, which should be extracted from the fit.

C is the covariance matrix between the number of counts with different BDT selection values. The statistical uncertainties of the MC templates are neglected. Because selections are progressively tighter and tighter and all signals for a given selection are also included in the samples with looser selections, the covariance term can be written, when i is a tighter selection than j, as:

$$C_{i,j,i\geq j} = \sigma_i^2 \,. \tag{5.6}$$

σ_i is the statistical uncertainty of Y_i, the number of raw J/ψ counts after selection i.

The minimization of χ^2 leads to:

$$\mathbf{N} = \mathbf{cov}(\mathbf{N}) \varepsilon^{\mathbf{T}} \mathbf{C}^{-1} \mathbf{Y} \tag{5.7}$$

with

$$\mathbf{cov}(\mathbf{N}) = (\varepsilon^{\mathbf{T}} \mathbf{C}^{-1} \varepsilon)^{-1} \,. \tag{5.8}$$

N is the vector of two elements containing the number of prompt and non-prompt counts in the original sample $N = (N_p \; N_{np})^T$. $\mathbf{cov}(\mathbf{N})$ is its covariance matrix, which contains the squared statistical uncertainties in the diagonal and the covariance between the number of prompt and non-prompt J/ψ in the off-diagonal terms. ε is the matrix which contains, for all the BDT selections i, ε_i^p in its first column, and ε_i^{np} in its second column.

The default number of selections is 20, going from 0 to 0.95, with an equal spacing of 0.05 between two selections. Selections giving a signal significance lower than 2 are removed. In addition, BDT selections with a very similar efficiency might lead to problems when calculating matrix inversion. Therefore, when two consecutive selections have very similar number of signal counts or variances, the second one is removed.

A fit example for the integrated MB sample, as well as for $39 \leq N_{\text{tracks}} < 46$, using HM trigger, is shown in Fig. 5.13 for illustration. The number of raw counts is shown as a function of the BDT selection value, and compared with the expected number of J/ψ counts from the fit. The latter reproduces quite well the raw number extracted from invariant mass fit. This shows the accuracy of the extraction of the number of prompt and non-prompt J/ψ, and excludes the possibility of a strong mismodeling of the prompt and non-prompt templates. The estimated fraction of non-prompt J/ψ in the MB sample is also very close to the one published in Ref.[80], using the same statistical sample, but with a different method. This validates the correct use of BDT for extracting the yields of prompt and non-prompt J/ψ.
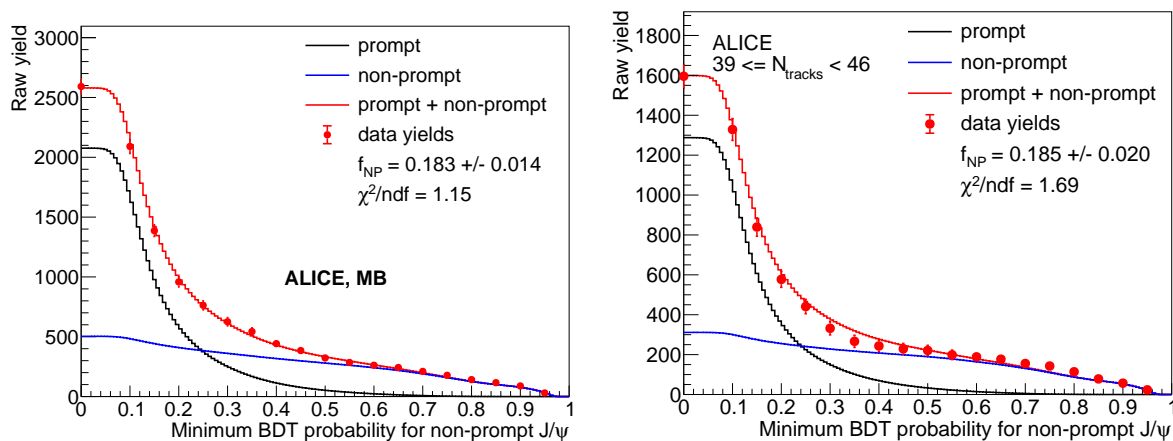
Figure 5.13.: Number of signal counts as a function of the selection value, and extraction of the number of prompt and non-prompt signals, for the MB sample (left), as well as the interval $39 \leq N_{\text{tracks}} < 46$, in the HM sample (right).

The templates of efficiencies for prompt and non-prompt J/ψ as a function of the BDT selection value are very important for obtaining the correct number of prompt and non-prompt J/ψ in the sample. Therefore, these MC templates should be corrected as much as possible in order to better reproduce what is expected from data. In addition, once the number of prompt and non-prompt J/ψ in the reconstructed sample is known, it is also necessary to correct for reconstruction efficiency in order to obtain the fully-corrected J/ψ yield. All these corrections will be presented in the next section.

5.4. Efficiency corrections

5.4.1. Acceptance and reconstruction efficiency

Due to all the selections applied for the electrons (kinematic selections, tracking, PID selections) and the pair invariant mass constraint, only a part of all the J/ψ mesons in the selected events is reconstructed. The acceptance and efficiency of these selections is estimated using the MC sample with injected J/ψ. In this case, the efficiency is independent of the rest of the event: no dependence on multiplicity is found [202], while the p_{T}-dependent efficiency is shown in Fig. 5.14.
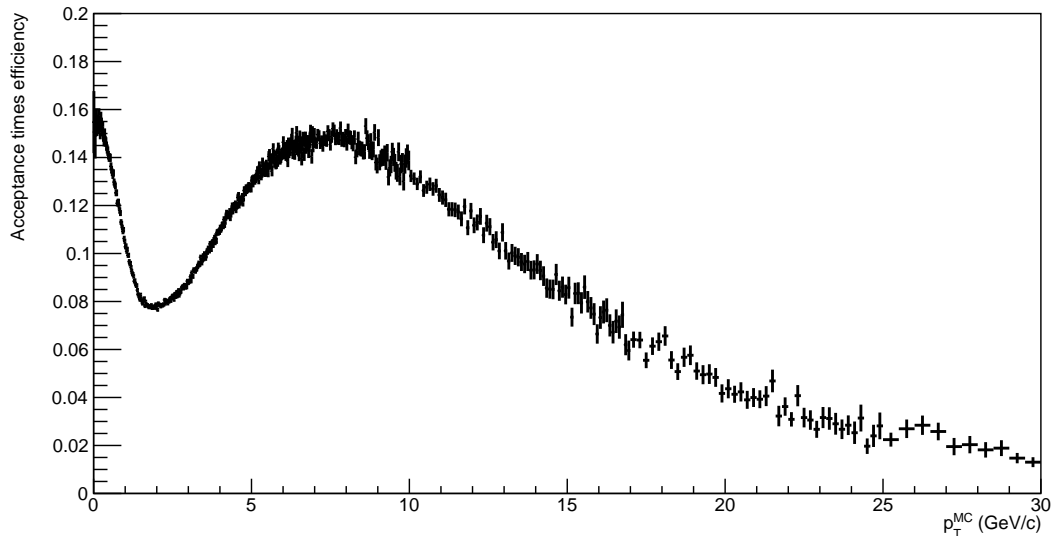
Figure 5.14.: Acceptance times efficiency of J/ψ reconstruction as a function of J/ψ transverse momentum.

If the multiplicity dependence was negligible, most of the acceptance-efficiency effect would cancel when normalizing quantities by their average in minimum-bias events. However, it should be noted that the p_T distribution, and thus the total acceptance-efficiency, may vary between different multiplicity intervals. This effect is not possible to see directly in the MC when the J/ψ mesons are added on top of minimum-bias events regardless of the event multiplicity. The variation of the p_T distribution with multiplicity is analyzed in Sec. 5.4.3.

In order to correct the p_T-integrated number of counts for acceptance and reconstruction efficiency from the p_T-dependent efficiency, two methods are possible. The first one is to take the p_T-integrated acceptance and efficiency in the MC, where the MC might be weighted in order to reproduce better the p_T distribution in data. The second method is to weight every J/ψ candidate in data by $1/\varepsilon(p_\mathrm{T})$. This method has the advantage that it does not rely on any assumption of p_T dependence of J/ψ production. However, a part of the signals is also lost when doing a selection on the BDT score. Since the BDT selection is applied after reconstruction requirements, the candidates should first be weighted by BDT selection efficiency before being corrected for reconstruction efficiency. Indeed, it is not possible to know if signals with a different BDT score would have a different reconstruction efficiency, because the BDT score is applied only to reconstructed candidates. It might be possible to correct for the efficiency for selection on background score for each candidate, since this efficiency is only slightly different between prompt and non-prompt J/ψ at a given p_T. However, the efficiency for the selection on the BDT non-prompt score cannot be corrected for on a candidate-by-candidate basis, because the whole method relies on the fact that the efficiencies are different for prompt and non-prompt J/ψ. For this reason, there is no candidate-by-candidate weighting in data, and the acceptance and efficiency corrections are taken from p_T-integrated MC.

5.4.2. TRD trigger efficiency

For the TRD sample, it is also important to correct for the efficiency of the trigger, which is strongly p_T-dependent because of the threshold at 2 GeV/c on the electron online-computed p_T.

An event with a J/ψ can be either triggered by the J/ψ daughters (called in the following self-trigger), or by any other track (called in the following Underlying Event (UE)).

UE efficiency:

The UE efficiency depends on the number of tracks in the event. Unbiased events are used in order to estimate the probability for any sample of N tracks to fire the trigger. For every event containing a J/ψ candidate, the UE efficiency is then determined by considering this probability, for the sample containing all tracks in the event except the daughters of the J/ψ candidate. For a given run i, the N_tracks-dependent efficiency is estimated as the number of events in the MB sample also passing TRD electron trigger requirements (this case is written $MB\&TRD$), divided by the total number of events in the MB sample:

$$\varepsilon_\text{UE, i}(N_\text{tracks}) = \frac{N_\text{MB\&TRD, i}(N_\text{tracks})}{N_\text{MB, i}(N_\text{tracks})}\,.\tag{5.9}$$

The efficiency is run-dependent because variations of the TRD gas gain and magnetic field can modify the trigger efficiency. In addition, if the TRD goes to an error state in the middle of a run, TRD triggers are not provided anymore, resulting in a lower trigger efficiency for this run. Then the total efficiency is obtained as a weighted mean of all runs, the weight being the number of TRD-triggered events considered for analysis:

$$1/\varepsilon_\text{UE}(N_\text{tracks}) = \sum_i \frac{N_\text{TRD, i}}{N_\text{TRD}} \times 1/\varepsilon_\text{UE, i}(N_\text{tracks})\,.\tag{5.10}$$

Here, the weights are applied to the inverse of the efficiency, which is necessary when combining efficiencies of two samples and using as weight the number of events after selection. The UE efficiency is shown in Fig. 5.15. As expected, it increases as a function of the multiplicity.

It is also possible that, at a given number of tracks, an event with a J/ψ behaves differently than an unbiased event, biasing the probability to find a J/ψ triggered by UE. A check has been done using a standalone PYTHIA simulation (i.e. without detector simulation). The TRD self-trigger efficiency is taken for electrons and positrons from data (as described later in this section), and a trigger is fired with this probability. For each J/ψ, it is known whether the event was triggered or not, and, in the case it was triggered, if it was triggered by one of its daughters or by the rest of the event.

The underlying event trigger efficiencies as a function of p_T are shown in Fig. 5.16 for prompt and non-prompt J/ψ. It can be observed that the UE efficiency is higher for non-prompt J/ψ compared to prompt J/ψ: this is due to the case when the event containing the J/ψ is triggered by an electron coming from the other b quark in the $b\bar{b}$ pair. This is weakly dependent on p_T,
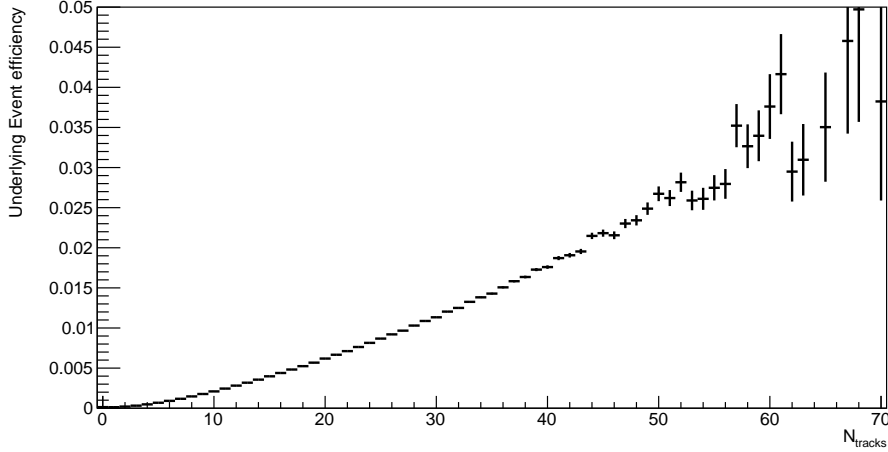
Figure 5.15.: TRD trigger UE efficiency as a function of N_{tracks}.

the small increase at high p_{T} could be due to the fact that high-p_{T} J/ψ are found more often in high-multiplicity events. This true UE efficiency value obtained is also compared with an estimation done using the same method as in data. This estimation considers the multiplicity dependence of J/ψ as well as the event UE efficiency as a function of multiplicity, both taken from PYTHIA. For prompt J/ψ, the agreement is within 15%. For non-prompt J/ψ, the correlation in the electrons from $b\bar{b}$ is assumed to be reproduced well enough, and to have negligible bias from the absence of detector effects, conversion of photons in the detector material, or triggers from pion contamination. Consequently, a constant value of 0.24% is added to the UE trigger efficiency in order to take into account the possible semi-leptonic decay for the other b quark.
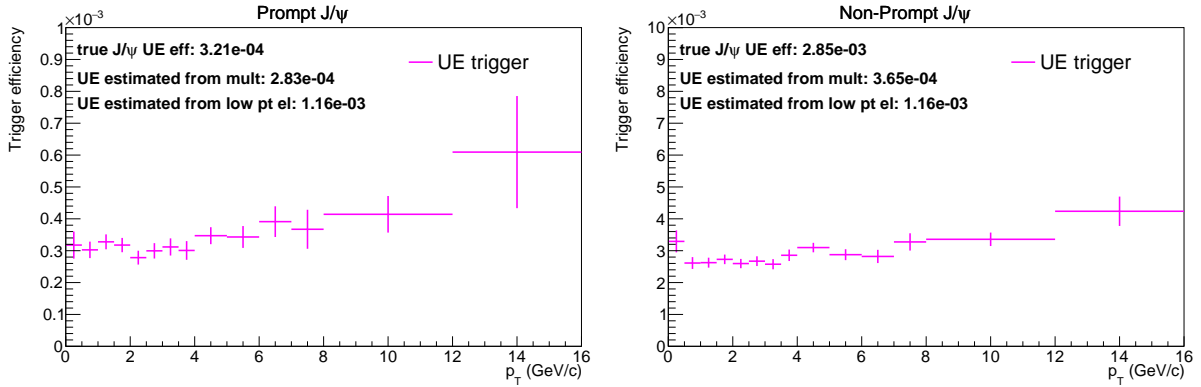
Figure 5.16.: TRD trigger UE efficiency from PYTHIA for prompt (left) and non-prompt (right) J/ψ. Note the different y axis values.

Self-trigger efficiency:

The self-trigger efficiency can be directly computed from the TRD trigger efficiency of electrons and positrons in a data-driven way. This single-leg efficiency is determined by studying electrons in MB events which also fulfill the TRD trigger conditions.

The electron and positron samples are created with selections similar to the ones for J/ψ daughter candidate selections. In addition, in order to increase purity, PID requirements are tightened. The TPC $n\sigma_{el}$ is taken between 0 and +3, the TPC $n\sigma_{\pi}$ is taken higher than 3. For $p_{\text{T}} < 1.4$

GeV/c, proton rejection is not done through TPC, but via the TOF with requiring TOF $n\sigma_{el}$ between -3 and +3. No proton rejection is done at higher p_{T}.

The trigger efficiency is calculated by taking the ratio of the electrons in the MB sample passing the TRD requirements to the total number of electrons in the MB sample. If the event passes the TRD requirements, all candidate electrons within this event are counted, without any attempt to find the exact track which fired the trigger. This is because finding this track would require that the ITS-TPC tracks are correctly matched to the TRD. However, a match is not always found, and, even when a probable matching is found, the matching is not always correct. It is also necessary to take into account change of data taking conditions, and this is done via a weighting of the run-dependent efficiencies. This weighting is applied the same way as in the event efficiency, in order to remain consistent in the estimation of efficiencies. The efficiency can thus be computed as:

$$\frac{1}{\varepsilon_{\mathrm{el}}(p_{\mathrm{T}})} = \frac{1}{N_{\mathrm{el,\ TRD,\ tot}}(p_{\mathrm{T}})} \sum_{i} N_{\mathrm{el,\ TRD,\ i}}(p_{\mathrm{T}}) \frac{N_{\mathrm{el,\ MB,\ i}}(p_{\mathrm{T}})}{N_{\mathrm{el,\ MB\&TRD,\ i}}(p_{\mathrm{T}})} \ . \tag{5.11}$$

Here, $N_{\mathrm{el,\ TRD,\ tot}}$ is the total number of electrons (or positrons) in the full TRD sample, while $N_{\mathrm{el,\ TRD,\ i}}$ is the total number of electrons for the i-th run in the TRD sample, and similarly for the MB or the MB&TRD samples. Because of the low number of electrons within a single run, the runs are grouped when they have similar conditions of TRD gas gain and magnetic field. It can be assumed that, within a run group, the properties of the trigger do not depend on the specific run, hence that the number of electrons per event $N_{\mathrm{el/ev,\ TRD,\ g}}$ is constant within a run group g. This leads to:

$$\frac{1}{\varepsilon_{\mathrm{el}}(p_{\mathrm{T}})} = \frac{1}{N_{\mathrm{el,\ TRD,\ tot}}(p_{\mathrm{T}})} \sum_{\mathrm{g}} \left(N_{\mathrm{el/ev,\ TRD,\ g}}(p_{\mathrm{T}}) \frac{N_{\mathrm{el/ev,\ MB,\ g}}(p_{\mathrm{T}})}{N_{\mathrm{el/ev,\ MB\&TRD,\ g}}(p_{\mathrm{T}})} \sum_{\mathrm{i\ in\ g}} N_{\mathrm{ev,\ TRD,\ i}} \frac{N_{\mathrm{ev,\ MB,\ i}}}{N_{\mathrm{ev,\ MB\&TRD,\ i}}} \right) . \tag{5.12}$$

The subscript el represents the number of electrons (or positrons), ev represents the number of events, and el/ev the number of electrons per event. It can be further assumed that $N_{\mathrm{el/ev,\ TRD,\ g}} = N_{\mathrm{el/ev,\ MB\&TRD,\ g}}$, i.e., in a given run group, the number of electrons per event is the same in the TRD and MB&TRD sample. This assumption comes from the fact that the MB trigger probably only modifies the number of events but does not bias the properties of the events.

The TRD single-leg efficiency is shown in Fig. 5.17, in the left panel for positrons and in the right panel for electrons. This efficiency contains a turn-on curve around $p_{\mathrm{T}} = 2$ GeV/c (the threshold is smeared because of the imperfect resolution of online-computed p_{T}), and a plateau after 2 GeV/c (or higher in the positron case). It can also be observed that the efficiency is higher for electrons than for positrons. This effect is due to the magnetic field, which deviates the drifting of electrons created when the particle passes through the detector gas.
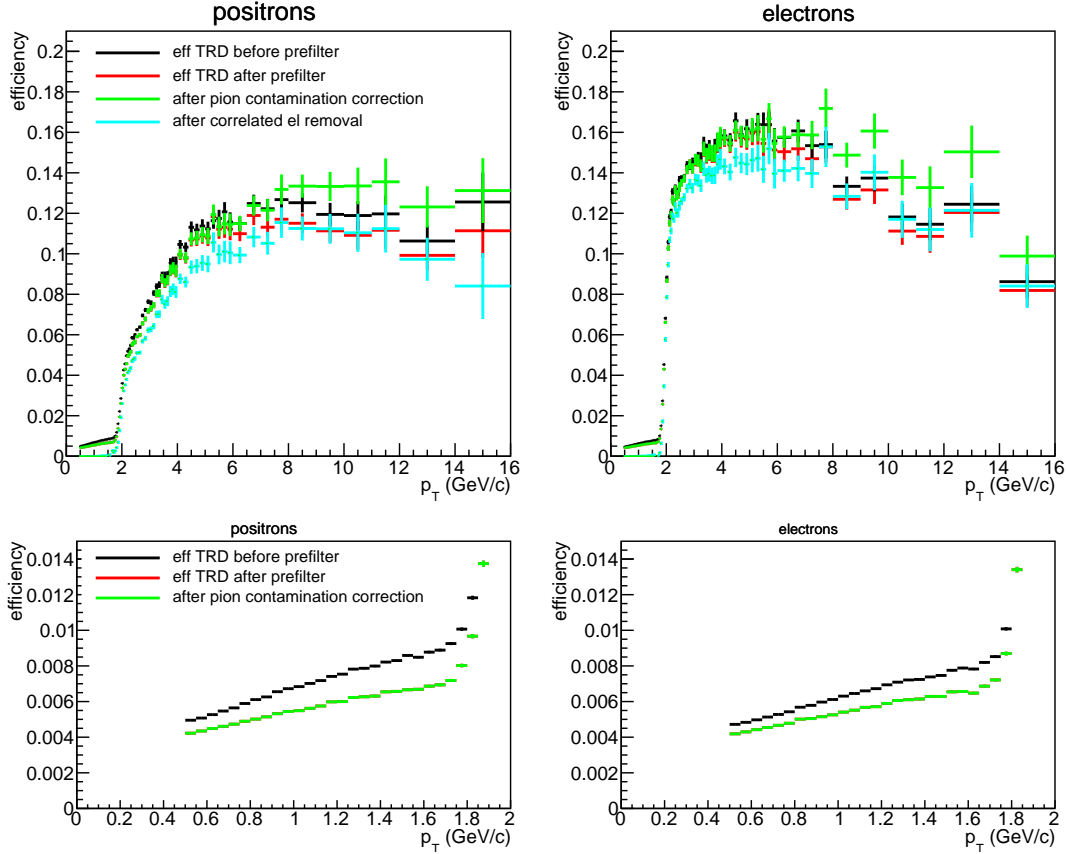
Figure 5.17.: TRD trigger single-leg efficiency for positrons (left) and electrons (right), for the whole p_{T} range (top) and only at low p_{T} (bottom). This is shown for the default case, as well as when the photonic electrons are removed from the estimation through prefiltering, and when the contamination from pions is also corrected for.

At high p_{T}, there can be a contamination from pions in the electron sample. These pions have a lower TRD trigger efficiency than electrons. The estimation of the contamination is done through p_{T}-dependent fits of the TPC $n\sigma_{el}$ distributions. Electrons and pions contributions are both modeled by a Gaussian. An example of a fit is shown in the left panel of Fig. 5.18. The right panel of the same figure shows the contamination as a function of p_{T} in MB sample, and TRD sample for positrons and electrons. The contamination reaches 40 % in the MB sample in the highest p_{T} interval considered.

In addition, it can be noticed that, even at low p_{T}, the TRD trigger efficiency is not zero. This can be noticed in the bottom panels of Fig. 5.17, which is focused on the low p_{T} part. This is due to the cases for which the electron considered is not the one which fired the trigger. This UE part is probably relatively flat and present on the whole p_{T} range. In order to calculate the J/ψ self-trigger efficiency, it is necessary to subtract the UE contribution from the single-leg efficiency. Indeed, otherwise, this UE efficiency would be counted three times: once as a function of N_{tracks} as was described before, once for the positron and once for the electron.

Moreover, a non-negligible part of the electrons and positrons come as pairs: as photon conversions (although part of the contributions are removed through the DCA selection), in Dalitz π_0 or η decays, in quarkonia dielectron decays, or as two correlated semi-leptonic decays
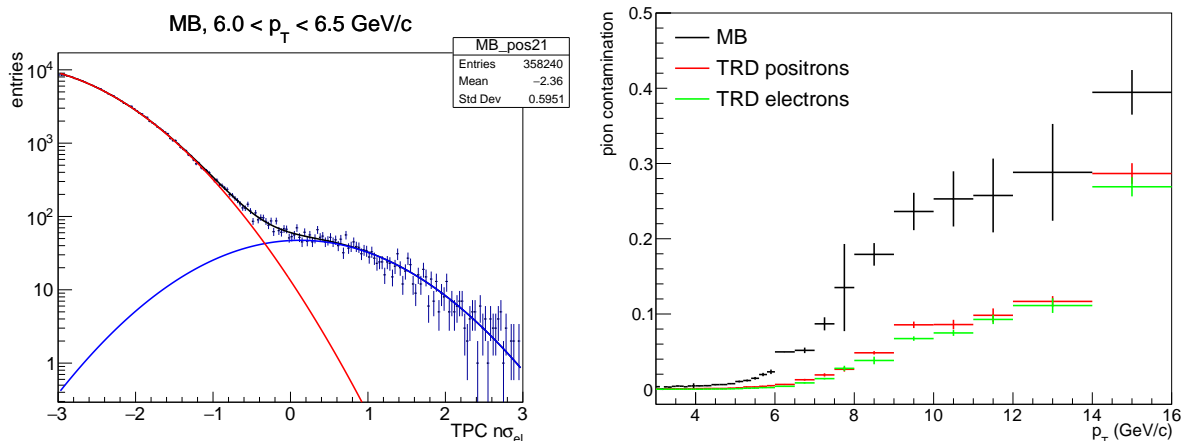
Figure 5.18.: Left: Fit of the TPC $n\sigma_{el}$ distribution, for $6 < p_T < 6.5$ GeV/c, with one Gaussian for electrons (in blue) and one Gaussian for pions (in red, sum of both Gaussians in black). Right: Pion contamination as a function of transverse momentum.

of heavy-flavored hadrons. Thus, it is possible that, in one of these pairs, only the electron fires the trigger, but both the electron and the positron are counted in the efficiency. This case corresponds to a self-trigger efficiency for the electron, and to a "correlated efficiency" for the associated positron. Moreover, this contribution could depend on p_T, since a high p_T positron is more likely to come with a high p_T electron, which has a higher probability to fire the trigger. The fact that the electron self-trigger efficiency is higher also results in a higher correlated efficiency for associated positrons than for associated electrons. This correlated efficiency should also be subtracted, because, when considering a dielectron decay, the correlated efficiency for one track is already accounted for in the self-trigger efficiency of the other track.

The contribution from correlated pairs is visible when looking in detail at low p_T in the bottom panels of Fig. 5.17, where the self-trigger efficiency is assumed to be negligible for $p_T < 1.7$ GeV/c (at the beginning of the turn-on curve). There is an increase with p_T, as well as a slight asymmetry between positrons and electrons (around 0.1% at $p_T = 1.6$ GeV/c). Because the UE trigger coming from uncorrelated tracks is expected to be symmetric for electrons and positrons, the asymmetry present at low p_T indicates that the event is sometimes triggered by a correlated electron. In order to subtract part of the correlated contributions due to photonic electrons (photon conversions or Dalitz decays), a prefilter is applied. Electrons (respectively positrons) are removed from the sample when they can be paired with a positron (respectively electron) found with looser selections, and the pair fulfills $m_{ee} < 140$ MeV/c^2. After applying the prefilter, both the p_T dependence and the asymmetry between electrons and positrons of the UE efficiency are smaller, as visible in the bottom panels of Fig. 5.17. The case after applying the prefilter and correcting for pion contamination is also shown.

Even after applying the prefilter, the UE efficiency caused by uncorrelated tracks and a part of the contributions from correlated electrons (heavy-flavor correlated electrons, photonic electrons escaping the tagging by the prefilter) are still present in the single-leg efficiency. The shape and magnitude of these correlated contributions are therefore analyzed through the PYTHIA standalone simulation of the TRD trigger. The detector effects are assumed small for the

TRD trigger efficiency, because these effects probably cancel between the denominator and the numerator.

In PYTHIA, the efficiency for a given correlated source is calculated as the number of electrons from this source for which the event is triggered by their associated positron, divided by the total number of electrons. It is assumed that a negligible amount of Dalitz decay electrons remain after prefiltering. This hypothesis is favored by the remaining asymmetry between positrons and electrons in the trigger efficiency after the prefilter, which amounts to ≈ 0.0003 at $p_\mathrm{T} = 1.7$ GeV/c. The asymmetry in the simulations would be too large if the contribution from Dalitz decay electrons contribution was kept. The efficiencies for the different sources after making this assumption, including the UE efficiency which contains contributions of electrons for which the particle which fired the trigger was uncorrelated, are shown in Fig. 5.19. It can be seen that all correlated contributions increase with p_T. The UE contribution also increases but with lower extent. The correlated efficiencies extracted from PYTHIA are directly subtracted from the single-leg efficiency. After this subtraction, the template of p_T-dependent UE efficiency from PYTHIA is scaled to the remaining single-leg efficiency within $p_\mathrm{T} < 1.7$ GeV/c, and also subtracted from the single-leg efficiency.
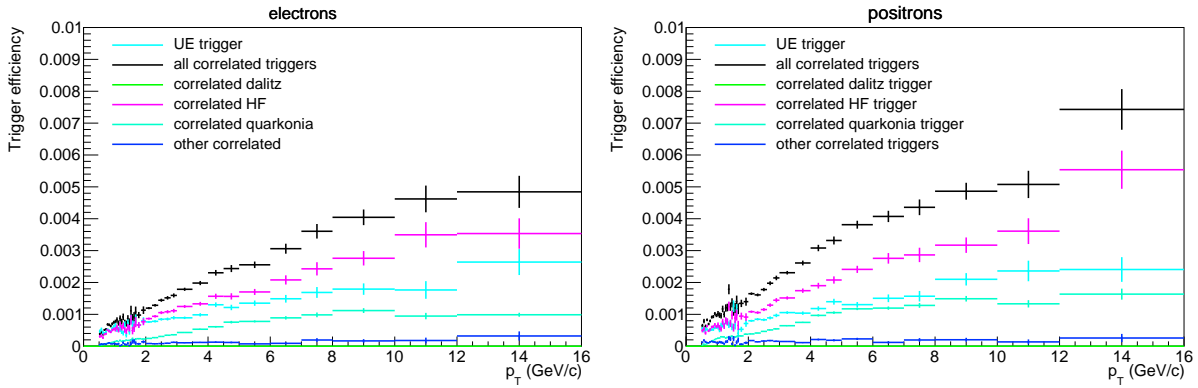
Figure 5.19.: TRD correlated and UE efficiencies from PYTHIA for different sources for electrons (left) and positrons (right). The Dalitz decay electrons are not considered in the electron and positron samples.

After the single-leg efficiency is obtained both for electrons and positrons, it needs to be converted to a pair efficiency. This is done using the kinematics of the J/ψ decay from MC simulations. Each J/ψ daughter is assigned a given probability to fire the trigger, depending on its p_T. For each J/ψ, the trigger probabilities of the two daughters are assumed independent and are combined in order to obtain the probability that the J/ψ is triggered by either of its daughters. The p_T-dependent self-trigger pair efficiency is obtained by dividing the number of J/ψ triggered this way by the total number of J/ψ. The pair efficiency obtained is shown in Fig. 5.20. Because, for the J/ψ in the Bremsstrahlung tail, the electron p_T are lower on average for the same J/ψ p_T, the efficiency are dependent on the mass. Therefore, at same p_T, the efficiency is smaller for the J/ψ with lower mass compared to the mass-integrated ones.

Trigger normalization factor:

When calculating absolute yields, it is also necessary to determine the fraction of events which were triggered, in order to know the equivalent number of INEL>0 events which were inspected.
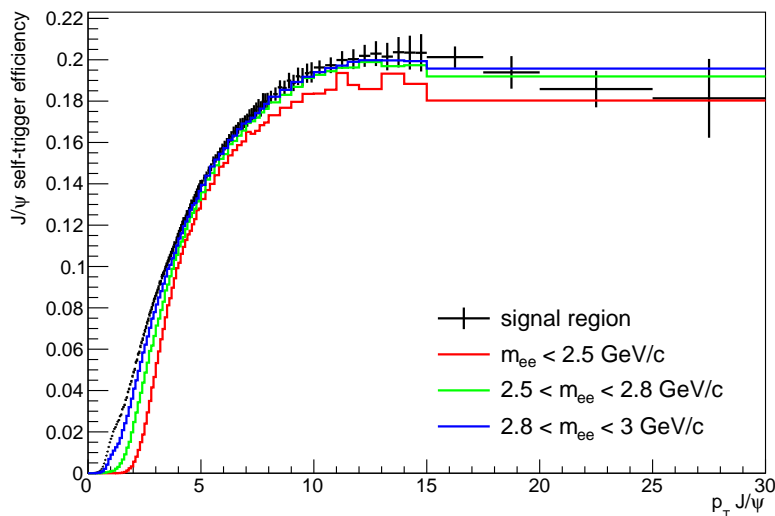
Figure 5.20.: J/ψ self-trigger efficiency as a function of J/ψ p_T, in the signal region and in different mass regions.

In this case, also the ratio between MB events which pass the TRD trigger conditions and all MB events, as in Eq. 5.9 and Eq. 5.10, are used, with weighting for run number, but integrated in multiplicity. For the full data sample, it gives an overall factor of 611 ± 3.

Correction applied in data:

The p_T-integrated TRD trigger efficiency could be estimated using the p_T distribution from the MC. However, in this case, due to the strong dependence on p_T, the uncertainty due to the p_T distribution used in MC would be large. In addition, at given p_T, the TRD trigger efficiency is the same for prompt and non-prompt J/ψ, with the only exception being due to the UE efficiency part coming from $b\bar{b}$ correlations. Since the TRD information is not used in the BDT, it can be assumed that the probability for a J/ψ at a given p_T to be triggered is independent of the BDT score. The TRD trigger efficiency for candidates after BDT selection would then be relatively similar to the trigger efficiency for candidates before selection. In this case, it is thus possible to correct for the efficiency of the TRD trigger, by counting every J/ψ candidate after BDT selection with a weight equal to:

$$\frac{1}{\varepsilon_{TRD}} = \frac{1}{\varepsilon(p_{\mathrm{T}_{\mathbf{J}/\psi}}) + \varepsilon_{UE}(N_{trks}) - \varepsilon(p_{\mathrm{T}_{\mathbf{J}/\psi}}) \times \varepsilon_{UE}(N_{trks})} \, . \tag{5.13}$$

Here, the product corrects for the rare cases when a track fires the trigger while another track from the underlying event also fires it. In this case, because it is not possible for every candidate individually whether it is prompt or non-prompt, the value of $\varepsilon_{UE}(N_{trks})$ for prompt J/ψ is used. For non-prompt J/ψ, the additional effect of 0.24% in UE efficiency from $b\bar{b}$ correlation must also be taken into account. This is done by multiplying the total efficiency for non-prompt J/ψ by the ratio of p_T-integrated TRD trigger efficiencies with and without these 0.24%, where the p_T-

integrated efficiency is calculated from the non-prompt J/ψ MC considering the p_T distribution of PYTHIA.

After correction for the TRD trigger efficiency, the INEL>0 results using the MB trigger or the TRD trigger are expected to give similar results. For absolute yields, the TRD trigger tends to estimate a yield per INEL>0 event which is higher ($\sim 8\%$) than the one estimated using the MB trigger. This discrepancy is nevertheless accounted for by assuming a large systematic uncertainty due to the TRD trigger efficiency. For self-normalized yields, the effects of the imperfect estimation of the TRD trigger efficiency cancel and both triggers give compatible results.

5.4.3. Corrections to the MC templates

Multiplicity dependence:

The resolution of the pseudo-proper decay time depends not only of the resolution of the secondary vertex, but also on the resolution of the primary vertex. The latter is mainly driven by the number of contributors to the primary vertex, hence by the multiplicity. Additionally, it is possible that the daughters of the J/ψ are included in the calculation of the primary vertex. In this case, displaced tracks would pull the primary vertex towards them, and the effect would be especially strong at low multiplicity where there are not enough other tracks originating from the primary vertex which would compensate for this effect.

The effect of the multiplicity is shown in Fig. 5.21, where the left and right panels show the case in which the J/ψ daughters are included and removed, respectively, in the computation of the primary vertex. The efficiency is shown in several N_{tracks} intervals for the three samples as a function of the selection value on the non-prompt BDT score. In the case with inclusion of the daughters for the primary vertex, the scores for the prompt sample are independent of the multiplicity, while the non-prompt sample has lower non-prompt score at low multiplicity: in this case, pulling the primary vertex towards itself makes the secondary vertex less displaced. In the case with removal of the daughters for the primary vertex, the scores for the prompt sample are not independent of the multiplicity anymore. This is due to the fact that the primary vertex resolution becomes worse at low multiplicity, making the separation between prompt and non-prompt J/ψ more difficult.

It should be noted that, in Fig. 5.21, the J/ψ daughters have been removed from the multiplicity estimator for establishing the multiplicity intervals in which the efficiencies are computed. The reason is that it can lead to autocorrelations. Indeed, if the daughters are allowed to be included in the multiplicity when they pass the required selections for the multiplicity estimator (which include tight selections in DCA), the case when they do not pass these requirements is correlated both with a higher DCA and a lower multiplicity. Events at low multiplicity, especially when a non-prompt J/ψ is present and pulls toward itself the primary vertex if its daughters are included in the primary vertex calculation, have candidates with higher DCA and thus higher BDT non-prompt score on average. This effect is in the opposite direction compared to the intuition that the separation power between prompt and non-prompt J/ψ is worse at low multiplicity.
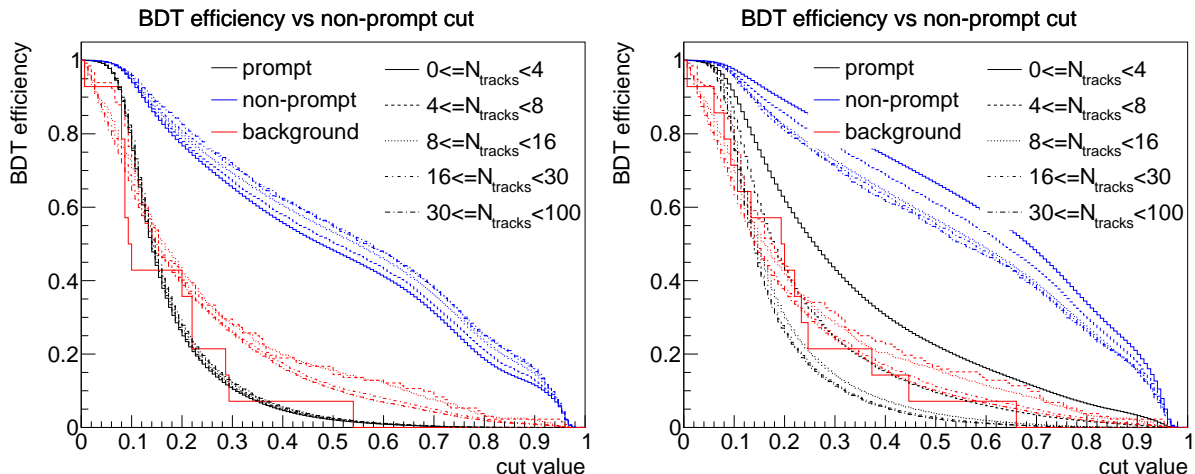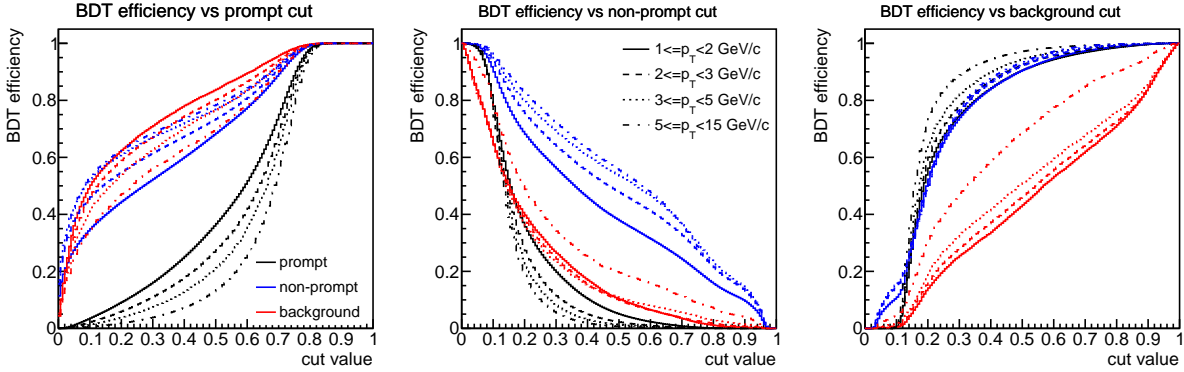
Figure 5.21.: Efficiency as a function of the BDT selection value on the non-prompt score for the three samples (prompt J/ψ, non-prompt J/ψ, background), in several N_{tracks} intervals. In the left panel, the J/ψ daughters are included in the calculation of the primary vertex, while in the right panel, the daughters are removed from the primary vertex calculation. In both cases, the daughters are not included in the calculation of the N_{tracks} value.

In the MC simulations where J/ψ signals are injected on top of minimum-bias events, the number of J/ψ per event is independent of the multiplicity. However, this is not what happens in data, where there are more J/ψ produced in higher multiplicity events. Because the multiplicity dependence of J/ψ counts in MC simulations is different compared to the one in data, the multiplicity dependence of the BDT scores could lead to a discrepancy in the selection efficiencies between data and MC. In order to reduce this discrepancy, the J/ψ signals are given multiplicity-dependent weights in MC. The weights are defined as the ratio between data and MC of the distributions of N_{tracks} values for J/ψ signals. In order to avoid autocorrelations, these weights are computed as a function of $N_{\text{tracks}}^{\text{w/o daughters}}$. The N_{tracks} distribution for J/ψ signals is known in the MC. However, it is not accessible directly in data. At a first iteration, this distribution is taken in data as the number of counts of opposite-sign pairs minus like-sign pairs in the signal region, for each value of N_{tracks}. In this case, the correlated background is not removed, but it is assumed to have a similar multiplicity dependence as J/ψ. At a second iteration, the multiplicity dependence of J/ψ production is approximated from a fit with a power-law of the inclusive self-normalized J/ψ yields per event as a function of N_{tracks}, and combined with the minimum-bias N_{tracks} distribution. In order to take into account different multiplicity dependence for prompt and non-prompt J/ψ, f_B values obtained at the first iteration are fitted with two linear functions: one linear function for $N_{\text{tracks}} < 10$ and another one with a different slope for $N_{\text{tracks}} \geq 10$.

Multiplicity-dependent weights are applied only for $N_{\text{tracks}} < 20$. Beyond this value, it is assumed that the multiplicity dependence is weak, and a common weight is applied for all signals with $N_{\text{tracks}} \geq 20$. The reason for the reweighting only at low multiplicity is that, at higher multiplicity, the number of J/ψ signals in the MC gets low. Then, weighting the J/ψ at high multiplicity could amplify statistical fluctuations. After weighting, it is possible to create different templates of BDT efficiency for all the multiplicity intervals. For the same reasons as explained before, the multiplicity intervals beyond $N_{\text{tracks}} = 20$ use a common template. The weights are applied not only in the testing sample, but also in the training samples. In the latter case, only the weights

obtained using the difference of opposite-sign and like-sign counts are used. With these weights, the model avoids to learn features which are present only at low multiplicity and bad vertex resolution. Indeed, these features are not very useful for J/ψ classification in data because most of the J/ψ signals are found in higher multiplicity events.

Correction of $\langle p_\mathrm{T} \rangle$ as a function of multiplicity:

Figure 5.22.: Efficiency of BDT selection for different p_T intervals, as a function of the selection value in prompt (left), non-prompt (middle), and background scores (right). This efficiency is obtained after selecting all signals with a score higher (for non-prompt J/ψ) or lower (for prompt J/ψ or background) than a given selection value.

Figure 5.22 shows the efficiencies for selection on prompt (left panel), non-prompt (middle panel) and background (right panel) BDT, for several p_T intervals. The efficiencies show a clear dependence on p_T. In particular, the separation between prompt and non-prompt sources is better at higher p_T, due to the better DCA resolution and larger secondary vertex displacement. Because of this p_T dependence, it is necessary that the MC has a correct p_T distribution in order to obtain accurate BDT score templates for prompt and non-prompt J/ψ. However, when J/ψ are injected on top of minimum-bias events in the MC, the p_T distribution is independent of the multiplicity of the event. In the MC, the minimum-bias p_T distribution for prompt J/ψ is weighted to reproduce a fit to previously published prompt cross-section [80] using the phenomenological formula from [203] with a few parameters:

$$\frac{d\sigma_{\mathrm{J}/\psi}}{dp_\mathrm{T}} \propto \frac{p_\mathrm{T}}{(1 + a \times (p_\mathrm{T}/\langle p_\mathrm{T} \rangle)^2)^n} . \tag{5.14}$$

The p_T distribution for minimum-bias non-prompt J/ψ is taken directly from PYTHIA. However, previous results [144] had shown that J/ψ at higher p_T are more often found in higher multiplicity events. The p_T distribution is then multiplicity-dependent, and it should be corrected in every N_tracks interval.

Due to limited statistics, it is not possible to extract a full p_T distribution in every multiplicity interval. The solution is then to extract in each case $\langle p_{\mathrm{T, J}/\psi} \rangle$, following a method used e.g. in Ref. [154].

The first step is to determine $\langle p_{\mathrm{T},ee} \rangle (m_{ee})$, the average transverse momentum of pair candidates as a function of invariant mass, for candidates with $p_\mathrm{T} > 0$ GeV/c. This is done while combining

the MB and HM samples, while the TRD sample is not used because the trigger threshold does not allow to reach low momentum. A selection in the BDT score is also done for background rejection, as was discussed in Sec. 5.3.4. $\langle p_{\mathrm{T},ee} \rangle(m_{ee})$ is a combination of the $\langle p_{\mathrm{T}} \rangle$ from the J/ψ signal and the one from the background, with the relative contributions depending on the fraction of signal at this specific invariant mass. This translates to the formula:

$$\langle p_{\mathrm{T},ee} \rangle(m_{ee}) \; = \; \alpha(m_{ee}) \cdot C(m_{ee}) \cdot \langle p_{\mathrm{T},\,J/\psi} \rangle \; + \; (1 - \alpha(m_{ee})) \cdot \langle p_{\mathrm{T},\,\mathrm{bkg}} \rangle(m_{ee}). \tag{5.15}$$

Here, $\alpha(m_{ee})$ is the fraction of signal, S/(S+B), at this specific invariant mass value, which can be fixed when extracting the number of J/ψ counts, and $\langle p_{\mathrm{T},\,\mathrm{bkg}} \rangle(m_{ee})$ is the mass-dependent $\langle p_{\mathrm{T}} \rangle$ for the background, assumed to follow a second-order polynomial distribution. $C(m_{ee})$ is a correction factor which takes into account the invariant mass dependence of $\langle p_{\mathrm{T},\,J/\psi} \rangle$, for example when the Bremsstrahlung tail biases the p_{T}. It is extracted from MC simulations, scaled so that its value inside the signal region is unity, and shown in Fig. 5.23.
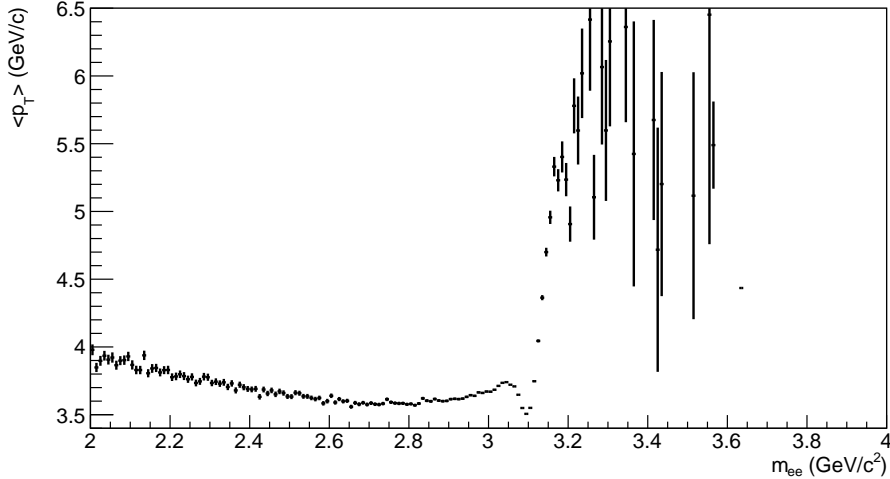
Figure 5.23.: $\langle p_{\mathrm{T}} \rangle$ as a function of invariant mass for J/ψ signals from MC simulations.

In order to take into account the fact that the acceptance and reconstruction efficiencies are not flat as a function of p_{T}, every candidate is given a weight $1/\varepsilon(p_{\mathrm{T}})$, where $\varepsilon(p_{\mathrm{T}})$ is the p_{T}-dependent acceptance times efficiency of J/ψ reconstruction and of BDT selection.

A fit of $\langle p_{\mathrm{T},ee} \rangle(m_{ee})$ using Eq. 5.15 is done, the free parameters in the fit being $\langle p_{\mathrm{T},\,J/\psi} \rangle$ as well as the three parameters for the second-order polynomial background distribution. Examples of such fits for two multiplicity intervals are shown in Fig. 5.24.

The $\langle p_{\mathrm{T}} \rangle$ values as a function of N_{tracks} are shown in Fig. 5.25. In the left panel, N_{tracks} is calculated in the full azimuthal angle, while in the right panel N_{tracks} is calculated in either of the three azimuthal regions with respect to J/ψ. All the cases except for the transverse region show a rising trend as a function of multiplicity. The multiplicity dependence is the strongest for $\langle p_{\mathrm{T},\,J/\psi} \rangle$ as a function of the toward multiplicity.

When the prompt and non-prompt J/ψ MC efficiency templates are built for every multiplicity interval, each candidate receives a weight depending on p_{T} and on the multiplicity interval
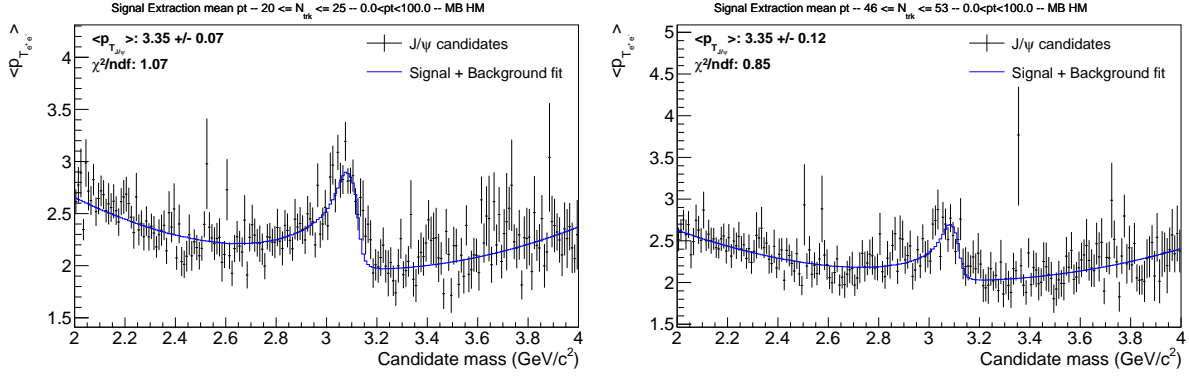
Figure 5.24.: Extraction of $\langle p_{\mathrm{T}} \rangle$ for $20 \leq N_{\mathrm{tracks}} < 26$ (left) and $46 \leq N_{\mathrm{tracks}} < 54$. All candidates with $p_{\mathrm{T}} > 0$ GeV/c are used.
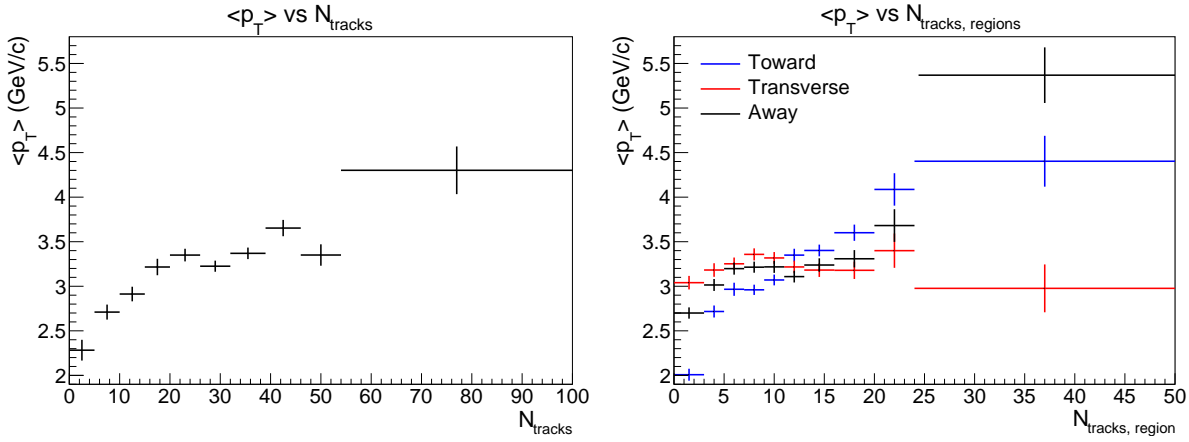
Figure 5.25.: Left: $\langle p_{\mathrm{T}} \rangle$ as a function of N_{tracks} extracted from data. Right: $\langle p_{\mathrm{T}} \rangle$ as a function of $N_{tracks,regions}$ extracted from data, for toward, transverse, and away region.

considered. The weights are built such that, for every multiplicity interval i, the new p_{T} distribution after applying the weights becomes

$$f_{\mathrm{i,\,new}}(p_{\mathrm{T}}) = f_{\mathrm{i,\,old}} \left(p_{\mathrm{T}} \times \frac{\langle p_{\mathrm{T}} \rangle_{\mathrm{MB,\,data}}}{\langle p_{\mathrm{T}} \rangle_{\mathrm{i,\,data}}} \times \frac{\langle p_{\mathrm{T}} \rangle_{\mathrm{i,\,MC}}}{\langle p_{\mathrm{T}} \rangle_{\mathrm{MB,\,MC}}} \right) . \tag{5.16}$$

$f_{\mathrm{i,\,old}}$ and $f_{\mathrm{i,\,new}}$ represent the p_{T} distribution of all true (i.e. before propagation to the detectors and reconstruction) J/ψ injected in the MC, before and after this weighting. The choice of this formula has been made because J/ψ p_{T}-dependent cross-section can be well described by the phenomenological formula from Eq. 5.14. Here, the value of the parameter n is assumed to be independent of the multiplicity, and the parameter a can be written exclusively as a function of n, which would mean that the p_{T}-dependent shape in a multiplicity interval varies only with $\langle p_{\mathrm{T}} \rangle$, as assumed in Eq. 5.16. The whole evolution of $\langle p_{\mathrm{T}} \rangle$ between minimum-bias collisions and the multiplicity interval is corrected, except for the effects already present in the MC templates, e.g. at very low multiplicity where auto-correlations give a lower $\langle p_{\mathrm{T}} \rangle$ or the effects due to other corrections. Both prompt and non-prompt distributions are corrected independently, using their own prompt and non-prompt p_{T} distributions in the MC template, but correcting with $\langle p_{\mathrm{T}} \rangle$ for inclusive J/ψ, which is the only one being available in data.

B hadron fractions:

Non-prompt J/ψ coming from different B hadrons can have different DCA and pseudo-proper decay length distributions, due to different $c\tau$ and different decay products of the B hadron. It is then necessary to model correctly the proportion of different B hadrons in the MC sample, in order to obtain distributions closer to the ones in data. However, it has been shown by ALICE at midrapidity in the charm sector (e.g. in Ref. [140]), and LHCb at forward rapidity in the beauty sector (e.g. in Ref. [117]), that the baryon-to-meson ratio increases at low p_T. This feature is not reproduced in PYTHIA simulations with the Monash tune such as the ones used for determining the BDT selection efficiency templates.

These publications have also shown that the baryon-to-meson ratio at low p_T is known to be better reproduced in PYTHIA when the settings for CR-BLC mode 2 are used [46]. The left panel of Fig. 5.26 shows the pseudo-proper decay length distribution for non-prompt J/ψ coming from the decays of several beauty hadron species (B^0, B^+, B_s^0, B_c, Λ_b^0, Ξ_b^-, Ξ_b^0 and Ω_b^-). This was obtained from PYTHIA using the CR-BLC mode 2 settings, where the beauty hadrons were forced to decay through a quarkonium decay channel. A species-dependent weight is applied in order to correct for this enhancement. It can be observed that the pseudo-proper decay length for J/ψ coming from beauty baryons decays is smaller than the ones in the cases of beauty mesons. B_c also decays faster, but its total contribution is negligible.
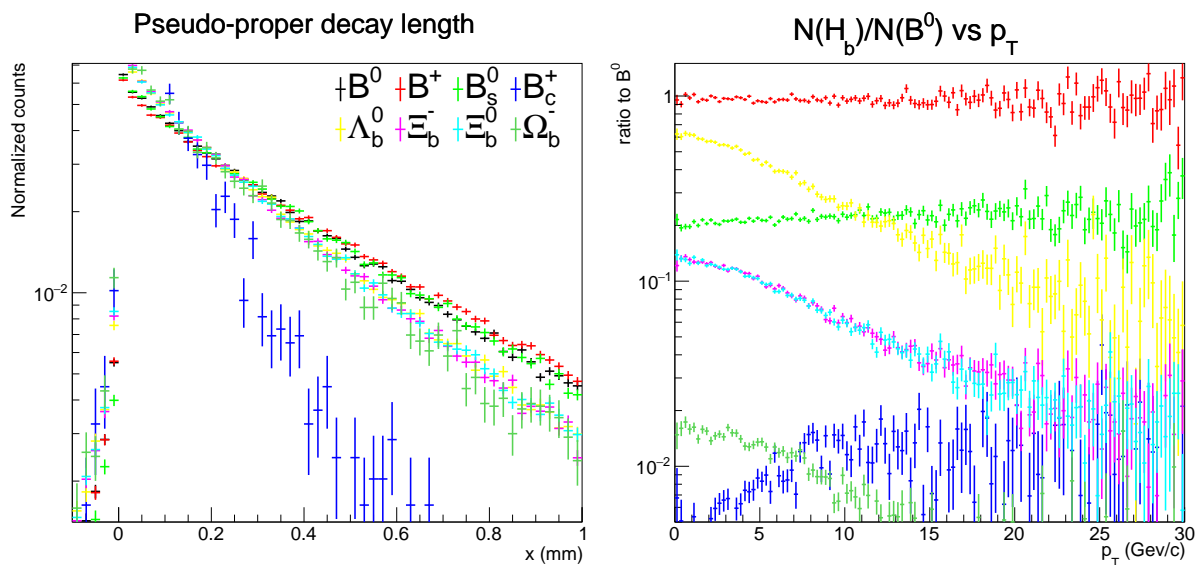
Figure 5.26.: Left: Pseudo-proper decay length distribution for non-prompt J/ψ coming from the decays of different beauty hadrons, with Color Reconnection Mode 2. Right: ratio between the p_T distribution of different beauty hadrons and B^0. The beauty hadrons decay to a J/ψ in ALICE acceptance. PYTHIA with CR-BLC mode 2 is used.

The ratio of the p_T distributions of different beauty hadrons, decaying to a J/ψ within ALICE acceptance, to the one for B^0 is shown in the right panel of Fig. 5.26. In this case, the fractions of beauty baryons, such as Λ_b, increase at low p_T. This is contrasting with the Monash tune for which this ratio is flat at ~ 0.1. From the ratio of these distributions for PYTHIA with CR-BLC mode 2 and Monash tune, weights depending on the beauty hadron species and p_T are extracted. These weights are applied to the non-prompt signals in the MC when creating the

BDT score templates and when calculating the efficiency corrections. The difference between the results with and without weighted template is nevertheless small.

5.5. Extrapolation of the prompt yield to $p_{\mathrm{T}} > 0$ GeV/c

Obtaining integrated yields with $p_{\mathrm{T}} > 0$ GeV/c allows a comparison and calculating the ratio with other species such as D^0. Indeed, if different species have different p_{T} distributions, the fraction of the yield removed by a selection on p_{T} will depend not only on the species, but also on the multiplicity, due to the hardening of the p_{T}-dependent cross-section with multiplicity.

The extrapolation is done for the prompt yield integrated in the INEL>0 and V0M 0-0.1% event classes. Between 0 and 1 GeV/c, it is possible to extract an inclusive yield for the MB- and HM-triggered sample. The non-prompt yield can then be subtracted using PYTHIA with CR-BLC mode 2. The non-prompt yield in the model is scaled to the non-prompt yield in data in the range $p_{\mathrm{T}} > 1$ GeV/c, so that only the p_{T}-dependent shape from the model matters. For extrapolation in the HM case, only the 0.1% with highest charged-particle multiplicity in the acceptance of the V0 detector are used. After removal of the non-prompt yield in $p_{\mathrm{T}} < 1$ GeV/c, the yield with $p_{\mathrm{T}} > 0$ GeV/c is taken as the sum between the prompt yield with $p_{\mathrm{T}} > 1$ GeV/c and the one with $p_{\mathrm{T}} < 1$ GeV/c.

5.6. Multiplicity unfolding with the bias from J/ψ candidates

5.6.1. Unfolding of the multiplicity-dependent J/ψ yield

In chapter 4, the unfolding of the multiplicity was done in Minimum-Bias events or High-Multiplicity events completely independently of whether a J/ψ meson is present or not. The method presented there consists in choosing an interval of N_{tracks}, and measuring both average N_{ch} and average J/ψ yield in this interval. In the ideal case, the chosen intervals would contain only one charged-particle multiplicity N_{ch} value. This is not possible due to smearing between N_{ch} and N_{tracks} and to the statistical uncertainties which restrain the choice to large N_{tracks} intervals, but the final results should intend to approach maximally the results from this one-N_{ch}-value case. Such a reference choice is needed, because different choices of N_{tracks} intervals might lead to different results. Indeed, in a large N_{tracks} interval, J/ψ mesons are found to be present more often in events at high multiplicity, and then more often in the higher part of the interval. Then, the question arises whether it could bring a bias to the unfolding correction for the multiplicity estimator.

A sketch of a possible bias is presented in Fig. 5.27. It shows the unfolding matrix from multiplicity-only unfolding, with the red line showing the average N_{ch} as a function of N_{tracks}. One of the chosen intervals of N_{tracks} is shown with vertical red lines. Most unbiased events are located around the $\langle N_{\mathrm{ch}} \rangle$ line in this case, shown by the lower red circle. However, events with J/ψ usually have higher N_{ch} values. That would mean there is a modification of the prior N_{ch} distribution: most events are located around the upper green circle, and in this case not anymore around the mean correlation line from unbiased events.
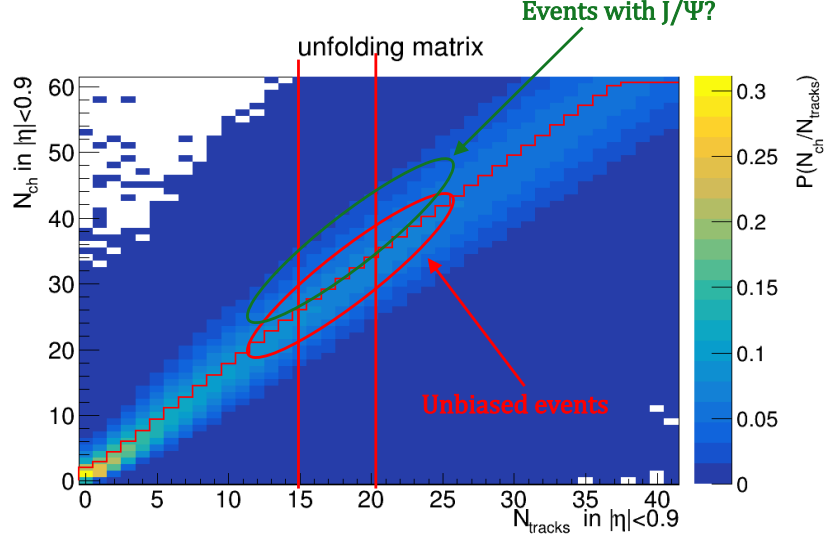
Figure 5.27.: Sketch of the effect of a possible bias due to the presence of J/ψ in the unfolding matrix.

In order to test if this bias is possible and would influence the results, three methods are compared. The first two methods do not take this bias into account while the third one does:

- The first one is the one presented before, a multiplicity-only unfolding, which for each interval of N_{tracks} assigns a full unfolded N_{ch} distribution in the bin. Then, the mean N_{ch} in this range is determined. For the final yields of J/ψ as a function of multiplicity, this only acts as a correction along the x axis.

- The second one uses also the unfolding matrix from the multiplicity-only unfolding. Rather than just moving the points along the x axis, the number of J/ψ is counted in intervals of N_{ch}, normalized by the number of INEL>0 events in this interval of N_{ch} determined from multiplicity-only unfolding. These J/ψ counts as a function of N_{ch} are obtained from the J/ψ counts as a function of N_{tracks} using the following formula:

$$N_{\text{J}/\psi}(N_{\text{ch}}) = \sum_{N'} P(N_{\text{ch}}|N'_{\text{tracks}}) \times N_{\text{J}/\psi}(N'_{\text{tracks}}) \,. \tag{5.17}$$

This formula can also be written as:

$$N_{\text{J}/\psi}(N_{\text{ch}}) = U \times N_{\text{J}/\psi}(N_{\text{tracks}}) \,. \tag{5.18}$$

U is the unfolding matrix from multiplicity-only unfolding, where the intervals coincide with the intervals in which extraction of J/ψ counts is done. $N_{\text{J}/\psi}$ are the vectors counting the total number of J/ψ in each N_{ch} or N_{tracks} multiplicity interval, before normalization by the number of events. This method also does not take the J/ψ bias into account, because the N_{ch} distribution used to build the unfolding matrix (from eq. 4.4) is the one from minimum-bias events.

- The third one is the only one intending to take into account the bias added by the presence of J/ψ mesons. Iterative bayesian unfolding is applied directly to the number of J/ψ in

each N_{tracks} interval, and the algorithm returns the number of J/ψ in each N_{ch} interval. The equations during the iteration of the procedure become therefore:

$$P_{\text{J}/\psi}(N_{\text{ch}}|N_{\text{tracks}}) = \frac{P_{\text{J}/\psi}(N_{\text{tracks}}|N_{\text{ch}}) \times P_{\text{J}/\psi}(N_{\text{ch}})}{\sum_{N'} P_{\text{J}/\psi}(N_{\text{tracks}}|N'_{\text{ch}}) \times P_{\text{J}/\psi}(N'_{\text{ch}})}. \tag{5.19}$$

$$N_{\text{J}/\psi}(N_{\text{ch}}) = \sum_{N'} P_{\text{J}/\psi}(N_{\text{tracks}}|N'_{\text{ch}}) \times N_{\text{J}/\psi}(N'_{\text{tracks}}). \tag{5.20}$$

The subscript J/ψ is present when the number of J/ψ counts is used in the detector response matrix or unfolding matrix, rather than the number of events. The difference compared to the second method is that the unfolding matrix has been iteratively corrected so that its projection on the y axis would match the distribution of the number of J/ψ, rather than the distribution of the number of unbiased events. This method presents the advantage that the unfolding procedure provides directly the J/ψ yield as a function of N_{ch}, without the need for an additional correction.

In Fig. 5.28, the unfolding matrix for multiplicity-only unfolding, present in the left panel, is compared with the unfolding matrix for direct unfolding of J/ψ yield, in the right panel. The comparison shows that in the same N_{tracks} intervals, the matrix in the right panel has higher N_{ch} values (for example, the terms just over the diagonal are higher in the right panel). That seems to be exactly the bias effect which was described previously in the sketch of Fig. 5.27.
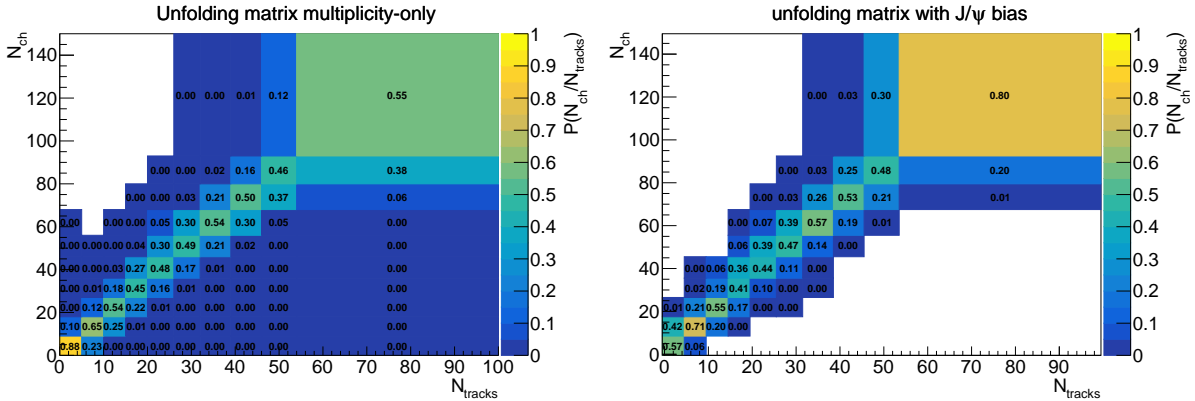
Figure 5.28.: Unfolding matrix for the multiplicity-only unfolding (left), compared with the unfolding matrix for the unfolding of multiplicity-dependent number of J/ψ counts (right).

In order to test how well the different methods work, a closure test is done using minimum-bias events from the MC. In this case, the true inclusive J/ψ yield per event can be obtained in any interval of N_{ch}. The number of J/ψ is first computed from the MC as a function of measured multiplicity, and the three different methods are used for unfolding. These methods are then compared to the reference (MC truth). This is shown in Fig. 5.29.

The comparison shows that, after unfolding, the second method constantly underestimates the results starting from three times the average multiplicity. The multiplicity-only unfolding matrix used here does not take into account the fact that events with J/ψ are biased towards higher multiplicity compared to events unbiased by the presence of J/ψ. Hence, multiplicity-only
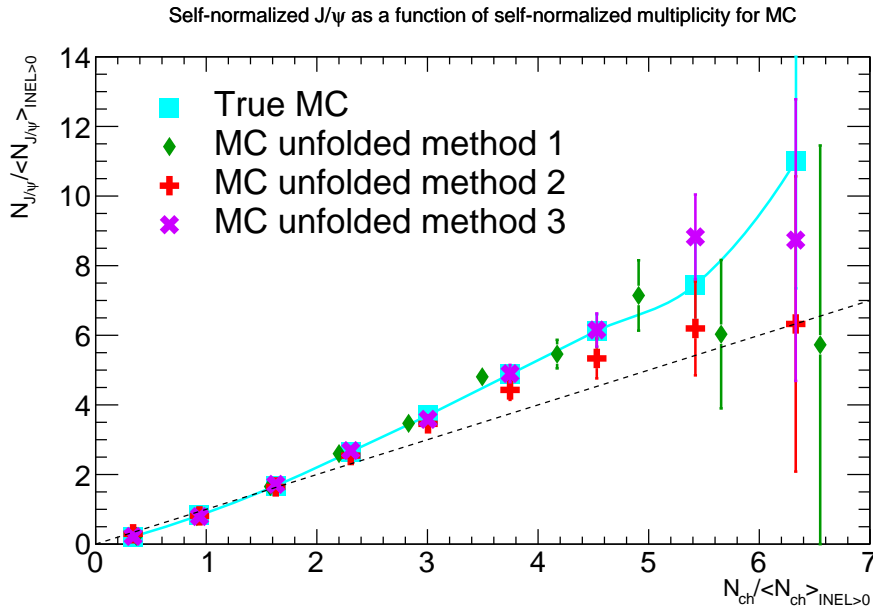
Figure 5.29.: Comparisons in MC of the results of different unfolding methods with the MC truth.

unfolding might not be enough. The first method still presents a good agreement with the MC truth value. The best agreement is the one provided by the third method, but large uncertainties do not allow a perfect confidence that both these methods work correctly. The better agreement as well as the missing J/ψ bias when unfolding only the unbiased multiplicity distribution could nevertheless favor the third method over the first one.

Both the multiplicity-only unfolding (first method) and direct unfolding of the J/ψ yield (third method) are applied in data to the inclusive yield with $p_T > 0$ GeV/c. The MB and HM samples are merged, in order to reproduce the conditions of the measurement in [144], although the method for unfolding is different there. This is shown in Fig. 5.30. Both methods seem to agree within statistical uncertainties (it is nonetheless important to keep in mind that these uncertainties are largely correlated because the same statistical sample is analyzed). In addition, the unfolding of the J/ψ counts is also shown with the detector response matrix extrapolated at high multiplicity, as explained in Sec. 4.4.4.

The resmeared distribution obtained when unfolding directly the J/ψ counts is compared with the J/ψ yields as a function of N_{tracks} in Fig. 5.31. Although they agree in the first multiplicity intervals, at high multiplicity they do not agree perfectly. This non-closure remains below the statistical uncertainties. It is likely due to bin migration effects: several counts which were initially in the highest N_{tracks} interval were migrated in the previous interval after unfolding and resmearing. Comparing the results without and with extrapolation shows the impact of the lack of high-multiplicity MC statistics when unfolding the J/ψ counts. In the latter case, the resmeared distribution gets much closer to the measured distribution. It shows quite an instability in the unfolding of J/ψ counts: a slight modification of the detector response matrix can lead to a large modification in the results after unfolding.

The results obtained with different number of iterations of the Bayesian unfolding are shown in Fig. 5.32. The left panel presents the results without extrapolation of the detector response
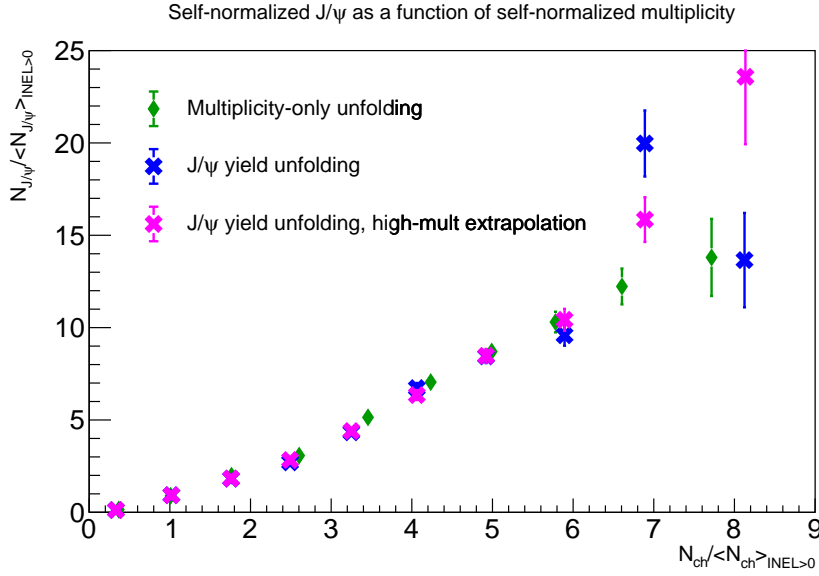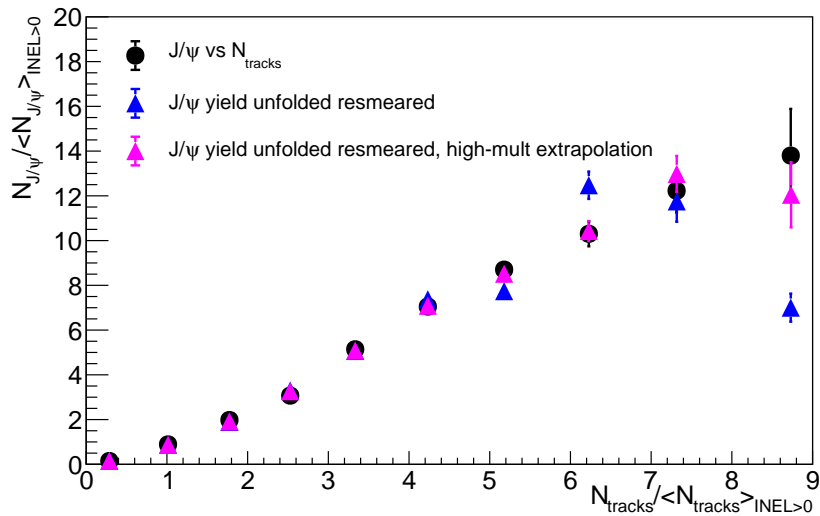
Self-normalized J/ψ as a function of self-normalized multiplicity

Figure 5.30.: Comparisons of the results of different unfolding methods in data.

matrix at high multiplicity, while the results in the right panel are obtained with this extrapolation. The dependence on number of iterations seems large: when there are too many iterations, an unphysical structure appears. For example, in the case without extrapolation, a large upward fluctuation is seen for the point with the second -highest multiplicity. However, the resmeared distribution seems to be always improved when the number of iterations is maximal. This is exactly the same problem which was mentioned in Sec. 4.4.4 and Fig. 4.11, where the statistical fluctuations in the data are amplified with the number of iterations.

In the case of the direct unfolding of the J/ψ counts, the measured distribution is the raw number of J/ψ counts in the different N_{tracks} intervals. This number can be affected by large fluctuations due to low number of counts or to the presence of background during the signal extraction. Then, in this case, the injection of the measured distribution adds at each iteration of the unfolding these fluctuations to the yields, on top of the fluctuations from previous iterations. After several iterations, this would lead to large statistical uncertainties, since there is no control on these fluctuations. This could be correlated to the strong variations observed when extrapolating the response matrix and modifying with the number of iterations.

This study shows that unfolding directly the J/ψ counts can lead to large instability and fluctuations. This happens for example when the detector response matrix is modified only slightly or with a different number of iterations. More iterations always lead to larger statistical uncertainties. These instabilities prevent the use of this method for the unfolding. However, the multiplicity-only unfolding, for which the $\langle N_{\text{ch}} \rangle$ is calculated for all selected N_{tracks} intervals, seems to miss a bias due to the presence of higher yields of J/ψ in higher multiplicity events. Hence, it is necessary to find another way to check and correct for this possible bias, as described in the next subsection.

Figure 5.31.: Resmearing of the self-normalized J/ψ yield as a function of self-normalized multiplicity using direct unfolding of J/ψ counts, with or without high-multiplicity extrapolation of the detector response matrix. It is compared to the measured self-normalized J/ψ yield as a function of N_{tracks}.

5.6.2. MC closure test with toy model

In order to check that the multiplicity-only unfolding makes the proper correction for the J/ψ yields as a function of self-normalized N_{ch}, a MC closure test is needed. In order not to be dominated by statistical uncertainties, but only checking systematics effects, a toy model can be a good alternative in order to generate the multiplicity-dependent J/ψ. In addition, MC generators may not reproduce the correlation well, and in this case the magnitude of possible non-closure might not reflect data perfectly.

The toy model consist in generating many data points. For each data point, the following procedure is applied:

- The starting point of the toy model is the N_{ch} distribution obtained after unfolding. A value of charged-particle multiplicity is chosen randomly from this distribution.

- The multiplicity-dependent J/ψ production is taken as a second-order polynomial (or power-law) fit to the results obtained in data after multiplicity-only unfolding. This is converted to a probability to obtain a J/ψ for each multiplicity value, allowing for each event to decide if a J/ψ is produced or not.

- Next, the multiplicity is smeared. Using the detector response matrix obtained from simulation of minimum-bias events with PYTHIA 8 and GEANT (Fig. 4.3), a value of N_{tracks} is chosen randomly.

After generating the data points, the full N_{tracks} distribution, as well as the number of J/ψ counts in chosen intervals of N_{tracks}, can be obtained. Therefore, the distribution can be unfolded the same way as it is done in data and compared with the generated self-normalized J/ψ as a function of self-normalized multiplicity distribution. The comparison is shown in the left panel of Fig. 5.33. It can be noticed that there is a small relative non-closure which is present, decreasing with multiplicity from 8% at low multiplicity to 0.5% at high multiplicity. The same closure test
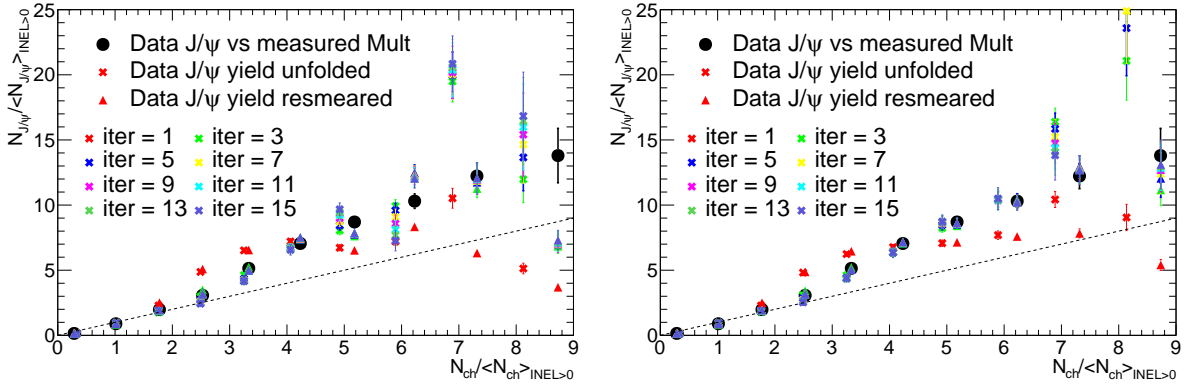
Figure 5.32.: Comparisons of the dependence of the J/ψ self-normalised yield on the number of iterations of the Bayesian unfolding algorithm for direct unfolding of the J/ψ yield, without (left) and with (right) extrapolation at high multiplicity. The resmeared distribution is also shown, in order to compare it to the distribution of J/ψ as a function of measured multiplicity (black). The color represents the number of iterations.

has been done with a power law rather than a second-order polynomial, in the right panel of Fig. 5.33. The non-closure is different in this case compared to the previous one, higher at low multiplicity but lower at high multiplicity.
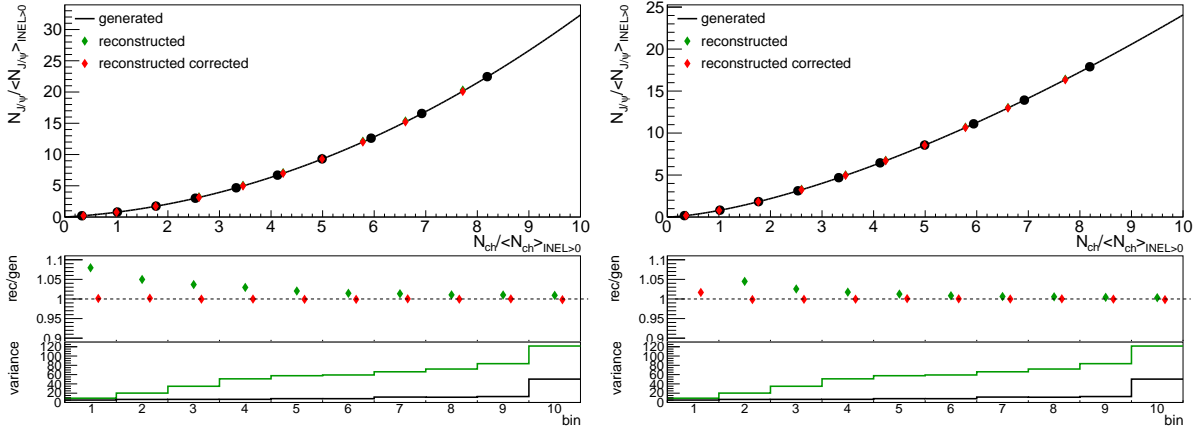
Figure 5.33.: Left: Generated self-normalized J/ψ distribution vs self-normalized multiplicity following a second-order polynomial, compared to reconstructed one, and corrected one with eq. 5.27 (top panel), ration between reconstructed and generated distribution (middle panel), and variance of the N_{ch} distribution as a function of the bin number. Right: same plot, but with the generated multiplicity-dependent J/ψ following a power-law distribution.

The explanation for this non-closure relies on the impact of the smearing. For example, some counts with high charged-particle multiplicity can be smeared to a lower value of N_{tracks}. Then, since unfolding is only done statistically, and not event by event, they can be counted in the previous interval. This interval then gets higher values of multiplicity-dependent J/ψ, because these counts come from a region with higher J/ψ production probability. There is also an opposite influence from the counts with lower N_{ch} value. However, these do not cancel completely the effect due to higher multiplicity, because of the stronger-than-linear increase of multiplicity-dependent J/ψ yields. The same problem appears as soon as there are several values of charged-particle multiplicity in the same interval: the lower values of J/ψ production in the lower-multiplicity

part of the interval do not compensate for the higher values in the higher-multiplicity part of the interval. This is directly linked to the dependence of the results on the choice of the N_{tracks} intervals, where the generated N_{ch}-dependent curve is the reference for which each N_{ch} value has its own J/ψ yield assigned.

This problem can be understood better, and eventually corrected, from a small calculation. An interval I with $i_0 \leq N_{\text{ch}} \leq i_1$ is considered, and X and Y are respectively the reconstructed values of the multiplicity and of the J/ψ yields in this interval.

$$X = \langle N_{\text{ch}} \rangle_{\text{I}} = \frac{\sum_{i=i_0}^{i_1} i \times N_{evt}(i)}{\sum_{i=i_0}^{i_1} N_{evt}(i)} \,. \tag{5.21}$$

$$Y = \frac{\sum_{i=i_0}^{i_1} N_{J/\psi}(i)}{\sum_{i=i_0}^{i_1} N_{evt}(i)} \,. \tag{5.22}$$

The self-normalization, which is not considered here, would only change the results by a constant factor and not affect the main idea described here. The correct estimate of the multiplicity-dependent J/ψ production is a function f which should be independent of the specific interval I. It would only give the number of J/ψ per event at the exact value of charged-particle multiplicity given by X:

$$f(x) = \frac{N_{J/\psi}(x)}{N_{evt}(x)} \,. \tag{5.23}$$

It can be assumed that the function f follows a second-order polynomial distribution $f(x) = \alpha x^2 + \beta x$. The difference between the reconstructed value Y and $f(X)$ can be found using:

$$Y = \frac{\sum_{i=i_0}^{i_1} f(i) \times N_{evt}(i)}{\sum_{i=i_0}^{i_1} N_{evt}(i)} \,. \tag{5.24}$$

$$Y = \alpha \times \frac{\sum_{i=i_0}^{i_1} i^2 \times N_{evt}(i)}{\sum_{i=i_0}^{i_1} N_{evt}(i)} + \beta \times \langle N_{\text{ch}} \rangle \,. \tag{5.25}$$

$$Y = f(X) + \alpha \times (< N^2 > - < N >^2) \,. \tag{5.26}$$

$$Y = f(X) + \alpha \times V(N_{\text{ch}}) \,. \tag{5.27}$$

In this case, the error in the reconstructed value is estimated easily and is dependent on the variance of the N_{ch} distribution $V(N_{\text{ch}})$ in the interval. In the case with real data, this would be the variance from the distribution in Fig. 4.12, which is mostly due to the size of N_{tracks} intervals at low multiplicity, and Poisson smearing between N_{ch} and N_{tracks} at higher multiplicity. This variance, shown in the bottom panels of Fig. 5.33, increase with multiplicity, meaning that the absolute value of the error in reconstructed value also increases with multiplicity. However, at low multiplicity the J/ψ yields are smaller, consequently the relative error is higher in this case.

The correction for the MC closure is thus applied by subtracting $\alpha \times V(N_{\text{ch}})$. This results in the corrected points in Fig. 5.33, which, after correction, describe exactly the generated curve. In a more general case for f, it is possible to approximate the error with replacing α by $f''(X)$. In

the power-law case, this correction also allows a better reproduction of the generated curve. In order to apply this correction in real data, it would be necessary to know the local value of the second-order derivative. This can be extracted from a fit to the J/ψ vs multiplicity distribution. Different fit functions would give different values of the correction. As a default value, the correction using a power-law fit is chosen, because this fit function gives better agreement at low multiplicity where the relative impact of this effect is the highest.

5.7. Impact of the J/ψ daughters on the multiplicity estimator

The J/ψ decay daughters and the number of global tracks are measured in the same pseudorapidity region $|\eta| < 0.9$. That means that the decay daughters of the J/ψ are counted in the multiplicity estimator, but only in part of the cases because of different track requirements between J/ψ daughters and global tracks. These autocorrelations might bias the results, also because of the selection of a single decay channel. This could make the interpretation from the comparison with models unclear, especially when the model does not come from a Monte-Carlo generator and the treatment of the decay daughters is not easy to handle.

For this reason, it was also tried to remove J/ψ daughters from the multiplicity estimators. For each J/ψ candidate, the value of N_{tracks} is decreased by 0, 1 or 2, depending on the number of its daughters passing the requirements for being included in the multiplicity estimator. However the full N_{tracks} distribution is not changed, because it is assumed than the number of J/ψ counts is negligible compared to the total number of events.

In addition, another problem could happen when the daughters are included in the multiplicity estimator: if there is already a J/ψ candidate in the event, the two daughters already pass several good quality criteria. Therefore, they have a higher probability than an average track in a minimum-bias event to be included in the multiplicity estimator. Moreover, it is important that the final result does not depend on the J/ψ daughters selection, and on whether these selections are similar to the ones used for the multiplicity estimator or not.

In order to avoid the dependence on track selections, the first idea could be to always count the daughters as two tracks in the multiplicity estimator, even if they do not pass the required selections. That means that the multiplicity would be always increased by two units compared to the case when daughters are removed. But in this case, the multiplicity coming from these two tracks would be corrected twice for the smearing between N_{ch} and N_{tracks}: once due to the fact that the daughters are always counted, and once due to the unfolding of charged-particle multiplicity. The solution to this problem would then be to cancel the second correction for these two tracks. This is done by counting these tracks in the multiplicity estimator always with a probability of 55% (i.e. the average selection efficiency for the tracks in the multiplicity estimator), even if they do not pass the global tracks requirements. This corrects the J/ψ daughter selection bias because, after this correction, the probability for any of the daughters to be counted in the multiplicity becomes the same as an average track in a minimum-bias event.

The impact of the J/ψ selection bias with daughters included in N_{tracks} is checked with the toy model. In this case, for every event with a J/ψ, two of the charged particles are assumed to be
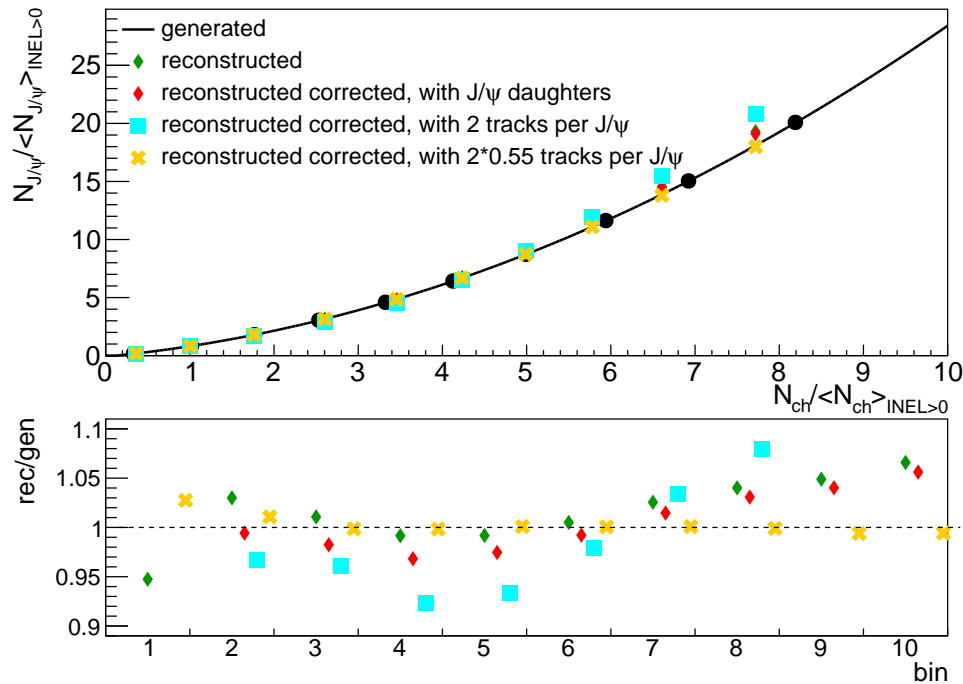
Figure 5.34.: MC closure test with a toy model. Different ways of counting the decay daughters in the multiplicity estimator are tested.

coming from the decay of J/ψ. It is assumed that the probability for each of these to pass the global tracks selections is 0.72 (this number is taken from data, for tracks which pass the J/ψ daughter selections). The $N_{ch} - 2$ particles from the rest of the event are smeared to a N_{tracks} value using the usual detector response matrix. In Fig. 5.34, three methods are tested: naively counting the daughters only if they pass the global track selections, always counting 2 tracks, or counting each daughter with a probability of 0.55. The comparison with the MC truth shows that only the last method is working correctly.

The number of raw inclusive J/ψ counts obtained in data when the daughters are included (using the method where each daughter is counted with a probability of 0.55) and when they are rejected are compared in Fig. 5.35. Since removing the decay daughters causes a smaller N_{tracks} value, less J/ψ are found at high multiplicity. This means that the multiplicity dependence would be weaker in this case compared to the case when the daughters are included.

5.8. Bias from the High-Multiplicity trigger

5.8.1. Bias with PYTHIA

The HM trigger selects the 0.1% events which have highest V0M amplitude. If there was a value of midrapidity multiplicity above which the HM trigger would select 100% of events, there would be no difference in the J/ψ event yields between INEL>0 and HM-triggered events for these high midrapidity multiplicities. However, such a value is not within reach. Therefore, it is possible that, at a given N_{ch} value, an INEL>0 event and an event triggered by the HM trigger would have different properties, and different J/ψ yield per event. The underlying event at forward
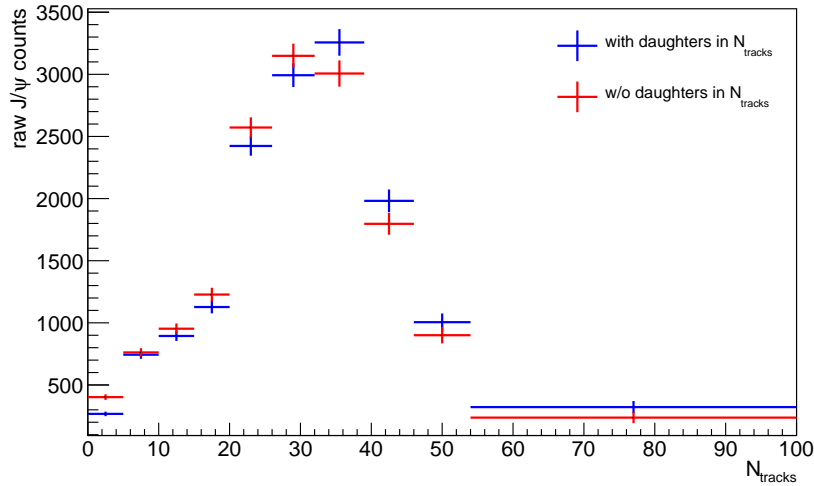
Figure 5.35.: Raw number of inclusive J/ψ with $p_\mathrm{T} > 0$ GeV/c as a function of N_tracks using MB and HM triggers. The case when the J/ψ daughters are included in the multiplicity estimator is compared to the case when the daughters are rejected from the multiplicity estimator.

rapidity could also have different properties if there is a J/ψ in the event, compared to other events. This especially depends on the correlations between multiplicity at forward rapidity, on which the trigger depends, and the multiplicity at midrapidity, as a function of which the yields are measured.

The statistical uncertainties in data do not allow a clear conclusion on whether such a bias is present or not. Therefore, a check is made in standalone PYTHIA8 simulations, without simulations of detectors with GEANT. The HM trigger is simulated by taking only the 0.1% events with highest charged-particle multiplicity in the acceptance of the V0 detector.

The multiplicity distribution at midrapidity for minimum-bias events and events selected by the HM trigger in PYTHIA is shown in the left panel of Fig. 5.36. The trigger efficiency increases as a function of multiplicity, but even at the highest available midrapidity multiplicity values, the trigger efficiency does not reach 100%, showing that a bias is possible. Due to the rise of trigger efficiency, if a bias was present, it would progressively decrease as a function of midrapidity multiplicity. The right panel of the same figure shows the average number of MPI as a function of midrapidity multiplicity for minimum-bias and high-multiplicity triggered collisions. At the same value of N_ch, the number of MPI is higher when requesting HM trigger. This indicates that this trigger indeed changes the topology and properties of the event. For example, the trigger could enhance the probability to find a jet with many particles within the V0 acceptance. Such an effect was indeed found significant in Ref. [204]. Another possibility is that, if a large multiplicity is to be found in both V0A and V0C, and if in addition there is a high-multiplicity at midrapidity, then isotropic events with a large number of MPI could be enhanced compared to jetty events.

The J/ψ yield as a function of multiplicity with all minimum-bias events, or with only HM events are compared in Fig. 5.37, for inclusive, prompt and non-prompt J/ψ. For inclusive J/ψ, MB and HM curves are compatible. However, when separating between prompt and non-prompt J/ψ, it can be observed that the non-prompt J/ψ is around 10% lower (for ~ 5 times the average
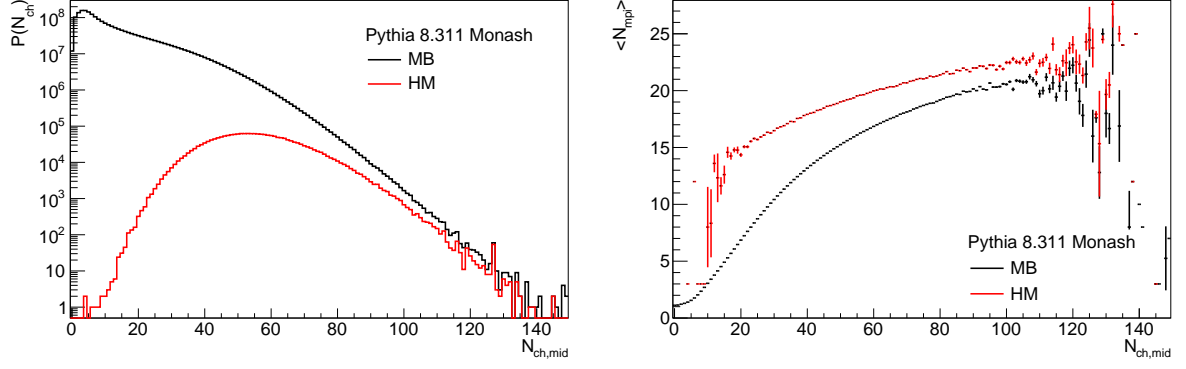
Figure 5.36.: $N_{\text{ch,mid}}$ (left) and $\langle N_{\text{MPI}} \rangle$ (right) as a function of $N_{\text{ch,mid}}$, for MB and HM triggers.

N_{ch}) with the HM trigger, whereas it is compensated by the prompt J/ψ, which is a few percent higher in the HM case.
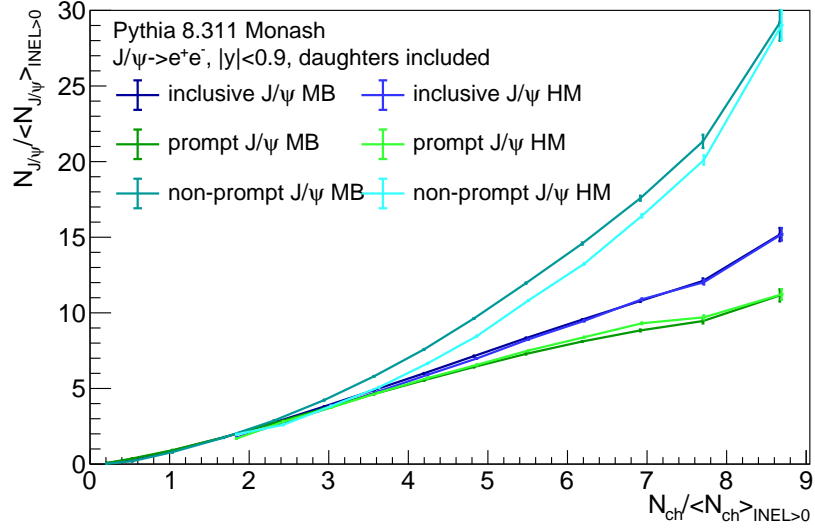
Figure 5.37.: Inclusive, prompt and non-prompt J/ψ yield as a function of multiplicity, with Minimum Bias or High Multiplicity selections.

The explanation for the bias could be that, with the HM trigger, if it is caused by a hard jet in the V0 acceptance, then this jet would not be present at midrapidity, reducing the midrapidity jet yield, and thus also reducing the non-prompt J/ψ yield, when considering jets induced by a b quark. It could also be possible that more isotropic events are selected than jetty ones, also causing in this case a probable suppression of beauty jets and non-prompt J/ψ.

In order to understand whether the bias could be linked to the jettiness/isotropy of the event, it could be useful to look at spherocity. This variable is defined as:

$$S_0 = \frac{\pi^2}{4} \min_{\vec{n}} \left(\frac{\sum_i |\vec{p}_{\text{T},i} \times \vec{n}|}{\sum_i p_{\text{T},i}} \right)^2 . \tag{5.28}$$

$\vec{p}_{\text{T},i}$ is the transverse momentum vector of the i-th particle (within $|\eta| < 0.9$), and $\vec{n}$ is a unit vector which minimizes this quantity, usually assumed aligned with one of the particles. In the

case of back-to-back jets, most particles would be aligned or anti-aligned with the $\vec{n}$ vector, and the vector product would give a value close to 0. For an isotropic event, particles could have any angle with respect to the $\vec{n}$ vector, and then the sphericity would be closer to 1, the maximal possible value.

The sphericity distribution is shown in the left panel of Fig. 5.38, for HM and MB triggers. HM events show higher values of sphericity, showing that they are more isotropic compared to MB. However, there could be a bias due to the fact that the midrapidity multiplicity is different in the two cases. Hence, the right panel of Fig. 5.38 shows the mean sphericity as a function of midrapidity multiplicity for MB, HM events, but also events with non-prompt J/ψ. Even at fixed multiplicity, HM events are more isotropic than MB events, while events with non-prompt J/ψ are more jetty, which means that the bias could be caused by the non-prompt J/ψ being missed in the more isotropic HM events. An idea in order to correct for the bias due to the HM trigger could then be to reweight the sphericity distribution of HM events so that it matches the one of MB events. Weights would be higher at lower sphericity, and then increase the jetty part of the event. However, the effect of reweighting events has been found to be too small (less than 2%) to correct for the whole bias in the non-prompt J/ψ case. An explanation for the smallness of the correction could be that the sphericity only uses midrapidity, which is too far from the V0 acceptance which determines the trigger. A correction would need to be more complex and take into account much more dimensions and parameters than just the sphericity.
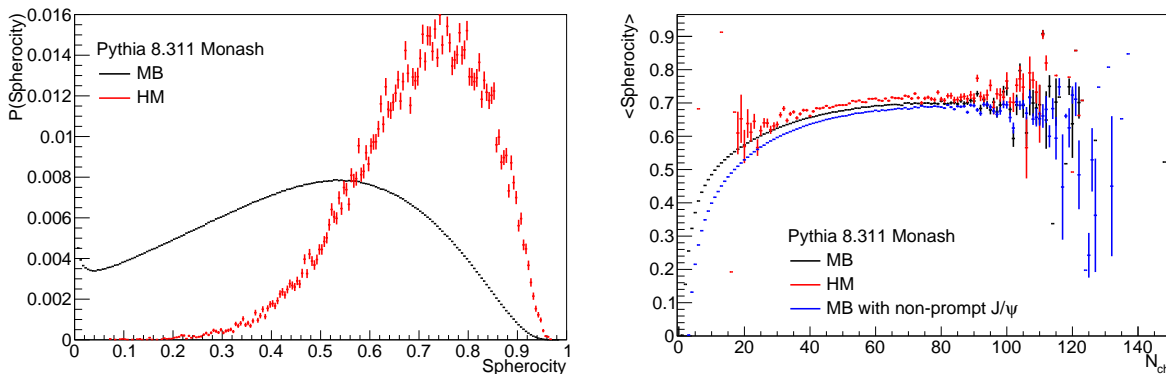
Figure 5.38.: Left: Distribution of sphericity for Minimum Bias and High-Multiplicity triggered events. Right: Mean sphericity as a function of charged-particle multiplicity at midrapidity for Minimum Bias, High-multiplicity triggered events, and events with non-prompt J/ψ.

It is also possible that the bias due to the HM trigger is different when computing the multiplicity in regions. In Fig. 5.39, the multiplicity-dependent J/ψ in the toward, transverse and away region are compared between minimum-bias events, and only events triggered by high forward multiplicity. For toward multiplicity, there also seems to be a small bias, similar to the one for inclusive multiplicity. The explanation there could be that the toward region contains the hardest part of the event. This is the part of the midrapidity multiplicity which could contain the strongest correlation with the multiplicity at forward rapidity. Because the magnitude of the bias depends on the correlation between the two rapidity regions, toward region and inclusive multiplicity would get a similar bias, for similar reasons. However, for transverse and away regions, there is a larger bias, with higher values of J/ψ production in the HM case, which can be seen especially for multiplicity values less than 6 times the average multiplicity. In these two

cases, the correlation with the forward rapidity is less strong than for the toward region. At given transverse or away multiplicity, the presence of a high forward multiplicity possibly enhances the probability to find a J/ψ, for example in a back-to-back jet where one jet is at forward rapidity and the other one at midrapidity in the toward region, where the J/ψ can be found. The away case has also a smaller bias for non-prompt J/ψ than for prompt J/ψ or compared to the transverse region. This could also be due to a stronger correlations due to back-to-back jet topologies. The HM bias is stronger at lower multiplicity, where only a small fraction of events are selected in the trigger, than at higher multiplicity, where many events are common to minimum-bias and HM triggers.
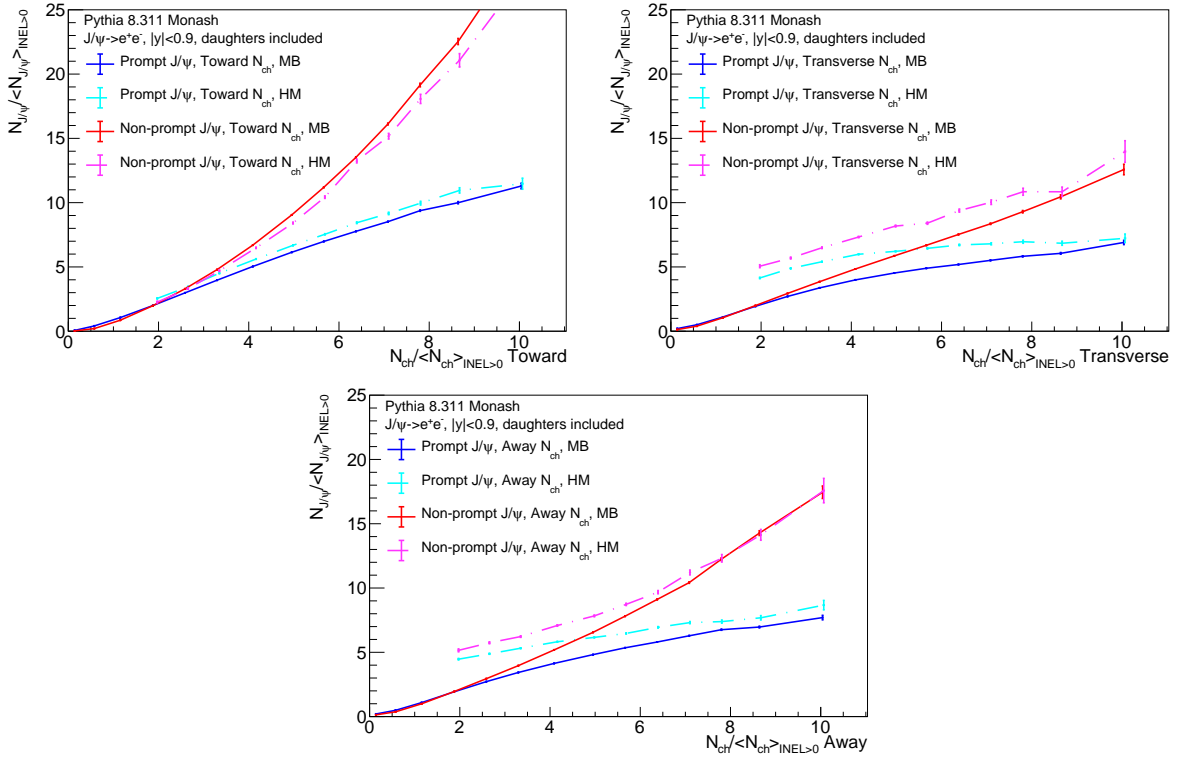
Figure 5.39.: Prompt and non-prompt J/ψ production as a function of multiplicity in regions, compared between minimum-bias and HM-triggered events. Top left: Toward region. Top right: Transverse region. Bottom: Away region.

Due to all the biases presented in this subsection, and the fact that a perfect correction could not be extracted, it would not make sense to merge MB and HM data points. These triggers select different physics processes, even at same N_{ch} values. For this reason, MB- and HM-triggered data will be shown separately in the final results

5.8.2. Additional bias when removing the daughters

The midrapidity multiplicity distributions for MB and HM events differ, and their ratio never reaches unity. Especially when the HM distribution rises while MB distribution is still increasing, the impact of removing the two daughters of the J/ψ would be different if the MB multiplicity distribution is considered compared to the case where the HM distribution is considered. Then,

an additional trigger bias would be found in the case when daughters are removed, in addition to the one described in Sec. 5.8.1.

For the understanding and the quantification of this possible bias, several assumptions are made. First, even if there is a bias from the HM trigger when including the daughters, this bias is small. Therefore, for simplification of the demonstration, it is assumed that there is no bias when including the daughters. The impact of the trigger can be understand by introducing a multiplicity-dependent event trigger efficiency ε_{trig} and J/ψ trigger efficiency $\varepsilon_{trig,\ \mathbf{J}/\psi}$. At a given N_{tracks}, if the multiplicity-dependent J/ψ yield was not modified by the presence of the HM trigger when the daughters are included, the event and J/ψ trigger efficiency would be similar: $\varepsilon_{trig,\ \mathbf{J}/\psi}(N_{\text{tracks}}) = \varepsilon_{trig}(N_{\text{tracks}})$. However, when removing the daughters from the multiplicity, the multiplicity associated to a J/ψ is biased by two tracks, while the multiplicity distribution for events without the requirement of the presence of a J/ψ is not modified.

If the daughters are removed, and if the trigger efficiency could be corrected, the factor entering the yield calculation would be:

$$
\frac{N_{\mathbf{J}/\psi}\left(N_{\text{tracks}}^{\text{w/o daughters}}\right)}{\varepsilon_{trig,\ \mathbf{J}/\psi}^{\text{w/o daughters}}\left(N_{\text{tracks}}^{\text{w/o daughters}}\right)} \frac{\varepsilon_{trig}\left(N_{\text{tracks}}^{\text{w/o daughters}}\right)}{N_{evt}\left(N_{\text{tracks}}^{\text{w/o daughters}}\right)} \,.
\tag{5.29}
$$

Up to a global scaling factor independent of the multiplicity, the event trigger efficiency ε_{trig} can be calculated with:

$$
\varepsilon_{trig}\left(N_{\text{tracks}}^{\text{w/o daughters}}\right) \propto \frac{N_{HM}\left(N_{\text{tracks}}^{\text{w/o daughters}}\right)}{N_{MB}\left(N_{\text{tracks}}^{\text{w/o daughters}}\right)} \,.
\tag{5.30}
$$

Because the trigger depends on forward rapidity multiplicity, for a given J/ψ, the trigger efficiency does not depend on whether the daughters of this J/ψ are counted on the multiplicity or not. Therefore, the J/ψ trigger efficiency at $N_{\text{tracks}}^{\text{w/o daughters}}$ when the daughters are removed $\varepsilon_{trig,\ \mathbf{J}/\psi}^{\text{w/o daughters}}$ is the same as the J/ψ trigger efficiency at N_{tracks} when the daughters are included $\varepsilon_{trig,\ \mathbf{J}/\psi}(N_{\text{tracks}})$. Because of the previous assumption that $\varepsilon_{trig,\ \mathbf{J}/\psi}(N_{\text{tracks}}) = \varepsilon_{trig}(N_{\text{tracks}})$ when the daughters are included, the J/ψ trigger efficiency can be estimated with:

$$
\varepsilon_{trig,\ \mathbf{J}/\psi}^{\text{w/o daughters}}\left(N_{\text{tracks}}^{\text{w/o daughters}}\right) = \varepsilon_{trig}(N_{\text{tracks}}) \propto \frac{N_{HM}(N_{\text{tracks}})}{N_{MB}(N_{\text{tracks}})} \,.
\tag{5.31}
$$

These equations show that the yields in the HM-triggered sample can be corrected for the trigger efficiency if a weight is applied for each J/ψ candidate. This weight corrects for the additional difference in trigger efficiencies for J/ψ and unbiased events, when the daughters are removed:

$$
\text{weight} = \frac{N_{HM}\left(N_{\text{tracks}}^{\text{w/o daughters}}\right)}{N_{MB}\left(N_{\text{tracks}}^{\text{w/o daughters}}\right)} \frac{N_{MB}(N_{\text{tracks}})}{N_{HM}(N_{\text{tracks}})} \,.
\tag{5.32}
$$

This weight is only based on the multiplicity distributions for MB and HM trigger not biased by any requirement on the presence of J/ψ. Its value is lower than 1, and depends on the slope of the HM trigger efficiency: the higher the multiplicity, the closer this weight is to 1, because the HM trigger becomes closer to being fully efficient. This weight only accounts for the additional bias which appears when removing the daughters compared to the case when the daughters are included in multiplicity. Contrary to the bias shown in the previous subsection, which depends on completely different physics processes, this bias is only caused by different multiplicity distributions. The impact of the removal of two tracks is easier to estimate, explaining why it is possible to correct for this additional bias. Moreover, the HM-trigger efficiency depends on the whole event, including the J/ψ itself, hence the assumption that this efficiency is more directly correlated to $N_{\text{tracks}}^{\text{with daughters}}$ than to $N_{\text{tracks}}^{\text{w/o daughters}}$. This might be the driving factor explaining why the bias of the HM trigger obtained with daughters inclusion is small.
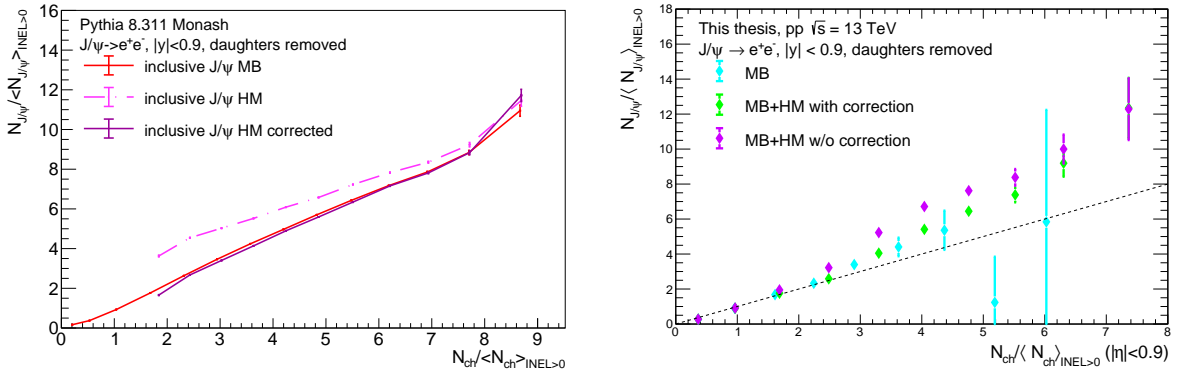
Figure 5.40.: Multiplicity-dependent inclusive p_{T}-integrated J/ψ yield where the daughters have been removed from the multiplicity, in PYTHIA (left) and data (right). A comparison is done between minimum-bias events, and HM events with and without the correction for additional trigger bias appearing when removing the daughters.

In order to check the impact when applying this weight, the multiplicity-dependent J/ψ is shown in Fig. 5.40, when removing the J/ψ daughters from the multiplicity, with the MB trigger, as well as with the HM trigger with or without this correction. The PYTHIA case, for inclusive J/ψ and $p_{\text{T}} > 0$ GeV/c is shown in the left panel of this figure, while the result in data is shown in the right panel. PYTHIA simulations show that, without this weight, the bias between MB and HM trigger becomes quite large. With this weight, the level of the bias is similar to the one present when the daughters are included in the multiplicity calculation. For data, a bias between the yields with MB data and with a combination of the MB and HM sample appears in the region where the measurements overlap. Applying the weights seems to correct for this bias.

6. Systematic uncertainties

An important part of the analysis is the correct estimate of the uncertainties related to the methods, modelings, or assumptions which were made while performing the analysis, and which could have systematically modified the result. These systematic uncertainties can affect both the measurement of the charged-particle multiplicity and of the J/ψ yields. Several sources are identified as potentially having an impact on the results. In most cases, the uncertainty is estimated by repeating the analysis several times, with variations in the methods or assumptions. Unless stated otherwise, the uncertainty on the value of a data point is thus estimated by taking the Root Mean Square (RMS), defined as:

$$\sigma = \frac{1}{\sqrt{N-1}} \sqrt{\sum_{i=1}^{N} \left(Y_{\text{var, i}} - Y_{\text{default}}\right)^2}. \tag{6.1}$$

N is the total number of variations, including the default one, and $Y_{\text{var, i}}$ is the value of this data point obtained when considering the given variation. For example, it means that, when there is only one default value and one variation, the uncertainty will be the difference between both. The uncertainties from all different sources are assumed uncorrelated, and they are summed in quadrature.

In the total uncertainty, the systematic uncertainties add in quadrature to the statistical uncertainties. These arise due to the limited size of the sample which, due to the random nature of processes such as J/ψ production, does not allow to estimate the true physical parameter with sufficient precision. When the systematic variations are themselves subject to statistical fluctuations, the corresponding uncertainty could be counted twice. In order to avoid this effect, when the variations are sensitive to statistical fluctuations, several multiplicity intervals are merged when computing the variations, and the same systematic uncertainty is assigned for all the intervals which were merged together.

6.1. Systematic uncertainties on the multiplicity

Several sources can affect the estimation of self-normalized multiplicity in all the intervals: the estimation of the trigger efficiency, the unfolding, and the correct description in the MC of the smearing matrix, including the MC generator used as well as the detector effects. Because of the self-normalization between the average multiplicity in a given N_{tracks} interval and the average multiplicity in INEL>0 events, part of these systematics would cancel. However some systematic effects might remain, due to effects which are dependent on multiplicity.

V0AND Trigger efficiency:

The efficiency of the V0AND trigger corrects from the measured multiplicity distribution in the MB sample to the one in INEL>0 events. Because the MC is used for trigger efficiency estimation, the accuracy of this estimation depends on how well the V0AND trigger is described in the MC. Trigger efficiency correction modifies $\langle N_{\mathrm{ch}} \rangle$, which means that all multiplicity intervals are affected in the self-normalization of the multiplicity in the same way. The only exception could be for the lowest multiplicity interval, where the trigger efficiency uncertainty might affect both the numerator and the denominator in the result, hence partly cancelling, but it is not taken into account. An uncertainty on $\langle N_{\mathrm{ch}} \rangle$ in INEL>0 events of 1.3% had been determined in [144], and the same value is used there.

Unfolding:

Possible sources of systematic uncertainties for the unfolding include:

- The unfolding algorithm: other unfolding algorithms could give different results. The Iterative, Dynamically Stabilized (IDS) unfolding [205] was tested. It also uses an iterative method which corrects the unfolded spectrum, but introduces in addition several regularization parameters. These parameters intend to avoid the unfolding of a possible background and control the propagation of the fluctuations. Left panel of Fig. 6.1 compares the INEL>0 N_{ch} distributions obtained with Bayesian and IDS unfolding. The ratio between both distributions differs from 1 by a maximum of 1%, and both methods give the same $\langle N_{\mathrm{ch}} \rangle$ values. The difference in the self-normalized N_{ch} values obtained with both methods is found to be negligible, to a level below 0.1%.

- Comparison between resmeared and measured distribution: This comparison has been shown in Fig. 4.7. The values of $N_{\mathrm{tracks}}/\langle N_{\mathrm{tracks}} \rangle$ for every multiplicity interval are found to be compatible within 0.1%.

- MC closure test: The N_{tracks} distribution in the MC is unfolded, with a prior distribution in the algorithm considered flat as a function of N_{ch}, and compared to the true generated N_{ch} distribution. This comparison is shown in the right panel of Fig. 6.1. Both distributions have the same $\langle N_{\mathrm{ch}} \rangle$ value, and the discrepancy is 2% at maximum: such differences in the N_{ch} distribution were found to have negligible impact in the final values when comparing IDS and Bayesian unfolding. Therefore, no uncertainty is assigned in this case.

- Choice of prior: the MC closure test was started with flat prior, and the generated N_{ch} distribution could still be reproduced. Therefore, the prior give negligible uncertainty.

- Number of iterations: The number of iterations for the unfolding algorithm was changed. The default with χ^2 stopping results in around 15–20 iterations, and the number of iterations was changed to 5 and to 10. In both cases, the difference in $N_{\mathrm{ch}}/\langle N_{\mathrm{ch}} \rangle$ are of the order of 0.1% maximum. Since the change in number of iterations is quite large, no systematic was assigned in this case.

- MC statistics: The detector response matrix is extrapolated at high multiplicity, as explained in Sec. 4.4.4. A comparison is done on the self-normalized multiplicity with and without this extrapolation. The only difference is in the last multiplicity interval, which differs by 0.2%.
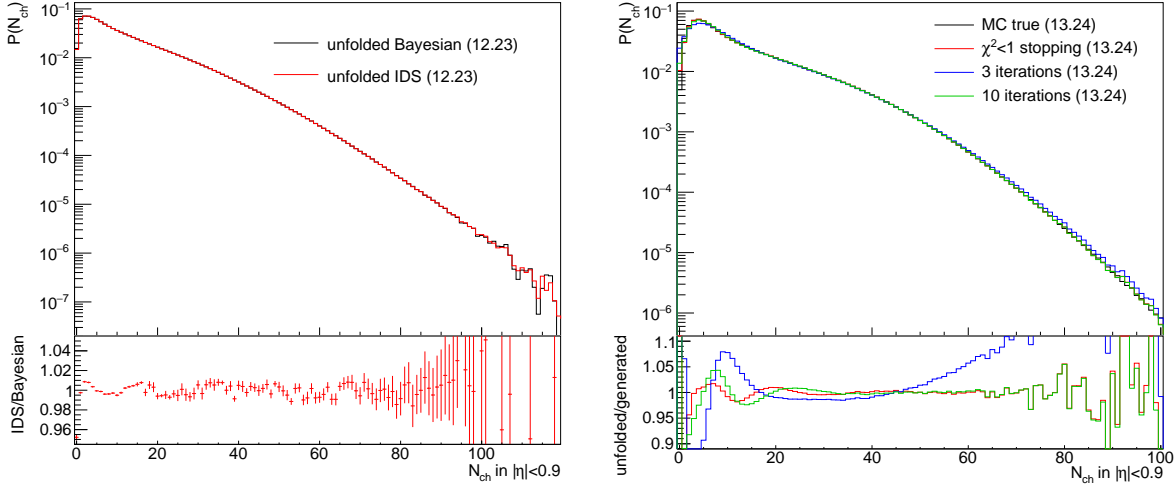

Figure 6.1.: (left) Comparison between the unfolded N_{ch} distribution in data obtained with Bayesian and IDS unfolding. (right) Monte-Carlo closure test. The MC generated N_{ch} distribution is compared with the unfolded distribution with different number of iterations in Bayesian unfolding algorithm. In both panels, bottom panel shows ratio between N_{ch} distributions, while legends show $\langle N_{ch} \rangle$.

Comparison between EPOS and PYTHIA:

By default, the detector response matrix has been extracted from simulations using PYTHIA. As discussed in Sec. 4.4.2, the track-level reconstruction efficiencies are particle species and p_T-dependent. Therefore, a correct description of the particle abundances in the MC is necessary for obtaining accurate results, and the results could be different when unfolded using two different generators such as EPOS or PYTHIA. Although the PCC corrects for this effect, other problems appear, especially due to the weighting which artificially enhances the smearing of N_{tracks} in the response matrix. Hence, a systematic uncertainty is assigned, by comparing the results obtained when using PYTHIA8 to unfold the multiplicity distribution and the ones when using EPOS LHC. The comparison between the unfolding with EPOS and PYTHIA for inclusive multiplicity is shown in Fig. 6.2. The left panel compares both unfolded multiplicity distributions while the right panel shows the ratio for the self-normalized values. The same comparison, but when the multiplicity is determined in azimuthal angle regions, is shown in Fig. 6.3. In both cases, at low multiplicity, both N_{ch} distributions agree. However at higher multiplicity, the data unfolded with EPOS, for which the effect of the PCC is smaller compared to PYTHIA because EPOS LHC reproduces particle abundances better, predicts a harder distribution. This produces discrepancies of a few percent. These discrepancies are larger for the multiplicity in azimuthal regions. This could be due to the fact that the smaller absolute N_{tracks} or N_{ch} values enhance more the relative fluctuations.
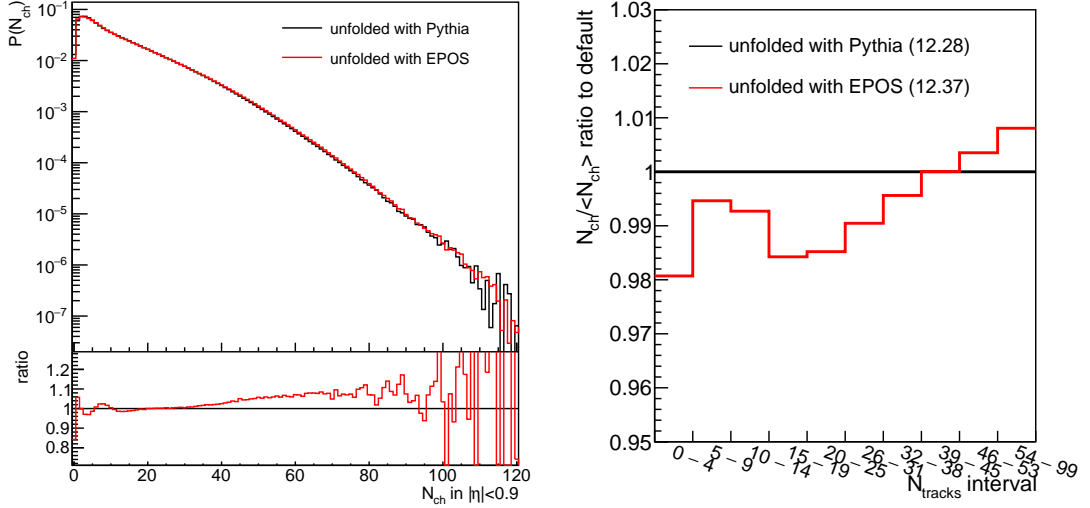
Figure 6.2.: (left) Comparison of the N_{ch} distribution obtained from unfolding the real data with distribution from PYTHIA and from EPOS generators. (right) Ratio of $N_{ch}/\langle N_{ch}\rangle$ for unfolding with PYTHIA with $N_{ch}/\langle N_{ch}\rangle$ with EPOS.
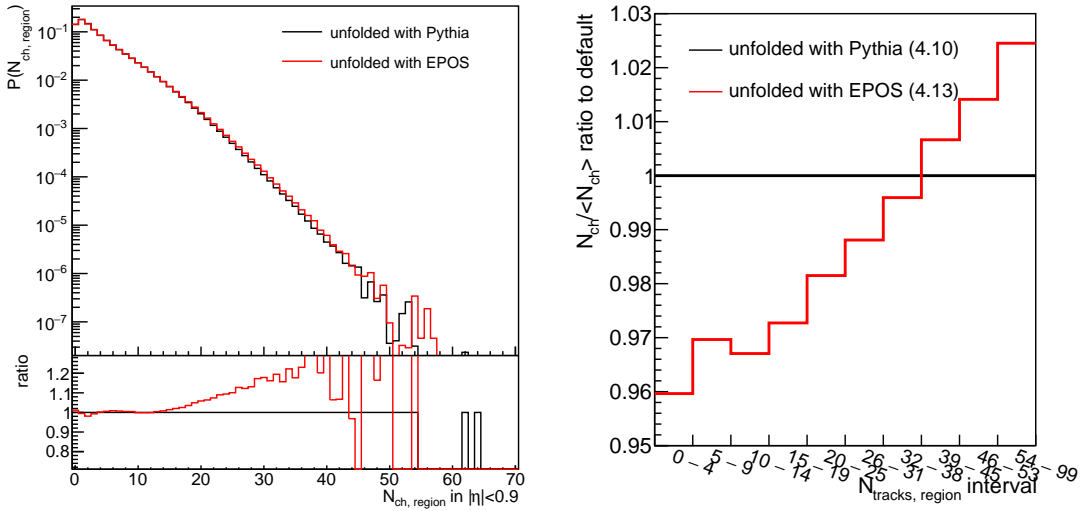

Figure 6.3.: (left) Comparison of the $N_{ch,regions}$ distribution obtained from unfolding the real data with distribution from PYTHIA and from EPOS generators. (right) Ratio for the azimuthal regions of $N_{ch}/\langle N_{ch}\rangle$ for unfolding with PYTHIA with $N_{ch}/\langle N_{ch}\rangle$ with EPOS.

Detector response matrix:

In addition to the wrong description of particle abundances depending on the MC generator, it is possible that a discrepancy between data and MC appears during the propagation to the detectors or the reconstruction. This would affect the estimation of the tracking efficiency and the correlation between N_{ch} and N_{tracks}. In order to estimate the discrepancy, the selection for the tracks in the multiplicity calculation is varied. If the smearing matrix was completely reproduced in the MC, the unfolded N_{ch} distribution would be independent of the multiplicity estimator. In contrast, if the efficiency is not perfectly estimated, different selections could give different results. This has been checked in Fig. 6.4, where several of the track requirements were changed. Only one of these requirements is modified at the same time, and either a looser or a tighter selection is applied. A small difference can be observed in the $\langle N_{ch}\rangle$ obtained with all

these different selections. However, this difference reaches 1% at maximum, which occurs when the requirement on fraction of crossed rows is tightened. This shows that the characteristics of the detectors and of the reconstruction are probably well reproduced in the MC.
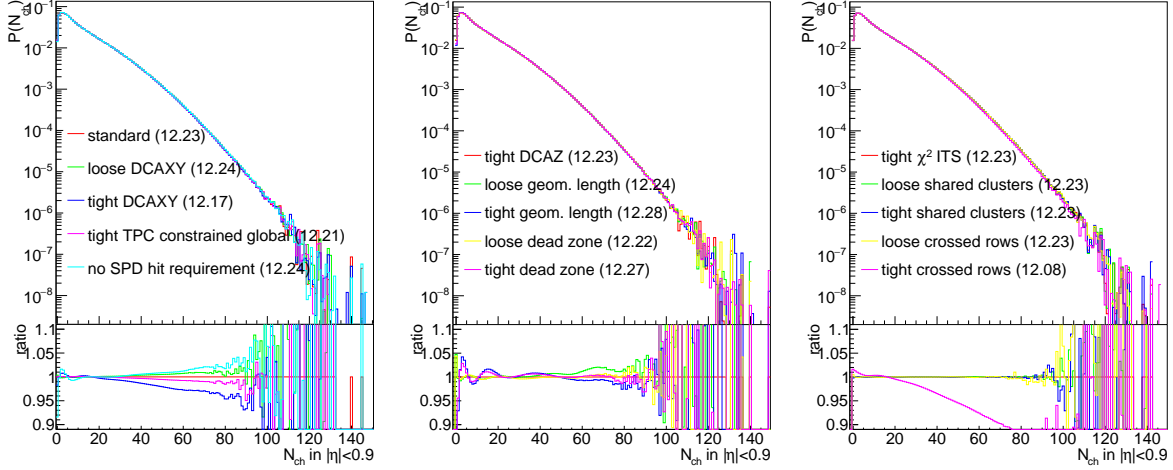

Figure 6.4.: Left, middle, and right: Comparison between unfolded distributions with variations of the multiplicity estimator, and ratio to the standard one (bottom panels). In parenthesis is the $\langle N_{\mathrm{ch}} \rangle$ in INEL>0 events.

In order to obtain a systematic uncertainty for the self-normalized multiplicity values, a first possibility could be to redo the full analysis many times. The J/ψ yields would be each time recalculated in different N_{tracks} intervals, with each time a new multiplicity estimator. However, in this case, it might lead to other problems. Due to the low number of J/ψ counts, statistical fluctuations can appear and would be difficult to decorrelate from the systematic effects. Additionally, intervals of N_{tracks} from different multiplicity estimators would give, after unfolding, different average N_{ch} value within this interval. Then, the variations would have different results for both the multiplicity on the x axis, and the J/ψ yields on the y axis. If they follow the same trend, for example with lower multiplicity and lower J/ψ yields, the uncertainties partially cancel. A possibility to bring a better estimation could be to fit the $J/\psi - N_{\mathrm{ch}}$ correlation, and use the fit to compare all the points at the same x or at the same y value. However, in this case, the uncertainties would depend on the quality of the fit function.

Due to these reasons, another method was used to estimate this uncertainty. The first step is the estimation of uncertainties on track-level efficiency. An upward systematic takes into account all the variations for which the $\langle N_{\mathrm{ch}} \rangle$ value after unfolding is lower than the default. If the standard variation reproduces correctly the efficiency in data, the reconstruction efficiency for these variations is overestimated. Each variation only modifies one individual requirement each time, and it is assumed that all these requirements are uncorrelated. Thus, all relative differences between $\langle N_{\mathrm{ch}} \rangle$ obtained with the considered variation and the default $\langle N_{\mathrm{ch}} \rangle$ are added in quadrature. The same is done for the downward systematic. The uncertainty of matching between ITS and TPC, obtained by comparing matching efficiency in data and MC, and which also depends on p_{T} and data taking period, is also added in quadrature to the track-level uncertainty.
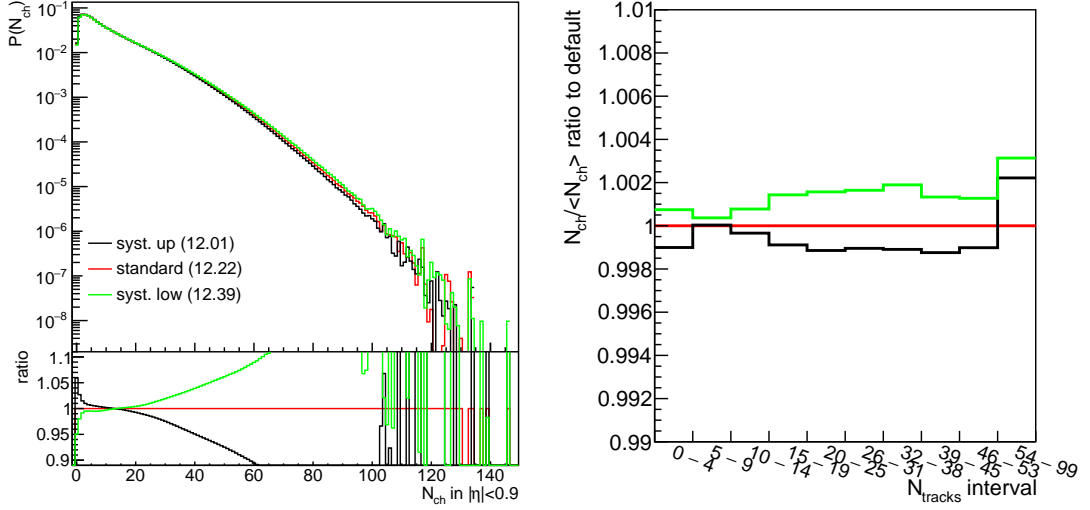
Figure 6.5.: Left: N_{ch} distribution in MB obtained with the standard selections and standard smearing matrix compared to the ones obtained with standard selections and modified smearing matrix. Right: systematic uncertainty on the self-normalized multiplicity from the change of smearing matrix.
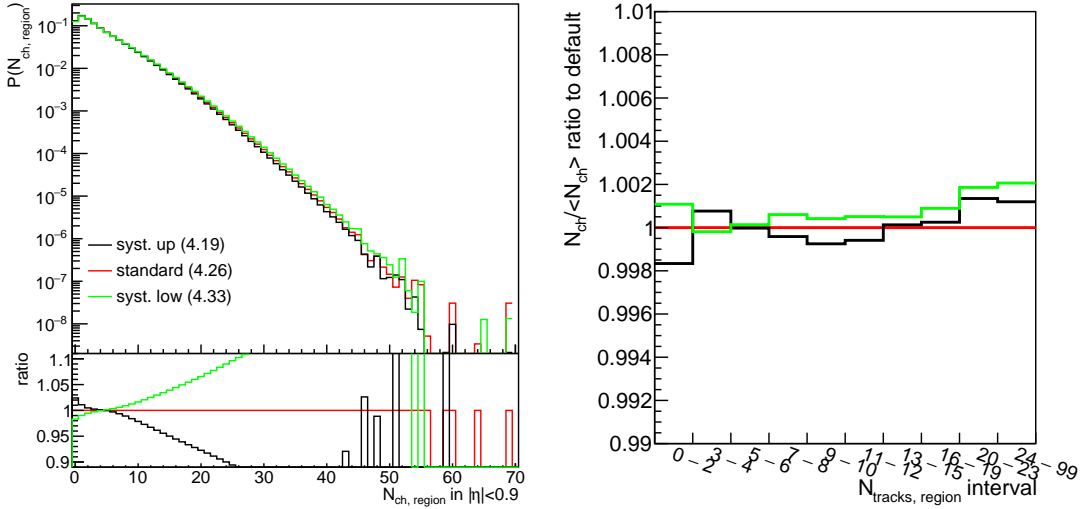
Figure 6.6.: Left: $N_{ch,regions}$ distribution in MB obtained with the standard selections and standard smearing matrix compared to the ones obtained with standard selections and modified smearing matrix. Right: systematic uncertainty on the self-normalized multiplicity for azimuthal regions from the change of smearing matrix.

The next step consists in using this track-level uncertainty in the MC in order to construct variations of the detector response matrix. The response matrix representing the upward possible value of the efficiency is built by randomly counting some tracks twice. The probability for this double-counting of tracks is equal to the upward track-level uncertainty. In contrast, the MC particle always counts as one in N_{ch}. This means that N_{ch} is not modified, while N_{tracks} is enhanced. The same is done for the downward variation, where each track has a given probability not to be counted at all. The multiplicity analysis is then repeated with the modified matrices. The new N_{ch} distribution, as well as the ratio between the self-normalized values of the variations and the self-normalized values in the default case are shown in Fig. 6.5 for inclusive multiplicity, and in Fig. 6.6 for azimuthal regions. The difference in $\langle N_{ch} \rangle$ reaches 2%,

but most of this difference cancels during self-normalization, making the uncertainty small. The maximum difference to the standard self-normalized multiplicity value is assigned as a systematic uncertainty.

Summary of the systematics on the multiplicity:

In table 6.1 is shown a summary of the systematics for the estimation of the azimuth-inclusive self-normalized multiplicity, and in table 6.2 for the case of multiplicity in regions.

Table 6.1.: Summary of the systematic uncertainties on the multiplicity

N_{tracks}	0–4	5–9	10–14	15–19	20–25	26–31	32–38	39–45	46–53	> 54
$N_{\text{ch}}/\langle N_{\text{ch}}\rangle$	0.37	1.01	1.76	2.60	3.46	4.23	4.99	5.78	6.61	7.72
V0AND Trigger efficiency	1.3%									
Unfolding	negligible									0.2%
Generator	2%	0.6%	0.8%	1.6%	1.5%	1%	0.4%	0%	0.4%	0.8%
Detector response matrix	0.1%			0.2%						0.3%
Total	2.4%	1.4%	1.5%	2.1%	2%	1.7%	1.4%	1.3%	1.4%	1.6%

Table 6.2.: Summary of the systematic uncertainties on the multiplicity in azimuthal angle region

$N_{\text{tracks,region}}$	0–2	3–4	5–6	7–8	9–10	11–12	13–15	16–19	20–23	> 24
$N_{\text{ch,region}}/\langle N_{\text{ch,region}}\rangle$	0.51	1.63	2.61	3.48	4.23	4.90	5.65	6.64	7.79	9.19
V0AND Trigger efficiency	1.3%									
Unfolding	negligible								0.2%	0.3%
Generator	4%	3%	3.3%	2.7%	1.9%	1.2%	0.4%	0.7%	1.4%	2.5%
Detector response matrix	0.2%	0.1%							0.2%	0.2%
Total	4.2%	3.3%	3.6%	3%	2.3%	1.8%	1.4%	1.5%	1.9%	2.8%

6.2. Systematic uncertainties on the prompt and non-prompt J/ψ yields

The other systematic uncertainties are related to the estimation of the prompt and non-prompt yields with the BDT. Similar to the self-normalized multiplicity, part of the errors cancels in the self-normalization, such as the ones due to reconstruction efficiency, assumed independent of the multiplicity. The uncertainties come from the trigger efficiency estimation (for V0AND and TRD triggers), unfolding, extraction of the J/ψ signal, training of the BDT, selections on the BDT score, p_{T} distribution and beauty hadron abundances in the MC, determination of the primary vertex position, and tracking efficiency in events with J/ψ. Due to a similar performance in the signal extraction between the MB and the HM samples at a given multiplicity value, the systematic uncertainties in these two samples are assumed similar and are estimated while merging the two samples. For the TRD sample, due to the different background, and the use of an independent BDT model, the systematic uncertainties are estimated independently, but the same methods are used for the estimation.

V0AND Trigger efficiency:

The trigger uncertainty could change the total number of INEL>0 events, while the raw J/ψ counts would be little affected because non-triggered events have very low multiplicity. Therefore, it will affect the total J/ψ yield per INEL>0 event. However, if a systematic variation gives a lower correction because of trigger efficiency, $\langle N_{ch} \rangle$ would be higher, and the self-normalized multiplicity will be lower. In addition, the total number of INEL>0 events will be lower, and the INEL>0-integrated yield will be higher. Then, the value of self-normalized yield will be lower. Since both x and y values of the data point are lower, the data point would stay on the same trend. Assigning this uncertainty for both self-normalized yield and self-normalized multiplicity would be double counting. Hence, no uncertainty due to this effect is assigned for the J/ψ yield, but only for the multiplicity.

In addition, it is possible that some J/ψ counts are missed, when they are part of events which are not MB-triggered. The number of such J/ψ signals is expected to be small, because the only events missing have very low multiplicity. It was checked on minimum-bias PYTHIA8 simulations, that the number of untriggered J/ψ in the MB is very small, around 0.2% for prompt J/ψ and 0.1% for non-prompt J/ψ. Thus, the J/ψ signals escaping trigger detection only matter in the first multiplicity interval, where the uncertainty amounts to around 2%. These values are assigned as systematic uncertainties.

TRD trigger efficiency:

For TRD-triggered data, an additional variation comes from the estimation of TRD trigger efficiency. The source of systematic uncertainties for the J/ψ self-trigger efficiency are the statistical uncertainty of the single-leg efficiency, as well as the removal of the correlated and UE component in the single-leg efficiency. The former one is evaluated by varying each point within its statistical uncertainty several times, and each time the pair efficiency and the self-normalized yields are recomputed. The uncertainty is found negligible. The latter one is estimated by, rather than removing UE and correlated triggers with templates from PYTHIA, only removing a template with an efficiency independent of p_T and amounting to 0.5%. The ratio between the variations of the pair self-trigger efficiency and the default value are shown in Fig. 6.7. The variation due to the correlated and UE template is large, and depends on p_T, with values reaching a minimum of around 5% in a plateau region around 3 GeV/c, while the variations are larger at lower or higher p_T.

The uncertainty of the UE efficiency is estimated via MC simulations, by comparing with PYTHIA the estimation of UE efficiency using the multiplicity dependence, as done in data, and its true value. It has already been shown in Fig. 5.16 that the estimation is off by 15%. The systematic uncertainty on the yields due to this source is estimated by comparing to the default yields the ones obtained by scaling the UE efficiency by $\pm 15\%$. For non-prompt J/ψ, the efficiency due to the $b\bar{b}$ correlations is also scaled by $\pm 15\%$.

The variations due to TRD trigger efficiency for inclusive J/ψ counts and f_B are shown in Fig. 6.8.
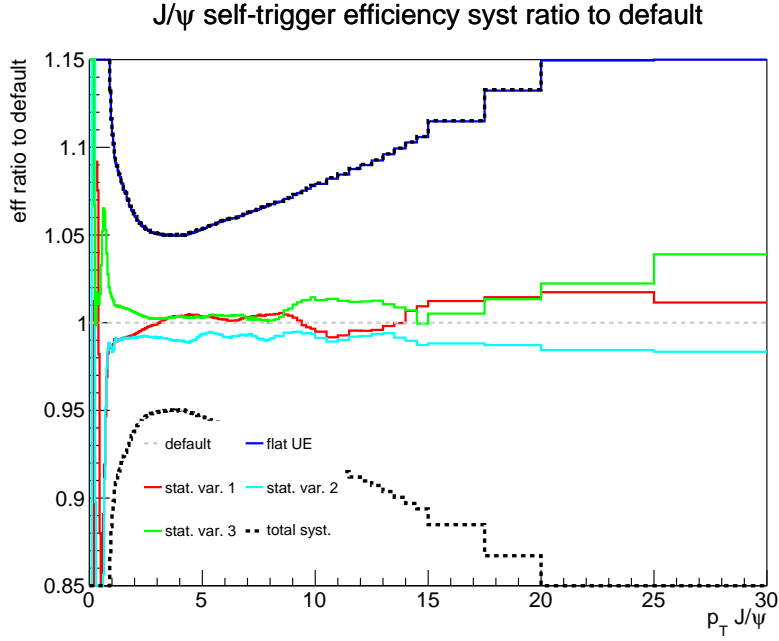
Figure 6.7.: Ratio between systematic variations of the TRD trigger pair efficiency and default case. As an indication, the sum in quadrature of both uncertainties is shown with black dashed line.
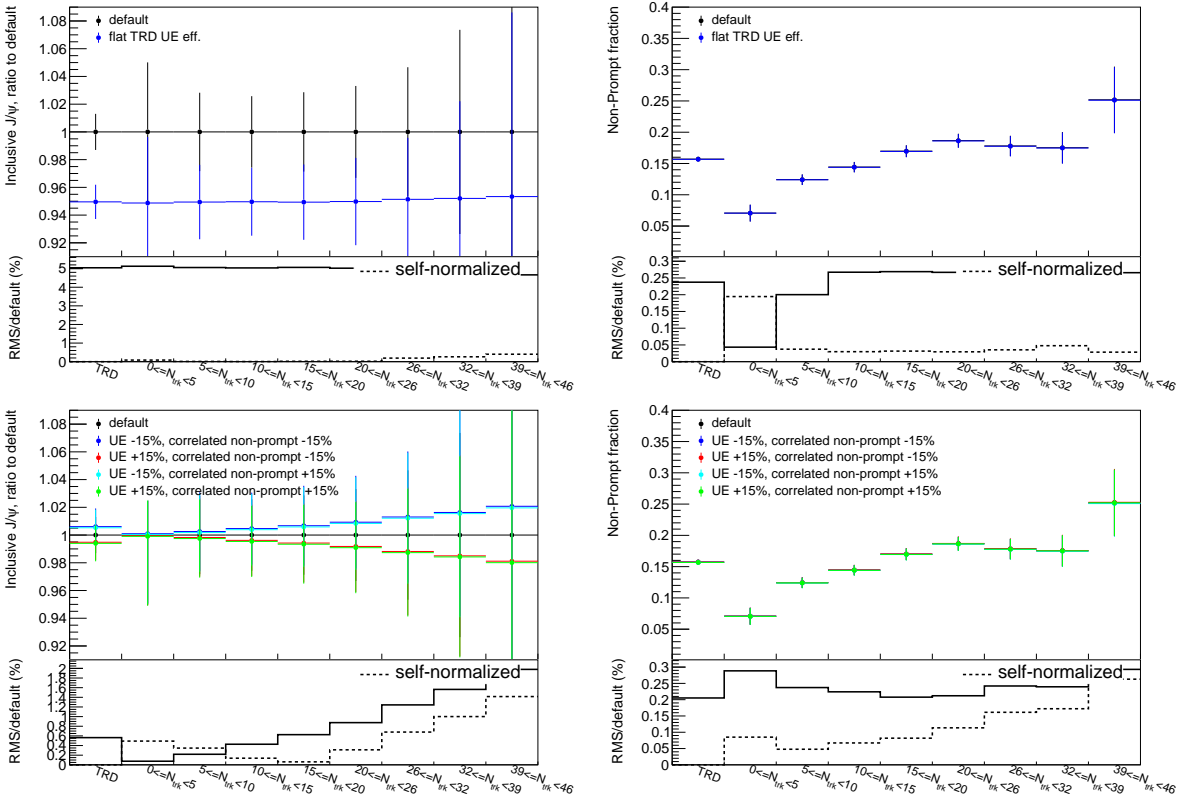
Figure 6.8.: Systematics on the TRD trigger efficiency for inclusive yield (left) and non-prompt fraction (right), for $p_T > 1\,\mathrm{GeV}/c$. Top panels show variation in UE removal for single-leg efficiency, middle panels show variations in single-leg statistical uncertainty, bottom panels show variation in UE efficiency. The corresponding uncertainty is shown, while the self-normalized uncertainty represents the uncertainty for $N_{inclusive}(mult)/N_{inclusive}(MB)$ or $f_B(mult)/f_B(MB)$.

Unfolding:

The toy-model described in Sec. 5.6.2 showed that, when unfolding only the multiplicity, it creates a small discrepancy in the values of multiplicity-dependent J/ψ yields compared to the generated ones. However, this discrepancy can be corrected if the second-order derivative of the J/ψ-$N_{\rm ch}$ correlation is known. It can be extracted from a fit to the data points with a power-law function. As a variation, the same correction is extracted with a fit using a second-order polynomial. The difference of the yields obtained with the two corrections is assigned as a systematic uncertainty.

Signal extraction:

The extraction of the J/ψ signal from an invariant mass fit relies on a correct estimation of the background. The selection on the BDT score helps to reduce this uncertainty because of the increase of the signal-over-background ratio. However, this selection could also change the shape of the background. Therefore, the background function is varied for the estimation of the corresponding systematic uncertainty. The combinatorial background is modified from the event mixing technique to like-sign pair subtraction, and the correlated background is varied between a second-order polynomial and an exponential function. This leads to four variations when each possibility for the combinatorial background is combined with each possibility for the correlated background. The RMS of the self-normalized yields obtained with these variations is assigned as a systematic uncertainty. In addition, it was tried to remove the correction which accounts for the change of the mixed-event shape when a BDT selection is applied, but no significant difference with the default results was found. It was also tried to use a first-order polynomial for modeling the correlated background. However, the χ^2 of the invariant mass fit in this case becomes large when a strong selection on the non-prompt score is made. Therefore, the first-order polynomial background was not taken into account, in order to avoid that this uncertainty is overestimated.

The description of the signal in the fit was also checked by changing the interval for counting the J/ψ signals after background subtraction. Eight variations were tested, changing the values of 2.92, 2.88, 2.84 and 2.80 GeV/c^2 for the lower mass window, and 3.16 and 3.2 GeV/c^2 for the upper mass window. In contrast to the multiplicity-dependent background, the description of the signal is assumed independent of the multiplicity. Therefore, no uncertainty related to the signal shape is assigned for the self-normalized yields. This uncertainty is accounted for only for the absolute yields and for f_B.

Finally, an uncertainty is also due to the invariant mass fit range used when fitting the correlated background and the signal shape. This is estimated by repeating the signal extraction with a lower fit mass range of 1.5, 1.8 and 2 GeV/c^2, and with an upper fit mass range of 2, 2.2 and 2.5 GeV/c^2.

The values of f_B and inclusive number of counts for all the variations, as well as the corresponding systematic uncertainty, are shown as a function of multiplicity in Fig. 6.9. The MB and HM triggered samples have been merged.
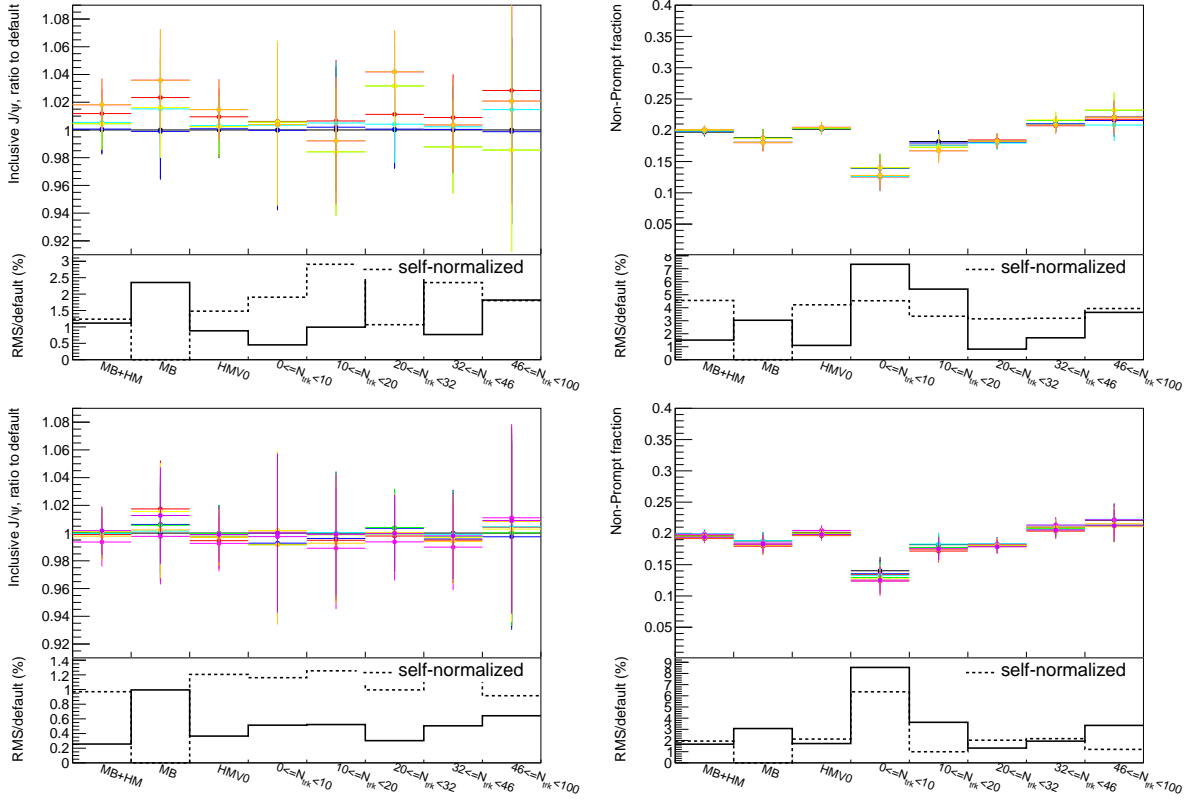
Figure 6.9.: Top: systematic variations of the background shape for inclusive yield (left) and non-prompt fraction (right), for $p_T > 1$ GeV/c. The first bin shows the MB+HM samples, the second bin shows the MB sample only, the third bin shows the HM sample only, and the subsequent bins show all the multiplicity intervals, using both triggers. The corresponding uncertainty is shown, while the self-normalized uncertainty represents the uncertainty for $N_{inclusive}(mult)/N_{inclusive}(MB)$ or $f_B(mult)/f_B(MB)$. Bottom: same plots, but for the variations of the fit range.

Training of the BDT:

The goal of the BDT algorithm is to create a new variable, the BDT score, by using all input variables. Once this variable is created, applying the BDT selection to the prompt and non-prompt J/ψ samples allows to obtain an efficiency as a function of the selection value. This efficiency in principle varies when the training of the BDT is modified, but the number of counts with the selections also vary. After correction for the BDT efficiency, the yield should be independent of the training process. This can be checked by varying the hyperparameters of the model. In Fig. 6.10, the non-prompt BDT score, for the prompt test sample in the left panel and the non-prompt test sample in the right panel, is shown for different choice of hyperparameters. The hyperparameters range from the shortest training time (low number of trees and low learning rate or shrinkage) in blue to the longest training time in red. Several variations in the model response appear: when the training is too short, the separation between prompt and non-prompt candidates is not good enough, but it becomes better when training for a longer time. However, when a sufficient training time is reached, the separation power stops to increase. Nevertheless, even in this case, the change of hyperparameters still causes variations of the BDT score distribution.
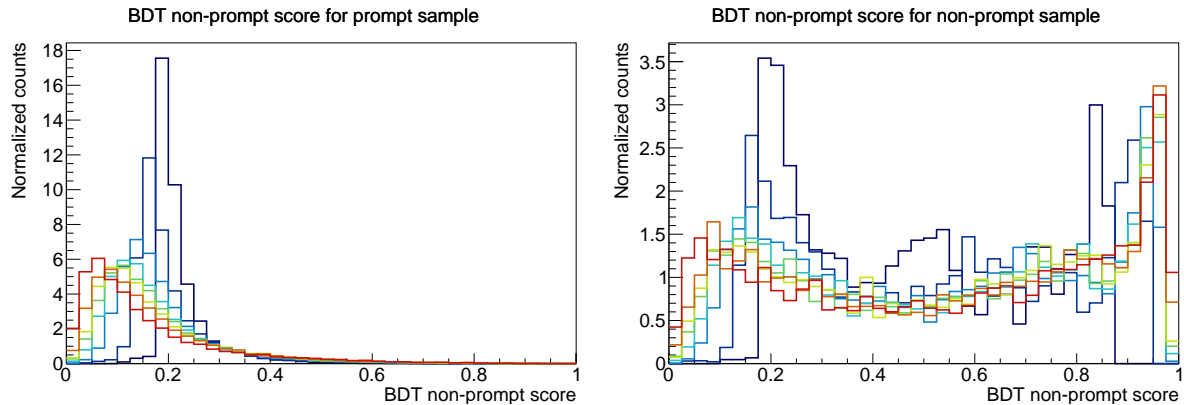
Figure 6.10.: Distribution of the BDT non-prompt score for the prompt sample (left) and for the non-prompt sample (right). Hyperparameters are varied from a short training (blue) to a long training (red).

The significant variations in the BDT score distributions could increase the instability of the results. Indeed, selecting at the same value of BDT score would lead to different J/ψ counts after the signal extraction. The χ^2 fit allowing to obtain prompt and non-prompt counts could be affected. The instability could be especially be caused by different sensitivity to the mismodeling of the variables and their correlations in the MC simulations. For example, if one set of hyperparameters constructs the BDT score by using mismodeled variables in the trees more often than another set of hyperparameters does, the description in the testing sample in the former case would be much worse. An instability could also be caused by the overfitting of the input samples. The overfitting would enhance the variations of the BDT score distribution due to the sample on which the BDT model is applied.

Varying the set of hyperparameters is also necessary because no ideal hyperparameter set could be found. Even if the ROC AUC have been optimized through bayesian optimization, other hyperparameters could give slightly lower, but close performances. If another observable had been used for the optimization of hyperparameters, other hyperparameters could have been chosen. A problem is also that the MC simulations used in the training might not model the data perfectly and, thus, optimized hyperparameters values for data and MC would be different.

The following hyperparameters were varied (the default variation is shown in bold):

- NTrees: 1032 1232 **1432** 1632 1832

- Shrinkage: 0.008 **0.018** 0.028

- GradBaggingFraction: **0.5** 0.8

- MaxDepth: 3 **4**

- nCuts: 50 **100** 200

When only one hyperparameter is modified at the same time, none of the variations shows a much worse χ^2 or significantly higher statistical uncertainties. In addition, there are no observed monotony in the response, which would have happened for example if a lower training time would always give a lower f_B, or the other way around. This indicates that these variations

of hyperparameters are probably reasonable, and within these variations the BDT performance does not change significantly. In addition, all the different parameters have been varied at the same time, leading to $5 \times 3 \times 2 \times 2 \times 3 = 180$ variations. In this case, the performance could become lower, for example when the values of all these parameters combined lead to a significantly lower training time. The mean of the six ROC AUC values for the test samples has been checked for all the variations in Fig. 6.11. This figure corresponds to the BDT trained for the MB and HM sample and for $p_{\mathrm{T}} > 1$ GeV/c. It can be observed that most of the variations have their ROC AUC around $\approx 0.82 - 0.84$, but several of these variations show lower values. The systematic uncertainty is assigned considering only the variations with a ROC AUC value higher than a defined value, which is different for different triggered sample and different p_{T} interval. This requirement removes the few outlier cases where the performance is too low. In the specific case shown in Fig. 6.11, the threshold is set to 0.815.
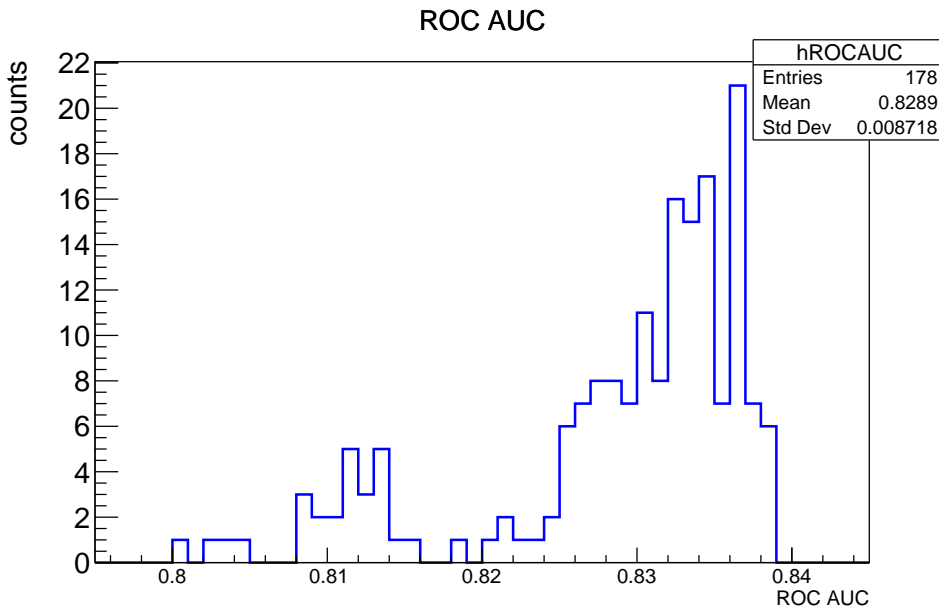
Figure 6.11.: Distribution of the ROC AUC for all the hyperparameters variations considered.

In addition, the sampling between the events which are assigned as training events and the ones which are assigned as testing events could play a role. This role could be significant, especially if the samples are small, which leads to large variations when the training is done with different events. The choice of an event being assigned to the testing or to the training sample is done on a random basis. Thus, in order to assign an uncertainty, the analysis is redone 20 times, and each time the seed for random number generation is modified, whereas it is by default fixed when considering the variations for the other sources of systematic uncertainties.

The systematic variations due to the hyperparameters and to the random seed are shown in Fig. 6.12.

BDT selections:

The efficiency of the selection on BDT scores is known from the BDT score distribution of prompt and non-prompt MC J/ψ. If the efficiency and the variables used in the training are
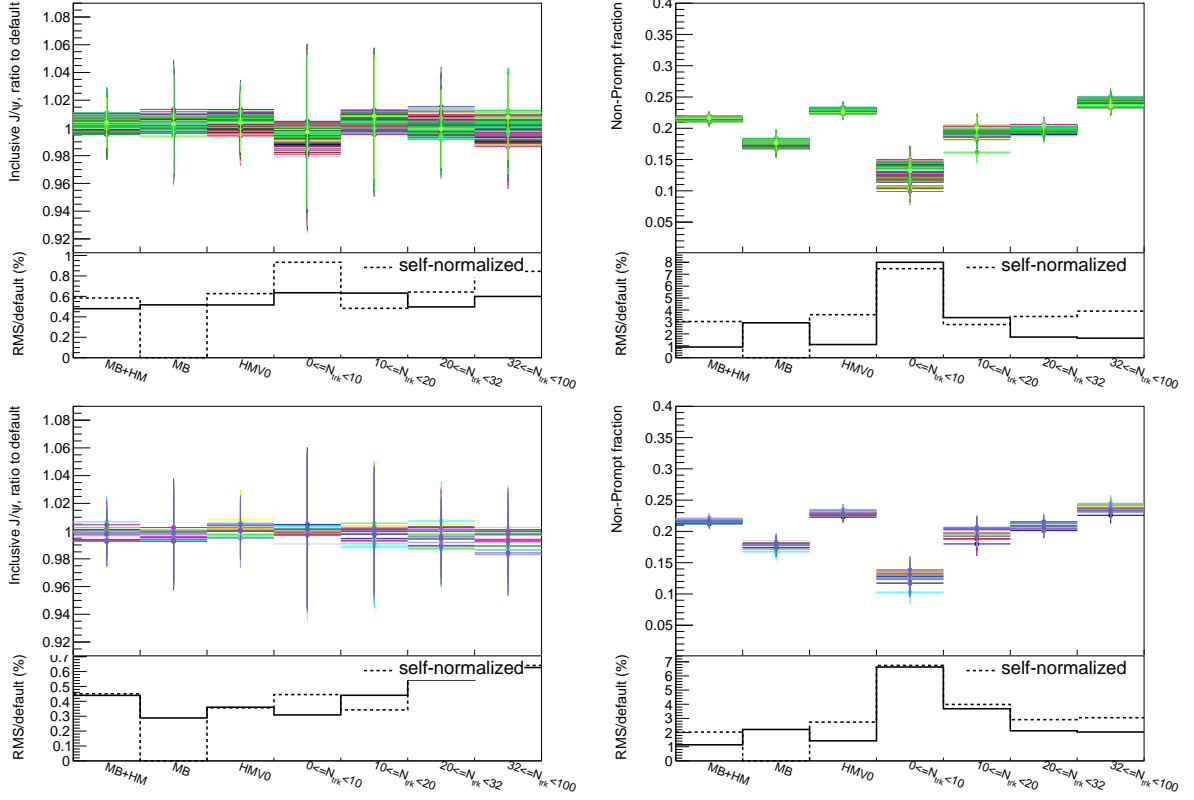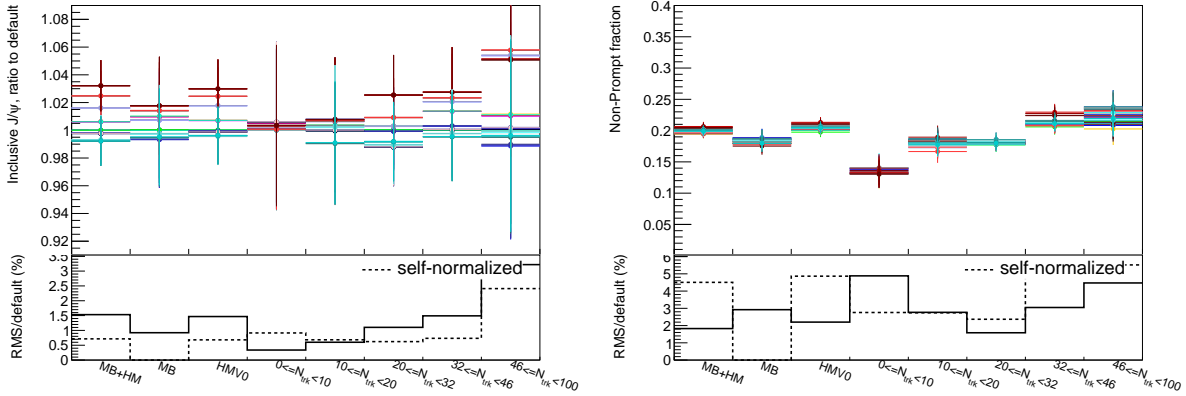
Figure 6.12.: Top: systematic variations of hyperparameters for inclusive yield (left) and non-prompt fraction (right), for $p_T > 1$ GeV/c. The corresponding uncertainty is shown, while the self-normalized uncertainty represents the uncertainty for $N_{inclusive}(mult)/N_{inclusive}(MB)$ or $f_B(mult)/f_B(MB)$. Bottom: same plots, but for the variation of the seed for random number generation.

well reproduced, every selection gives the same result after efficiency correction. Varying the selections on the BDT would then test the correct reproduction of this efficiency due to the topological and PID variables in the MC. In order to assign an uncertainty, the selection on the BDT background score is varied by $\pm$ 0.05, 0.1, 0.15 and 0.2. It is possible that, with looser selections, the background becomes too large, or that, with tighter selections, the efficiency becomes too small. Because these variations have a lower statistical performance, they should not be considered. Therefore, a given systematic variation is taken into account only when the expected significance with this BDT selection is within 10% of the maximal expected significance.

In addition, the selections on the non-prompt score are also varied. This allows to test specifically the description of the topological variables, which enable separation between prompt and non-prompt J/ψ, as well as probing the uncertainty of the cut variation method. The number of selections used for the fit of the J/ψ counts as a function of the non-prompt score is changed from 20 (default) to 10 or 40. The choice of the selection values is also varied from evenly-spaced in the default case (selections at BDT score values of 0.05, 0.1, 0.15...) to constant values of BDT non-prompt efficiency (selections at BDT scores corresponding to 95%, 90%, 85%, ... of non-prompt efficiency). The BDT values at which the selection is done in the latter case changes from one training to another, and might reproduce better the changes in the BDT templates when the training is modified. It would also give more selections at high BDT non-prompt score, where the number of non-prompt J/ψ shows large variations with the selection value.

All the combinations of all the variations for these three sources (background score selection value, number of non-prompt score selection and their values) are considered. The only exception is the variation with 40 non-prompt selections and where the BDT selection values depend on BDT non-prompt efficiency, for which many fits have a large χ^2. The presence of these large χ^2 is due to the fact that many selections have a very close number of counts when a tight selection on the non-prompt score is applied. This worsens the accuracy of the matrix inversions necessary for the determination of prompt and non-prompt J/ψ counts. The systematic variations, as well as their RMS, for inclusive J/ψ yield and non-prompt fraction are shown in Fig. 6.13.

Figure 6.13.: Systematic variations of BDT selections for inclusive yield (left) and non-prompt fraction (right), for $p_T > 1$ GeV/c. The corresponding uncertainty is shown, while the self-normalized uncertainty represents the uncertainty for $N_{inclusive}(mult)/N_{inclusive}(MB)$ or $f_B(mult)/f_B(MB)$.

p_T **distribution:**

The p_T distribution of prompt and non-prompt J/ψ is not known with perfect precision. The p_T distribution of J/ψ in the MC testing sample, used for acceptance and efficiency corrections, as well as for the BDT selection efficiency templates, are modified by giving a weight to all the J/ψ signals.

The minimum-bias p_T distribution for prompt J/ψ is by default a fit to the measured prompt J/ψ cross-section [80] using a standard function (Eq. 5.14). For non-prompt J/ψ, the p_T distribution is taken directly from PYTHIA with injected non-prompt J/ψ. As a variation, the prompt J/ψ is assumed to follow the p_T distribution from PYTHIA with the Monash tune, while the prediction from FONLL calculations is used for non-prompt J/ψ. This leads to four variations, considering either the default or the variation for prompt J/ψ, and the default or the variation for non-prompt J/ψ.

The evolution of $\langle p_T \rangle$ with N_{tracks} can also lead to an uncertainty. For the default case, the p_T distribution in each N_{tracks} interval is modified by considering the increase of inclusive $\langle p_T \rangle$ calculated from data, and applying it similarly to prompt and non-prompt templates. As a variation, the prompt and non-prompt evolutions of $\langle p_T \rangle$ are taken from PYTHIA8 with the oniaShower settings. $\langle p_T \rangle$ is shown in Fig. 6.14 as a function of N_{tracks} for prompt (black) and non-prompt (blue) J/ψ using PYTHIA with the oniaShower settings. These $\langle p_T \rangle$ values are used to reweight the p_T distribution according to the formula in Eq. 5.16. The systematic variations

due to the minimum-bias p_{T} distributions as well as the ones due to the evolution of $\langle p_{\mathrm{T}} \rangle$ with multiplicity are shown in Fig. 6.15.
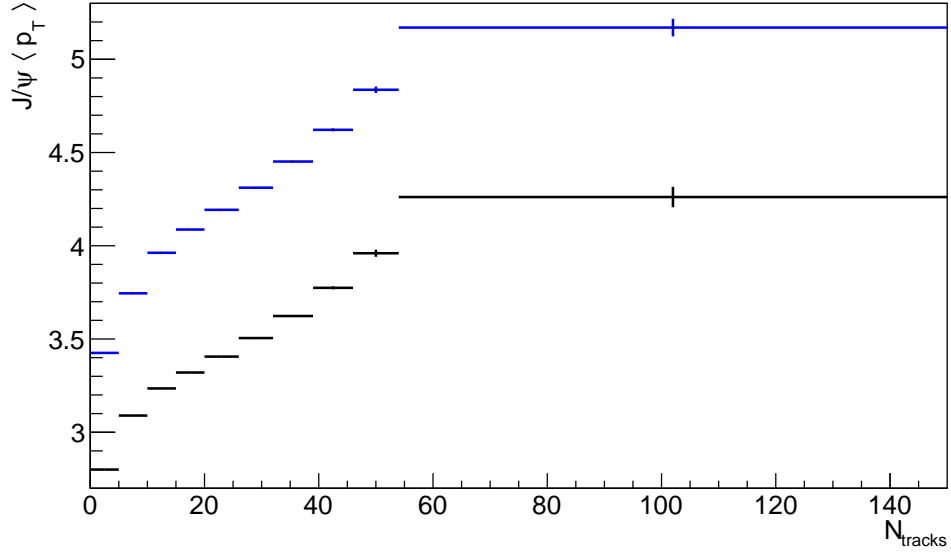
Figure 6.14.: $\langle p_{\mathrm{T}} \rangle$ as a function of N_{tracks} for prompt (black) and non-prompt (blue) J/ψ, using PYTHIA with the oniaShower settings.
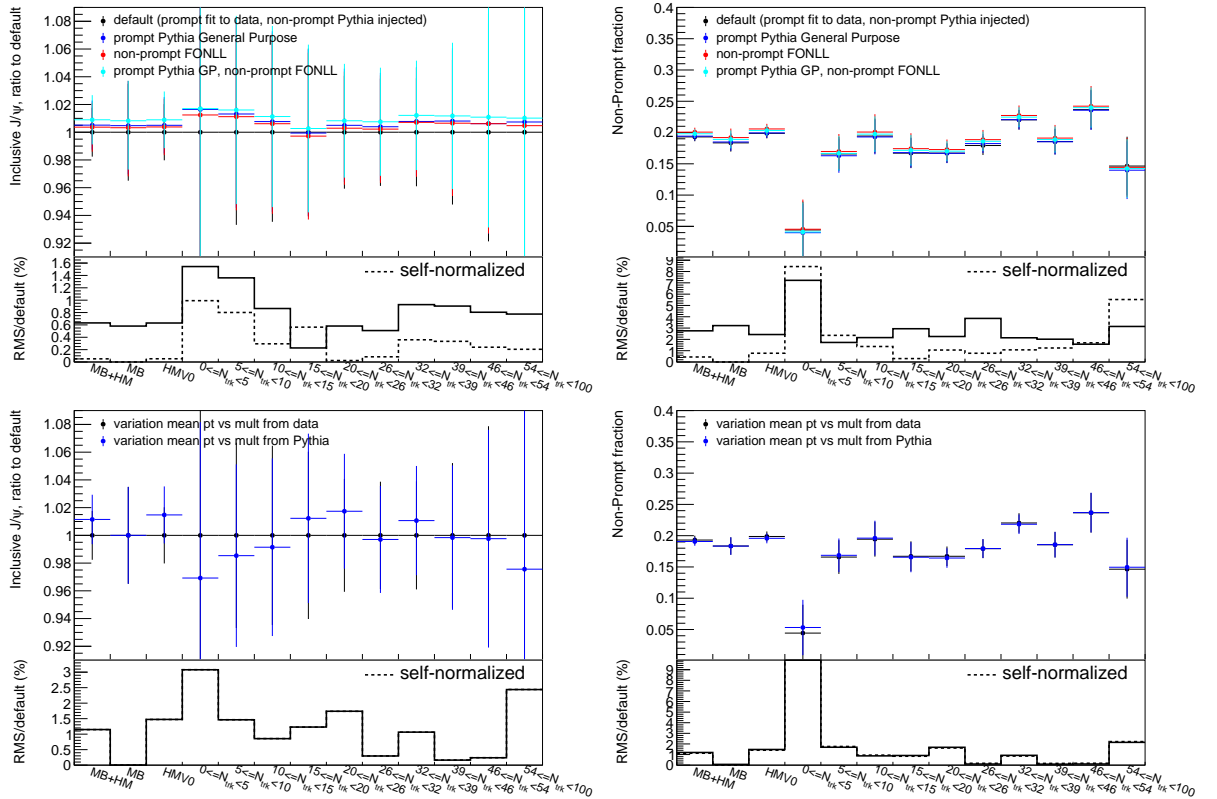
Figure 6.15.: Top: systematic variations of the MB p_{T} distribution for inclusive yield (left) and non-prompt fraction (right), for $p_{\mathrm{T}} > 1$ GeV/c. The corresponding uncertainty is shown, while the self-normalized uncertainty represents the uncertainty for $N_{inclusive}(mult)/N_{inclusive}(MB)$ or $f_B(mult)/f_B(MB)$. Bottom: same plots, but for the variation of the N_{tracks} dependence of $\langle p_{\mathrm{T}} \rangle$.

Beauty hadrons composition:

Beauty hadron fractions in the MC non-prompt sample were already modified in order to improve the agreement with MB data. In addition, it is also possible that the beauty hadron fractions depend on the charged-particle multiplicity. For example, LHCb observed that, at forward rapidity, the ratios between B_s^0 and B^0 [206] and between Λ_b^0 and B^0[117] increase with multiplicity. At midrapidity, ALICE has measured the Λ_c-over-D^0 ratio as a function of mutiplicity [140]). In this case, a mild dependence was observed, but uncertainties were still large. These results show that this possible multiplicity dependence, which is not present in Monash, should be considered. The model comparison done in Ref. [140] suggests that CR-BLC mode 2 might overestimate the multiplicity dependence of baryon-to-meson ratio. However, because of large uncertainties, no solid conclusion could be taken. Therefore, the multiplicity-dependent beauty hadron fractions are extracted from CR-BLC mode 2, and are compared to the ones in the case for which no multiplicity dependence is assumed.

The ratio in PYTHIA with CR-BLC mode 2 of beauty hadron p_T-integrated yields to the one for B^0 is shown in the left panel of Fig. 6.16 as a function of charged-particle multiplicity. The relative abundances of beauty baryons increase with charged-particle multiplicity, in contrast to the ones of beauty mesons. As shown in the right panel of Fig. 6.16, the $\langle p_T \rangle$ of the beauty hadrons also increase as a function of multiplicity, with a separation between baryons and mesons. Weights in the non-prompt J/ψ simulations are applied in each N_{tracks} interval, in order to correct the p_T distributions and beauty hadron abundances as a function of multiplicity. These weights correspond to the ratio between the distributions in N_{tracks} intervals and in minimum-bias collisions. In these standalone PYTHIA simulations, the N_{tracks} is determined by smearing N_{ch} event-by-event using MC N_{ch}-N_{tracks} correlation matrix from simulations with detector propagation.
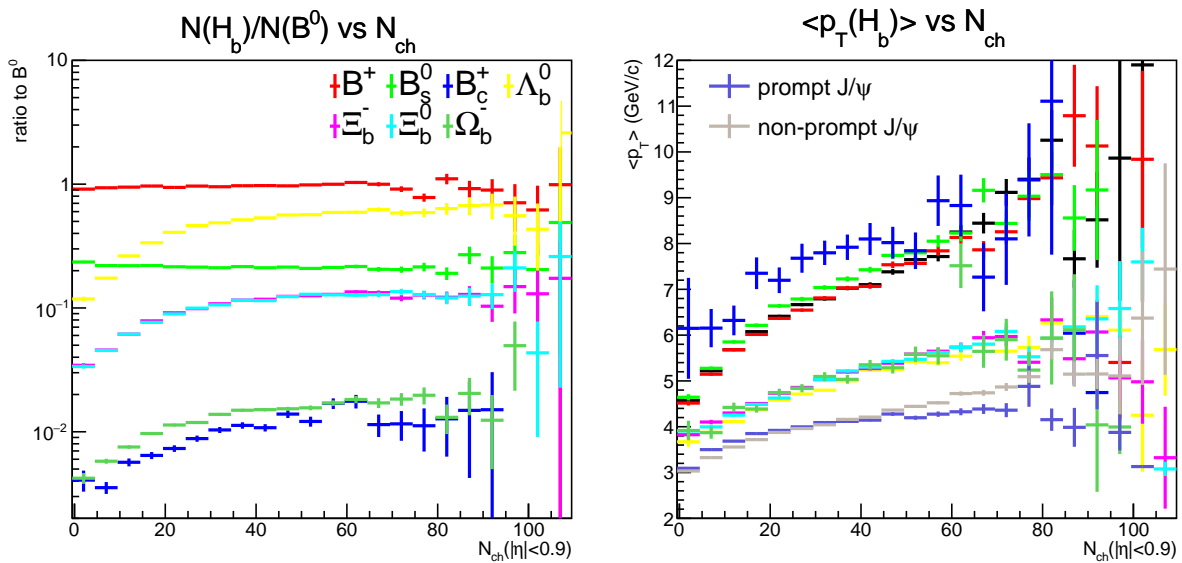
Figure 6.16.: Left: ratio of yields of different beauty hadrons to the B^0 yield as a function of multiplicity, using PYTHIA with CR-BLC mode 2. Right: $\langle p_T \rangle$ for different beauty hadrons as a function of multiplicity, with CR-BLC mode 2, as well as for prompt and non-prompt J/ψ.

The systematic variations due to the beauty hadron composition are shown in Fig. 6.17. The multiplicity dependence in CR-BLC mode 2 could be overestimated, as was shown in Ref.[140] for charm hadrons. It is thus assumed to be the largest possible variation, while variations in between are equally probable. An uncertainty from a one-sided uniform distribution is thus assumed, which amounts to $(Y_{\max} - Y_{\text{default}})/\sqrt{3}$, where the default variation as no multiplicity dependence of the beauty hadron fractions. This uncertainty is found to be small.
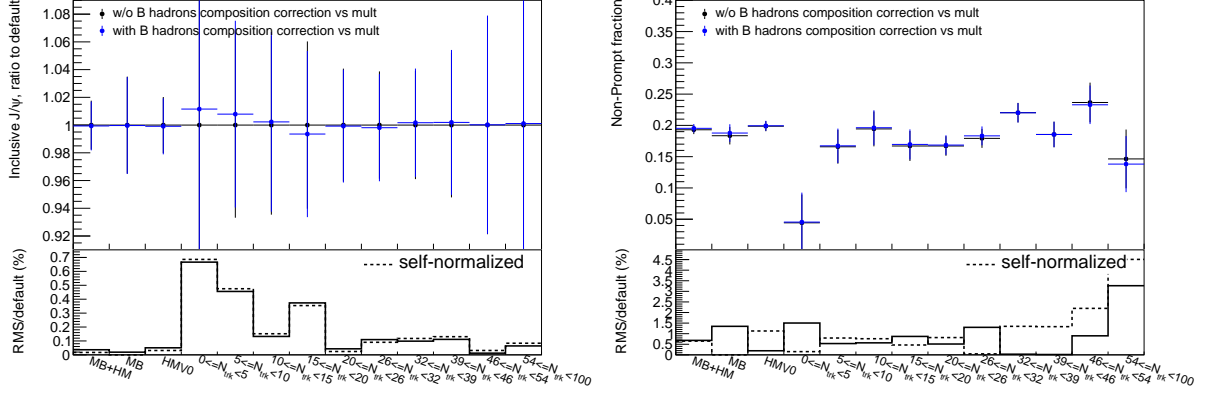
Figure 6.17.: Top: systematic variations of the MB B hadrons fractions distribution for inclusive yield (left) and non-prompt fraction (right), for $p_{\text{T}} > 1$ GeV/c. The corresponding uncertainty is shown, while the self-normalized uncertainty represents the uncertainty for $N_{inclusive}(mult)/N_{inclusive}(MB)$ or $f_B(mult)/f_B(MB)$. Bottom: same plots, but for variation of the N_{tracks} dependence of the B hadron fractions.

Primary vertex position calculation:

At low multiplicity, the resolution of the position of the primary vertex becomes worse. In addition, the daughter tracks from a non-prompt J/ψ do not come directly from the primary vertex. Including the track in the primary vertex calculation could bias the vertex position. Therefore, it might be important to remove the J/ψ daughters from the calculation of the vertex. If these daughters are removed in a similar way in data and MC, and if the MC described the data perfectly, the results would not vary compared to the case where the daughters are allowed to be included in the vertex calculation. Thus, the comparison between both cases could be used to probe how well the vertex calculation is described in the MC, especially due to the multiplicity dependence of the prompt and non-prompt J/ψ yields.

The correct method for removing the daughters from the vertex should be to keep the information on all tracks used for the vertex, and, for each pair candidate, recreate a new vertex using all the vertex contributors except the daughters. For computational reasons, this method was not applied on the full sample, but only on a small subsample of the Monte-Carlo with injected J/ψ signals. For each event, and for each primary vertex contributor, the vertex position was calculated with and without including this track. This allows to extract the ratio between the DCA without including the track in the vertex and the DCA when it is included. This ratio depends both on the p_{T} of the track and on the number of vertex contributors. The projections of this ratio as a function of p_{T} and vertex contributors are shown in the left and right panel of Fig. 6.18, respectively. There are two cases: SPDfirst when there is a hit in the first SPD layer, and

SPDsecond when the first hit occurs only in the second SPD layer. The values of the ratio are always above 1. This is expected because the tracks tend to pull the vertex towards itself when they are included in the primary vertex calculation, and this lowers the track DCA. The ratio is larger at higher p_{T} and at lower number of vertex contributors. Because of the large uncertainties when the number of vertex contributors is low, a fit is done for every p_{T} interval as a function of the number of vertex contributors, with the function $f(N_{\mathrm{vtx\ contrib.}}) = A + B/N_{\mathrm{vtx\ contrib.}}{}^{C}$. The values of this ratio between DCA are used in order to modify the position of the primary vertex for every J/ψ candidate in the data and MC samples. For each one of the J/ψ daughters included in the primary vertex calculation, the primary vertex is shifted away from this daughter, in order to mimic the larger daughter DCA. Afterward, all topological quantities for the considered J/ψ and its daughters are recomputed relative to the new vertex.
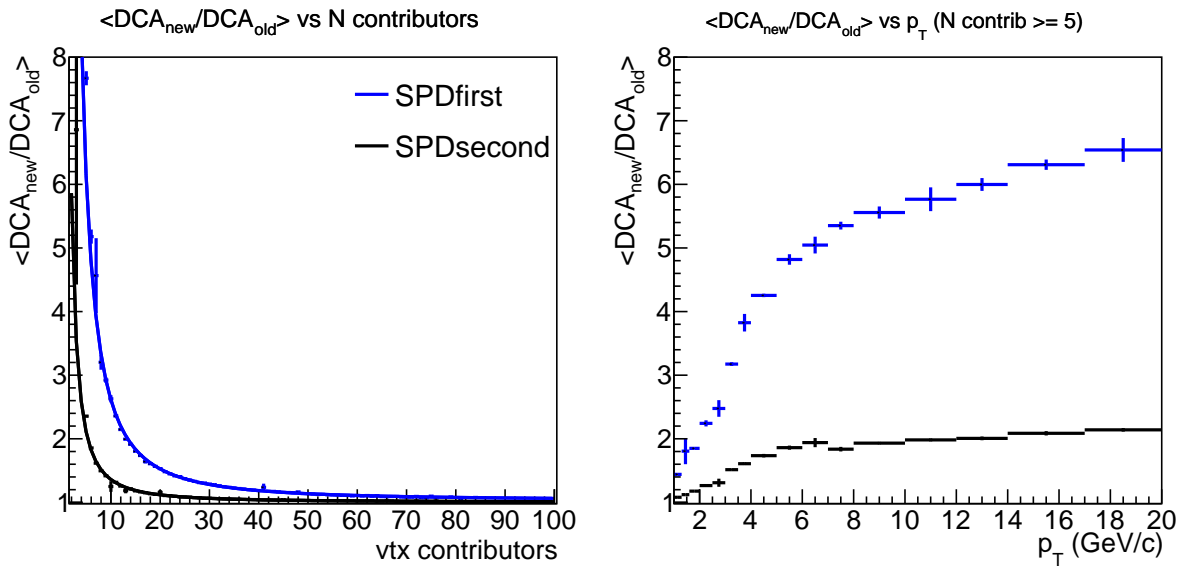

Figure 6.18.: Left: mean value of ratio between DCA after removing track from the primary vertex calculation and DCA including the track in the primary vertex calculation, as a function of number of vertex contributors in the primary vertex (excluding this track). This is shown separately for tracks with a hit in first SPD layer (SPD first) and tracks with only a hit in second SPD layer (SPD second). Right: same quantity, but as a function of the track p_{T}.

The BDT is trained using the recomputed topological variables and similar BDT selections are applied. The new J/ψ counts and non-prompt fraction are compared to the previous ones in Fig. 6.19. In order to avoid a too large impact of the statistical uncertainties, N_{tracks} intervals have been merged at high multiplicity. The uncertainty is mostly present at low multiplicity.

Tracking efficiency in events with J/ψ:

In the method which unfolds the multiplicity only and not the J/ψ yield and when checking the correctness of this method with the toy model, it was implicitly assumed that the tracking efficiency for inclusive charged particles is the same in minimum-bias events and in events with a J/ψ. The only exception to that assumption is the treatment of the J/ψ daughters, for which the bias in tracking efficiency is corrected, by counting them in the multiplicity with a probability exactly equal to the minimum-bias tracking efficiency value. However, a difference in the tracking
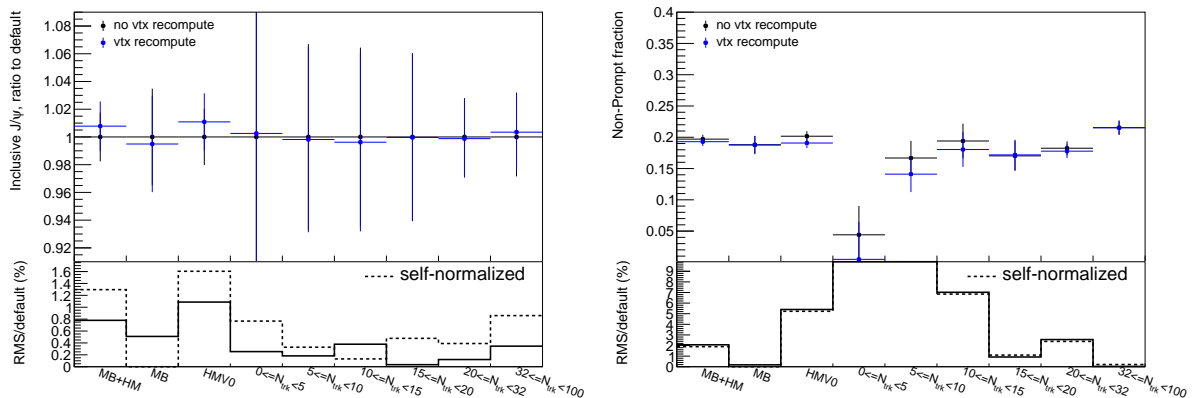
Figure 6.19.: Systematics on the vertex calculation for inclusive yield (left) and non-prompt fraction (right), for $p_T > 1$ GeV/c. The corresponding uncertainty is shown, while the self-normalized uncertainty represents the uncertainty for $N_{inclusive}(mult)/N_{inclusive}(MB)$ or $f_B(mult)/f_B(MB)$.

efficiency in events with a J/ψ at a given multiplicity could be present, for example due to different particle composition or to different momentum distribution of the particles in the event.

In the non-prompt J/ψ case, such bias could also be caused by the additional displaced tracks coming from the decay of the beauty hadron, which are less often counted in the multiplicity estimator than an average track. In the MC, the comparison between electrons from prompt J/ψ and from non-prompt J/ψ shows that the probability for the latter to be included in the multiplicity estimator is 10% smaller at $p_T = 1$ GeV/c and 40% smaller at $p_T = 6$ GeV/c than for the former. Even though this effect is corrected for the J/ψ daughters when they are counted with fixed probabilities, the other decay products of the beauty hadrons, and potentially the charged particles coming from the hadronization and decay of the other beauty quark, could be affected. PYTHIA standalone simulations of $b\bar{b}$ events were used to determine the average number of additional displaced tracks in the acceptance when a non-prompt J/ψ is present. This number amounts to around 1.8 for J/ψ $p_T > 1$ GeV/c, and is higher at high p_T. Similarly, the average p_T of these tracks was determined, and it was found to be lower than the J/ψ daughter p_T. The effect of these several charged particles with a lower probability to be included in the multiplicity estimator was simulated in the toy model described in Sec. 5.6.2, without modifying the unfolding method. The discrepancy between the generated and the reconstructed J/ψ yield is shown in the left panel of Fig. 6.20, and is assigned as a systematic uncertainty.

In addition, the tracking efficiency depends slightly on the azimuthal angle. This is due to the spatial configurations of the detectors, such as the presence of the readout chambers in the edge of the 18 TPC sectors, of support material or of dead detector channels for some data taking periods. Fig. 6.21 shows the number of tracks measured as a function of the azimuthal angle, extracted from data. This dependence is also shown for J/ψ mesons, extracted from MC simulations. In the latter case, the φ-dependence of the J/ψ reconstruction is the combination of the φ-dependence for each one of the decay electrons, and depends on the decay kinematics.

For azimuth-inclusive multiplicity, this dependence is not a problem because only the azimuth-integrated efficiency is considered. However, when studying regions of $\Delta\varphi = \varphi_{track} - \varphi_{J/\psi}$, this
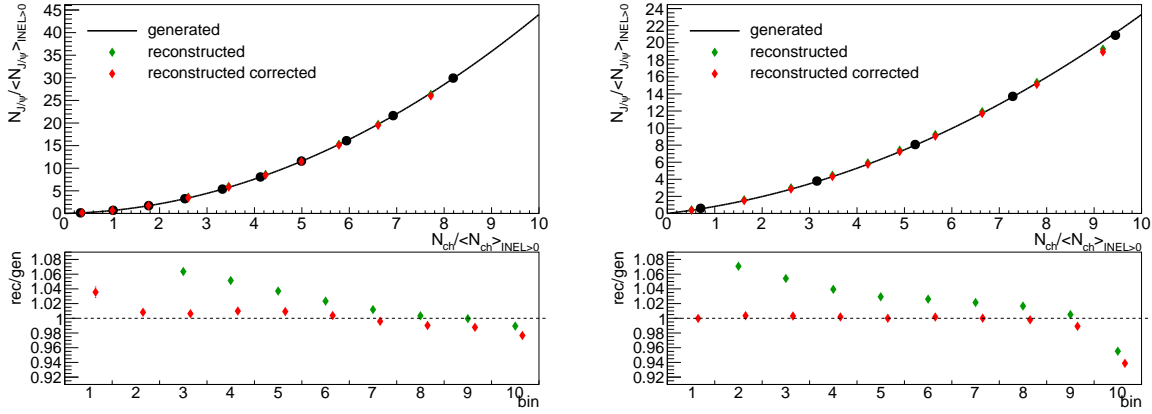
Figure 6.20.: Ratio between reconstructed and generated J/ψ yields in a toy model. Left: for non-prompt J/ψ. The tracking efficiency has been modified for few particles potentially coming from beauty hadron decay. Right: for prompt J/ψ, with the multiplicity in the toward region. The tracking efficiency for events with a J/ψ meson has been modified by around 0.1%.
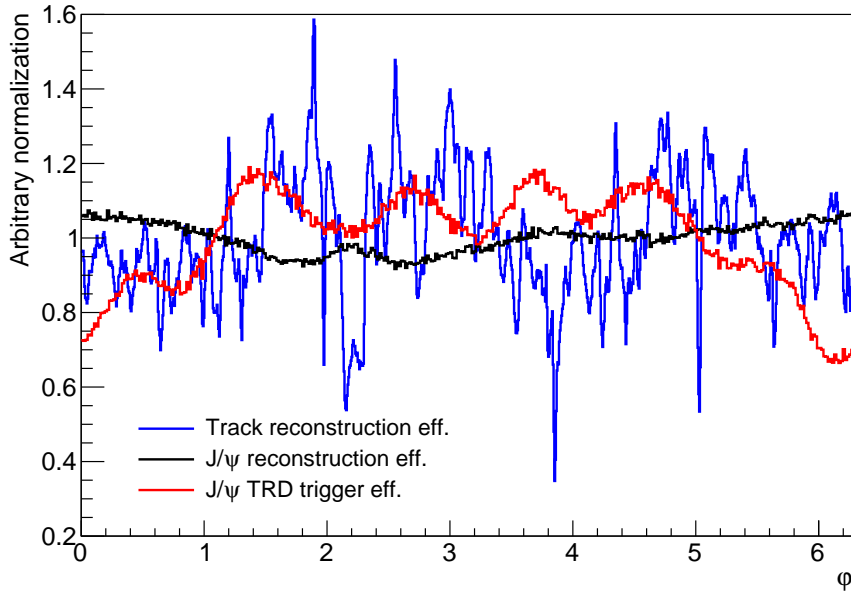

Figure 6.21.: Dependence on the azimuthal angle of the tracking, J/ψ reconstruction, and J/ψ TRD trigger efficiency, with J/ψ $p_T > 1$ GeV/c.

dependence could play a role. For example, if a specific azimuthal angle shows a lower efficiency for both track and J/ψ reconstruction, a drop in the efficiency will be observed at $\Delta\varphi = 0$. In this case, the efficiency would be lower in the toward region compared to azimuth-integrated efficiency, and the multiplicity would be lower. For minimum-bias events, the regions are defined with respect to a random angle, and they are not affected on average. However, because the unfolding is only done with unbiased events, it does not account for lower or higher efficiencies in specific azimuthal regions for the J/ψ yields.

For this reason, the dependence on $|\Delta\varphi|$ of the tracking efficiency is extracted using the φ-dependence for J/ψ and tracks. This is shown in Fig. 6.22, for several p_T intervals. While, at low p_T, the decay electrons can decay with large opening angle, averaging out the φ dependence, at higher p_T, the J/ψ is more boosted in one specific direction, and both the electron and the

positron could hit the same azimuthal region which shows a reduced efficiency. The impact of the φ dependence of the TRD trigger efficiency is also shown as a dashed line in the same figure. The maximal difference in the efficiency is of the order of 1%, as shown in the left panel. However, when integrating in each of the three azimuthal regions, as shown in the right panel, the difference is at maximum 0.3%, and in most cases does not exceed 0.2%.
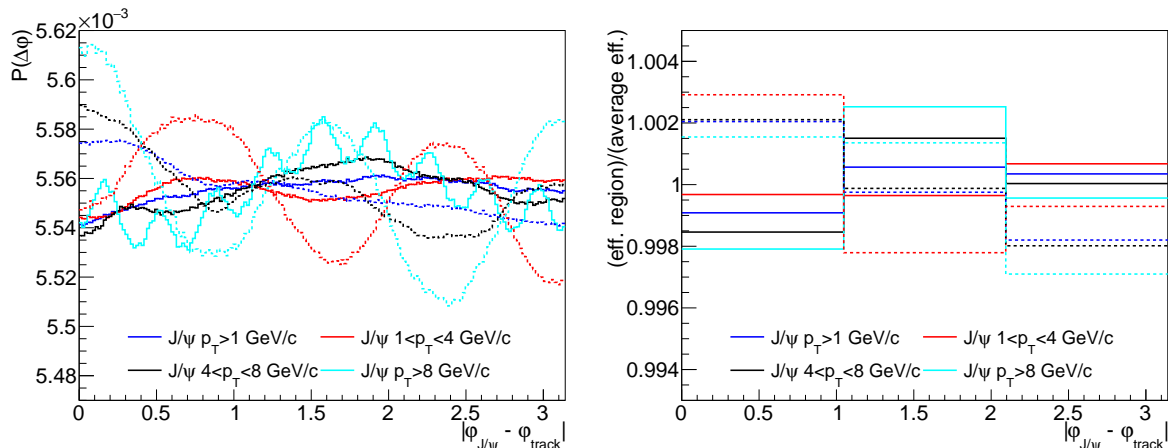

Figure 6.22.: Left: Dependence on $|\Delta\varphi|$ of the efficiency, considering J/ψ reconstruction efficiency (solid line), and J/ψ TRD trigger efficiency (dashed lines). Several p_T intervals are shown. Right: same as left panel, but the efficiency is integrated in the three regions.

This difference in tracking efficiency in J/ψ events is converted into an uncertainty using the toy model. For each track, depending on the analyzed region, the probability to be counted in the multiplicity is modified. The discrepancy between the generated and the reconstructed yields is shown in Fig. 6.20 for the toward region. In this case, the uncertainty is small, except for the highest multiplicity interval. Indeed, similar to the effect of removing the daughters from the multiplicity, the effect of having more or less tracks counted in the multiplicity depends on the steepness of the slope of the multiplicity distribution. Besides the fact that, at higher multiplicity, more tracks are affected by modified efficiency, the steeper decrease explains why the effect becomes strong at high multiplicity.

Extrapolation to $p_T > 0$ GeV/c:

The systematic uncertainty due to the extrapolation of the prompt yield is estimated by repeating the extrapolation using several calculations. PYTHIA with CR-BLC mode 2 [46] is the default model while PYTHIA with CR-BLC mode 3 [46], PYTHIA Monash [40] and FONLL [113]) are used for systematic estimation. For FONLL calculations, also the downward and upward variations of the theory uncertainties are taken into account. For the HM extrapolation, FONLL calculations are not possible. In Fig. 6.23 is shown the prompt yield per event in $p_T < 1$ GeV/c after removal of the non-prompt with different models, for INEL>0 events in the left panel, and V0M 0-0.1% in the right panel. The scaling to the non-prompt yield for $p_T > 1$ GeV/c is also a source of systematic uncertainty. Therefore, the results where the data non-prompt yields in $p_T > 1$ GeV/c, used for the scaling of the models, have been increased or decreased by the sum in quadrature of their statistical and systematic uncertainties are also shown. The difference between the highest (lowest) variation and the default value is taken as

the upward (downward) extrapolation systematic uncertainty. Because FONLL gives the largest uncertainty in the MB case, but is not available for HM, in the HM case, its relative uncertainty estimated in MB is added in quadrature to the uncertainty from the PYTHIA variations.
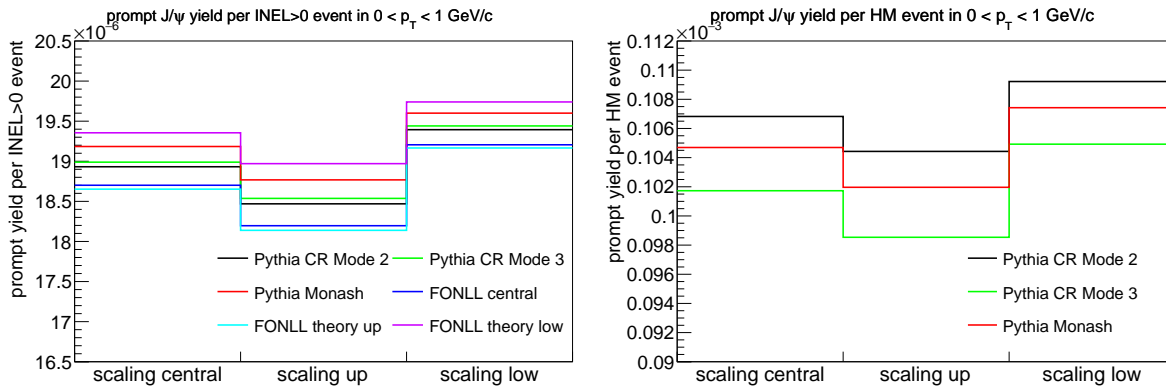
Figure 6.23.: Prompt yield per INEL>0 (left) or HM (right) event for $p_\mathrm{T} < 1$ GeV/c. Different models are used for removing non-prompt yields. In the first bin of the histograms, the scaling for $p_\mathrm{T} > 1$ GeV/c of non-prompt yield is done using the central value in data. In the second (third) bin, this scaling uses the central value, increased (decreased) by the sum in quadrature of the statistical and systematic uncertainties.
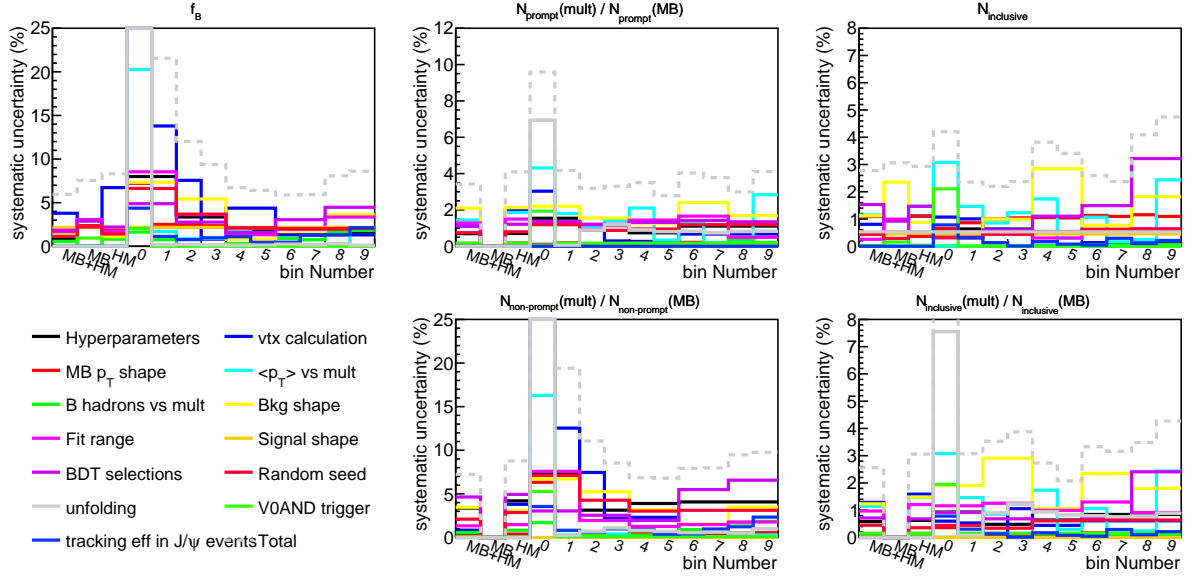
Summary of the systematics for BDT:

A summary of the systematics of the BDT for $p_\mathrm{T} > 1$ GeV/c with MB and HM triggers is shown in Fig. 6.24. Here are shown the individual sources, and the sum in quadrature of all systematic sources, for f_B and for self-normalized prompt and non-prompt yields. The uncertainty is also shown for self-normalized inclusive J/ψ counts, and inclusive J/ψ counts without self-normalization.

For the first multiplicity interval, especially in the non-prompt case, the systematic uncertainties due to the unfolding are large. This is due to the very small number of non-prompt J/ψ in this specific interval, making the relative uncertainty very high. Except in few cases, such as at low multiplicity where the uncertainty due to the vertex is very high, the total uncertainties amount to between 6 and 10% for the non-prompt fraction and the non-prompt self-normalized yields, and to between 3 and 5% for the prompt self-normalized yield. For inclusive and prompt J/ψ, the p_T distribution is the main uncertainty, while for non-prompt J/ψ, there are several major uncertainties, such as the signal extraction, BDT training or BDT selections.

In addition, in Fig. 6.25, 6.26 and 6.27, the total systematic uncertainties are shown in the cases where the multiplicity is calculated in the toward, transverse and away region, respectively. Most of the uncertainties are similar to the uncertainties in the inclusive multiplicity case.

The systematic uncertainties for the TRD trigger are also shown for the case with azimuth-inclusive multiplicity in Fig. 6.28. In general, the systematic uncertainties for the TRD-triggered data are of the same order as for the MB and HM samples. The only exception occurs for the normalization of the TRD trigger efficiency, which gives uncertainties of about 5% in the normalization, but cancels when considering f_B or self-normalized quantities. The MB and TRD

Figure 6.24.: Summary of all systematics, for $p_\mathrm{T} > 1$ GeV/c, for both MB and HM together, MB only, HM only (first 3 bins in all histograms), and all multiplicity bins (10 subsequent bins). Are shown: non-prompt fraction (top left), self-normalized prompt J/ψ counts (top middle), self-normalized non-prompt J/ψ counts (bottom middle), inclusive J/ψ counts (top right), and self-normalized inclusive J/ψ counts (bottom right).
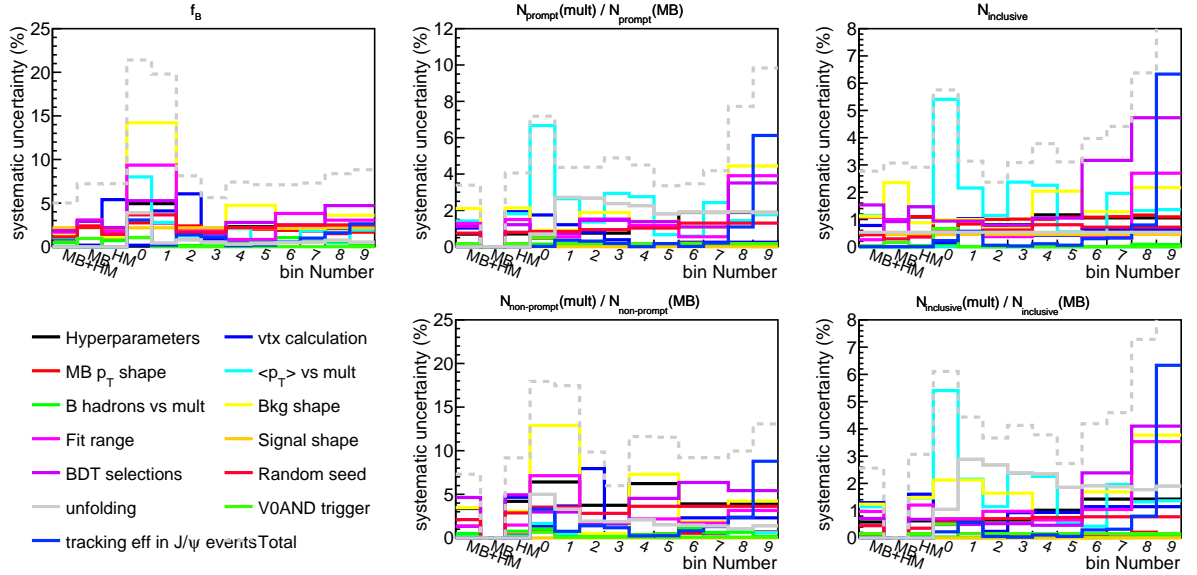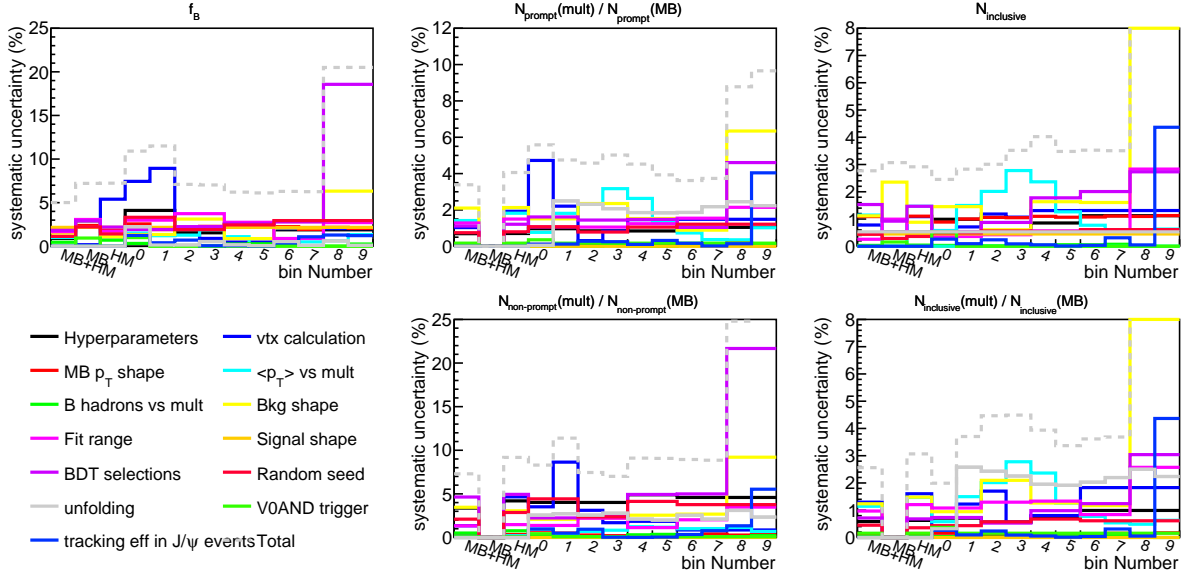

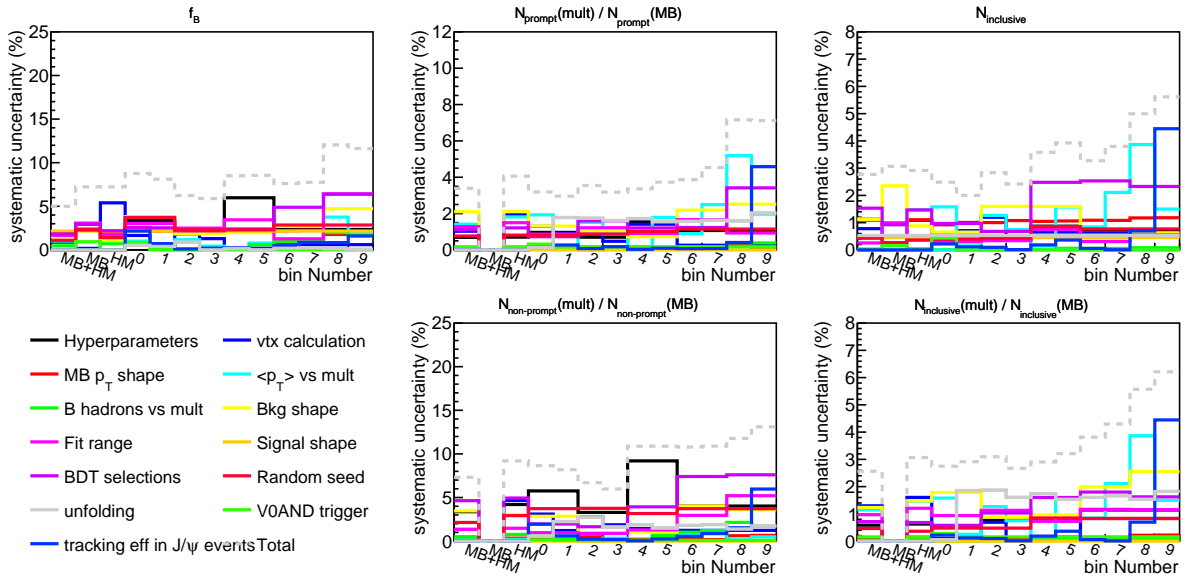**Figure 6.25.:** Same as Fig. 6.24, but for multiplicity in toward region.

data points are merged together. This is done by combining the values in both samples while applying a weight proportional to:

$$\frac{1}{\sigma_\mathrm{stat}^2 + \sigma_\mathrm{uncorr.\ syst}^2}.$$

(6.2)

The weight takes into account the statistical uncertainties σ_stat and the systematic uncertainties which are uncorrelated between MB and TRD samples $\sigma_\mathrm{uncorr.\ syst}$.

Figure 6.26.: Same as Fig. 6.24, but for multiplicity in transverse region.

Figure 6.27.: Same as Fig. 6.24, but for multiplicity in away region.

For the systematic uncertainties of the merged point, uncorrelated uncertainties are added in quadrature, while correlated uncertainties are added linearly. The classification between systematics which are correlated and not between triggers is:

- **Correlated:** V0AND trigger efficiency, unfolding, invariant mass signal shape, beauty hadrons fractions, p_{T} distribution, branching fraction (which gives an uncertainty of 0.5%, only for the J/ψ-to-D^0 ratio).

- **Partially correlated:** primary vertex calculation (it is correlated except for the large p_{T} dependence). In this case, the part which is uncorrelated systematic is assumed to be $\sigma^2_{uncorr\ syst} = \sigma^2_{syst,max} - \sigma^2_{syst,min}$ for the one between TRD and MB sample which has higher systematic uncertainties, and $\sigma^2_{uncorr\ syst} = 0$ for the one with lower systematic uncertainties.
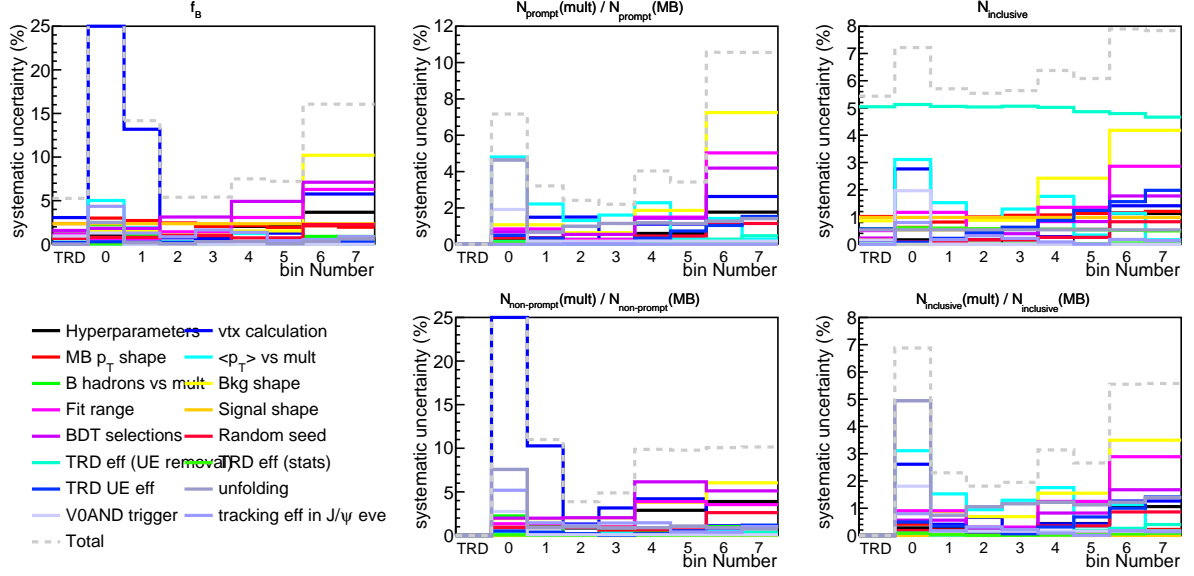
Figure 6.28.: Same as Fig. 6.24, but for TRD-triggered data.

- **Uncorrelated:** signal extraction (background shape and fit range), training of the BDT (due to the use of different BDT models between MB and TRD), choice of BDT selection values, TRD trigger efficiency.

In addition, the prompt yield with $p_\mathrm{T} > 0$ GeV/c in the INEL>0 and V0M 0-0.1% event classes is obtained by summing the prompt yield between 0 and 1 GeV/c and the one for $p_\mathrm{T} > 1$ GeV/c. The systematic uncertainties which are uncorrelated between the two p_T intervals are summed in quadrature, while correlated systematic uncertainties are summed linearly.

- **Correlated:** V0AND trigger efficiency, invariant mass signal shape, B hadrons fractions, branching fraction.

- **Partially correlated:** extrapolation uncertainty due to the scaling to non-prompt yield for $p_\mathrm{T} > 1$ GeV/c (it is completely correlated to systematics and statistical uncertainties for $p_\mathrm{T} > 1$ GeV/c, but uncorrelated to the uncertainties for $p_\mathrm{T} < 1$ GeV/c, so the relevant covariance terms are added here).

- **Uncorrelated:** signal extraction (background shape and fit range), training of the BDT, BDT selections, TRD trigger efficiency (because $p_\mathrm{T} < 1$ GeV/c only uses MB sample), primary vertex calculation (due to the large p_T dependence), p_T distribution (the shape in $p_\mathrm{T} < 1$ GeV/c is largely independent from the shape in $p_\mathrm{T} > 1$ GeV/c, because the former is increasing while the latter is decreasing), extrapolation uncertainty due to the models.

7. Results

This section presents the results obtained using ALICE data within the work of this thesis. The self-normalized yields of prompt and non-prompt J/ψ, whose analysis has been detailed in Chapter 5, are shown as a function of the self-normalized multiplicity, for which the analysis has been reported in Chapter 4. The multiplicity is also divided into several azimuthal regions defined with respect to the J/ψ emission direction, which are also described in Chapter 4. For further interpretation, the results are compared with models, especially to the EPOS4HQ and PYTHIA MC generators. But before presenting these results, a discussion is made on the possible inclusion or removal of the decay daughters in the multiplicity calculation. Finally, the evolution with multiplicity of the ratio between J/ψ and D^0 is shown across several collision systems.

7.1. Discussion on the inclusion of the decay daughters in the multiplicity and on the baseline

When the J/ψ yields and the multiplicity are measured in the same rapidity region, the decay daughters of the J/ψ enter in the multiplicity calculation. In the measurement in Ref. [147] by the PHENIX Collaboration, it was tried to remove the daughters explicitly from the multiplicity calculation, in order to check the impact they may have due to autocorrelations. A strong decrease of the correlation was found. The impact of the daughter removal on the correlation is mainly due to the steepness of the decrease of the multiplicity distribution, and how much a shift of two charged particles in the multiplicity distribution modifies $P(N_{\text{ch}})$. At LHC energies, the higher average charged-particle multiplicity, as well as the larger multiplicity fluctuations, makes the multiplicity distribution less steep. Thus, the presence or not of the two daughters is expected to have a smaller impact at LHC than at RHIC.

In Fig. 7.1, the self-normalized prompt J/ψ yields with $p_{\text{T}} > 1$ GeV/c are shown as a function of self-normalized multiplicity, and compared when including or removing the decay daughters in the multiplicity calculation. The INEL>0 (i.e. minimum-bias) and V0M (corresponding to the High-Multiplicity trigger) cases have been separated. In the latter case, when removing the daughters, a weight is introduced for correcting the different impact of removing two daughters considering MB and HM multiplicity distributions, as was described in Sec. 5.8.2. The decrease with removal of the daughters is found to be of the order of 20% for a multiplicity equal to 7 times the average charged-particle multiplicity, and it is reproduced in PYTHIA. The events with a J/ψ are associated to a lower multiplicity value when the daughters are removed than when they are included. In the calculation of the J/ψ yield, the total number of unbiased events (i.e. without the requirement of the presence of a J/ψ) at this lower multiplicity value is higher,
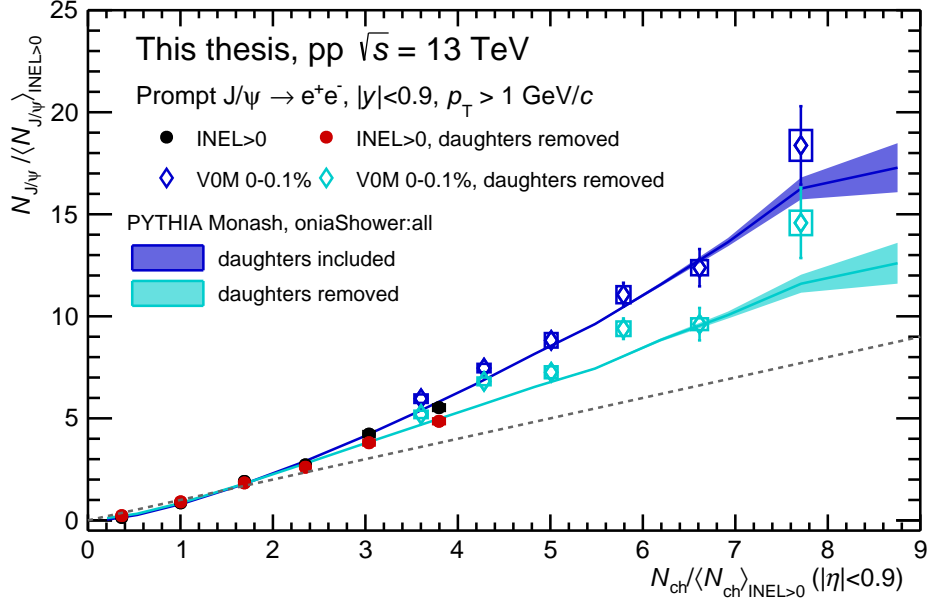
Figure 7.1.: Self-normalized prompt J/ψ with $p_T > 1$ GeV/c as a function of self-normalized charged-particle multiplicity within $|\eta| < 0.9$. The case when the J/ψ dielectron daughters are included in multiplicity calculation is compared with the case when both daughters are removed from the multiplicity calculation. The J/ψ in the multiplicity intervals are selected either in INEL> 0 events, or in HM-triggered events (V0M 0-0.1%). The yields are compared to PYTHIA 8.311 [39] using oniaShower:all settings [125], with and without removing the daughters from the multiplicity calculation.

thus reducing the J/ψ yield per event. This shows that autocorrelations brought by the J/ψ decay daughters are present.

Given the different results obtained with or without the daughters, a choice has to be made between the two possibilities, depending on what is intended to be shown with the final results. Both have biases, advantages and drawbacks, which are described in the following.

If the choice is to include the daughters in the multiplicity, then autocorrelations are kept. One problem is that the results would depend on the decay channel: a decay channel with more than two decay daughters would lead to a stronger increase. However, in the ALICE measurement of Ref. [144], the inclusive multiplicity-dependent J/ψ yield as a function of midrapidity multiplicity has been estimated in two ways. The first way was to estimate the yield directly as a function of the number of tracklets at midrapidity. The second way was to estimate the yield as a function of the multiplicity in the V0 detector. Then, the correlation between V0 multiplicity and midrapidity multiplicity in unbiased event was used in order to obtain a result as a function of midrapidity multiplicity without any bias from the J/ψ decay daughters. Both results were found to be very similar. A possible interpretation of this would not be that there is no autocorrelations, but that the impact of the autocorrelations from the daughters is similar in this case as the impact of having a J/ψ in the event in general. The impact of the J/ψ could be seen in the V0 for example if there is a recoil jet emitted at forward rapidity. In this case, both the recoil jet, when converted to a midrapidity multiplicity, and the decay daughters would result on average to a similar additional multiplicity at midrapidity. Therefore, the bias of the inclusion of the daughters seems present but small in this case.

On the other hand, if it is chosen to remove the daughters from the multiplicity, the autocorrelations are removed. However, another problem arises in this case: the measurement is not done anymore as a function of the total multiplicity, but as a function of the multiplicity except what comes from the J/ψ. One might argue that the J/ψ is neutral, while the measurement is done on charged particles. However, here, charged particles are a proxy for the total number of particles (charged + neutral), which is not directly accessible in the experiment. Except for the autocorrelation effects, charged particles should not bias the event. When measuring J/ψ production as a function of the total event multiplicity except the J/ψ, a decorrelation bias appears, which artificially decreases the correlation compared to the case when the J/ψ production is measured as a function of the total event. This can be understood when looking at the right panel of Fig. 7.2. In this case, the self-normalized yield of charged pions at midrapidity, predicted by PYTHIA with the Monash tune, is shown as a function of self-normalized multiplicity at midrapidity. Pions account for a large fraction of inclusive charged hadrons. Thus, they represent the baseline for soft particle production. If there was no difference between hard and soft particle production, the J/ψ yield would follow this baseline. If the pion itself is counted in the multiplicity, the baseline is almost linear. However, when the pion is removed from the multiplicity calculation, the baseline is not linear anymore. In this case, for the estimation of the multiplicity associated to a given pion, only this pion is removed from the multiplicity, even if there are several pions in the event. The effect of the removal of the pion is stronger at lower center-of-mass energy. This would make the interpretation of the result more complex, especially because, when excluding the J/ψ daughters, two particles are removed, and the impact could then be larger than when only one pion is removed from multiplicity. The additional complexity comes for example in the naive expectation of linearity with the number of MPI, which was described in Sec. 2.2. In this simple picture, the J/ψ yield would be directly proportional to the number of hard MPI, itself proportional to the total number of MPI, leading to a linear correlation between number of J/ψ and number of MPI. If the MPI related to the J/ψ is excluded from the multiplicity, the correlation measured would be between $N_{\mathrm{J}/\psi}$ and $N_{MPI} - 1$. This baseline is not anymore linear and depends on the distribution of N_{MPI}: in this case, the possibility of a straightforward interpretation has been lost. This demonstrates that, removing the daughters also introduce a bias in the result. With this bias, the interpretation of the results based on the interplay between hard and soft particle production is not as straightforward as when the daughters are included.

Since the bias when the daughters are included seems smaller than the bias with daughters excluded, the decision is made that for subsequent results the daughters are not removed in the multiplicity calculation.

Another problem is the comparison to the models. For MC generators such as PYTHIA or EPOS, the choice of including the decay daughters can be made similar as in data. However, for the models which do not rely on MC generators, the treatment of the daughters is not straightforward. In general, daughters are not removed or included explicitly. If there is a mechanism which would take into account the additional impact on the multiplicity of the presence of a J/ψ in the event, then the model calculations should be compared to the result with inclusion of the daughter. The same should be done if there is a direct correlation done between
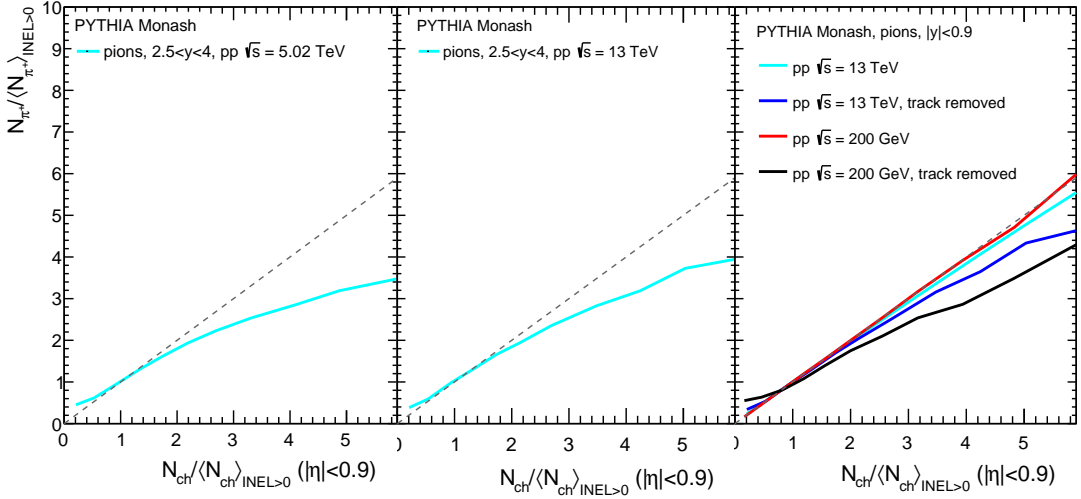
Figure 7.2.: Self-normalized pion yield predicted by PYTHIA as a function of self-normalized multiplicity. Left and middle: The pion yields are measured at forward rapidity, while the multiplicity is estimated at midrapidity, for $\sqrt{s} = 5.02$ TeV (left) and $\sqrt{s} = 13$ TeV (middle). Right: The pions yields and the multiplicity are measured at midrapidity.

the J/ψ yield and the total N_{MPI} (or $N_{\mathrm{gluon\text{-}gluon}}$ or N_{pomerons}, depending on the model, but not with $N_{\mathrm{MPI}} - 1$), and the hard MPI is not explicitly rejected from the multiplicity estimation. In contrast, if the hard part, or the J/ψ itself, is explicitly not counted in the multiplicity, then the model calculations should be compared to the results with daughter removal. In general, the treatment of the autocorrelations is done differently in the models compared to what is done in data. Thus, an explicit comparison of the yields predicted by the models to the experimental measurements may be possible in neither case, whether or not the daughters are included in the multiplicity calculation.
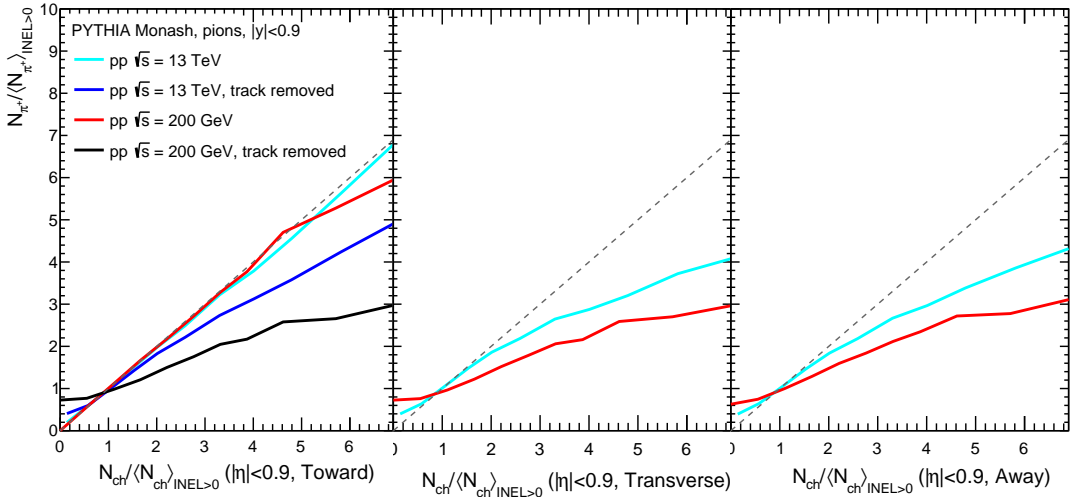

Figure 7.3.: Self-normalized pion yield predicted by PYTHIA as a function of self-normalized multiplicity in toward (left), transverse (middle), and away (right) regions.

PYTHIA simulations also allow to analyze the bias on the baseline in other cases. In the left and middle panels of Fig. 7.2, the pion yields at forward rapidity from PYTHIA are shown as a function of midrapidity multiplicity. The increase is weaker than linear, which is a sign of the bias

due to rapidity correlations, as explained in Sec. 2.2. This shows that the comparison to a linear increase when the J/ψ is measured at forward rapidity and the multiplicity at midrapidity does not make complete sense. The pion yields are also shown as a function of multiplicity in azimuthal angle regions in Fig. 7.3. For each pion, the azimuthal regions are defined with respect to the pion emission direction. While, due to the fluctuations effects described in Sec. 4.5, this baseline is weaker-than-linear for the transverse and away regions, the pion yields increase almost linearly with the toward multiplicity. When the pion itself is removed, the increase is weaker-than-linear, but still stronger than in the transverse and away regions. This shows that the definition of the regions itself seems to introduce a bias which is dependent on the studied regions. This kind of bias appears independently of the hardness of the process producing the particle. This should be kept in mind when the measurement of the J/ψ yields as a function of multiplicity will be interpreted.

7.2. Multiplicity-dependent prompt and non-prompt J/ψ yields
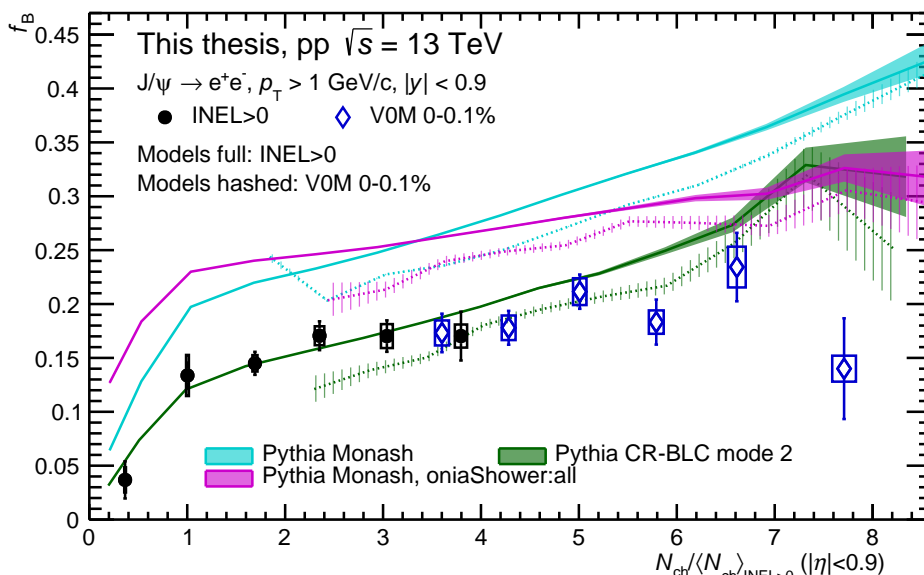
Figure 7.4.: Fraction of J/ψ with $p_{\mathrm{T}} > 1$ GeV/c coming from the decay of beauty hadrons as a function of self-normalized charged-particle multiplicity within $|\eta| < 0.9$. The J/ψ in the multiplicity intervals are selected either in INEL> 0 events, or in HM-triggered events (V0M 0-0.1%). The fraction is compared to PYTHIA 8.311 using different settings [40, 46, 125].

The fraction of J/ψ with $p_{\mathrm{T}} > 1$ GeV/c coming from the decay of beauty hadrons, f_B, as a function of self-normalized multiplicity is shown in Fig. 7.4. This fraction gives information on the difference in the evolution with multiplicity between charm and bottom hadrons, as well as the difference between open heavy-flavor hadrons and quarkonium. It is shown separately for INEL>0 events, and for events selected with HM trigger. At very low multiplicity, the non-prompt fraction is very small. One reason for this is that the other decay products of the beauty hadrons are possibly included in the multiplicity. In addition, another beauty hadron from the hadronization of the other b quark in the $b\bar{b}$ pair could potentially fall into the acceptance of the detector, also contributing to additional particles in the multiplicity. Therefore, it is very unlikely to find non-prompt J/ψ in very low multiplicity events. At higher multiplicity, the non-

prompt fraction shows a hint of an increase with multiplicity. The slope obtained with a fit of the non-prompt fraction, using a linear function and excluding the first multiplicity interval, is found to be 2.6 σ away from 0. This means that there is a slight difference between prompt and non-prompt J/ψ, either due to the flavor of the heavy quark, through the quark mass and the hardness of the event or through the higher number of decay processes, or due to the quarkonium hadronization process.

The data is compared with PYTHIA 8.311 using different settings: the Monash tune [40], the QCD-based CR-BLC mechanism mode 2 [46], and the oniaShower process [125] with Monash tune. In general, the models predict a higher non-prompt fraction compared to data, especially at high multiplicity. They also predict a stronger increase with multiplicity than what is seen in data, with a possible exception for the oniaShower process. In this case, the slight increase is well reproduced but the non-prompt fraction is overestimated. All models also predict a decrease of the non-prompt fraction at very low multiplicity.

In order to compare the models to the HM-triggered data, the 0.1% events with highest charged-particle multiplicity in the ALICE V0M acceptance region are selected. The model calculations when this selection is incorporated are shown with hashed lines. The models predict that the HM event selection could bias the distribution towards a lower non-prompt fraction at same charged-particle multiplicity, as was discussed in detail in Sec. 5.8.1. This means that, potentially, the non-prompt fraction in data at high values of charged-particle multiplicity could be higher in minimum-bias events as it is observed now. It means that the difference in the multiplicity dependence between prompt and non-prompt J/ψ could be larger if the bias was not there. In data, the INEL>0 and HM-triggered events seem compatible for the multiplicity values where both are measured. However, it is still possible that the apparent compatibility is due to the statistical fluctuations.

In Fig. 7.5, the prompt and non-prompt J/ψ yields are shown as a function of charged-particle multiplicity. Both quantities are normalized by their average value in INEL>0 events. For reference, a linear increase with slope 1 is also shown as a dashed grey line, while the bottom panels show the ratio between the data points and the linear increase. Both prompt and non-prompt J/ψ show a stronger-than-linear increase with multiplicity, similar to the one found for inclusive J/ψ in [144]. The non-linear trend shows that J/ψ, created in hard scattering, has a different behavior than an average charged particle, mostly created in soft scattering. This stronger-than-linear increase could be interpreted as a saturation of soft particles, possibly suppressed in high-density environment compared to low-density environment, or as an increase of the associated particle production for hard probes. The fact that the increase is similar between prompt and non-prompt J/ψ shows that the multiplicity dependence of the yields is only moderately influenced by how heavy quarks hadronize.

In order to better understand the cause for the stronger-than-linear increase, the data is further compared to models. PYTHIA with Monash tune strongly underestimates the prompt J/ψ yields for a multiplicity higher than four times the average multiplicity. The same conclusion applies to the CR-BLC mode 2, which predicts an even lower prompt J/ψ yield at high-multiplicity. This means that the specific detail of the color reconnection process has moderate influence
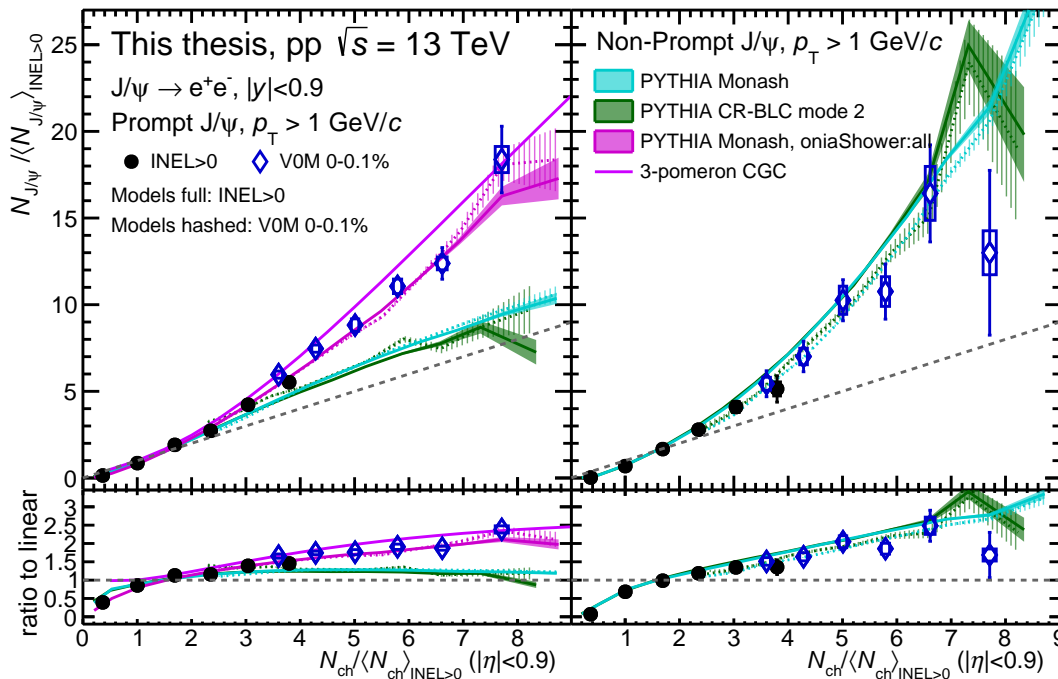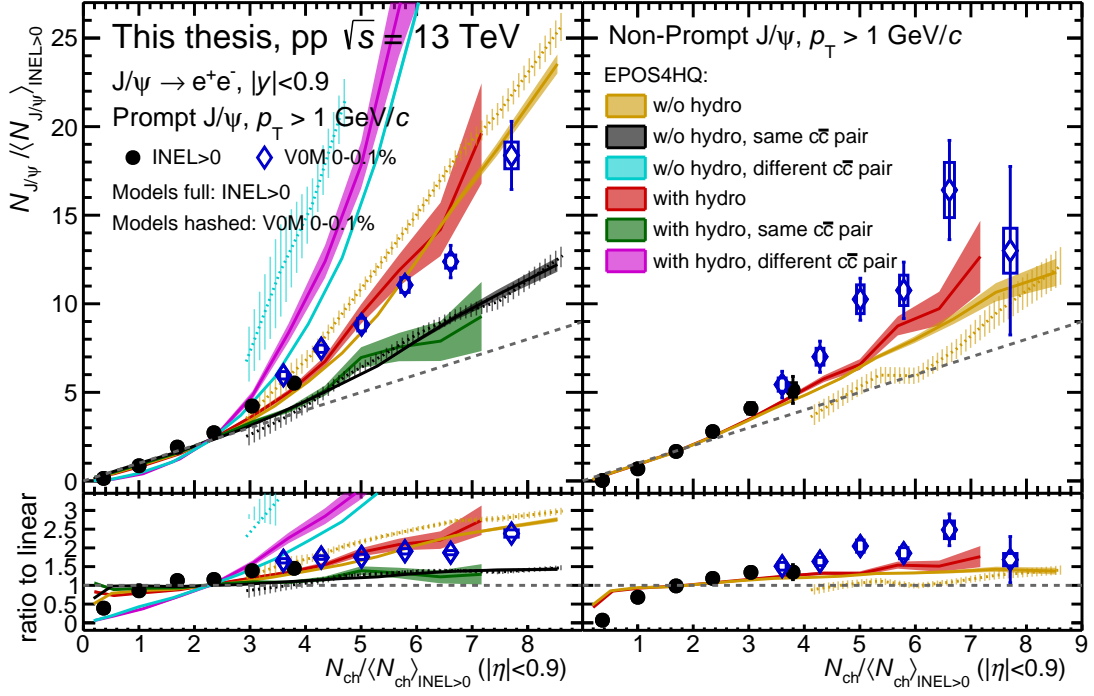
Figure 7.5.: Self-normalized prompt (left) and non-prompt (right) J/ψ with $p_T > 1$ GeV/c as a function of self-normalized charged-particle multiplicity within $|\eta| < 0.9$. The J/ψ in the multiplicity intervals are selected either in INEL> 0 events, or in HM-triggered events (V0M 0-0.1%). The yields are compared to PYTHIA 8.311 using different settings [39, 46, 125], as well as the 3-pomeron CGC model [129]. Lower panels show the ratio to a linear increase.

on the correlation between J/ψ and multiplicity. In contrast, the oniaShower setting provides a much better agreement with data. This could show that the production process of the prompt J/ψ, and the particles emitted alongside this production process, have a strong influence on the evolution of the J/ψ yield with multiplicity. This influence seems much stronger than the one of the underlying event, since the change in the predicted J/ψ yield when the oniaShower setting is added is larger than when the CR mechanism is modified. For non-prompt J/ψ, both PYTHIA with Monash tune and CR-BLC mode 2 reproduce well the trend as a function of multiplicity. The oniaShower process is not shown in the non-prompt case, as it only modifies prompt J/ψ production.

A comparison with the 3-pomeron CGC model [129] is also shown for prompt J/ψ. There seems to be a slight overestimation at high multiplicity. However, it should be noted that this model does not report uncertainties and does not take into account the bias of the HM trigger. The correct description shows that the influence of the CGC saturation effects in the initial state, as well as the influence of the production process of the J/ψ, can explain the observed correlation.

The comparison with EPOS4HQ calculations, with and without the hydrodynamic evolution, is shown in Fig. 7.6. EPOS4HQ describes the prompt J/ψ measurements well, even if the data seems slightly overestimated at high multiplicity. The prompt J/ψ yield is separated between the cases where the c and the $\bar{c}$ producing charmonium come from the same $c\bar{c}$ pair and the other cases. The strong increase of the prompt yields is mainly due to the combinatorial enhancement from c and $\bar{c}$ coming from different $c\bar{c}$ pairs, more frequent at higher multiplicity.
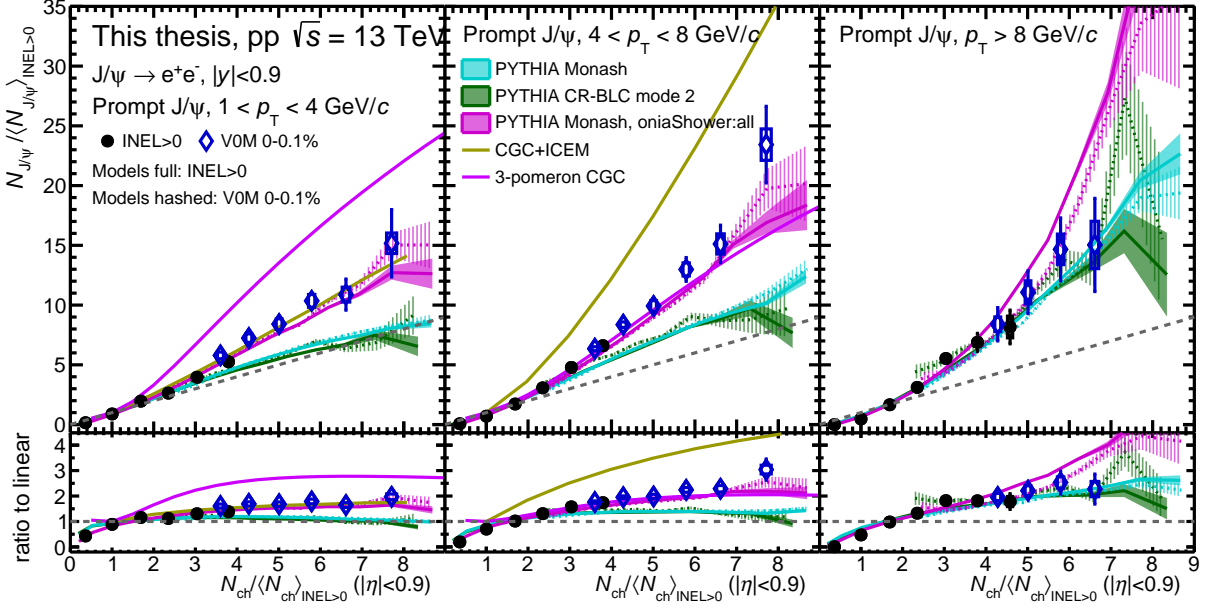
Figure 7.6.: Self-normalized prompt (left) and non-prompt (right) J/ψ with $p_T > 1$ GeV/c as a function of self-normalized charged-particle multiplicity within $|\eta| < 0.9$. The J/ψ in the multiplicity intervals are selected either in INEL> 0 events, or in HM-triggered events (V0M 0-0.1%). The yields are compared to EPOS4HQ calculations [50–53]. Lower panels show the ratio to a linear increase.

The results presented in this thesis could help the tuning of the coalescence model parameters. These parameters could in turn impact the relative fractions of J/ψ produced from c and $\bar{c}$ coming from same and from different $c\bar{c}$ pairs. A slightly stronger increase is found when hydrodynamic evolution is activated compared to when it is not. This is due to a reduction in the multiplicity, because the available energy for particle production has been transferred to flow [52]. This adds to the initial-state saturation effects of the soft pomerons which are still present when the hydrodynamic evolution is disabled. However, the smallness of the effect from hydrodynamics means that it is difficult to make a conclusion on whether final-state effects are necessary to reproduce the data. EPOS4HQ calculations also underestimate the non-prompt J/ψ measurements, which do not benefit from this combinatorial enhancement, for a relative multiplicity larger than 3.

Fig. 7.7 shows the multiplicity-dependent self-normalized yields for prompt J/ψ in several p_T intervals ($1 < p_T < 4$ GeV/c, $4 < p_T < 8$ GeV/c, and $p_T > 8$ GeV/c). Fig. 7.9 shows the same quantity for non-prompt J/ψ. As was also shown for inclusive J/ψ, the increase is stronger at higher p_T. In all cases, the increase is still stronger-than linear. The p_T-dependent increase for prompt J/ψ seems stronger between the first and second intervals, than between second and third intervals. However, it could still be due to the large uncertainties for $p_T > 8$ GeV/c.

When comparing prompt data to the models, PYTHIA with the Monash tune and CR-BLC mode 2 underestimate the results in the first two p_T intervals. In contrast, the oniaShower process slightly underestimates the data in the first two p_T intervals, and slightly overestimates them at higher p_T. While the CGC+ICEM model can reproduce prompt J/ψ data at low p_T

Figure 7.7.: p_T-differential measurement of prompt J/ψ as a function of self-normalized charged-particle multiplicity within $|\eta| < 0.9$. The J/ψ in the multiplicity intervals are selected either in INEL> 0 events, or in HM-triggered events (V0M 0-0.1%). The yields are compared to PYTHIA 8.311 using different settings [39, 46, 125], as well as the 3-pomeron CGC model [129] and the CGC+ICEM model [126]. Left panels: $1 < p_T < 4$ GeV/c. Middle panels: $4 < p_T < 8$ GeV/c. Right panels: $p_T > 8$ GeV/c. Lower panels show the ratio to a linear increase.
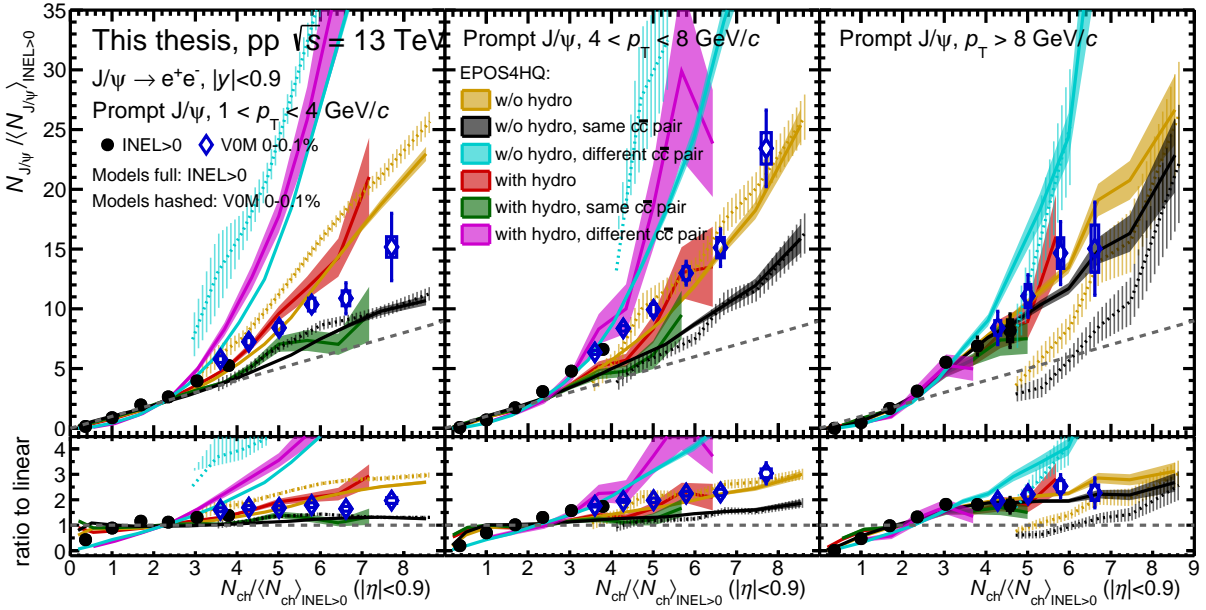
Figure 7.8.: p_T-differential measurement of prompt J/ψ as a function of self-normalized charged-particle multiplicity within $|\eta| < 0.9$. The J/ψ in the multiplicity intervals are selected either in INEL> 0 events, or in HM-triggered events (V0M 0-0.1%). The yields are compared to EPOS4HQ calculations [50–53]. Left panels: $1 < p_T < 4$ GeV/c. Middle panels: $4 < p_T < 8$ GeV/c. Right panels: $p_T > 8$ GeV/c. Lower panels show the ratio to a linear increase.
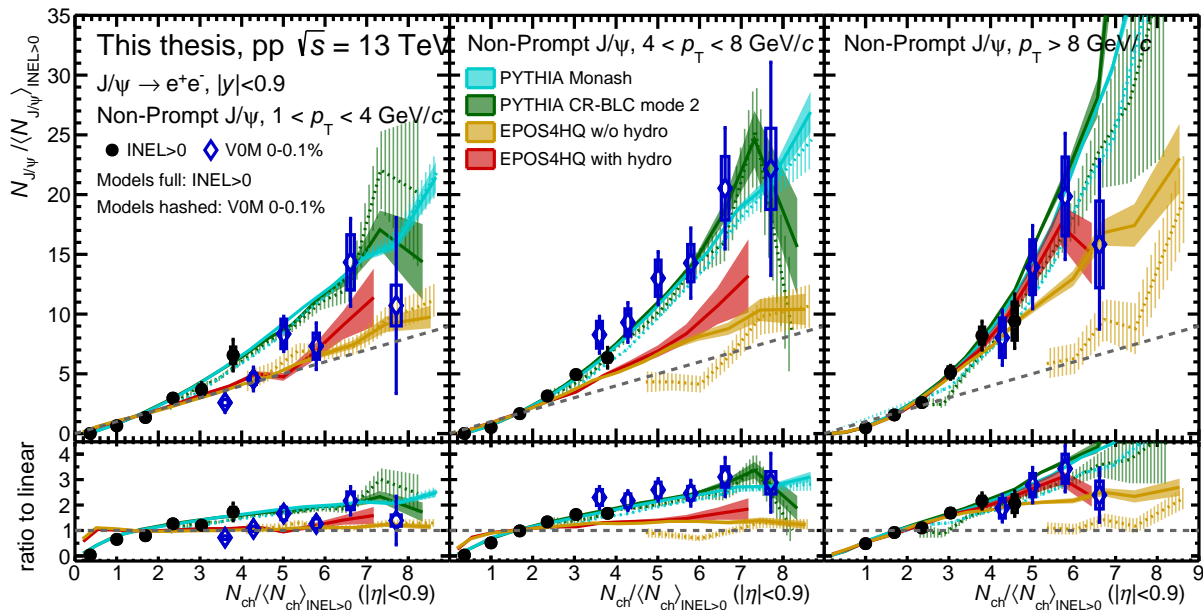
Figure 7.9.: p_T-differential measurement of non-prompt J/ψ as a function of self-normalized charged-particle multiplicity within $|\eta| < 0.9$. The J/ψ in the multiplicity intervals are selected either in INEL> 0 events, or in HM-triggered events (V0M 0-0.1%). The yields are compared to PYTHIA 8.311 [39] using different settings. Left panels: $1 < p_T < 4$ GeV/c. Middle panels: $4 < p_T < 8$ GeV/c. Right panels: $p_T > 8$ GeV/c. Lower panels show the ratio to a linear increase.

but not at intermediate p_T, the correlation is opposite for the 3-pomeron CGC, which predicts weaker increase at higher p_T. A common interpretation of all CGC-based models cannot be made and different implementations of specific effects can lead to different evolutions with multiplicity and transverse momentum. EPOS4HQ calculations for prompt J/ψ, shown in Fig. 7.8, do not show a strong modification between low- and high-p_T J/ψ, leading to an overestimation at high multiplicity and low momentum. However, the yields of J/ψ when considering only c quarks coming from the same $c\bar{c}$ pair show a stronger increase at higher p_T. This means that the weak modification with the p_T in EPOS4HQ is due to a larger fraction of the combinatorial contribution at low p_T, responsible for the strong increase at low p_T. Indeed, charm quarks are more abundant at low momentum, increasing the probability to obtain a J/ψ from several different $c\bar{c}$ pairs compared to higher momentum.

For non-prompt J/ψ, in addition, low p_T J/ψ yields seem to exhibit a strong bias in the high-multiplicity triggered case. All the PYTHIA tunes seem compatible within the large uncertainties. However, the EPOS4HQ calculations, with and without hydrodynamics, significantly underestimate the results at high multiplicity, except for $p_T > 8$ GeV/c for which the uncertainties are large.

In this section, it has been observed that prompt and non-prompt J/ψ both present a very similar stronger-than-linear increase. The small difference is hinted at the level of 2.9σ by the slight increase of the non-prompt fraction.

Comparison between J/ψ and other particles such as D^0 could also help to understand whether the behavior of prompt J/ψ in high-multiplicity collisions is unique compared to other hard processes.

7.3. J/ψ-to-D^0 ratio

The ratio between prompt quarkonium and open charm allows to test the difference in their production process, by cancelling several experimental and theoretical uncertainties. It was for example shown in Pb-Pb collisions that this ratio is increasing when going from semi-central to central collisions [101], likely due to regeneration of J/ψ from uncorrelated c and $\bar{c}$ quarks in a dense medium with high number of $c\bar{c}$, while at lower energies in LHCb fixed-target heavy-ion collisions this ratio was found to be decreasing with system size [207]. The multiplicity dependence of the ratio in pp collisions thus allows to check if dense medium effects could also be seen in small system.
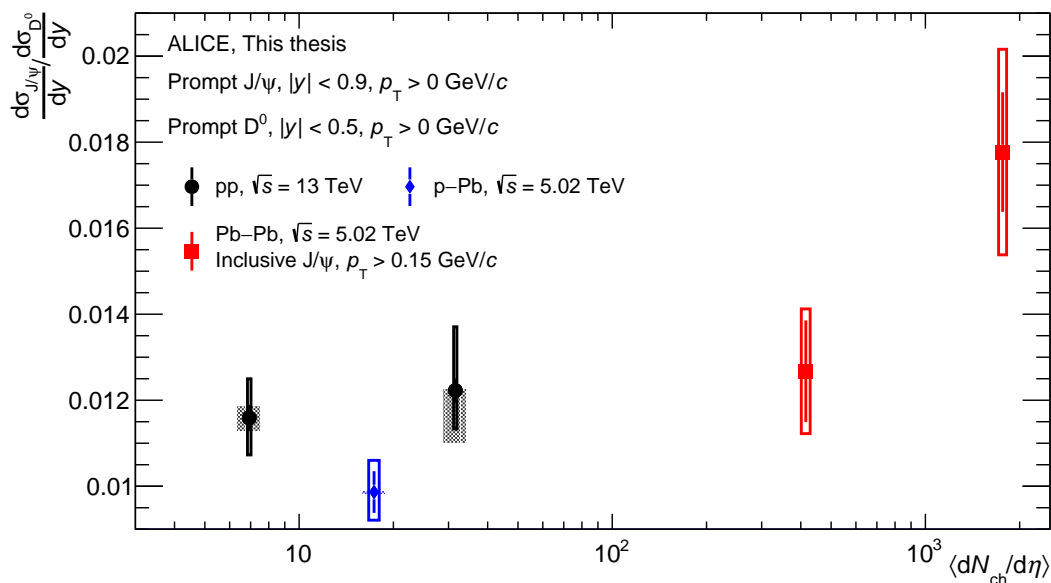
Figure 7.10.: Ratio between the p_T-integrated yields of prompt J/ψ and prompt D^0 as a function of charged-particle multiplicity in several collision systems. Results for p–Pb collisions at 5.02 TeV are taken from Ref. [208, 209]. Results for Pb–Pb collisions at 5.02 TeV are taken from Ref. [101].

In Fig. 7.10, the ratio between prompt J/ψ and prompt D^0 yields is shown as a function of charged-particle multiplicity across several colliding systems, with data taken from previous ALICE measurements in p–Pb collisions at $\sqrt{s_\mathrm{NN}} = 5.02$ TeV (Refs. [208, 209]), and Pb–Pb collision at the same energy (Ref. [101]). For pp collisions, the results are shown for integrated INEL>0 collisions, and high-multiplicity triggered events. The data for prompt D^0 is taken from Ref. [140].

The main observation from these results is that, in pp collisions, no modification of the ratio can be observed within uncertainties. While the ratio in p–Pb collisions is smaller than in pp collisions, the ratio in semi-central Pb–Pb collisions is compatible with the one in pp collisions within uncertainties. This shows that, within uncertainties, the effects of a possible medium which could act differently on J/ψ and D^0 are small even in high-multiplicity pp collisions.

Therefore, the ratio between prompt J/ψ and D^0 shows that, in high-multiplicity pp collisions, no large difference appears between the production yields of prompt quarkonium and other hard particles.

The origin of the increase of the yields with multiplicity still remains unknown for both prompt and non-prompt J/ψ. It could come from a saturation of the soft particles, or because of the effect of additional particles emitted in the same production process as the J/ψ. Therefore, by separating the multiplicity in three azimuthal regions defined with respect to the J/ψ emission direction, as described in Sec. 2.2.3, results in the next section intend to give more hints towards the understanding of the causes for the observed stronger-than-linear trend. In particular, the effect of autocorrelations from particles emitted during J/ψ production could be studied.

## 7.4. Results as a function of multiplicity in azimuthal regions
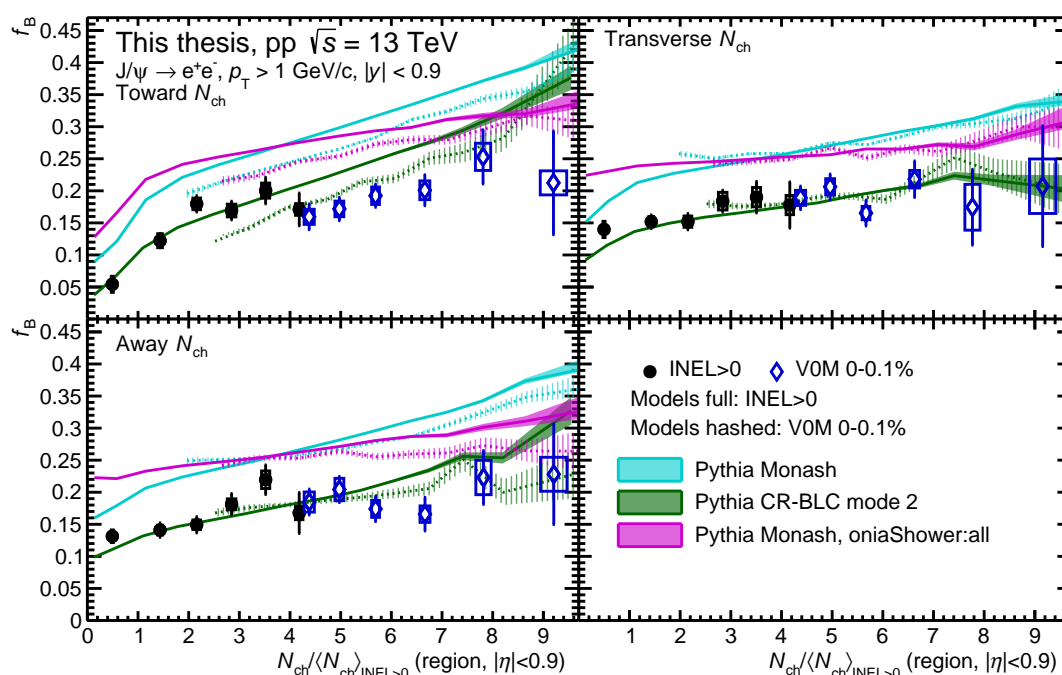
Figure 7.11.: Fraction of J/ψ with $p_{\mathrm{T}} > 1$ GeV/c. coming from the decay of beauty hadrons as a function of self-normalized charged-particle multiplicity selected in several azimuthal regions with respect to the J/ψ emission direction within $|\eta| < 0.9$. The J/ψ in the multiplicity intervals are selected either in INEL> 0 events, or in HM-triggered events (V0M 0-0.1%). The fraction is compared to PYTHIA 8.311 using different settings [40, 46, 125]. The self-normalized multiplicity is measured either in the region toward (top left), transverse to (top right), or away to (bottom left) the J/ψ emission direction.

In Fig. 7.11, the fraction of J/ψ with $p_{\mathrm{T}} > 1$ GeV/c coming from the decay of beauty hadrons is shown as a function of self-normalized multiplicity in the toward, transverse and away azimuthal angle regions. If a similar evolution of the non-prompt fraction with the multiplicity is seen for all regions, it could favor the hypothesis that the slight difference between prompt and non-prompt J/ψ is due to a global property, caused for example by a harder $b\bar{b}$ event in general. Conversely, if, in the toward region, a stronger increase than in the other regions is observed, the difference between prompt and non-prompt J/ψ would probably be due to local correlations such as fragmentation or decays. When comparing the evolution of the non-prompt J/ψ fraction as a function of multiplicity between all three regions, all regions present a hint of an increase. The hint is stronger when looking as a function of toward multiplicity (significance of 2.9σ compared to a flat trend) than as a function of away (2.4σ significance) or transverse multiplicity (2.5σ

significance). However, the uncertainties here do not allow a robust conclusion on the occurrence of one or the other case.

The slightly faster increase of the non-prompt fraction in the toward case is in general reproduced by the models. Especially PYTHIA with CR-BLC mode 2 reproduces well the magnitude and evolution with transverse multiplicity. All models also predict a stronger bias of the high-multiplicity trigger in the toward region. A hint of this bias seems also to be present in data, although the uncertainties do not allow for a definitive conclusion.
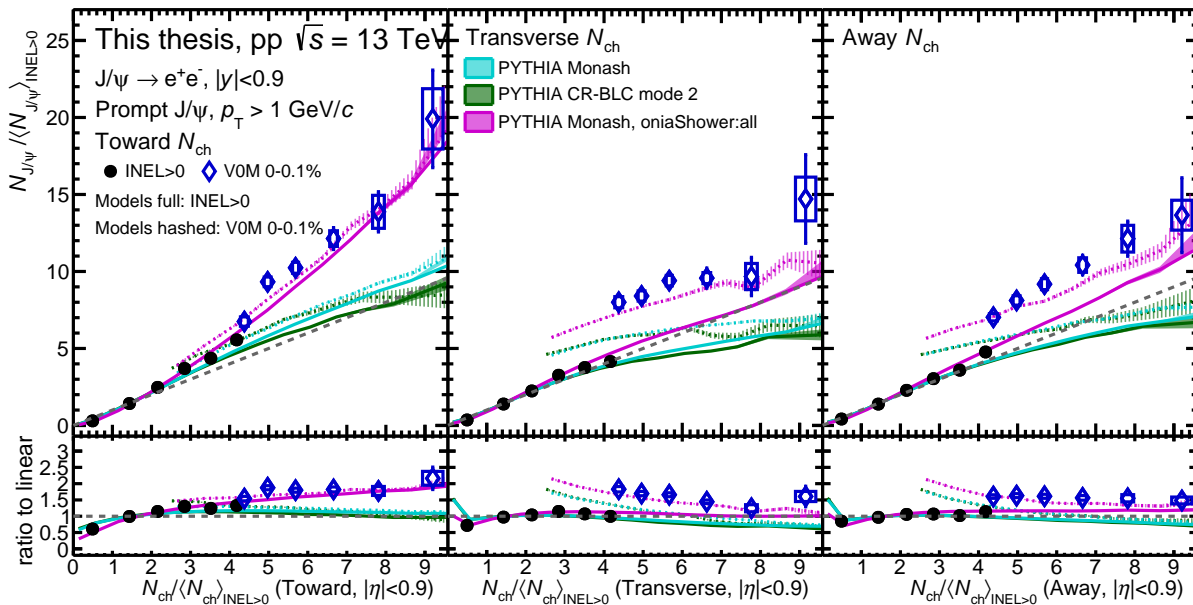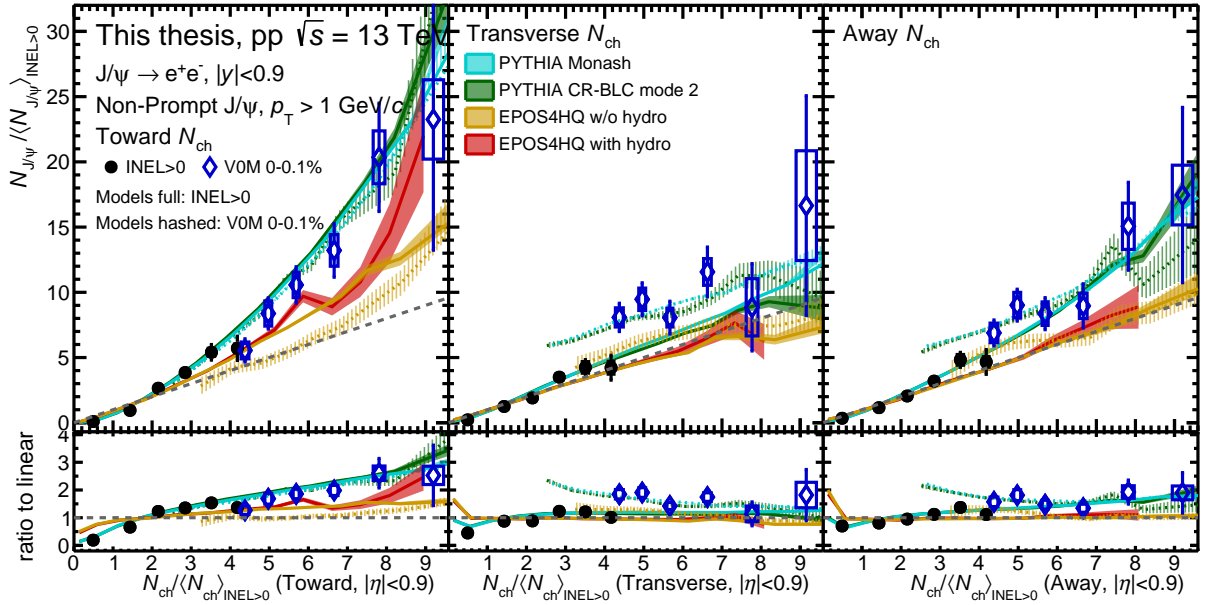

Figure 7.12.: Self-normalized prompt J/ψ with $p_T > 1$ GeV/c as a function of self-normalized charged-particle multiplicity selected in several azimuthal regions with respect to the J/ψ emission direction within $|\eta| < 0.9$. TThe J/ψ in the multiplicity intervals are selected either in INEL> 0 events, or in HM-triggered events (V0M 0-0.1%). The yields are compared to PYTHIA 8.311 using different settings [40, 46, 125]. The self-normalized multiplicity is measured either in the region toward (left), transverse to (middle), or away to (right) the J/ψ emission direction. Lower panels show the ratio to a linear increase.

Fig. 7.12 shows the self-normalized prompt J/ψ yield as a function of self-normalized multiplicity in the three azimuthal angle regions, while the same is shown for the non-prompt J/ψ case in Fig. 7.14. For both prompt and non-prompt J/ψ, the increase is significantly stronger for the toward region compared to the other regions. This shows the importance of the autocorrelations with associated particles emitted during the same production process as the J/ψ in the rise with multiplicity. However, as was found when studying the baseline with PYTHIA, part of the difference between the regions could be due to the specific definition of the regions. Therefore, the impact of autocorrelations is probably smaller than what is hinted from the difference of the results between the regions. For non-prompt J/ψ, these autocorrelations seem even more important since the high-multiplicity yield in the toward region is slightly higher than for prompt J/ψ, while the transverse yields are similar between prompt and non-prompt J/ψ.

For the results as a function of transverse or away multiplicity, the measurement also shows a strong bias induced by the high-multiplicity trigger. This bias is less significant in the toward region. As explained in Sec. 5.8.1, this is possibly due to a strong correlation between the hardest
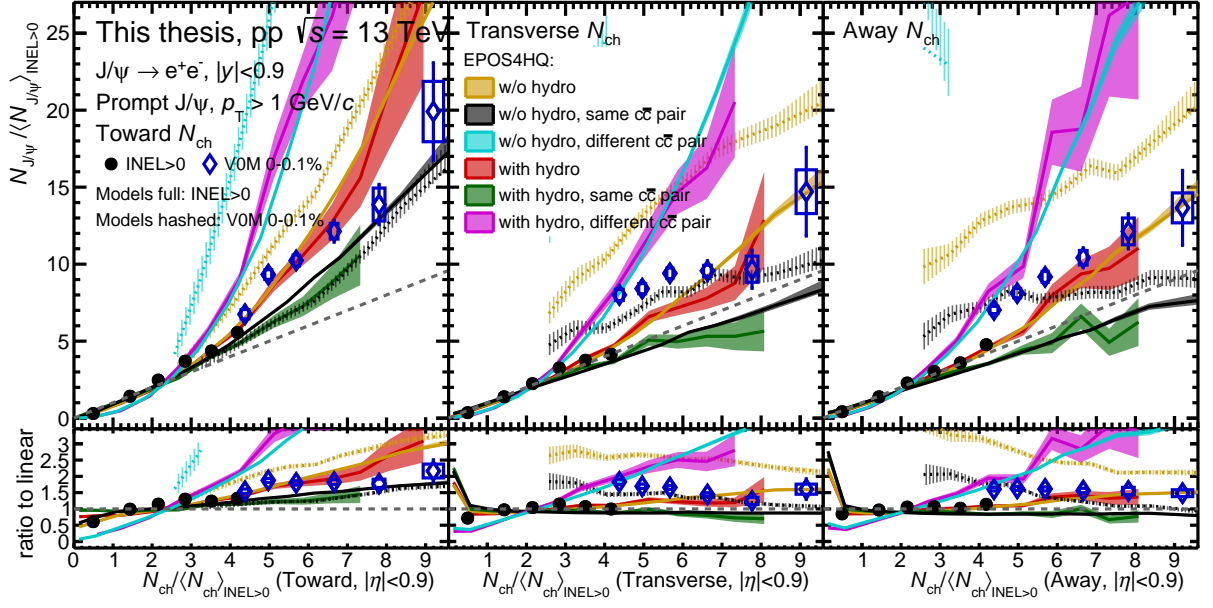
Figure 7.13.: Self-normalized prompt J/ψ with $p_T > 1$ GeV/c as a function of self-normalized charged-particle multiplicity selected in several azimuthal regions with respect to the J/ψ emission direction within $|\eta| < 0.9$. The J/ψ in the multiplicity intervals are selected either in INEL> 0 events, or in HM-triggered events (V0M 0-0.1%). The yields are compared to EPOS4HQ calculations with and without hydrodynamics activated [52, 57]. The self-normalized multiplicity is measured either in the region toward (left), transverse to (middle), or away to (right) the J/ψ emission direction. Lower panels show the ratio to a linear increase.

Figure 7.14.: Self-normalized non-prompt J/ψ with $p_T > 1$ GeV/c as a function of self-normalized charged-particle multiplicity selected in several azimuthal regions with respect to the J/ψ emission direction within $|\eta| < 0.9$. The J/ψ in the multiplicity intervals are selected either in INEL> 0 events, or in HM-triggered events (V0M 0-0.1%). The yields are compared to PYTHIA 8.311 using different settings [40, 46, 125], as well as EPOS4HQ with and without hydrodynamics activated [52, 57]. The self-normalized multiplicity is measured either in the region toward (left), transverse to (middle), or away to (right) the J/ψ emission direction. Lower panels show the ratio to linear increase.

part of the event located in the toward region and the multiplicity at forward rapidity. At fixed transverse or away multiplicity, events with a large multiplicity at forward rapidity are more likely to also produce hard particles at midrapidity in the toward region than events with a forward multiplicity below the HM trigger threshold. Hence, the probability to find a J/ψ is higher. If the toward multiplicity is fixed, the high multiplicity at forward rapidity cannot bring a strong bias on what happens in the toward region. The presence of the bias from the HM trigger in data could in principle make the interpretation of the results more difficult. However, this bias is also present in the models, and the magnitude seems well reproduced, at least in the PYTHIA calculations. Therefore, conclusions can still be taken from the results. It should also be noted that this bias decreases when increasing multiplicity. This is due to the fact that the high-multiplicity trigger selects a higher and higher fraction of all minimum-bias events.

For the transverse and away multiplicity estimators, the J/ψ yields increase with multiplicity is only slightly stronger than linear. Nevertheless, the baseline shown in Sec. 7.1 is weaker than linear. Even if this baseline has been calculated with PYTHIA, it is expected that, in measured data, the baseline would follow the same qualitative trend. The J/ψ yield is then significantly higher than the baseline. This shows that there is also a strong reduction of the soft particle yield compared to the hard part from the J/ψ production in the other regions. It means that not only autocorrelations play a role in the multiplicity dependence of the J/ψ yields, but that there is also a difference in the hard and soft particle production besides these autocorrelations.

PYTHIA with oniaShower seems to reproduce the prompt results well in the three regions, while PYTHIA Monash and CR-BLC mode 2 always underestimate them. The modification of the increase of the yield as a function of toward multiplicity when the production process is modified is expected, and a stronger increase in the case of the away region could be caused by back-to-back jets. It is also interesting to notice that the yield as a function of transverse multiplicity is also increased with the oniaShower process compared to the standard Monash tune. This could be due to large angle radiation in the parton shower. This means that some autocorrelations can still be found in the transverse region, although with a smaller impact. In addition, at low p_{T}, when the J/ψ is not boosted, the decay daughters of the J/ψ can also be included in other regions than the one towards the J/ψ emission direction. For the EPOS4HQ calculations, shown in Fig. 7.13, the prompt yield seems to be overestimated at high multiplicity in the toward region. In addition, there is also a large bias which appears with the HM trigger selection. Furthermore, for prompt J/ψ in the toward region, the increase is slightly stronger when hydrodynamic evolution is not present than when it is activated, while the increase was slightly weaker without hydrodynamics in the inclusive multiplicity case. For transverse and away region, EPOS4HQ also predicts a strong increase for prompt J/ψ as well as a strong trigger bias, which clearly overestimates the high-multiplicity data.

For non-prompt J/ψ, both PYTHIA tunes reproduce the data trends in all three regions. They also predict a stronger increase as a function of away multiplicity than as a function of transverse multiplicity due to back-to-back $b\bar{b}$ correlations. However, the uncertainties in data do not allow to conclude on possible differences between the results for the transverse and away regions. Further conclusions are also prevented by the bias from the high-multiplicity trigger. This bias is predicted to be smaller in the away case, possibly due to a strong correlation of the away

multiplicity with the hard part of the event and with the forward multiplicity in back-to-back jet cases. In the non-prompt case, EPOS4HQ also consistently underestimates the high-multiplicity yield for all regions. The hydrodynamic effect increases the correlation significantly only in the toward region.
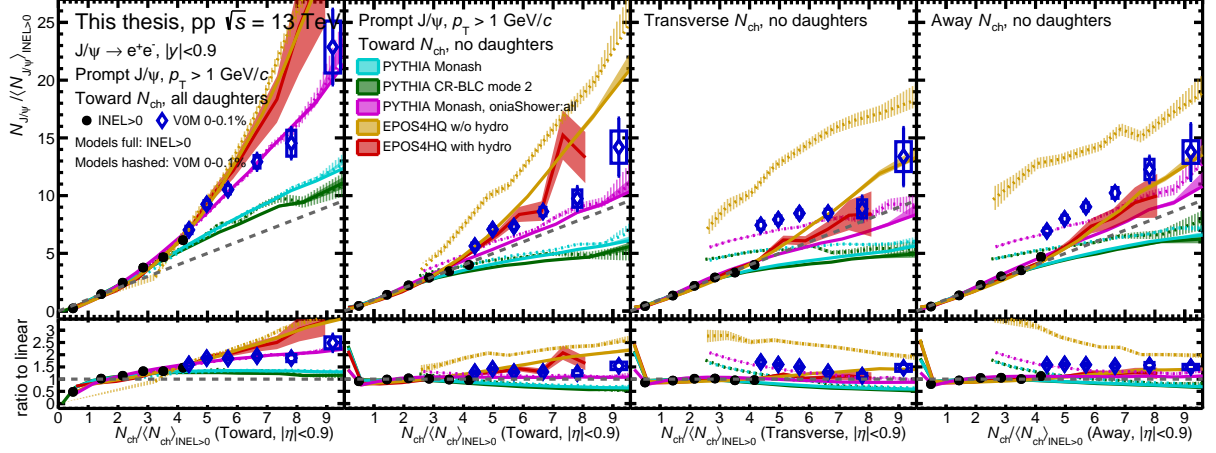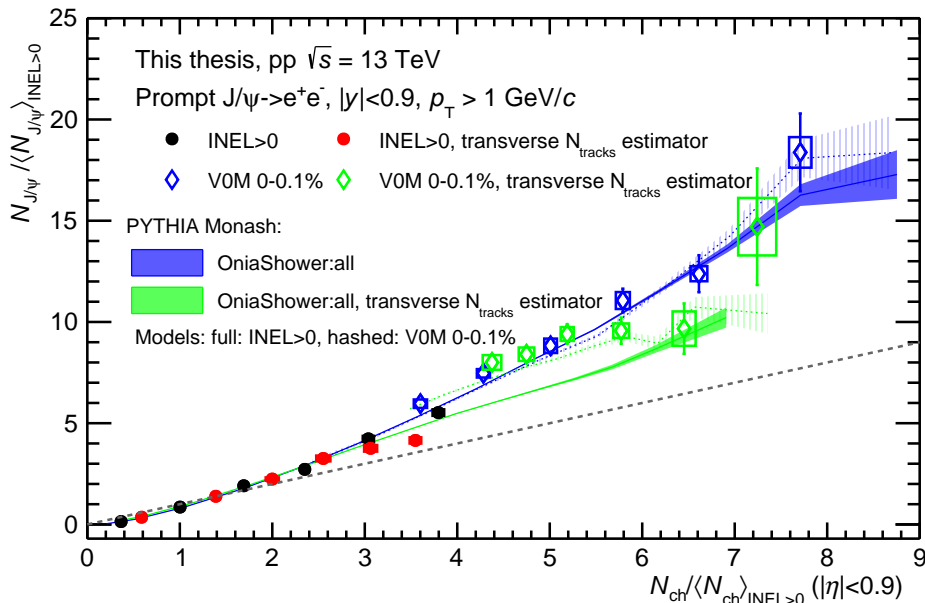

Figure 7.15.: Self-normalized prompt J/ψ with $p_T > 1$ GeV/c as a function of self-normalized charged-particle multiplicity selected in several azimuthal regions with respect to the J/ψ emission direction within $|\eta| < 0.9$. The J/ψ in the multiplicity intervals are selected either in INEL> 0 events, or in HM-triggered events (V0M 0-0.1%). The yields are compared to PYTHIA 8.311 using different settings [40, 46, 125], as well as EPOS4HQ with and without hydrodynamics activated [52, 57]. The self-normalized multiplicity is measured either in the region toward the J/ψ emission direction with including all the daughters (leftmost) or removing all the daughters from the multiplicity (second leftmost). The multiplicity is also measured in the regions transverse to (second rightmost), or away to (rightmost) the J/ψ emission direction, in both cases with removing all the daughters from the multiplicity. Lower panels show the ratio to linear increase.

As explained before, depending on the J/ψ p_T, it is possible that the daughters are found in a different region than the J/ψ emission direction. In the previous results shown in this section, the daughters are counted in the region to which they belong depending on their azimuthal angle. However, an alternative could be to count the daughters always in the toward region. Indeed, the accounting of the decay daughters in the multiplicity is usually done in order to account for the presence of the J/ψ itself when looking at the total particle production of the event (and not the total particle production except the J/ψ). Thus, because the J/ψ itself is always located in the toward region, it could make sense to count the daughters also in the toward region. That is also a simple way to reduce the amount of autocorrelations present in the transverse region, in addition to removing the dependence on the kinematics of the J/ψ decay. The results for prompt J/ψ after counting all the daughters in the toward region is shown in Fig. 7.15. The case where all daughters are also removed from the toward region is also shown. Because the impact of the J/ψ decay is similar for non-prompt J/ψ, the result for non-prompt J/ψ is not shown in this case. When these results are compared to the case for which all the daughters are included in the region where they are found, no difference appears for the away region, while the transverse region is slightly reduced and the toward increases slightly.

When removing all the daughters also in the toward region, the yields in the toward region become similar to the yields in the other regions. This is similar to what was observed when analyzing the pion baseline with PYTHIA in Fig. 7.3. In this case, the effects due to the definition

of the regions and to the inclusion of the daughters could cancel, causing the baseline to be similar to the ones for transverse and away regions. It could therefore show that the ratio to the baseline is similar in all three regions, hence that the impact of autocorrelation effects on the stronger-than-linear increase of the yields, apart from the daughters, would be small. However, in the pion baseline, only one charged particle was removed, compared to two charged particles in the J/ψ case. Therefore, the comparison with a baseline when removing two daughters is probably biased and does not allow to make a clear interpretation on the autocorrelation effects.
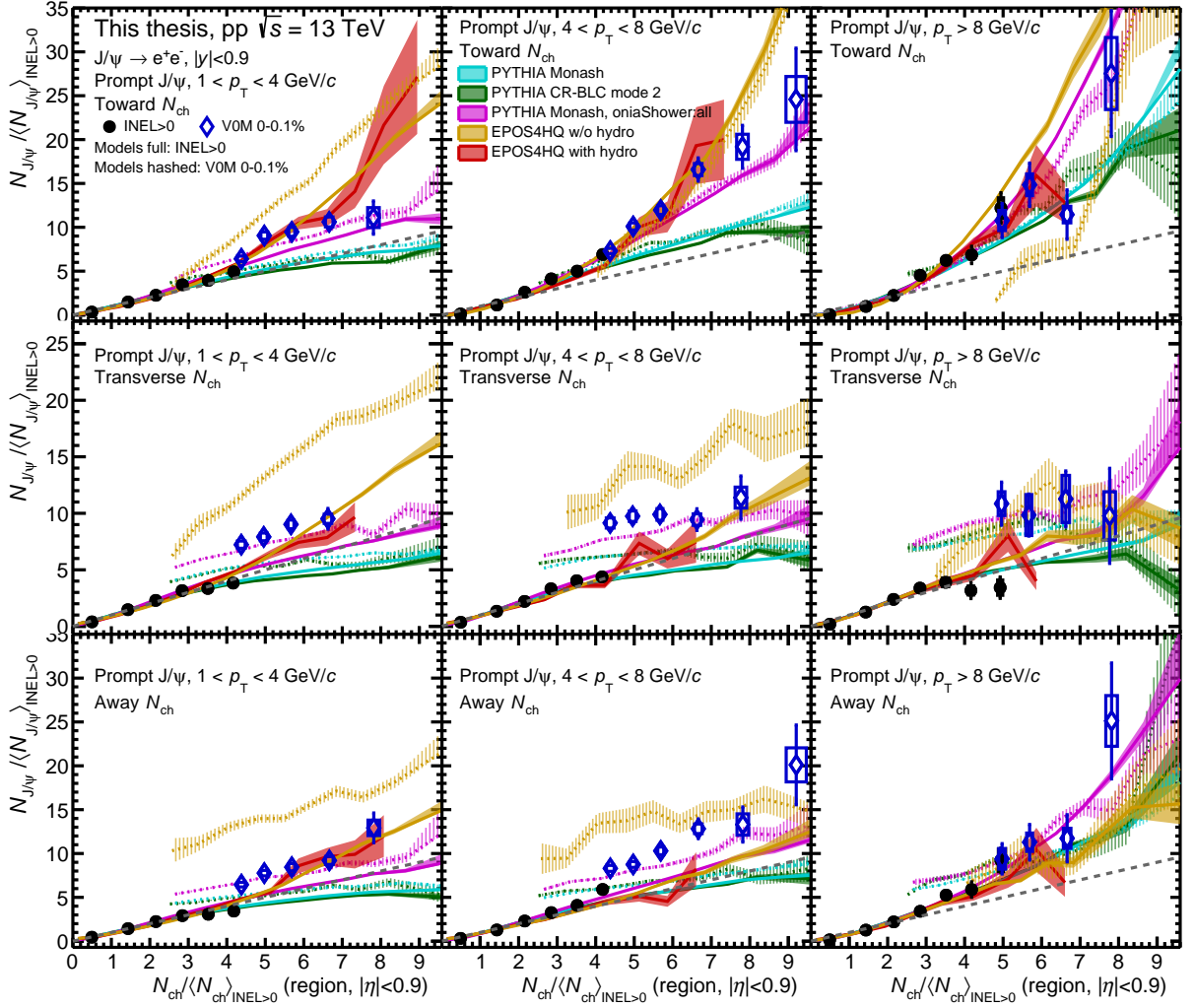

Figure 7.16.: Self-normalized prompt J/ψ with $p_T > 1$ GeV/c as a function of self-normalized charged-particle multiplicity. The case where the multiplicity is directly estimated at midrapidity is compared with the case where the multiplicity is estimated in the region transverse to the J/ψ and converted to a midrapidity multiplicity using unbiased events. The J/ψ in the multiplicity intervals are selected either in INEL> 0 events, or in HM-triggered events (V0M 0-0.1%). The yields are compared to PYTHIA using the oniaShower settings.

In Ref. [144] the inclusive J/ψ yields were measured as a function of azimuthally-inclusive multiplicity. It was shown that, when estimating the multiplicity at forward rapidity, and using minimum-bias events to convert the forward multiplicity to a midrapidity multiplicity, the results agree with the case when the multiplicity is estimated directly at midrapidity. The forward rapidity estimator was assumed to be free of autocorrelations. This study can be repeated while replacing the forward multiplicity by the multiplicity in the transverse region, which is expected to be less affected by autocorrelations. The correlation between transverse and azimuth-integrated multiplicity can be extracted unbiased events (i.e. without the requirement of the presence of a J/ψ) in data. For unbiased events, the transverse multiplicity within this correlation is estimated with respect to a random angle. This correlation allows to obtain a N_{trks} distribution for every $N_{trks,\,transverse}$ intervals where the J/ψ are selected, and each of the N_{trks} distribution can be unfolded to obtain the $\langle N_{ch} \rangle$ corresponding to this $N_{trks,\,transverse}$ interval. The yields after the correction are shown in Fig. 7.16, and compared to the yields directly using the midrapidity multiplicity estimator. The yields with transverse estimation also show a bias from the high-multiplicity trigger. If the assumption that the bias is reproduced in PYTHIA is made, the J/ψ

yields without HM trigger bias and with transverse estimation seem to be slightly lower than the azimuth-inclusive estimation, contrary to what was observed with the forward rapidity estimator. This is possibly explained by the fact that the forward estimator contains some remaining autocorrelations, for example if the J/ψ recoils on a jet at forward rapidity. The transverse multiplicity estimator would then contain less autocorrelations, and the weaker increase in this case could show that the autocorrelations do play a role in the correlation between J/ψ and multiplicity.

7.5. Results for azimuthal regions and p_T intervals of the J/ψ

Figure 7.17.: p_T differential self-normalized prompt J/ψ as a function of self-normalized charged-particle multiplicity selected in several azimuthal regions with respect to the J/ψ emission direction within $|\eta| <$ 0.9. The J/ψ in the multiplicity intervals are selected either in INEL> 0 events, or in HM-triggered events (V0M 0-0.1%). The yields are compared to PYTHIA 8.311 using different settings [40, 46, 125], as well as EPOS4HQ with and without hydrodynamics activated [52, 57]. The self-normalized multiplicity is measured either in the region toward (top row), transverse to (middle row), or away to (bottom row) the J/ψ emission direction. Left column: $1 < p_T < 4$ GeV/c. Middle column: $4 < p_T < 8$ GeV/c. Right column: $p_T > 8$ GeV/c.

Finally, Fig. 7.17 (for prompt J/ψ) and 7.18 (for non-prompt J/ψ) show the p_T-differential self-normalized J/ψ yields as a function of self-normalized multiplicity in the three azimuthal
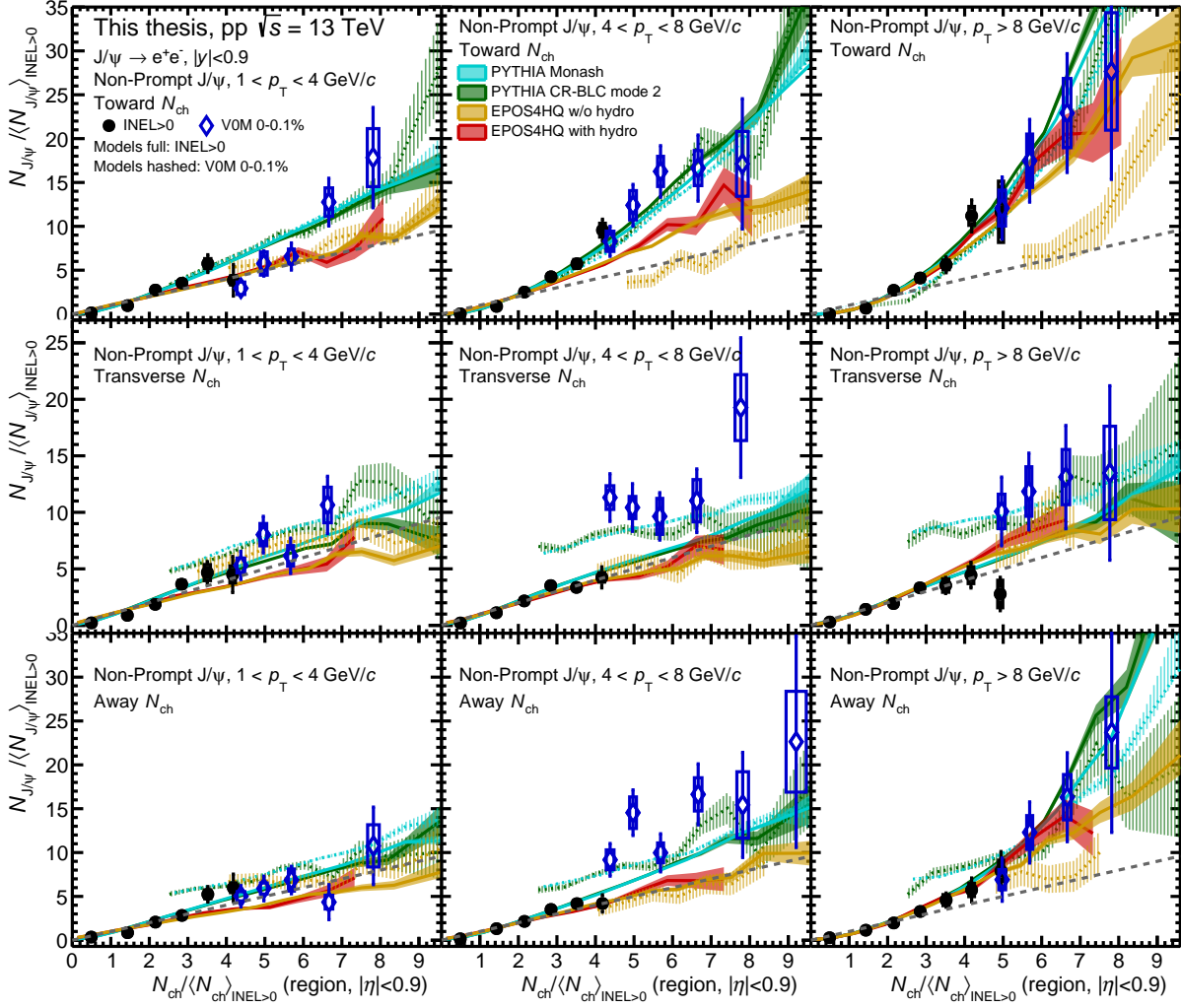
Figure 7.18.: p_T differential self-normalized non-prompt J/ψ as a function of self-normalized charged-particle multiplicity selected in several azimuthal regions with respect to the J/ψ emission direction within $|\eta| < 0.9$. The J/ψ in the multiplicity intervals are selected either in INEL> 0 events, or in HM-triggered events (V0M 0-0.1%). The yields are compared to PYTHIA 8.311 using different settings [40, 46, 125], as well as EPOS4HQ with and without hydrodynamics activated [52, 57]. The self-normalized multiplicity is measured either in the region toward (top row), transverse to (middle row), or away to (bottom row) the J/ψ emission direction. Left column: $1 < p_T < 4$ GeV/c. Middle column: $4 < p_T < 8$ GeV/c. Right column: $p_T > 8$ GeV/c.

regions. This allows to investigate the origin of the stronger increase of the multiplicity-dependent yields at higher p_T. For prompt J/ψ, the difference between different p_T intervals is very strong for the toward region, while there is only little to no modification when increasing p_T for the transverse or away regions. This shows that the stronger increase of the multiplicity-dependent yield with higher p_T comes from higher associated particle production. This could happen for example when the J/ψ meson are found in harder jets which would emit more particles. The modification with the p_T of the J/ψ probably does not come from global event properties linked to the underlying event, such as the ones which could be due to higher relative saturation effects in the soft particle production. It should still be noted that the p_T dependence in the transverse and away region could also be affected by the momentum dependence of different effects. Such effects include jet productions, the jets being more collimated at high p_T where also three-jets topologies become more frequent, as well as the additional presence of the decay daughters of the

J/ψ in the transverse and away regions at low p_T. These effects would have opposite influence as a function of p_T, and therefore could hide the influence of global effects, such as a potential modification of the underlying event in the transverse region with increasing p_T.
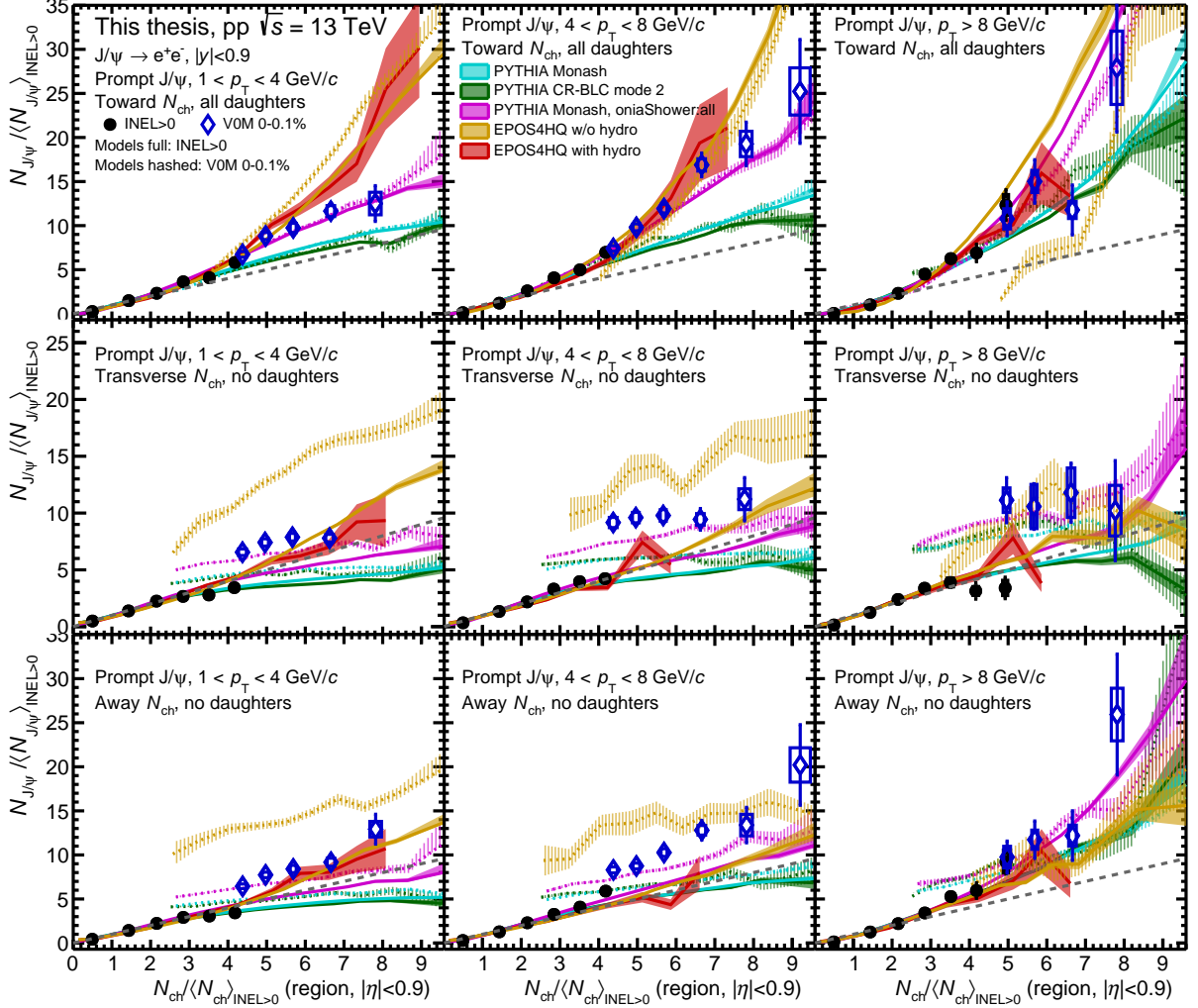
Figure 7.19.: p_T differential self-normalized prompt J/ψ as a function of self-normalized charged-particle multiplicity selected in several azimuthal regions with respect to the J/ψ emission direction within $|\eta| <$ 0.9. The J/ψ in the multiplicity intervals are selected either in INEL$>$ 0 events, or in HM-triggered events (V0M 0-0.1%). The self-normalized multiplicity is measured either in the region toward (top row), transverse to (middle row), or away to (bottom row) the J/ψ emission direction. All J/ψ daughters are counted in the toward region. Left column: $1 < p_T < 4$ GeV/c. Middle column: $4 < p_T < 8$ GeV/c. Right column: $p_T > 8$ GeV/c.

Because, at high p_T, the decay daughters are found more often in the toward region, the presence of the decay daughters could bias the result differently in different p_T intervals. Therefore, in Fig. 7.19, the multiplicity-dependent yields for prompt J/ψ in the p_T intervals and azimuthal regions are shown when all daughters are counted in the toward region. In particular, in the transverse region, when comparing to the case where the daughters are always counted in the region where they are found, the yields decrease more at low p_T but remain the same at high p_T. Therefore, the modification of the trend of the multiplicity dependence with the p_T of the J/ψ is slightly higher in this case. However, the effect is small, and this modification remains much

smaller than in the toward region, confirming that the p_T dependence of the trend is mostly due to autocorrelations.

Prompt J/ψ yields are well reproduced by PYTHIA with oniaShower settings, while other PYTHIA settings underestimate the data. As observed in data, EPOS4HQ calculations show a stronger increase of the correlation at higher p_T in the toward region, but not for the transverse or away region. However, data is not reproduced quantitatively, with overestimation of the high-multiplicity results in most of the cases.

For non-prompt J/ψ, it seems that, in addition to the yields as a function of toward multiplicity, also the ones as a function of away multiplicity show a stronger increase at higher p_T. This is even the case for the results as a function of transverse multiplicity, although with a smaller magnitude. The fact that an increase with transverse momentum is seen also in the transverse and away region, contrary to what is observed for prompt J/ψ, might be related to different production processes, with the influence of strong back-to-back $b\bar{b}$ correlations for example. As was observed before, the PYTHIA calculations tend to reproduce non-prompt J/ψ yields well. In contrast, EPOS4HQ constantly underestimates the high-multiplicity yields in every region for the first two p_T intervals. The highest p_T interval is better reproduced for all three regions. It is also interesting to notice that, as could be hinted by data, for all regions, the increase of the non-prompt yield with multiplicity is stronger at higher p_T. This is possibly due to the fact that the correlation between hard and soft scale is impacted by the saturation scale introduced for the initial state. The initial-state saturation impacts all regions, because the saturation scale is a global property.

As a conclusion, this section has shown the high influence of the particles emitted in the same production process as the J/ψ on the correlation between J/ψ and multiplicity. These particles are especially responsible for the stronger increase observed at higher p_T, as was shown when comparing the evolution of the J/ψ yield as a function of the multiplicity in the toward region compared to the transverse and away regions. The measurement in azimuthal regions also helps to understand the production process for prompt J/ψ, which could influence the multiplicity in the toward region, as was shown by the different correlations predicted by different PYTHIA settings. In addition, the increase of the yield has also been observed in the transverse and away region to be stronger than a baseline of soft particles. This shows that autocorrelations is not the only effect at play in explaining the multiplicity dependence of J/ψ yields, and the difference in hard and soft particle production, besides the autocorrelations, might play a role.

8. Conclusions and outlook

This thesis analyzed the multiplicity dependence of the yields of prompt and non-prompt J/ψ in pp collisions at $\sqrt{s} = 13$ TeV using data collected by the ALICE experiment during the Run 2 of the LHC. This quantity allows to study the interplay between hard and soft particle production. The multiplicity and the J/ψ yields are both normalized by their average value in minimum-bias events. The multiplicity is estimated within $|\eta| < 0.9$ through the number of global tracks. The J/ψ are reconstructed through their dielectron decay within $|y| < 0.9$, and prompt and non-prompt J/ψ are separated using Boosted Decision Trees.

The yields of prompt and non-prompt J/ψ show both a stronger-than-linear increase with the multiplicity. No large difference is observed between prompt and non-prompt J/ψ. This shows the similarity in the multiplicity dependence between charm and beauty and between open heavy-flavor hadrons and quarkonia. However, a hint of a slight increase with multiplicity of the fraction of non-prompt J/ψ is observed. In addition, as studies using the PYTHIA8 generator show, the high-multiplicity trigger used to collect the data might introduce a small bias in the measured multiplicity dependence. The effect of this bias could be different for prompt and non-prompt J/ψ. In addition, a stronger increase with the multiplicity is observed for higher transverse momentum of the J/ψ. The ratio between J/ψ and D^0 also does not indicate a significant dependence on the multiplicity in pp collisions.

The yields of J/ψ are compared to several models. These include PYTHIA8, for which several settings (Monash tune, CR-BLC mode 2, and oniaShower) have been tested, EPOS4HQ with and without hydrodynamic simulations, and two models based on the CGC framework. The different models explain the stronger-than-linear increase of the J/ψ yields through initial-state or final-state effects. While EPOS4HQ respectively underestimate non-prompt J/ψ and overestimate prompt J/ψ yields at high multiplicity, the CGC-based models are not able to reproduce the results in all the p_T intervals. In addition, the autocorrelations from particles produced in the same production process as the J/ψ might also play a role in the observed dependence. This is particularly visible when comparing to the PYTHIA calculations. Indeed, while the Monash and CR-BLC tune are able to describe the non-prompt J/ψ yields, they significantly underestimate prompt J/ψ. However, when modifying the production process of the J/ψ through the oniaShower setting, the prompt J/ψ is estimated correctly.

In order to investigate the impact of autocorrelations, the multiplicity is separated in three azimuthal regions with respect to the J/ψ emission direction: toward, transverse, and away. The yields as a function of toward multiplicity, which is supposed to contain most of the autocorrelations, show a stronger increase than the yields as a function of transverse or away multiplicity. This indicates that the impact of the autocorrelations in the dependence of the

J/ψ yields with multiplicity could be large. In addition, both the transverse and away region suffer from a strong bias from the high-multiplicity trigger. However, this bias is reproduced by the PYTHIA8 generator, and therefore conclusions are possible. Although the increase in the transverse and away region appears close to linear, the study of a pion baseline with PYTHIA shows that, for any particle species, a weaker increase of its yield as a function of transverse or away multiplicity is expected compared to the measurement as a function of azimuth-integrated multiplicity. This is possibly due to larger Poisson fluctuations when the multiplicity measurement region is smaller than the J/ψ measurement region. Actually, according to PYTHIA, the definition of the regions create a stronger increase in toward region than in the other regions also for pions. The fact that the J/ψ yields present a stronger increase compared to a baseline of soft particles in all three regions demonstrates that autocorrelations are not the only effect at play in explaining the difference between hard and soft probes. Finally, the dependence on the multiplicity in azimuthal regions has also been analyzed in several p_{T} intervals. The modification with the J/ψ p_{T} is much stronger in the toward region than in the transverse region, indicating that autocorrelations are the main driver of the dependence of the multiplicity-dependent yields on the transverse momentum.

For the Run 3 of the LHC, ALICE has conducted a significant upgrade of its detectors. This upgrade allows to collect data at a much higher rate in a continuous mode which does not require the need for hardware triggers. In addition, the improvement on the pointing resolution allows for a better separation between prompt and non-prompt J/ψ. Therefore, the statistics collected will enable more precise results with smaller uncertainties. In particular, results obtained in an analysis similar to the one presented in this thesis will be free from the bias of the high-multiplicity trigger. In addition, the measurement of the multiplicity dependence of the ratio between excited states, such as $\psi(2S)$, and J/ψ becomes possible and will allow to understand the impact of final-state effects in small systems. These effects could also be studied with a more precise J/ψ-to-D^0 ratio, although additional effects, especially from autocorrelations, might be present in this case. Finally, the systematic selection of different rapidity regions for the measurement of the multiplicity and the J/ψ yields, with and without a rapidity or azimuthal angle difference, could help to scan the rapidity dependence of these potential initial- or final-state effects. It might also help to disentangle between both cases. The multiplicity-dependent results could also be analyzed with more precision in proton-nucleus collisions.

A. Signal extraction in multiplicity intervals
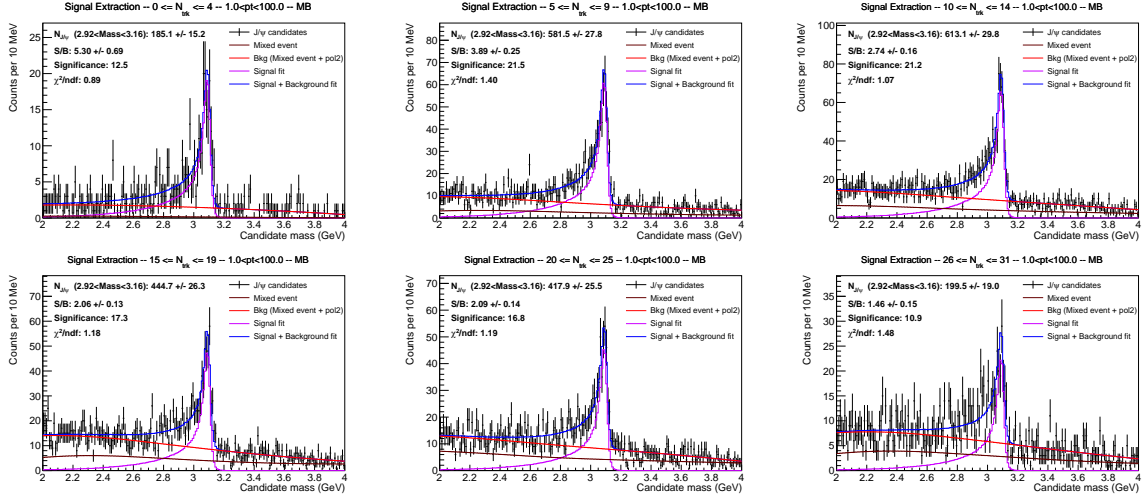
Figure A.1.: Extraction of the J/ψ signal for several multiplicity intervals, with $p_T > 1$ GeV/c, using the MB trigger. A selection on the BDT score is applied to remove a part of the background.
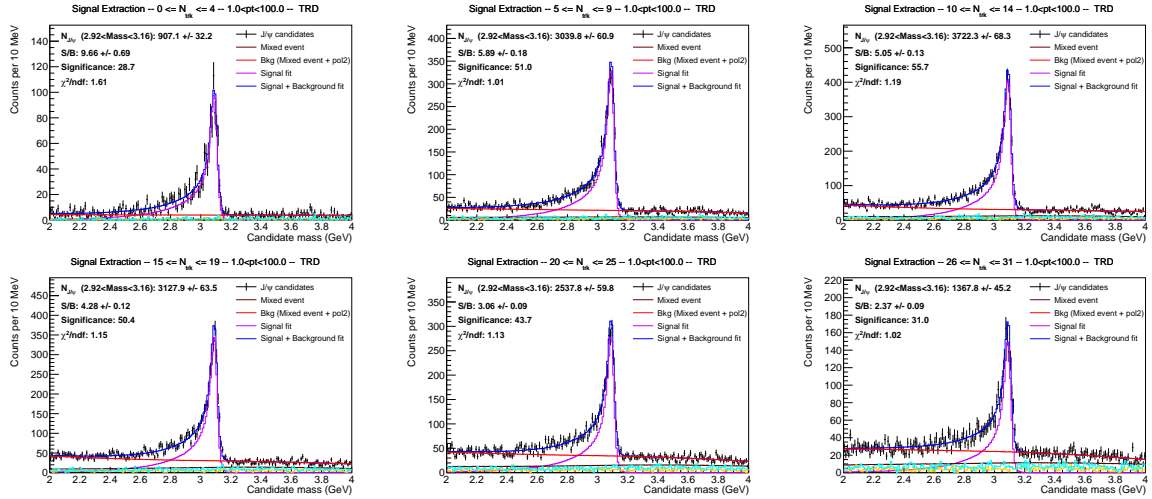
Figure A.2.: Extraction of the J/ψ signal for several multiplicity intervals, with $p_T > 1$ GeV/c, using the TRD trigger. A selection on the BDT score is applied to remove a part of the background.
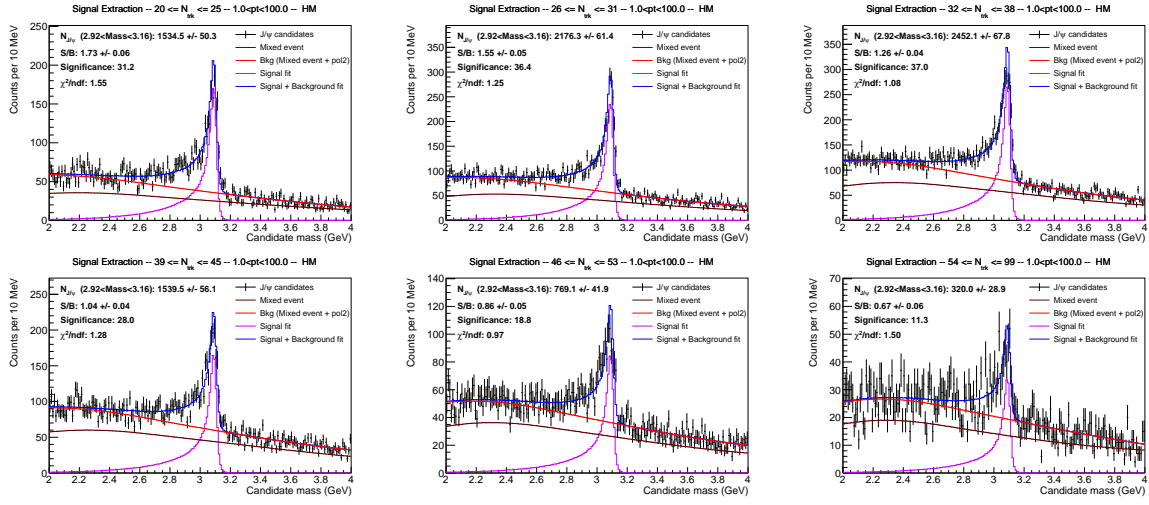
Figure A.3.: Extraction of the J/ψ signal for several multiplicity intervals, with $p_\text{T} > 1$ GeV/c, using the HM trigger. A selection on the BDT score is applied to remove a part of the background.

Figure A.4.: Extraction of the J/ψ signal for several p_T intervals, using the MB (left), TRD (middle), and HM (right) triggers. A selection on the BDT score is applied to remove a part of the background. Top: $1 < p_\text{T} < 4$ GeV/c. Middle: $4 < p_\text{T} < 8$ GeV/c. Bottom: $p_\text{T} > 8$ GeV/c.

Figure A.5.: Extraction of the J/ψ signal for several intervals of toward multiplicity, with $p_T > 1$ GeV/c, using the MB trigger. A selection on the BDT score is applied to remove a part of the background.

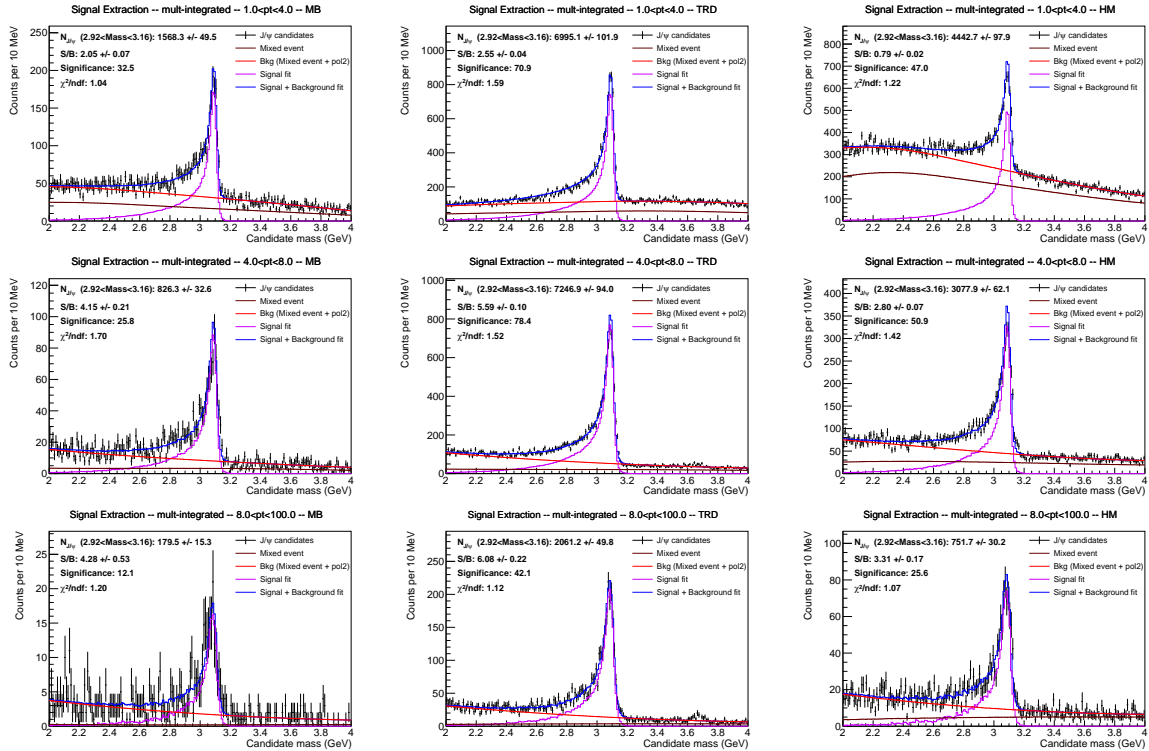**Figure A.6.:** Extraction of the J/ψ signal for several intervals of toward multiplicity, with $p_T > 1$ GeV/c, using the TRD trigger. A selection on the BDT score is applied to remove a part of the background.

Figure A.7.: Extraction of the J/ψ signal for several intervals of toward multiplicity, with $p_T > 1$ GeV/c, using the HM trigger. A selection on the BDT score is applied to remove a part of the background.

Figure A.8.: Extraction of the J/ψ signal for several intervals of transverse multiplicity, with $p_{\mathrm{T}} > 1$ GeV/c, using the MB trigger. A selection on the BDT score is applied to remove a part of the background.
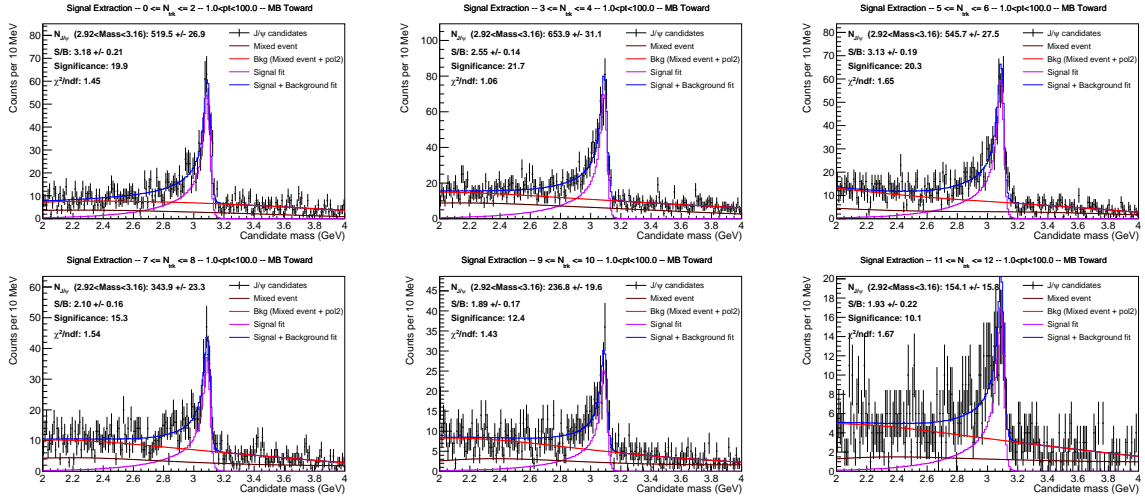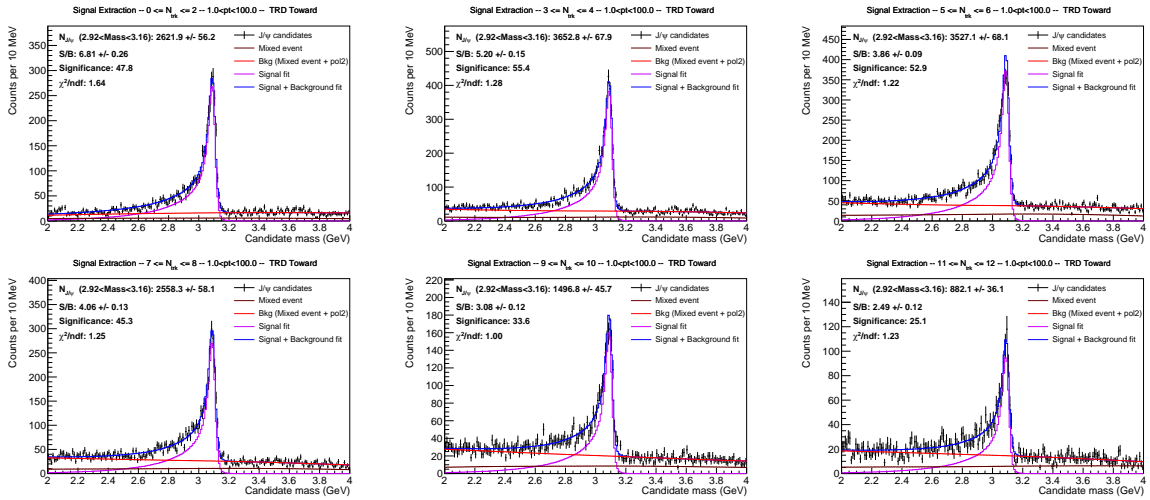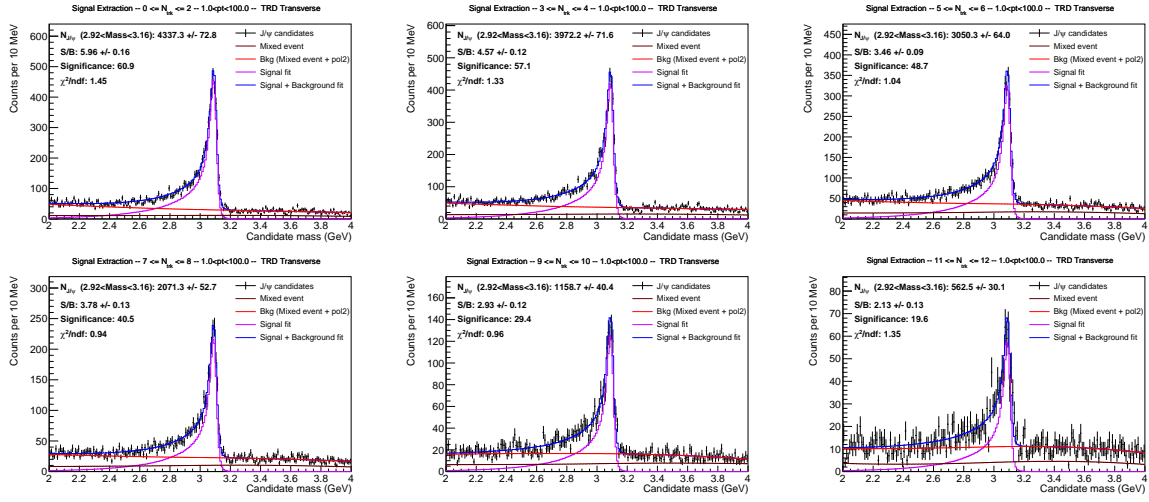

Figure A.9.: Extraction of the J/ψ signal for several intervals of transverse multiplicity, with $p_{\mathrm{T}} > 1$ GeV/c, using the TRD trigger. A selection on the BDT score is applied to remove a part of the background.
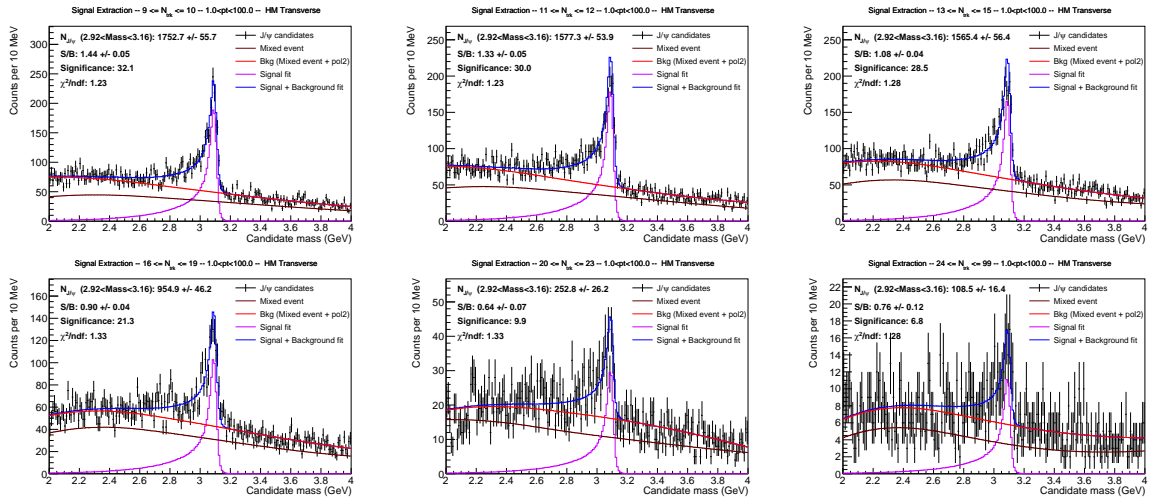
Figure A.10.: Extraction of the J/ψ signal for several intervals of transverse multiplicity, with $p_{\mathrm{T}} > 1$ GeV/c, using the HM trigger. A selection on the BDT score is applied to remove a part of the background.
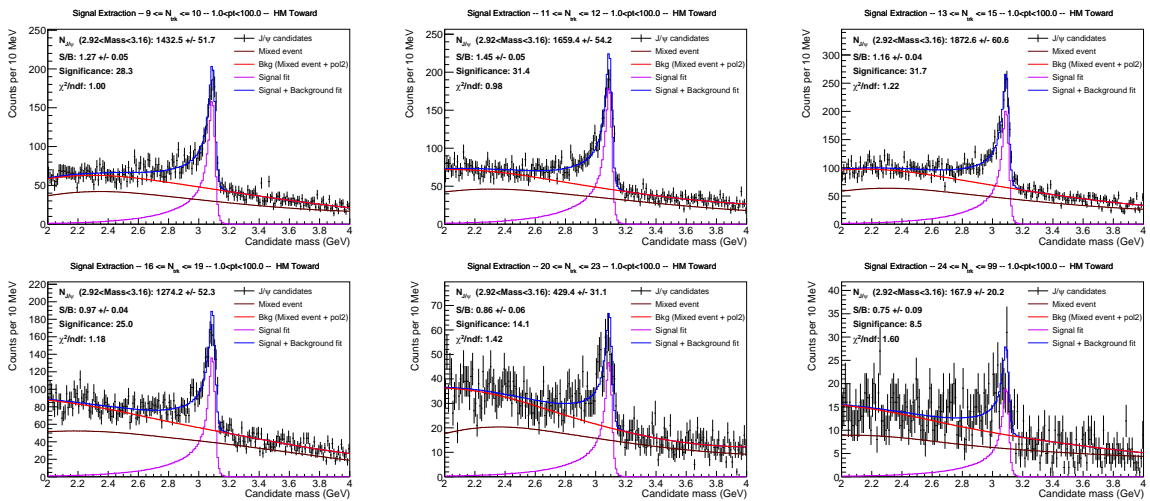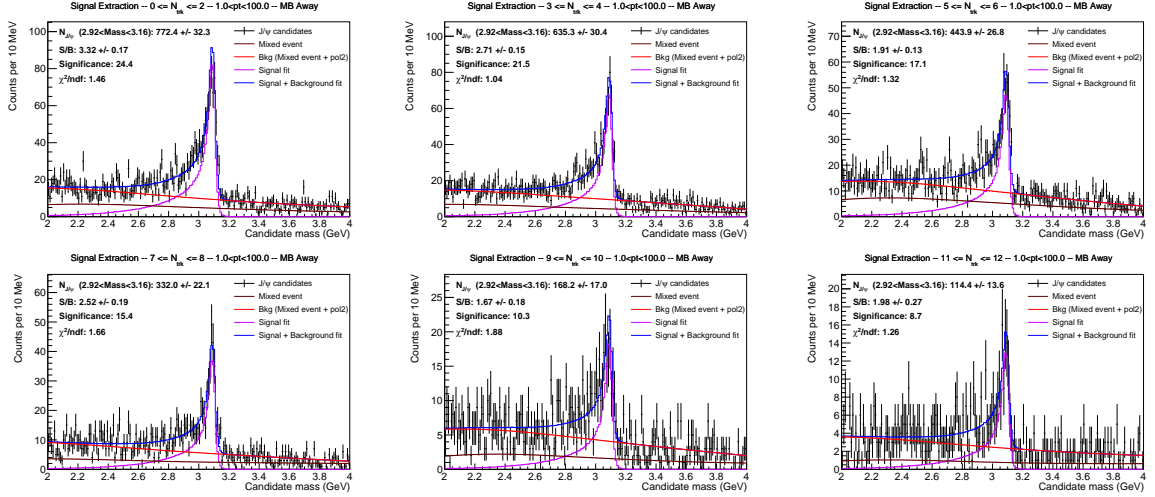
Figure A.11.: Extraction of the J/ψ signal for several intervals of away multiplicity, with $p_{\mathrm{T}} > 1$ GeV/c, using the MB trigger. A selection on the BDT score is applied to remove a part of the background.

Figure A.12.: Extraction of the J/ψ signal for several intervals of away multiplicity, with $p_{\mathrm{T}} > 1$ GeV/c, using the TRD trigger. A selection on the BDT score is applied to remove a part of the background.

Figure A.13.: Extraction of the J/ψ signal for several intervals of away multiplicity, with $p_{\mathrm{T}} > 1$ GeV/c, using the HM trigger. A selection on the BDT score is applied to remove a part of the background.
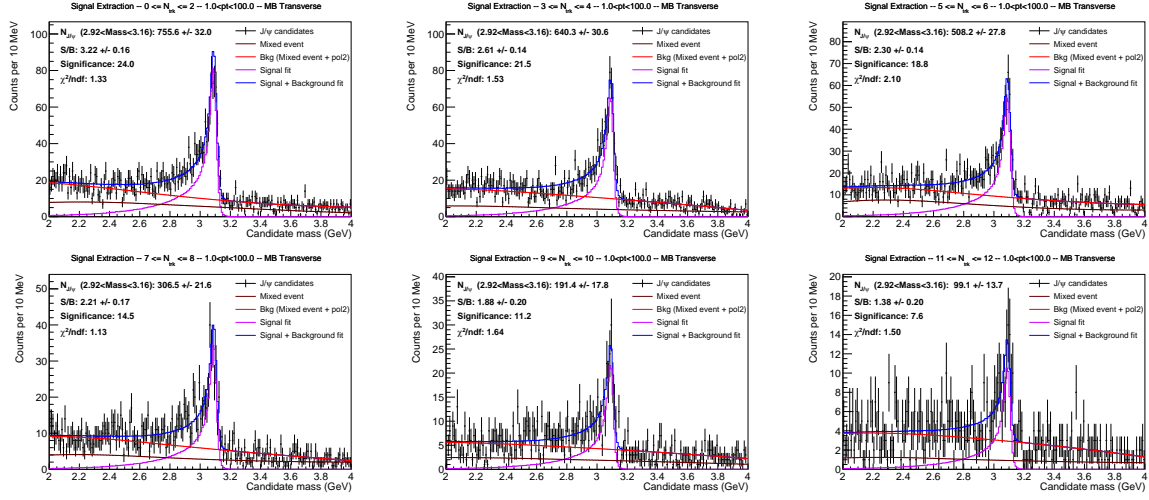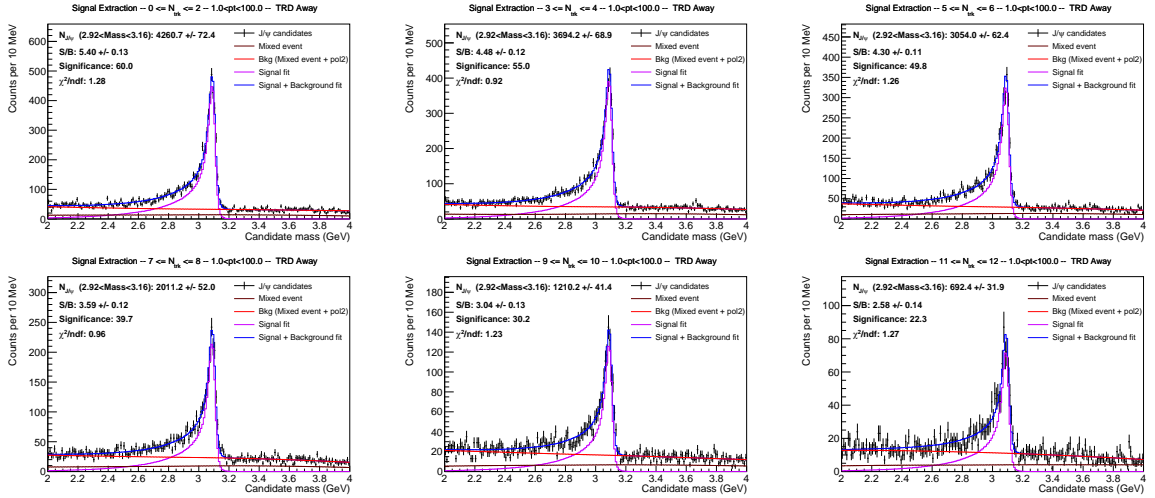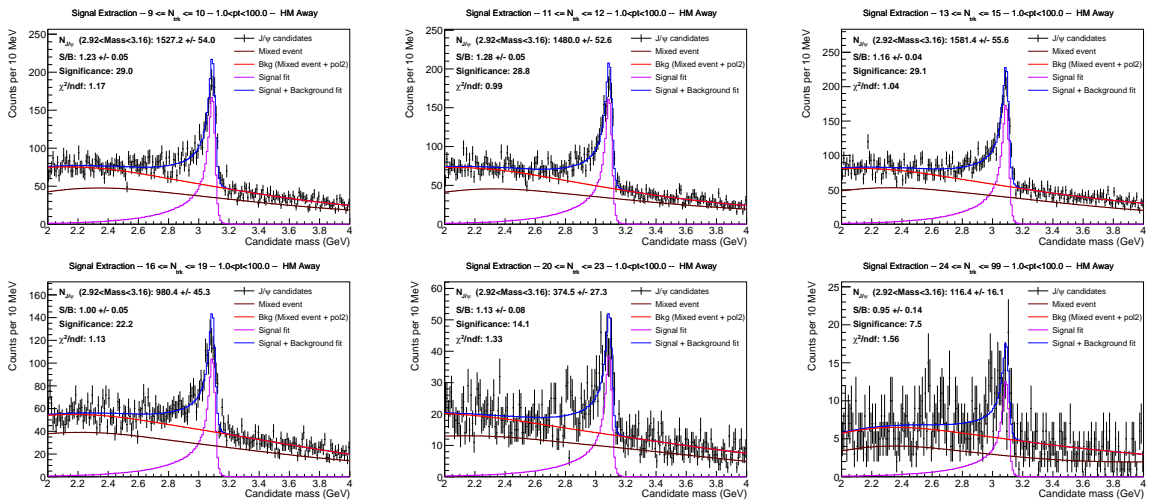
References

[1] **S. Navas et al.** "Review of particle physics", *Phys. Rev. D* 110.3 (2024), p. 030001. DOI: 10.1103/PhysRevD.110.030001.

[2] **Wikimedia Commons**. *Standard Model of Elementary Particles*, https://commons.wikimedia.org/wiki/File:Standard_Model_of_Elementary_Particles.svg. Accessed: September 30th 2025.

[3] **P. Langacker**. "Structure of the standard model", *Adv. Ser. Direct. High Energy Phys.* 14 (1995), pp. 15–36. arXiv: hep-ph/0304186.

[4] **Wikimedia Commons**. *Feynman diagram gluon radiation*, https://commons.wikimedia.org/wiki/File:Feynmann_Diagram_Gluon_Radiation.svg. Accessed: September 30th 2025.

[5] **A. Pich**. "Quantum chromodynamics", *1994 European School of High-energy Physics*. May 1995, pp. 157–207. arXiv: hep-ph/9505231.

[6] **D. J. Gross and F. Wilczek**. "Ultraviolet Behavior of Nonabelian Gauge Theories", *Phys. Rev. Lett.* 30 (1973). Ed. by J. C. Taylor, pp. 1343–1346. DOI: 10.1103/PhysRevLett.30.1343.

[7] **H. D. Politzer**. "Reliable Perturbative Results for Strong Interactions?", *Phys. Rev. Lett.* 30 (1973). Ed. by J. C. Taylor, pp. 1346–1349. DOI: 10.1103/PhysRevLett.30.1346.

[8] **N. Cabibbo and G. Parisi**. "Exponential Hadronic Spectrum and Quark Liberation", *Phys. Lett. B* 59 (1975), pp. 67–69. DOI: 10.1016/0370-2693(75)90158-6.

[9] **E. V. Shuryak**. "Theory of Hadronic Plasma", *Sov. Phys. JETP* 47 (1978), pp. 212–219.

[10] **R. Hagedorn**. "Statistical thermodynamics of strong interactions at high-energies", *Nuovo Cim. Suppl.* 3 (1965), pp. 147–186.

[11] **S. Borsanyi et al.** "Full result for the QCD equation of state with 2+1 flavors", *Phys. Lett. B* 730 (2014), pp. 99–104. arXiv: 1309.5258 [hep-lat].

[12] **J. N. Guenther**. "Overview of the QCD phase diagram: Recent progress from the lattice", *Eur. Phys. J. A* 57.4 (2021), p. 136. arXiv: 2010.15503 [hep-lat].

[13] **A. Bazavov et al.** "Chiral crossover in QCD at zero and non-zero chemical potentials", *Phys. Lett. B* 795 (2019), pp. 15–21. arXiv: 1812.08235 [hep-lat].

[14] **J. C. Collins, D. E. Soper, and G. F. Sterman**. "Factorization of Hard Processes in QCD", *Adv. Ser. Direct. High Energy Phys.* 5 (1989), pp. 1–91. arXiv: hep-ph/0409313.

[15] **G. Altarelli and G. Parisi**. "Asymptotic Freedom in Parton Language", *Nucl. Phys. B* 126 (1977), pp. 298–318. DOI: 10.1016/0550-3213(77)90384-4.

[16] **R. D. Ball et al.** "The path to proton structure at 1% accuracy", *Eur. Phys. J. C* 82.5 (2022), p. 428. arXiv: 2109.02653 [hep-ph].

[17] **D. Diakonov**. "QCD scattering: from DGLAP to BFKL", *CERN courier* (2010). URL: https://cerncourier.com/a/qcd-scattering-from-dglap-to-bfkl/.

[18] **I. I. Balitsky and L. N. Lipatov**. "The Pomeranchuk Singularity in Quantum Chromodynamics", *Sov. J. Nucl. Phys.* 28 (1978), pp. 822–829.

[19] **F. Gelis et al.** "The Color Glass Condensate", *Ann. Rev. Nucl. Part. Sci.* 60 (2010), pp. 463–489. arXiv: 1002.0333 [hep-ph].

[20] **M. L. Miller et al.** "Glauber modeling in high energy nuclear collisions", *Ann. Rev. Nucl. Part. Sci.* 57 (2007), pp. 205–243. arXiv: nucl-ex/0701025.

[21] **A. Toia**. "Participants and spectators at the heavy-ion fireball", *CERN courier* (2013). URL: https://cerncourier.com/a/participants-and-spectators-at-the-heavy-ion-fireball/.

[22] **W. Busza, K. Rajagopal, and W. van der Schee**. "Heavy Ion Collisions: The Big Picture, and the Big Questions", *Ann. Rev. Nucl. Part. Sci.* 68 (2018), pp. 339–376. arXiv: 1802.04801 [hep-ph].

[23] **S. Acharya et al.** "The ALICE experiment: a journey through QCD", *Eur. Phys. J. C* 84.8 (2024), p. 813. arXiv: 2211.04384 [nucl-ex].

[24] **K. Aamodt et al.** "Higher harmonic anisotropic flow measurements of charged particles in Pb-Pb collisions at $\sqrt{s_{NN}}$=2.76 TeV", *Phys. Rev. Lett.* 107 (2011), p. 032301. arXiv: 1105.3865 [nucl-ex].

[25] **L. Adamczyk et al.** "Inclusive charged hadron elliptic flow in Au + Au collisions at $\sqrt{s_{NN}}$ = 7.7 - 39 GeV", *Phys. Rev. C* 86 (2012), p. 054908. arXiv: 1206.5528 [nucl-ex].

[26] **J. Adam et al.** "Anisotropic flow of charged particles in Pb-Pb collisions at $\sqrt{s_{\mathrm{NN}}}$ = 5.02 TeV", *Phys. Rev. Lett.* 116.13 (2016), p. 132302. arXiv: 1602.01119 [nucl-ex].

[27] **C. Shen et al.** "The iEBE-VISHNU code package for relativistic heavy-ion collisions", *Comput. Phys. Commun.* 199 (2016), pp. 61–85. arXiv: 1409.8164 [nucl-th].

[28] **B. Schenke, S. Jeon, and C. Gale**. "(3+1)D hydrodynamic simulation of relativistic heavy-ion collisions", *Phys. Rev. C* 82 (2010), p. 014903. arXiv: 1004.1408 [hep-ph].

[29] **M. Virta, J. Parkkila, and D. J. Kim**. "Enhancing Bayesian parameter estimation by adapting to multiple energy scales in heavy-ion collisions at RHIC and at the LHC", *Phys. Rev. C* 111.4 (2025), p. 044903. arXiv: 2411.01932 [hep-ph].

[30] **D. Everett et al.** "Multisystem Bayesian constraints on the transport coefficients of QCD matter", *Phys. Rev. C* 103.5 (2021), p. 054904. arXiv: 2011.01430 [hep-ph].

[31] **A. Andronic et al.** "Decoding the phase structure of QCD via particle production at high energy", *Nature* 561.7723 (2018), pp. 321–330. arXiv: 1710.09425 [nucl-th].

[32] **B. B. Abelev et al.** "Multi-strange baryon production at mid-rapidity in Pb-Pb collisions at $\sqrt{s_{NN}}$ = 2.76 TeV", *Phys. Lett. B* 728 (2014). [Erratum: Phys.Lett.B 734, 409–410 (2014)], pp. 216–227. arXiv: 1307.5543 [nucl-ex].

[33] **G. Aad et al.** "Observation of a Centrality-Dependent Dijet Asymmetry in Lead-Lead Collisions at $\sqrt{s_{NN}} = 2.77$ TeV with the ATLAS Detector at the LHC", *Phys. Rev. Lett.* 105 (2010), p. 252303. arXiv: `1011.6182` `[hep-ex]`.

[34] **J. W. Harris and B. Müller**. ""QGP Signatures" Revisited", *Eur. Phys. J. C* 84.3 (2024), p. 247. arXiv: `2308.05743` `[hep-ph]`.

[35] **J. F. Grosse-Oetringhaus and U. A. Wiedemann**. "A Decade of Collectivity in Small Systems", (July 2024). arXiv: `2407.07484` `[hep-ex]`.

[36] **S. Acharya et al.** "Emergence of Long-Range Angular Correlations in Low-Multiplicity Proton-Proton Collisions", *Phys. Rev. Lett.* 132.17 (2024), p. 172302. arXiv: `2311.14357` `[nucl-ex]`.

[37] **J. Adam et al.** "Enhanced production of multi-strange hadrons in high-multiplicity proton-proton collisions", *Nature Phys.* 13 (2017), pp. 535–539. arXiv: `1606.07424` `[nucl-ex]`.

[38] **S. Schlichting and P. Tribedy**. "Collectivity in Small Collision Systems: An Initial-State Perspective", *Adv. High Energy Phys.* 2016 (2016), p. 8460349. arXiv: `1611.00329` `[hep-ph]`.

[39] **C. Bierlich et al.** "A comprehensive guide to the physics and usage of PYTHIA 8.3", *SciPost Phys. Codeb.* 2022 (2022), p. 8. arXiv: `2203.11601` `[hep-ph]`.

[40] **P. Skands, S. Carrazza, and J. Rojo**. "Tuning PYTHIA 8.1: the Monash 2013 Tune", *Eur. Phys. J. C* 74.8 (2014), p. 3024. arXiv: `1404.5630` `[hep-ph]`.

[41] **C. Bierlich et al.** "The Angantyr model for Heavy-Ion Collisions in PYTHIA8", *JHEP* 10 (2018), p. 134. arXiv: `1806.10820` `[hep-ph]`.

[42] **T. Sjöstrand**. "The Development of MPI Modeling in Pythia", *Adv. Ser. Direct. High Energy Phys.* 29 (2018), pp. 191–225. arXiv: `1706.02166` `[hep-ph]`.

[43] **B. Andersson, G. Gustafson, and B. Söderberg**. "A general model for jet fragmentation", English. *European Physical Journal C* 20.4 (Dec. 1983), pp. 317–329. DOI: `10.1007/BF01407824`.

[44] **T. Sjöstrand**. "Status and developments of event generators", *PoS* LHCP2016 (2016). Ed. by J. Bijnens, A. Hoecker, and J. Olsen, p. 007. arXiv: `1608.06425` `[hep-ph]`.

[45] **G. Gustafson**. "Multiple Interactions, Saturation, and Final States in pp Collisions and DIS", *Acta Phys. Polon. B* 40 (2009). Ed. by K. Golec-Biernat and M. Praszalowicz, pp. 1981–1996. arXiv: `0905.2492` `[hep-ph]`.

[46] **J. R. Christiansen and P. Z. Skands**. "String Formation Beyond Leading Colour", *JHEP* 08 (2015), p. 003. arXiv: `1505.01681` `[hep-ph]`.

[47] **C. Bierlich et al.** "Effects of Overlapping Strings in pp Collisions", *JHEP* 03 (2015), p. 148. arXiv: `1412.6259` `[hep-ph]`.

[48] **C. Bierlich, G. Gustafson, and L. Lönnblad**. "A shoving model for collectivity in hadronic collisions", (Dec. 2016). arXiv: `1612.05132` `[hep-ph]`.

[49] **C. Bierlich et al.** "Strangeness enhancement across collision systems without a plasma", *Phys. Lett. B* 835 (2022), p. 137571. arXiv: `2205.11170` `[hep-ph]`.

[50] **K. Werner**. "Parallel scattering, saturation, and generalized Abramovskii-Gribov-Kancheli (AGK) theorem in the EPOS4 framework, with applications for heavy-ion collisions at sNN of 5.02 TeV and 200 GeV", *Phys. Rev. C* 109.3 (2024), p. 034918. arXiv: 2310.09380 [hep-ph].

[51] **K. Werner and B. Guiot**. "Perturbative QCD concerning light and heavy flavor in the EPOS4 framework", *Phys. Rev. C* 108.3 (2023), p. 034904. arXiv: 2306.02396 [hep-ph].

[52] **K. Werner**. "Revealing a deep connection between factorization and saturation: New insight into modeling high-energy proton-proton and nucleus-nucleus scattering in the EPOS4 framework", *Phys. Rev. C* 108.6 (2023), p. 064903. arXiv: 2301.12517 [hep-ph].

[53] **K. Werner**. "Core-corona procedure and microcanonical hadronization to understand strangeness enhancement in proton-proton and heavy ion collisions in the EPOS4 framework", *Phys. Rev. C* 109.1 (2024), p. 014910. arXiv: 2306.10277 [hep-ph].

[54] **H. J. Drescher et al.** "Parton based Gribov-Regge theory", *Phys. Rept.* 350 (2001), pp. 93–289. arXiv: hep-ph/0007198.

[55] **S. A. Bass et al.** "Microscopic models for ultrarelativistic heavy ion collisions", *Prog. Part. Nucl. Phys.* 41 (1998), pp. 255–369. arXiv: nucl-th/9803035.

[56] **M. Bleicher et al.** "Relativistic hadron hadron collisions in the ultrarelativistic quantum molecular dynamics model", *J. Phys. G* 25 (1999), pp. 1859–1896. arXiv: hep-ph/9909407.

[57] **J. Zhao et al.** "Heavy flavor as a probe of hot QCD matter produced in proton-proton collisions", *Phys. Rev. D* 109.5 (2024), p. 054011. arXiv: 2310.08684 [hep-ph].

[58] **J. Zhao et al.** "Heavy-flavor hadron production in relativistic heavy ion collisions at energies available at BNL RHIC and at the CERN LHC in the EPOS4HQ framework", *Phys. Rev. C* 110.2 (2024), p. 024909. arXiv: 2401.17096 [hep-ph].

[59] **S. Acharya et al.** "Charged-particle pseudorapidity density at mid-rapidity in p-Pb collisions at $\sqrt{s_{\mathrm{NN}}} = 8.16$ TeV", *Eur. Phys. J. C* 79.4 (2019), p. 307. arXiv: 1812.01312 [nucl-ex].

[60] **S. Acharya et al.** "Multiplicity dependence of charged-particle production in pp, p-Pb, Xe-Xe and Pb-Pb collisions at the LHC", *Phys. Lett. B* 845 (2023). [Erratum: Phys.Lett.B 853, 138700 (2024)], p. 138110. arXiv: 2211.15326 [nucl-ex].

[61] **L. McLerran and P. Tribedy**. "Intrinsic Fluctuations of the Proton Saturation Momentum Scale in High Multiplicity p+p Collisions", *Nucl. Phys. A* 945 (2016), pp. 216–225. arXiv: 1508.03292 [hep-ph].

[62] **J. J. Aubert et al.** "Experimental Observation of a Heavy Particle *J*", *Phys. Rev. Lett.* 33 (1974), pp. 1404–1406. DOI: 10.1103/PhysRevLett.33.1404.

[63] **J. E. Augustin et al.** "Discovery of a Narrow Resonance in e^+e^- Annihilation", *Phys. Rev. Lett.* 33 (1974), pp. 1406–1408. DOI: 10.1103/PhysRevLett.33.1406.

[64] **E. Eichten et al.** "Charmonium: The Model", *Phys. Rev. D* 17 (1978). [Erratum: Phys.Rev.D 21, 313 (1980)], p. 3090. DOI: 10.1103/PhysRevD.17.3090.

[65]   **J.-P. Lansberg**. "New Observables in Inclusive Production of Quarkonia", *Phys. Rept.* 889 (2020), pp. 1–106. arXiv: `1903.09185 [hep-ph]`.

[66]   **A. Andronic et al.** "Heavy-flavour and quarkonium production in the LHC era: from proton–proton to heavy-ion collisions", *Eur. Phys. J. C* 76.3 (2016), p. 107. arXiv: `1506.03981 [nucl-ex]`.

[67]   **J. F. Amundson et al.** "Colorless states in perturbative QCD: Charmonium and rapidity gaps", *Phys. Lett. B* 372 (1996), pp. 127–132. arXiv: `hep-ph/9512248`.

[68]   **Y.-Q. Ma and R. Vogt**. "Quarkonium Production in an Improved Color Evaporation Model", *Phys. Rev. D* 94.11 (2016), p. 114029. arXiv: `1609.06042 [hep-ph]`.

[69]   **C.-H. Chang**. "Hadronic Production of J/ψ Associated With a Gluon", *Nucl. Phys. B* 172 (1980), pp. 425–434. DOI: `10.1016/0550-3213(80)90175-3`.

[70]   **G. T. Bodwin, E. Braaten, and G. P. Lepage**. "Rigorous QCD analysis of inclusive annihilation and production of heavy quarkonium", *Phys. Rev. D* 51 (1995). [Erratum: Phys.Rev.D 55, 5853 (1997)], pp. 1125–1171. arXiv: `hep-ph/9407339`.

[71]   **M. Butenschoen and B. A. Kniehl**. "Reconciling J/ψ production at HERA, RHIC, Tevatron, and LHC with NRQCD factorization at next-to-leading order", *Phys. Rev. Lett.* 106 (2011), p. 022003. arXiv: `1009.5662 [hep-ph]`.

[72]   **T. Song et al.** "Bottomonium production in pp and heavy-ion collisions", *Phys. Rev. C* 108.5 (2023), p. 054908. arXiv: `2305.10750 [nucl-th]`.

[73]   **J. Zhao et al.** "Quarkonium production in high energy pp collisions", *EPJ Web Conf.* 296 (2024), p. 09014. arXiv: `2312.11349 [hep-ph]`.

[74]   **V. Cheung and R. Vogt**. "Production and polarization of prompt J/ψ in the improved color evaporation model using the k_T-factorization approach", *Phys. Rev. D* 98.11 (2018), p. 114029. arXiv: `1808.02909 [hep-ph]`.

[75]   **S. P. Baranov and A. V. Lipatov**. "Are there any challenges in the charmonia production and polarization at the LHC?", *Phys. Rev. D* 100.11 (2019), p. 114021. arXiv: `1906.07182 [hep-ph]`.

[76]   **F. Hautmann and H. Jung**. "Transverse momentum dependent gluon density from DIS precision data", *Nucl. Phys. B* 883 (2014), pp. 1–19. arXiv: `1312.7875 [hep-ph]`.

[77]   **Y.-Q. Ma and R. Venugopalan**. "Comprehensive Description of J/ψ Production in Proton-Proton Collisions at Collider Energies", *Phys. Rev. Lett.* 113.19 (2014), p. 192301. arXiv: `1408.4075 [hep-ph]`.

[78]   **L. Motyka and M. Sadzikowski**. "On relevance of triple gluon fusion in J/ψ hadroproduction", *Eur. Phys. J. C* 75.5 (2015), p. 213. arXiv: `1501.04915 [hep-ph]`.

[79]   **E. Levin and M. Siddikov**. "J/ψ production in hadron scattering: three-pomeron contribution", *Eur. Phys. J. C* 79.5 (2019), p. 376. arXiv: `1812.06783 [hep-ph]`.

[80]   **S. Acharya et al.** "Prompt and non-prompt J/ψ production cross sections at midrapidity in proton-proton collisions at $\sqrt{s} = 5.02$ and 13 TeV", *JHEP* 03 (2022), p. 190. arXiv: `2108.02523 [nucl-ex]`.

[81] **Y.-Q. Ma, K. Wang, and K.-T. Chao**. "$J/\psi(\psi')$ production at the Tevatron and LHC at $\mathcal{O}(\alpha_s^4 v^4)$ in nonrelativistic QCD", *Phys. Rev. Lett.* 106 (2011), p. 042002. arXiv: `1009.3655 [hep-ph]`.

[82] **R. Aaij et al.** "Study of J/ψ Production in Jets", *Phys. Rev. Lett.* 118.19 (2017), p. 192001. arXiv: `1701.05116 [hep-ex]`.

[83] **P. Faccioli et al.** "Towards the experimental clarification of quarkonium polarization", *Eur. Phys. J. C* 69 (2010), pp. 657–673. arXiv: `1006.2738 [hep-ph]`.

[84] **R. Aaij et al.** "Measurement of J/ψ polarization in *pp* collisions at $\sqrt{s} = 7$ TeV", *Eur. Phys. J. C* 73.11 (2013), p. 2631. arXiv: `1307.6379 [hep-ex]`.

[85] **S. Acharya et al.** "Measurement of the inclusive J/ ψ polarization at forward rapidity in pp collisions at $\sqrt{s} = 8$ TeV", *Eur. Phys. J. C* 78.7 (2018), p. 562. arXiv: `1805.04374 [hep-ex]`.

[86] **E. Braaten, B. A. Kniehl, and J. Lee**. "Polarization of prompt J/ψ at the Tevatron", *Phys. Rev. D* 62 (2000), p. 094005. arXiv: `hep-ph/9911436`.

[87] **Y.-Q. Ma, T. Stebel, and R. Venugopalan**. "J/ψ polarization in the CGC+NRQCD approach", *JHEP* 12 (2018), p. 057. arXiv: `1809.03573 [hep-ph]`.

[88] **S. Acharya et al.** "J/ψ-hadron correlations at midrapidity in pp collisions at $\sqrt{s} = 13$ TeV", *JHEP* 07 (2025), p. 023. arXiv: `2409.04364 [nucl-ex]`.

[89] **A. Tumasyan et al.** "Fragmentation of jets containing a prompt J/ψ meson in PbPb and pp collisions at $\sqrt{s_{\mathrm{NN}}} = 5.02$ TeV", *Phys. Lett. B* 825 (2022), p. 136842. arXiv: `2106.13235 [hep-ex]`.

[90] **R. Bain et al.** "NRQCD Confronts LHCb Data on Quarkonium Production within Jets", *Phys. Rev. Lett.* 119.3 (2017), p. 032002. arXiv: `1702.05525 [hep-ph]`.

[91] **R. Aaij et al.** "Measurements of $\psi(2S)$ and $\chi_{c1}(3872)$ production within fully reconstructed jets", *Eur. Phys. J. C* 85.5 (2025), p. 562. arXiv: `2410.18018 [hep-ex]`.

[92] **A.-P. Chen, X. Liu, and Y.-Q. Ma**. "Shedding Light on Hadronization by Quarkonium Energy Correlator", *Phys. Rev. Lett.* 133 (2024), p. 19. arXiv: `2405.10056 [hep-ph]`.

[93] **T. Matsui and H. Satz**. "J/ψ Suppression by Quark-Gluon Plasma Formation", *Phys. Lett. B* 178 (1986), pp. 416–422. DOI: `10.1016/0370-2693(86)91404-8`.

[94] **M. Laine et al.** "Real-time static potential in hot QCD", *JHEP* 03 (2007), p. 054. arXiv: `hep-ph/0611300`.

[95] **Y. Burnier, O. Kaczmarek, and A. Rothkopf**. "Quarkonium at finite temperature: Towards realistic phenomenology from first principles", *JHEP* 12 (2015), p. 101. arXiv: `1509.07366 [hep-ph]`.

[96] **A. Bazavov et al.** "Unscreened forces in the quark-gluon plasma?", *Phys. Rev. D* 109.7 (2024), p. 074504. arXiv: `2308.16587 [hep-lat]`.

[97] **P. Braun-Munzinger and J. Stachel**. "The quest for the quark-gluon plasma", *Nature* 448 (2007), pp. 302–309. DOI: `10.1038/nature06080`.

[98]   **A. Tumasyan et al.** "Observation of the $\Upsilon(3S)$ Meson and Suppression of Υ States in Pb-Pb Collisions at $\sqrt{s_{\mathrm{NN}}} = 5.02$ TeV", *Phys. Rev. Lett.* 133.2 (2024), p. 022302. arXiv: `2303.17026` [`hep-ex`].

[99]   **B. Alessandro et al.** "A New measurement of J/psi suppression in Pb-Pb collisions at 158-GeV per nucleon", *Eur. Phys. J. C* 39 (2005), pp. 335–345. arXiv: `hep-ex/0412036`.

[100]   **J. Adam et al.** "Measurement of inclusive J/ψ suppression in Au+Au collisions at $\sqrt{s_{NN}} = 200$ GeV through the dimuon channel at STAR", *Phys. Lett. B* 797 (2019), p. 134917. arXiv: `1905.13669` [`nucl-ex`].

[101]   **S. Acharya et al.** "Measurements of inclusive J/ψ production at midrapidity and forward rapidity in Pb–Pb collisions at $\sqrt{s_{NN}} = 5.02$ TeV", *Phys. Lett. B* 849 (2024), p. 138451. arXiv: `2303.13361` [`nucl-ex`].

[102]   **P. Braun-Munzinger and J. Stachel**. "(Non)thermal aspects of charmonium production and a new look at J/ψ suppression", *Phys. Lett. B* 490 (2000), pp. 196–202. arXiv: `nucl-th/0007059`.

[103]   **A. Andronic et al.** "Transverse momentum distributions of charmonium states with the statistical hadronization model", *Phys. Lett. B* 797 (2019), p. 134836. arXiv: `1901.09200` [`nucl-th`].

[104]   **A. Andronic et al.** "Transverse dynamics of charmed hadrons in ultra-relativistic nuclear collisions", *JHEP* 10 (2024), p. 229. arXiv: `2308.14821` [`hep-ph`].

[105]   **K. Zhou et al.** "Medium effects on charmonium production at ultrarelativistic energies available at the CERN Large Hadron Collider", *Phys. Rev. C* 89.5 (2014), p. 054911. arXiv: `1401.5845` [`nucl-th`].

[106]   **X. Yao et al.** "Coupled Boltzmann Transport Equations of Heavy Quarks and Quarkonia in Quark-Gluon Plasma", *JHEP* 01 (2021), p. 046. arXiv: `2004.06746` [`hep-ph`].

[107]   **B. Wu and R. Rapp**. "Charmonium Transport in Heavy-Ion Collisions at the LHC", *Universe* 10.6 (2024), p. 244. arXiv: `2404.09881` [`nucl-th`].

[108]   **S. Delorme et al.** "Quarkonium dynamics in the quantum Brownian regime with non-abelian quantum master equations", *JHEP* 06 (2024), p. 060. arXiv: `2402.04488` [`hep-ph`].

[109]   **N. Brambilla et al.** "Regeneration of bottomonia in an open quantum systems approach", *Phys. Rev. D* 108.1 (2023), p. L011502. arXiv: `2302.11826` [`hep-ph`].

[110]   **T. Miura et al.** "Simulation of Lindblad equations for quarkonium in the quark-gluon plasma", *Phys. Rev. D* 106.7 (2022), p. 074001. arXiv: `2205.15551` [`nucl-th`].

[111]   **X. Bai et al.** "Data-driven analysis of the beauty hadron production in pp collisions at the LHC with Bayesian unfolding", *JHEP* 11 (2024), p. 018. arXiv: `2405.01444` [`nucl-ex`].

[112]   **S. Acharya et al.** "Λ_c^+ Production and Baryon-to-Meson Ratios in pp and p-Pb Collisions at $\sqrt{s_{NN}}$=5.02 TeV at the LHC", *Phys. Rev. Lett.* 127.20 (2021), p. 202301. arXiv: `2011.06078` [`nucl-ex`].

[113] **M. Cacciari, M. Greco, and P. Nason**. "The p_T spectrum in heavy-flavour hadroproduction.", *JHEP* 05 (1998), p. 007. arXiv: `hep-ph/9803400`.

[114] **B. A. Kniehl et al.** "Inclusive D*+- production in p anti-p collisions with massive charm quarks", *Phys. Rev. D* 71 (2005), p. 014018. arXiv: `hep-ph/0410289`.

[115] **M. Lisovyi, A. Verbytskyi, and O. Zenaiev**. "Combined analysis of charm-quark fragmentation-fraction measurements", *Eur. Phys. J. C* 76.7 (2016), p. 397. arXiv: `1509.01061 [hep-ex]`.

[116] **S. Acharya et al.** "Charm production and fragmentation fractions at midrapidity in pp collisions at $\sqrt{s} = 13$ TeV", *JHEP* 12 (2023), p. 086. arXiv: `2308.04877 [hep-ex]`.

[117] **R. Aaij et al.** "Enhanced Production of Λ_b^0 Baryons in High-Multiplicity pp Collisions at $\sqrt{s} = 13$ TeV", *Phys. Rev. Lett.* 132.8 (2024), p. 081901. arXiv: `2310.12278 [hep-ex]`.

[118] **V. Minissale, S. Plumari, and V. Greco**. "Charm hadrons in pp collisions at LHC energy within a coalescence plus fragmentation approach", *Phys. Lett. B* 821 (2021), p. 136622. arXiv: `2012.12001 [hep-ph]`.

[119] **M. He and R. Rapp**. "Charm-Baryon Production in Proton-Proton Collisions", *Phys. Lett. B* 795 (2019), pp. 117–121. arXiv: `1902.08889 [nucl-th]`.

[120] **F. Prino and R. Rapp**. "Open Heavy Flavor in QCD Matter and in Nuclear Collisions", *J. Phys. G* 43.9 (2016), p. 093002. arXiv: `1603.00529 [nucl-ex]`.

[121] **G. D. Moore and D. Teaney**. "How much do heavy quarks thermalize in a heavy ion collision?", *Phys. Rev. C* 71 (2005), p. 064904. arXiv: `hep-ph/0412346`.

[122] **S. Acharya et al.** "Prompt D^0, D^+, and D^{*+} production in Pb–Pb collisions at $\sqrt{s_{NN}} = 5.02$ TeV", *JHEP* 01 (2022), p. 174. arXiv: `2110.09420 [nucl-ex]`.

[123] **S. Porteboeuf and R. Granier de Cassagnac**. "J/Ψ yield vs. multiplicity in proton-proton collisions at the LHC", *Nucl. Phys. B Proc. Suppl.* 214 (2011). Ed. by Z. Conesa del Valle et al., pp. 181–184. arXiv: `1012.0719 [hep-ex]`.

[124] **E. Norrbin and T. Sjostrand**. "Production mechanisms of charm hadrons in the string model", *Phys. Lett. B* 442 (1998), pp. 407–416. arXiv: `hep-ph/9809266`.

[125] **N. Cooke et al.** "Non-relativistic quantum chromodynamics in parton showers", *Eur. Phys. J. C* 84.4 (2024), p. 432. arXiv: `2312.05203 [hep-ph]`.

[126] **Y.-Q. Ma et al.** "Event engineering studies for heavy flavor production and hadronization in high multiplicity hadron-hadron and hadron-nucleus collisions", *Phys. Rev. D* 98.7 (2018), p. 074025. arXiv: `1803.11093 [hep-ph]`.

[127] **Y. N. Lima, A. V. Giannini, and V. P. Goncalves**. "D0 meson production in pp collisions at large Q_s^2J■", *Phys. Rev. D* 109.9 (2024), p. 094035. arXiv: `2405.03581 [hep-ph]`.

[128] **F. Salazar, B. Schenke, and A. Soto-Ontoso**. "Accessing subnuclear fluctuations and saturation with multiplicity dependent J/ψ production in p+p and p+Pb collisions", *Phys. Lett. B* 827 (2022), p. 136952. arXiv: `2112.04611 [hep-ph]`.

[129] **E. Levin, I. Schmidt, and M. Siddikov**. "Multiplicity dependence of quarkonia production in the CGC approach", *Eur. Phys. J. C* 80.6 (2020), p. 560. arXiv: `1910.13579 [hep-ph]`.

[130] **E. Gotsman and E. Levin**. "High energy QCD: multiplicity dependence of quarkonia production", *Eur. Phys. J. C* 81.2 (2021), p. 99. arXiv: `2008.10911 [hep-ph]`.

[131] **R. Terra and F. S. Navarra**. "Charmonium production in high multiplicity pp collisions and the structure of the proton", *Phys. Rev. D* 108.5 (2023), p. 054002. arXiv: `2306.14298 [hep-ph]`.

[132] **B. Z. Kopeliovich et al.** "J/ψ in high-multiplicity pp collisions: Lessons from pA collisions", *Phys. Rev. D* 88.11 (2013), p. 116002. arXiv: `1308.3638 [hep-ph]`.

[133] **B. Z. Kopeliovich et al.** "Heavy quarkonium in the saturated environment of high-multiplicity *pp* collisions", *Phys. Rev. D* 101.5 (2020), p. 054023. arXiv: `1910.09682 [hep-ph]`.

[134] **E. G. Ferreiro and C. Pajares**. "High multiplicity *pp* events and *J/ψ* production at LHC", *Phys. Rev. C* 86 (2012), p. 034903. arXiv: `1203.5936 [hep-ph]`.

[135] **E. G. Ferreiro**. "Charmonium dissociation and recombination at LHC: Revisiting comovers", *Phys. Lett. B* 731 (2014), pp. 57–63. arXiv: `1210.3209 [hep-ph]`.

[136] **E. G. Ferreiro**. "Excited charmonium suppression in proton–nucleus collisions as a consequence of comovers", *Phys. Lett. B* 749 (2015), pp. 98–103. arXiv: `1411.0549 [hep-ph]`.

[137] **Y. Bai and B. Chen**. "Probing QGP droplets with charmonium in high-multiplicity proton–proton collisions", *Eur. Phys. J. C* 84.11 (2024), p. 1193. arXiv: `2407.10566 [nucl-th]`.

[138] **C. R. Singh et al.** "Charmonium suppression in ultra-relativistic proton–proton collisions at LHC energies: a hint for QGP in small systems", *Eur. Phys. J. C* 82.6 (2022), p. 542. arXiv: `2109.07967 [hep-ph]`.

[139] **J. Adam et al.** "Measurement of charm and beauty production at central rapidity versus charged-particle multiplicity in proton-proton collisions at $\sqrt{s} = 7$ TeV", *JHEP* 09 (2015), p. 148. arXiv: `1505.00664 [nucl-ex]`.

[140] **S. Acharya et al.** "Observation of a multiplicity dependence in the p_{T}-differential charm baryon-to-meson ratios in proton–proton collisions at $\sqrt{s} = 13$ TeV", *Phys. Lett. B* 829 (2022), p. 137065. arXiv: `2111.11948 [nucl-ex]`.

[141] **S. Acharya et al.** "Inclusive and multiplicity dependent production of electrons from heavy-flavour hadron decays in pp and p-Pb collisions", *JHEP* 08 (2023), p. 006. arXiv: `2303.13349 [nucl-ex]`.

[142] **S. Acharya et al.** "Charged-particle production as a function of multiplicity and transverse spherocity in pp collisions at $\sqrt{s} = 5.02$ and 13 TeV", *Eur. Phys. J. C* 79.10 (2019), p. 857. arXiv: `1905.07208 [nucl-ex]`.

[143] **J. Adam et al.** "Measurement of D-meson production versus multiplicity in p-Pb collisions at $\sqrt{s_{\mathrm{NN}}} = 5.02$ TeV", *JHEP* 08 (2016), p. 078. arXiv: `1602.07240 [nucl-ex]`.

[144] **S. Acharya et al.** "Multiplicity dependence of J/ψ production at midrapidity in pp collisions at $\sqrt{s} = 13$ TeV", *Phys. Lett. B* 810 (2020), p. 135758. arXiv: `2005.11123` `[nucl-ex]`.

[145] **S. Acharya et al.** "Forward rapidity J/ψ production as a function of charged-particle multiplicity in pp collisions at $\sqrt{s} = 5.02$ and 13 TeV", *JHEP* 06 (2022), p. 015. arXiv: `2112.09433` `[nucl-ex]`.

[146] **S. Acharya et al.** "Multiplicity-dependent inclusive J/ψ production at forward rapidity in pp collisions at $\sqrt{s} = 13$ TeV", *JHEP* 07 (2025), p. 238. arXiv: `2504.00686` `[hep-ex]`.

[147] **N. J. Abdulameer et al.** "Multiplicity dependent J/ψ and $\psi(2S)$ production at forward and backward rapidity in $p+p$ collisions at $\sqrt{s} = 200$ GeV", (Sept. 2024). arXiv: `2409.03728` `[hep-ex]`.

[148] **J. Adam et al.** "J/ψ production cross section and its dependence on charged-particle multiplicity in $p + p$ collisions at $\sqrt{s} = 200$ GeV", *Phys. Lett. B* 786 (2018), pp. 87–93. arXiv: `1805.03745` `[hep-ex]`.

[149] **S. Chatrchyan et al.** "Event Activity Dependence of Y(nS) Production in $\sqrt{s_{NN}}$=5.02 TeV pPb and $\sqrt{s}$=2.76 TeV pp Collisions", *JHEP* 04 (2014), p. 103. arXiv: `1312.6300` `[nucl-ex]`.

[150] **S. Acharya et al.** "Multiplicity dependence of Υ production at forward rapidity in pp collisions at $\sqrt{s} = 13$ TeV", *Nucl. Phys. B* 1011 (2025), p. 116786. arXiv: `2209.04241` `[nucl-ex]`.

[151] **B. E. Aboona et al.** "Measurements of Υ states production in p+p collisions at $\sqrt{s} = 500$ GeV with STAR: Cross sections, ratios, and multiplicity dependence", *Phys. Rev. D* 112.3 (2025), p. 032004. arXiv: `2502.03769` `[hep-ex]`.

[152] **S. Acharya et al.** "J/ψ production as a function of charged-particle multiplicity in p-Pb collisions at $\sqrt{s_{\text{NN}}} = 8.16$ TeV", *JHEP* 09 (2020), p. 162. arXiv: `2004.12673` `[nucl-ex]`.

[153] **M. Aaboud et al.** "Measurement of quarkonium production in proton–lead and proton–proton collisions at 5.02 TeV with the ATLAS detector", *Eur. Phys. J. C* 78.3 (2018), p. 171. arXiv: `1709.03089` `[nucl-ex]`.

[154] **D. Adamová et al.** "J/ψ production as a function of charged-particle pseudorapidity density in p-Pb collisions at $\sqrt{s_{\text{NN}}} = 5.02$ TeV", *Phys. Lett. B* 776 (2018), pp. 91–104. arXiv: `1704.00274` `[nucl-ex]`.

[155] **S. Acharya et al.** "System-size dependence of the charged-particle pseudorapidity density at $\sqrt{s_{NN}} = 5.02$ TeV for pp, pPb, and PbPb collisions", *Phys. Lett. B* 845 (2023), p. 137730. arXiv: `2204.10210` `[nucl-ex]`.

[156] **S. Acharya et al.** "Measurement of $\psi(2S)$ production as a function of charged-particle pseudorapidity density in pp collisions at $\sqrt{s} = 13$ TeV and p-Pb collisions at $\sqrt{s_{\text{NN}}} = 8.16$ TeV with ALICE at the LHC", *JHEP* 06 (2023), p. 147. arXiv: `2204.10253` `[nucl-ex]`.

[157] **R. Aaij et al.** "Multiplicity dependence of $\sigma_{\psi(2S)}/\sigma_{J/\psi}$ in pp collisions at $\sqrt{s} = 13$ TeV", *JHEP* 05 (2024), p. 243. arXiv: `2312.15201` `[hep-ex]`.

[158] **A. M. Sirunyan et al.** "Investigation into the event-activity dependence of Υ(nS) relative production in proton-proton collisions at $\sqrt{s}$ = 7 TeV", *JHEP* 11 (2020), p. 001. arXiv: 2007.04277 [hep-ex].

[159] **R. Aaij et al.** "Measurement of the multiplicity dependence of Υ production ratios in pp collisions at $\sqrt{s}$ = 13 TeV", *JHEP* 05 (2025), p. 011. arXiv: 2501.12611 [hep-ex].

[160] **T. Martin, P. Skands, and S. Farrington**. "Probing Collective Effects in Hadronisation with the Extremes of the Underlying Event", *Eur. Phys. J. C* 76.5 (2016), p. 299. arXiv: 1603.05298 [hep-ph].

[161] **S. G. Weber et al.** "Elucidating the multiplicity dependence of J/ψ production in proton–proton collisions with PYTHIA8", *Eur. Phys. J. C* 79.1 (2019), p. 36. arXiv: 1811.07744 [nucl-th].

[162] **E. Mobs**. "The CERN accelerator complex. Complexe des accélérateurs du CERN", (2016). General Photo. URL: https://cds.cern.ch/record/2197559.

[163] **G. Aad et al.** "The ATLAS Experiment at the CERN LHC", *Journal of Instrumentation* 3:S08003 (2008). DOI: 10.1088/1748-0221/3/08/S08003.

[164] **S. Chatrchyan et al.** "The CMS Experiment at the CERN LHC", *Journal of Instrumentation* 3:S08003 (2008). DOI: 10.1088/1748-0221/3/08/S08004.

[165] **A. Augusto Alves Jr et al.** "The LHCb Detector at the LHC", *Journal of Instrumentation* 3:S08003 (2008). DOI: 10.1088/1748-0221/3/08/S08005.

[166] **K. Aamodt et al.** "The ALICE experiment at the CERN LHC", *Journal of Instrumentation 1430044* 3 (2008). DOI: 10.1088/1748-0221/3/08/S08002.

[167] **G. Aad et al.** "Observation of a new particle in the search for the Standard Model Higgs boson with the ATLAS detector at the LHC", *Phys. Lett. B* 716 (2012), pp. 1–29. arXiv: 1207.7214 [hep-ex].

[168] **S. Chatrchyan et al.** "Observation of a New Boson at a Mass of 125 GeV with the CMS Experiment at the LHC", *Phys. Lett. B* 716 (2012), pp. 30–61. arXiv: 1207.7235 [hep-ex].

[169] **E. Abbas et al.** "Performance of the ALICE VZERO system", *JINST* 8 (2013), P10016. arXiv: 1306.3130 [nucl-ex].

[170] **J. Alme et al.** "The ALICE TPC, a large 3-dimensional tracking device with fast readout for ultra-high multiplicity events", *Nucl. Instr. Meth. A* 622.1 (Oct. 2010), pp. 316–367. URL: http://dx.doi.org/10.1016/j.nima.2010.04.042.

[171] **C. Lippmann et al.** *Upgrade of the ALICE Time Projection Chamber*, tech. rep. Mar. 2014.

[172] **S. Acharya et al.** "The ALICE Transition Radiation Detector: construction, operation, and performance", *Nucl. Instrum. Meth. A* 881 (2018), pp. 88–127. arXiv: 1709.02743 [physics.ins-det].

[173] **B. Abelev et al.** "Performance of the ALICE Experiment at the CERN LHC", *Int. J. Mod. Phys. A* 29 (2014), p. 1430044. arXiv: 1402.4476 [nucl-ex].

[174] **S. Acharya et al.** "Performance of the ALICE Electromagnetic Calorimeter", *JINST* 18.08 (2023), P08007. arXiv: `2209.04216 [physics.ins-det]`.

[175] **S. Acharya et al.** "Calibration of the photon spectrometer PHOS of the ALICE experiment", *JINST* 14.05 (2019), P05025. arXiv: `1902.06145 [physics.ins-det]`.

[176] **J. Adam et al.** "Determination of the event collision time with the ALICE detector at the LHC", *Eur. Phys. J. Plus* 132.2 (2017), p. 99. arXiv: `1610.03055 [physics.ins-det]`.

[177] **E. Bruna et al.** *Vertex reconstruction for proton-proton collisions in ALICE*, tech. rep. 2009.

[178] **Y. Belikov, K. Safařík, and B. Batyunya**. "Kalman Filtering Application for Track Recognition and Reconstruction in ALICE Tracking System", (1997).

[179] **P. Billoir**. "Track fitting with multiple scattering: a new method", *Nuclear Instruments and Methods in Physics Research* 225 (1984), pp. 352–366. DOI: `https://doi.org/10.1016/0167-5087(84)90274-6`.

[180] **A. Maire**. "Production des baryons multi-étranges au LHC dans les collisions proton-proton avec l'expérience ALICE", PhD thesis. Strasbourg U., 2011. URL: `https://cds.cern.ch/record/1490315`.

[181] **Y. Belikov et al.** "TPC tracking and particle identification in high density environment", *eConf* C0303241 (2003), TULT011. arXiv: `physics/0306108`.

[182] **W. Blum, L. Rolandi, and W. Riegler**. *Particle detection with drift chambers*, Particle Acceleration and Detection. 2008. DOI: `10.1007/978-3-540-76684-1`.

[183] **B. Abelev et al.** *Upgrade of the ALICE Experiment: Letter of Intent*, tech. rep. Geneva: CERN, 2014. URL: `https://cds.cern.ch/record/1475243`.

[184] **S. Acharya et al.** "ALICE upgrades during the LHC Long Shutdown 2", *JINST* 19.05 (2024), P05062. arXiv: `2302.01238 [physics.ins-det]`.

[185] **X. Lu**. "Exploring the performance limits of the ALICE Time Projection Chamber and Transition Radiation Detector for measuring identified hadron production at the LHC", PhD thesis. Heidelberg U., 2013. URL: `https://cds.cern.ch/record/1622225`.

[186] **R. Brun and F. Rademakers**. "ROOT: An object oriented data analysis framework", *Nucl. Instrum. Meth. A* 389 (1997). Ed. by M. Werlen and D. Perret-Gallix, pp. 81–86. DOI: `10.1016/S0168-9002(97)00048-X`.

[187] **S. Acharya et al.** "The ALICE definition of primary particles", *ALICE-PUBLIC-2017-005* (2017). URL: `https://cds.cern.ch/record/2270008`.

[188] **S. Acharya et al.** "Transverse momentum spectra and nuclear modification factors of charged particles in pp, p-Pb and Pb-Pb collisions at the LHC", *JHEP* 11 (2018), p. 013. arXiv: `1802.09145 [nucl-ex]`.

[189] **R. Brun et al.** "GEANT Detector Description and Simulation Tool", *CERN-W5013, CERN-W-5013, W5013, W-5013* (1994).

[190] **G. D'Agostini**. "A Multidimensional unfolding method based on Bayes' theorem", *Nucl. Instrum. Meth. A* 362 (1995), pp. 487–498. DOI: `10.1016/0168-9002(95)00274-X`.

[191] **L. Brenner et al.** "Comparison of unfolding methods using RooFitUnfold", *Int. J. Mod. Phys. A* 35.24 (2020), p. 2050145. arXiv: `1910.14654 [physics.data-an]`.

[192] **T. Adye**. "Unfolding algorithms and tests using RooUnfold", (2011). `https://arxiv.org/abs/1105.1160`. DOI: `10.48550/ARXIV.1105.1160`.

[193] **D. Lange**. "The EvtGen particle decay simulation package", *Nucl. Instrum. Meth. A* 462 (2001), pp. 152–155. DOI: `10.1016/S0168-9002(01)00089-4`.

[194] **E. Barberio, B. van Eijk, and Z. Was**. "PHOTOS – a universal Monte Carlo for QED radiative corrections in decays", *Computer Physics Communications* 66 (1991), pp. 115–128. DOI: `http://dx.doi.org/10.1016/0010-4655(91)90012-A`.

[195] **H. Sharma**. "Prompt and non-prompt J/ψ production in Pb–Pb collisions at $\sqrt{s_{NN}} = 5.02$ TeV with ALICE experiment", PhD thesis. Cracow, INP, 2023.

[196] **L. Musa**. *Conceptual Design Report for the Upgrade of the ALICE ITS*, tech. rep. Geneva: CERN, 2012. URL: `https://cds.cern.ch/record/1431539`.

[197] **S. Gorbunov and I. Kisel**. *Reconstruction of decayed particles based on the Kalman filter*, CBM-SOFT-note-2007-003, GSI, Darmstadt, 7 May 2007.

[198] **T. Chen and C. Guestrin**. "XGBoost: A Scalable Tree Boosting System", *Proceedings of the 22nd ACM SIGKDD International Conference on Knowledge Discovery and Data Mining*. KDD '16. ACM, Aug. 2016, pp. 785–794. URL: `http://dx.doi.org/10.1145/2939672.2939785`.

[199] **A. Hocker et al.** "TMVA - Toolkit for Multivariate Data Analysis", (Mar. 2007). arXiv: `physics/0703039`.

[200] **R. Martinez-Cantin**. "BayesOpt: A Bayesian Optimization Library for Nonlinear Optimization, Experimental Design and Bandits", *Journal of Machine Learning Research* 15 (Nov. 2014), 39153919.

[201] **S. Acharya et al.** "Measurement of beauty and charm production in pp collisions at $\sqrt{s} = 5.02$ TeV via non-prompt and prompt D mesons", *JHEP* 05 (2021), p. 220. arXiv: `2102.13601 [nucl-ex]`.

[202] **S. G. Weber**. "Multiplicity dependent J/ψ production in proton-proton collisions at the LHC", PhD thesis. Darmstadt, Tech. Hochsch., 2018.

[203] **F. Bossu et al.** "Phenomenological interpolation of the inclusive J/ψ cross section to proton-proton collisions at 2.76 TeV and 5.5 TeV", (Mar. 2011). arXiv: `1103.2394 [nucl-ex]`.

[204] **S. Acharya et al.** "Search for jet quenching effects in high-multiplicity pp collisions at $\sqrt{s} = 13$ TeV via di-jet acoplanarity", *JHEP* 05 (2024), p. 229. arXiv: `2309.03788 [hep-ex]`.

[205] **B. Malaescu**. "An Iterative, dynamically stabilized method of data unfolding", (2009). arXiv: `0907.3791 [physics.data-an]`.

[206] **R. Aaij et al.** "Evidence for modification of b quark hadronization in high-multiplicity pp collisions at $\sqrt{s} = 13$ TeV", *Phys. Rev. Lett.* 131 (2023), p. 061901. arXiv: `2204.13042 [hep-ex]`.

[207] **R. Aaij et al.** "J/ψ and D^0 production in $\sqrt{s_{\mathrm{NN}}} = 68.5\,\mathrm{GeV}$ PbNe collisions", *Eur. Phys. J. C* 83.7 (2023), p. 658. arXiv: `2211.11652` `[hep-ex]`.

[208] **S. Acharya et al.** "Measurement of prompt D^0, D^+, D^{*+}, and D_S^+ production in p–Pb collisions at $\sqrt{s_{\mathrm{NN}}} = 5.02$ TeV", *JHEP* 12 (2019), p. 092. arXiv: `1906.03425` `[nucl-ex]`.

[209] **S. Acharya et al.** "Inclusive, prompt and non-prompt J/ψ production at midrapidity in p-Pb collisions at $\sqrt{s_{\mathrm{NN}}} = 5.02$ TeV", *JHEP* 06 (2022), p. 011. arXiv: `2105.04957` `[nucl-ex]`.

Acronyms

ACORDE ALICE COsmic Ray DEtector. 59

ALICE A Large Ion Collider Experiment. iii, v, vii, viii, 1, 12–14, 19, 20, 26, 27, 30, 32–35, 42–48, 52–60, 62–64, 66–72, 75, 89, 123, 156, 166, 167, 171, 176, 187, 188

ATLAS A Toroidal LHC ApparatuS. 13, 54, 55

BC Bunch Crossing. 54, 55

BDT Boosted Decision Trees. viii, 97, 99, 100, 103–110, 117–121, 123, 124, 146, 149–154, 158, 162, 165, 189–193

BNL Brookhaven National Laboratory. 8, 21

CEM Color Evaporation Model. 23, 24, 26

CERN European Organization for Nuclear Research. 8, 53, 54

CGC Color Glass Condensate. 10, 15, 20, 26, 32, 38, 39, 43, 45, 51, 172–175, 187

CMS Compact Muon Solenoid. 29, 30, 46–49, 54, 55

CNM Cold Nuclear Matter. 10, 29, 31, 32

CR Color Reconnection. 16, 17, 172

CR-BLC Color Reconnection Beyond Leading Color. 17, 33, 123, 124, 156, 157, 161, 171–173, 178, 180, 187

CSM Color Singlet Model. 24, 26, 27

CTP Central Trigger Processor. 60

DCA Distance of Closest Approach. 74, 76, 89, 94, 95, 100, 102, 103, 114, 118, 120, 123, 157, 158

DGLAP Dokshitzer–Gribov–Lipatov–Altarelli–Parisi. 9, 18, 40

EMCAL ElectroMagnetic CALorimeter. 59, 60, 66, 67

EPN Event Processing Nodes. 67

EPOS Energy conserving quantum mechanical approach, based on Partons, parton ladders, strings, Off-shell remnants, and Saturation of parton ladders. 15, 17–19, 38, 43, 45, 79–81, 142, 143, 166, 168, 172–175, 179–181, 183, 184, 186, 187

FIT Fast Interaction Trigger. 67

FLP First Level Processors. 67, 68

FMD Forward Multiplicity Detector. 59

FONLL Fixed Order plus Next-to-Leading Logarithm. 32, 33, 154, 161, 162

GM-VFNS General-Mass Variable-Flavor-Number Scheme. 32

HM High-Multiplicity. 61, 73, 75, 79, 83–86, 90–93, 100, 104–106, 109, 121, 124, 127, 133–139, 146, 149, 150, 152, 161–163, 166, 167, 170–175, 177–185, 190–193

HMPID High-Momentum Particle IDentification. 59, 66, 67

HRG Hadron Resonance Gas. 6, 7

ICEM Improved Color Evaporation Model. 24, 26, 27, 45, 173, 174

IDS Iterative, Dynamically Stabilized. 141, 142

ITS Inner Tracking System. 56, 57, 63, 66, 67, 74, 76, 89, 93, 113, 144

LDME Long-Distance Matrix Elements. 24, 25, 27

LHC Large Hadron Collider. iii, v, vii, 1, 8, 29, 30, 33, 40–43, 45, 46, 49, 53–55, 79, 142, 166, 187, 188

LHCb Large Hadron Collider beauty. 27, 42, 48, 54, 123, 156, 176

LO Leading Order. 3, 5, 24, 27

LS Long Shutdown. viii, 53, 67

MB Minimum-Bias. 60, 73–77, 79, 83, 86, 87, 90–93, 100, 105, 106, 109, 111–114, 117, 118, 121, 124, 127, 134–137, 139, 141, 145–147, 149, 150, 152, 155–157, 162–166, 189–193

MC Monte-Carlo. viii, 15, 19, 43, 51, 75–85, 91, 92, 94–96, 99, 100, 102, 104, 106, 108–110, 116–123, 126, 127, 129, 131, 133, 140–146, 151–154, 156–159, 166, 168

MFT Muon Forward Tracker. 67

MIP Minimum Ionizing Particle. 64, 69

MPI Multiple Partonic Interactions. 16, 33, 36, 50, 87, 134, 168, 169

MPV Maximal Probable Value. 69, 70

MWPC Multi-Wire Proportional Chambers. 57–59, 66–68

NLO Next-to-Leading Order. 3, 33

nPDF nuclear Parton Distribution Function. 9, 10

NRQCD Non-Relativistic Quantum Chromodynamics. 24, 26, 27, 37, 38

PCC Particle Composition Correction. 79–81, 142

PDF Parton Distribution Function. 8–10, 16, 24, 26, 32, 33

PHENIX Pioneering High Energy Nuclear Interaction eXperiment. 46, 48, 166

PHOS Photon Spectrometer. 58, 59, 67

PI Partonic Interaction. 16, 17, 37, 38, 50

PID Particle IDentification. vii, 55, 59, 61, 64, 65, 70, 105, 109, 112, 153

PMD Photon Multiplicity Detector. 60

pQCD perturbative Quantum Chromodynamics. 5, 8, 9, 19, 23, 25, 28, 33, 34

PS Proton Synchrotron. 53

QCD Quantum Chromodynamics. iii, v, vii, 1, 3–8, 13, 14, 16, 17, 21, 22, 28, 29, 31, 34, 54, 171

QGP Quark-Gluon Plasma. iii, v, vii, 1, 5–8, 10–16, 18, 19, 28–30, 33–35, 41, 49, 60

RHIC Relativistic Heavy-Ion Collider. 8, 41, 45, 46, 49, 166

RMS Root Mean Square. 140, 149, 154

ROC Receiver Operating Characteristic. 99, 102

ROC AUC Area Under the Receiver Operating Characteristic Curve. 99, 102, 151, 152

SDD Silicon Drift Detectors. 56, 57, 66, 67

SHM Statistical Hadronization Model. 12, 13, 30, 31

SLAC Stanford Linear Accelerator Center. 21

SPD Silicon Pixel Detectors. 56, 60, 61, 67, 73, 74, 89, 90, 95, 100, 101, 103, 157, 158

SPS Super Proton Synchrotron. 8, 53

SSD Silicon Strip Detectors. 56, 57, 66, 67

STAR Solenoidal Tracker at RHIC. 30, 46, 48

TF Time Frame. 67, 68

TOF Time-Of-Flight. 59, 63, 65, 66, 113

TPC Time Projection Chamber. 57, 58, 60, 62–67, 69, 74, 76, 89–91, 100, 101, 103, 106, 112–115, 144, 159

TRD Transition Radiation Detector. viii, 53, 58, 60, 61, 63, 65–71, 73, 90–93, 100, 111–118, 121, 146–148, 160–165, 189–193

UE Underlying Event. 111, 112, 114–117, 147, 148

UrQMD Ultra-relativistic Quantum Molecular Dynamics. 19

ZDC Zero-Degree Calorimeter. 60

Acknowledgments

These four years in Münster working on my thesis have been a great time thanks to many people.

The first "Thank you" goes to my supervisor Anton, who motivated me for choosing to do this PhD with him in Münster, and then always found some time for discussion about our progress, even with his very busy timetable.

I would also like to thank all my colleagues in Münster. That includes especially the J/ψ group, for the mutual help and discussion when it was necessary: Tabea, Ailec, Alexander, Yuan, etc. and more generally the whole AG, for helping me to find my marks at my arrival in Germany, for the great moments in the office, at lunch, in the coffee room, or outside, and for reviewing my thesis: Jona, Peter, Archita, Julius, Felix, Luisa, Adrian, Axel, Tim, Lucia, Christian, Leonardo, Lucas, etc. You are all thanked, even the ones whose name is not given.

A great thanks also to everyone from the Jpsi2ee PAG "big family", especially Ionut for the many long discussions on our analysis and paper.

Finally, I also need to thank my parents for their support for already 28 years now.

Curriculum Vitae

Gauthier Legras

Geburtsdatum: 01/10/1997
Geburtsort: Châtenay-Malabry, Frankreich
Staatsangehörigkeit: Franzözich
Eltern: Michel Legras und Christine Legras (geboren Malaval)

Research experience

2021 – 2025
- **Universität Münster**: studying for PhD (supervisor: Anton Andronic)
  - Member of ALICE experiment (central shifts, gain calibration of TRD...)
  - Analysis of prompt and non-prompt J/ψ production as a function of multiplicity in pp collisions
  - Supervision of practical exercises

2020 – 2021
- **CEA, Saclay**: research internship (supervisor: Michael Winn)
  - Feasibility of χ_c and Ξ_{cc} reconstruction in Pb-Pb collisions with LHCb
  - Algorithm for track matching studies in LHCb

2020
- **Kansas University**: research internship (supervisor: Christophe Royon)
  - Monte-Carlo analysis with Root for search of Beyond Standard Model Physics in $\gamma\gamma WW$ coupling
  - Space particles detector: Near-Earth particle flux estimation for its calibration

2018 – 2019
- **Observatoire de Paris**: research internship (supervisor: Jérémie Vaubaillon)
  - Detection of satellite trajectories in sky images (with python)
  - Programming (python) image classification of satellites with deep learning

Education

2021 – 2025
- **Universität Münster, Institut für Kernphysik**
  Studying for PhD. (in progress)

2017 – 2021
- **École des Mines de Paris - Member of PSL (Paris Sciences et Lettres)**
  Diplôme d'ingénieur (Equivalent Master 2) – Option : Nuclear Engineering

Education

2015 – 2017
- **Lycée Louis-le-Grand – Paris**
  Two-year intensive maths and physics course - preparation for engineering school

Publications and talks

Publications

- A list of publications can be found on [InspireHEP](#).
- **Multiplicity dependence of prompt and non-prompt J/ψ production at midrapidity in pp collisions at $\sqrt{s} = 13$ TeV**
  In preparation, ALICE paper with significant contribution

Talks and posters at international conferences

2023
- **Quarkonium production as a function of multiplicity in pp collisions with ALICE** (talk)
  Deep Inelastic Scattering 2023, East Lansing, 30/03/2023

2023
- **Quarkonia as probes of initial and final states in small systems with ALICE** (poster)
  European Physical Society Conference on High-Energy Physics 2023, Hamburg, 22/08/2023

2024
- **Multiplicity dependence of J/ψ production in pp collisions with ALICE** (poster)
  From Hadron Structure to Heavy-Ion Collisions summer school, Orsay, 11/06/2024

2024
- **Multiplicity dependence of quarkonium production in small systems with ALICE** (poster)
  LHCC students poster session, CERN, 18/11/2024

2025
- **Multiplicity dependence of quarkonium production** (talk)
  Quarkonia As Tools workshop, Aussois, 09/01/2025

Talks at regional and ALICE meetings

2023
- **Prompt and non-prompt Jψ production as a function of multiplicity in pp collisions with ALICE** (talk)
  DPG spring meeting, Dresden, 21/03/2023

2023
- **Recent multiplicity-dependent J/ψ results at midrapidity with Run 2 data** (talk)
  ALICE Physics Week, Bucharest, 13/06/2023

2024
- **Multiplicity dependence of prompt and non-prompt J/ψ in pp collisions with ALICE** (talk)
  DPG spring meeting, Giessen, 12/03/2024

2024
- **Multiplicity dependence of J/ψ production in pp collisions** (talk)
  ALICE Week Juniors day, CERN, 11/07/2024

Skills

Languages	• French (mother language), English (fluent), Spanish (intermediate), German (intermediate)
Coding	• Python, C++ (ROOT), LaTeX